Master's Thesis (Academic Year 2018)

A study of beam background from SuperKEKB on Belle II Silicon Vertex Detector

(Belle II シリコン崩壊点位置検出器の受ける SuperKEKB からのビームバックグラウンドの研究)

The University of Tokyo
Department of Physics, Graduate School of Science

Hikaru Tanigawa

January 31, 2019

Abstract

The Belle II experiment plans to start its full operation in March 2019 hosted by KEK in Tsukuba, Japan. The SuperKEKB accelerator has been upgraded to collide e^+ and e^- beams at a rate forty times higher than its predecessor. The Belle II detector detects the decay products of the particles created after e^+e^- annihilations to explore new areas of flavor physics.

This thesis focuses on the silicon vertex detector at the core of the Belle II detector. The upgrade of SuperKEKB introduces a challenging environment for the silicon vertex detector in two ways: the high data acquisition rate leads to an unignorable dead time of its readout ASIC and the intense beam background causes detector performance to deteriorate. We developed a firmware module which emulates the data processing procedure of the readout ASIC and minimizes the dead time by optimal trigger-veto. We investigated the beam background condition with a subset of the detector in the commissioning phase which ran from March to July of 2018. Based on our estimation of the beam background level in full operation, the full silicon vertex detector was installed in the Belle II detector.

Contents

Chapter 1

Introduction

The Belle II experiment is conducted at the SuperKEKB collider in Tsukuba, Japan. The center-of-mass energy of the asymmetric-energy e^+e^- collider is set at the resonance of $\Upsilon(4S)$ meson, which predominantly decays into a pair of B and anti-B mesons. The previous Belle experiment measured CP-violating parameters in the B decays to confirm the Kobayashi-Maskawa theory. One of the physical goals of the Belle II experiment is a high-precision measurement of the parameters with high-statistics data. To produce more $B\overline{B}$ pairs, SuperKEKB will achieve forty-fold higher peak luminosity than its predecessor by introducing a "nano-beam" scheme and increasing beam currents. Thus, the Belle II detector is required to record data at a much higher rate while dealing with much more intense beam backgrounds.

The operation of the SuperKEKB collider and the Belle II detector is separated into three phases. In Phase 1, the accelerator was commissioned without beam collisions. Single-beam backgrounds were studied with several background monitors in the absence of the Belle II detector. In Phase 2, beam collisions were realized and the Belle II detector without the Vertex Detector (VXD) was installed. Instead of the VXD, a subset of the VXD sensors and another set of background monitors were installed at the core of the Belle II detector. The verification of the nano-beam scheme, the commissioning of the Belle II detector with collision data and the measurement of the beam backgrounds were performed in Phase 2. In Phase 3, the full operation will start with all the subdetectors to accumulate physics data.

The important observables of the Belle II experiment include time-dependent CP asymmetries in the B decays. The $B\overline{B}$ mesons produced almost at rest in the center-of-mass frame fly along the beam axis, boosted due to the asymmetric beam energies. The flight lengths are translated into decay times to measure the time-dependent CP asymmetries. Here the precise measurement of the decay vertices with the VXD plays a crucial role. The VXD consists of two types of silicon detectors, the inner Pixel Detector (PXD) and the outer Silicon Vertex Detector (SVD). These detectors measure the trajectories of charged particles. The main roles of the SVD are as follows: determination of the readout region of the PXD by extrapolating the tracks, vertex reconstruction of long-lived K_S^0 mesons decaying outside the PXD volume, and measurement of the momenta of low-momentum tracks.

This thesis focuses on two issues related to the SVD arising from the upgrade of the experiment. Firstly, the limited size of the trigger buffer in the readout ASIC used in the SVD causes trigger dead time at the high data acquisition rate in Belle II. We developed a firmware module that is to be loaded in an FPGA in the trigger distributing system. The firmware is

optimized for the ASIC and vetoes triggers in a way that minimizes the trigger dead time. The development and performance of the firmware are reported in this thesis. Secondly, the intense beam backgrounds lead to deterioration of the tracking performance and radiation damage on the detector. We report on the beam background studies in Phase 2 conducted with a subset of the SVD. Based on these studies, we estimate the beam backgrounds in Phase 3 to resolve two points: One is if the SVD can start running with good performance at the beginning of Phase 3 and the other is if it can go through the whole Phase 3 without suffering serious radiation damage. We also confirm the correlation between the SVD and the radiation monitor system in order to ensure the effective protection of the SVD by the radiation monitors.

The remaining chapters in the thesis are as follows. In Chapter 2, we introduce the physics motivation for the Belle II experiment. In Chapter 3, we describe the properties of the SuperKEKB accelerator and the Belle II detector. In Chapter 4, we explain the issue on the trigger dead time, and the development and the performance evaluation of the trigger-veto module. In Chapter 5, we describe the effect of the beam background on the SVD and the various beam background sources in SuperKEKB. In Chapter 6, we focus on the simulation of the beam backgrounds. In Chapter 7, the results of the beam background studies in Phase 2 are discussed. In Chapter 8, we summarize the thesis by describing our achievements and remaining studies.

Chapter 2

Physics motivation

2.1 Quark sector of the Standard Model

The Standard Model (SM) of elementary particles is a chiral gauge field theory with $SU(3)_C \times SU(2)_L \times U(1)_Y$ symmetry. It contains three generations of up-type and down-type quarks shown in Tab. 2.1. While the left-handed fields form doublets of the $SU(2)_L$ group, the right-handed fields are singlets. The $U(1)_Y$ hypercharge Y is also different. The quark fields couple with the Higgs field which is an $SU(2)_L$ doublet via the Yukawa interaction. Because the Higgs field has a nonzero vacuum expectation value v, the Yukawa interaction gives rise to the quark mass terms:

$$\mathcal{L}_m = -v\ \overline{u}'_{Lj} Y^u_{jk} u'_{Rk} - v\overline{d}'_{Lj} Y^d_{jk} d'_{Rk} + \text{h.c.} \tag{2.1}$$

Here, $u'_{L,Rj}$ and $d'_{L,Rj}$ are weak eigenstates of the quark fields with generation index j, Y^u and Y^d are 3×3 complex matrices, h.c. stands for Hermitian conjugate. The terms are summed over the repeated indices. The Yukawa matrices $Y^{u,d}$ are transformed into diagonal matrices with real numbers by the unitary rotation of the quark fields in the generation space

Table 2.1: The quantum numbers of the quark fields. $u_{L(R)}$ and $d_{L(R)}$ represent left-handed (right-handed) up-type and down-type quark fields, respectively. The index $j = 1, 2, 3$ denotes the generation. T_3 is the third component of weak isospin, Y is hypercharge, Q is electric charge of $U(1)_{EM}$ symmetry.

	T_3	Y	Q
$\begin{pmatrix} u_{Lj} \\ d_{Lj} \end{pmatrix}$	$+\frac{1}{2}$ $-\frac{1}{2}$	$+\frac{1}{3}$	$+\frac{2}{3}$ $-\frac{1}{3}$
u_{Rj}	0	$+\frac{4}{3}$	$+\frac{2}{3}$
d_{Rj}	0	$-\frac{2}{3}$	$-\frac{1}{3}$

$u'_{L(R)j} = S^u_{L(R)jk} u_{L(R)k}$, $d'_{L(R)j} = S^d_{L(R)jk} d_{L(R)k}$ [1]:

$$\begin{aligned}
\mathcal{L}_m &= -v\overline{u}_{Lj} S^{u\dagger}_{Ljl} Y^u_{lm} S^u_{Rmk} u_{Rk} - v\overline{d}_{Lj} S^{d\dagger}_{Ljl} Y^d_{lm} S^d_{Rmk} d'_{Rk} + \text{h.c.} && (2.2)\\
&= -\overline{u}_{Lj} M^u_{jk} u_{Rk} - \overline{d}_{Lj} M^d_{jk} d_{Rk} + \text{h.c.} && (2.3)\\
&= -\sum_{q=u,d,s,c,b,t} m_q(\overline{q}_L q_R + \overline{q}_R q_L) && (2.4)\\
&= -\sum_{q=u,d,s,c,b,t} m_q \overline{q} q && (2.5)\\
& && (2.6)
\end{aligned}$$

where $M^u = S^{u\dagger} Y^u S^u = \text{diag}(m_u, m_c, m_t)$ and $M^d = S^{d\dagger} Y^d S^d = \text{diag}(m_d, m_s, m_b)$ are diagonal matrices with quark masses, $u_{L(R)1,2,3} = u_{L(R)}, c_{L(R)}, t_{L(R)}$ and $d_{L(R)1,2,3} = d_{L(R)}, s_{L(R)}, b_{L(R)}$ are mass eigenstates, and $q = q_L + q_R$ denotes the Dirac fields of quarks.

The interactions are described by the gauge symmetry; $SU(3)_C$ describes the strong interaction. Because of the nonzero vacuum expectation value of the Higgs field, $SU(2)_L \times U(1)_Y$ spontaneously breaks to $U(1)_{EM}$. Consequently, the $SU(2)_L$ and $U(1)_Y$ gauge bosons are mixed into photons and weak bosons, which respectively mediate the electromagnetic and weak interaction. By using the weak eigenstates, the charged current of weak interaction is expressed as

$$\mathcal{L}_W = \frac{g_2}{\sqrt{2}} \left[\overline{u}'_{Lj} \gamma^\mu d'_{Lj} W^+_\mu + \overline{d}'_{Lj} \gamma^\mu d'_{Lj} W^-_\mu \right] \tag{2.7}$$

where $W^\pm_\mu$ denotes the W bosons, γ^μ is gamma matrices, and g_2 is the coupling constant of $SU(2)_L$. This is also transformed by the unitary rotation of the left-handed quark fields $S^{u,d}_L$:

$$\begin{aligned}
\mathcal{L}_W &= \frac{g_2}{\sqrt{2}} \left[\overline{u}_{Lj} S^{u\dagger}_{Ljl} \gamma^\mu S^d_{Llk} d_{Lk} W^+_\mu + \overline{d}_{Lk} S^{d\dagger}_{Ljl} \gamma^\mu S^u_{lk} d_{Lj} W^-_\mu \right] && (2.8)\\
&= \frac{g_2}{\sqrt{2}} \left[\overline{u}_{Lj} V_{jk} \gamma^\mu d_{Lk} W^+_\mu + \overline{d}_{Lk} V^*_{jk} \gamma^\mu d_{Lj} W^-_\mu \right] && (2.9)
\end{aligned}$$

where $V = S^{u\dagger} S^d$ is a 3×3 unitary matrix in the generation space called the Cabibbo-Kobayashi-Maskawa (CKM) matrix. Therefore, the weak doublets of quarks are redefined as

$$\begin{pmatrix} u \\ d' \end{pmatrix}_L \begin{pmatrix} c \\ s' \end{pmatrix}_L \begin{pmatrix} t \\ b' \end{pmatrix}_L \tag{2.10}$$

where the weak eigenstates of the down-type quarks relate to the mass eigenstates via the CKM matrix:

$$\begin{pmatrix} d' \\ s' \\ b' \end{pmatrix} = V \begin{pmatrix} d \\ s \\ b \end{pmatrix} = \begin{pmatrix} V_{ud} & V_{us} & V_{ub} \\ V_{cd} & V_{cs} & V_{cb} \\ V_{td} & V_{ts} & V_{tb} \end{pmatrix} \begin{pmatrix} d \\ s \\ b \end{pmatrix}. \tag{2.11}$$

2.2 The CKM matrix and Unitarity triangle

Generally, a 3×3 unitary matrix is characterized by three rotation angles and six complex phases. Since the mass terms and kinetic terms of quarks are invariant under the phase rotation of the individual quark Dirac fields, five phases of the CKM matrix are absorbed by rotating

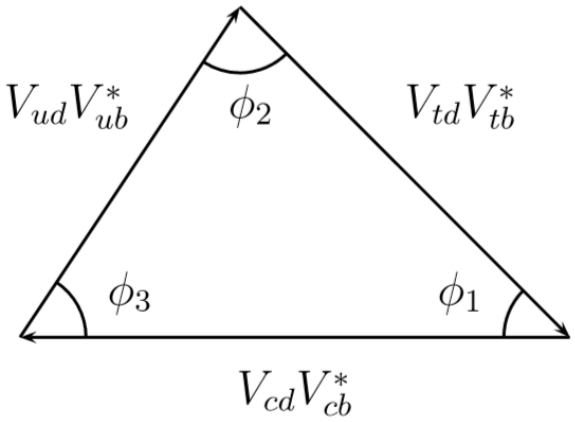

Figure 2.1: The unitarity triangle [3].

the relative phases of the six quark fields. Thus, the CKM matrix is parametrized by three angles $\theta_{ij}(ij = 12, 13, 23)$ and one complex phase δ:

$$V = \begin{pmatrix} c_{12}c_{13} & s_{12}c_{13} & s_{13}e^{-i\delta} \\ -s_{12}c_{23} - c_{12}s_{23}s_{13}e^{i\delta} & c_{12}c_{23} - s_{12}s_{23}s_{13}e^{i\delta} & s_{23}c_{13} \\ s_{12}s_{23} - c_{12}c_{23}s_{13}e^{i\delta} & -c_{12}s_{23} - s_{12}c_{23}s_{13}e^{i\delta} & c_{23}c_{13} \end{pmatrix} \tag{2.12}$$

where $s_{ij} = \sin\theta_{ij}, c_{ij} = \cos\theta_{ij}$. The complex phase δ potentially causes CP violation in the weak interaction of quarks. Since it is experimentally known that $1 \gg s_{12} \gg s_{23} \gg s_{13}$, the Wolfenstein parametrization is often used to explicily show the hierarchy:

$$V = \begin{pmatrix} 1 - \lambda^2/2 & \lambda & A\lambda^3(\rho - i\eta) \\ -\lambda & 1 - \lambda^2/2 & A\lambda^2 \\ A\lambda^3(1 - \rho - i\eta) & -A\lambda^2 & 1 \end{pmatrix} + O(\lambda^4). \tag{2.13}$$

Here, $\lambda \simeq 0.22$ and $A, \rho, \eta = O(1)$.

The unitarity of the CKM matrix is expressed by twelve equations [2]. Among those, the following two equations are suitable for measurements since all the terms on the left hand side are of equal order, $O(A\lambda^3)$:

$$V_{ud}V_{ub}^* + V_{cd}V_{cb}^* + V_{td}V_{tb}^* = 0 \tag{2.14}$$

$$V_{td}V_{ud}^* + V_{ts}V_{us}^* + V_{tb}V_{ub}^* = 0. \tag{2.15}$$

They are expressed as triangles in the complex plane. The first triangle shown in Fig. 2.1 is called the "unitarity triangle" and their angles are given by

$$\phi_1 = arg\left(-\frac{V_{cd}V_{cb}^*}{V_{td}V_{tb}^*}\right) \tag{2.16}$$

$$\phi_2 = arg\left(-\frac{V_{td}V_{tb}^*}{V_{ud}V_{ub}^*}\right) \tag{2.17}$$

$$\phi_3 = arg\left(-\frac{V_{ud}V_{ub}^*}{V_{cd}V_{cb}^*}\right). \tag{2.18}$$

The triangle of Eq. (2.15) has the equal angles up to corrections of $O(\lambda^2)$. ϕ_1, ϕ_2, and ϕ_3 are independent observables that relate to ρ and η, which are not well measured compared to A and λ. The independent measurents of the three angles lead to the verification of the SM. This is one of the physics goals of the Belle II experiment.

Among the three angles, ϕ_1 has been most precisely measured by the Belle experiment through time-dependent CP asymmetry measurement of $B^0 \to J/\psi K^0_S$. The determination of $\sin 2\phi_1$ through $b \to c\bar{c}s$ tree processes is important in the Belle II experiment. One can also determine $\sin 2\phi_1$ by the time-dependent CP asymmetry of $b \to s\bar{q}q$ penguin processes, which is suppressed in the SM and hence sensitive to new physics.

The second angle ϕ_2 is determined by measuring the time-dependent CP asymmetry of $b \to u\bar{u}d$ transitions. The isospin analyses of $B \to \pi\pi,\ \rho\rho,\ \rho\pi$ decays individually determine ϕ_2.

Finally, ϕ_3 is extracted from the interference of $b \to c\bar{u}s$ and $b \to u\bar{c}s$ transitions in $B \to DK$ decays. Since the decay modes include no penguin contribution, they provide theoritically clean measurement of ϕ_3.

Chapter 3

The Belle II experiment

In this chapter, we describe the important features of the Belle II experiment. In particular, we will devote particular attention to the SVD, which we mainly use for our study.

3.1 Operation schedule

The Belle II experiment is conducted in three phases. During Phase 1 in 2016, the accelerator was commissioned without the Belle II detector and the superconducting magnets for final focusing of the beams (called "QCS" magnets). Single-beam backgrounds without beam collisions were studied with several types of dedicated background monitors collectively known as BEAST II [4]. Phase 2 commissioning was conducted from March to July in 2018. In Phase 2, the positron damping ring started its operation to improve the emittance of the injected positron beam, which led to better injection efficiency. The beam collisions were realized by focusing the beams with the QCS magnets. The Belle II detector without the Vertex Detector (VXD) was installed in the interaction region (IR) to record collision data. Instead of the VXD, a subset of the VXD sensors and dedicated background monitors also called BEAST II detectors were installed in the VXD volume of the Belle II detector. Verification of the nano-beam scheme, commissioning of the Belle II detector with collision data and measurement of beam backgrounds were performed in Phase 2. Phase 3 operation will start in March 2018 in order to accumulate physics data, where all the subdetectors including the VXD are installed[1].

3.2 SuperKEKB

The SuperKEKB collider, shown in Fig. 3.1, is an electron-positron collider which consists of a linear accelerator (linac) and the main storage ring. The two rings have asymmetric energies: the 7 GeV electron ring is called the High Energy Ring (HER), and the 4 GeV positron ring the Low Energy Ring (LER).

[1]The second layer of the PXD lacks ten ladders out of twelve. The installation of the whole PXD is planned in 2020.

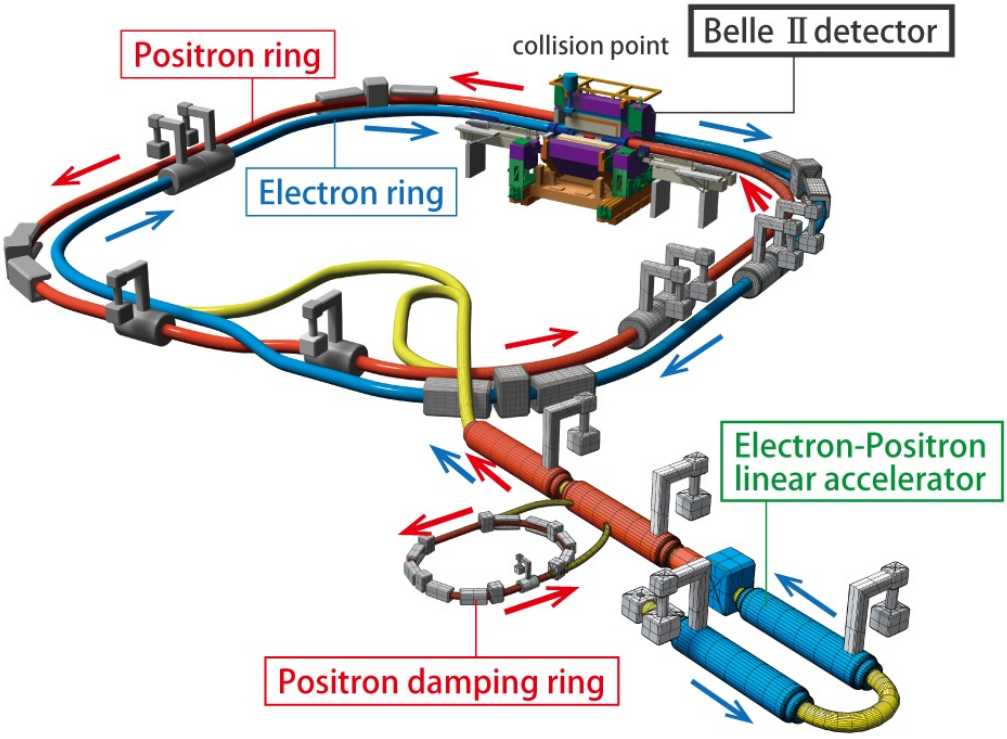

Figure 3.1: The SuperKEKB collider [5].

3.2.1 Main storage ring

The main storage ring consists of four arc sections and four straight sections. Dipole and quadrupole magnets are aligned along the circumference of 3016 m to bend and focus the beams. Together with other correction magnets, these magnets determine how the beam particles propagate along the ring, which is called beam optics. In the middle of the Tsukuba straight section, there are sets of superconducting quadrupole magnets (QCS) for the final focusing of the beam before the collision at the interaction point (IP). The IP is surrounded by the Belle II detector. The radio frequency of the accelerating cavities is 509 MHz. Thus, the ring has 5120 "buckets", in which a bunch of beam particles is stably accelerated by the cavities. In the designed situation, where every other bucket is filled by a bunch of the beam particles, the HER and LER bunches cross each other every 4 ns. The machine parameters of SuperKEKB in Phase 2 and 3 are listed in Tab. 3.1.

The pressures inside the beam pipes are monitored by cold cathode gauges (CCGs). The CCGs are installed together with the sputter ion pumps located approximately every 10 m along the ring. The residual gas composition is analyzed by mass spectroscopy with two residual gas analyzers (RGAs). The vertical and horizontal beam sizes are monitored by X-ray monitors and synchrotron radiation monitors, respectively. Each ring has a bunch current monitor, a DCCT (Direct Current Current Transformer) to monitor the beam current, and over 400 beam position monitors.

For beam background mitigation, movable collimators are installed along the ring. In KEKB,

Table 3.1: The machine parameters of SuperKEKB. The Phase 2 parameters are the typical ones achieved in the late Phase 2. The Phase 3 parameters are taken from [6].

	Phase 2		Phase 3	
Parameter [unit]	LER (e^+)	HER (e^-)	LER (e^+)	HER (e^-)
Beam energy [GeV]	4.0	7.007	4.0	7.007
Beam current I [mA]	327	279	3600	2600
Number of bunches n_b	789	789	2500	2500
Bunch current I/n_b [mA]	0.414	0.353	1.44	1.04
Horizontal emittance [nm]	1.7	4.6	3.2	4.6
Vertical emittance [pm]	–	–	8.64	12.9
Horizontal beta function at IP β_x^* [mm]	200	100	32	25
Vertical beta function at IP β_y^* [mm]	3	3	0.27	0.3
Horizontal beam size at IP σ_x^* [μm]	–	–	10.1	10.7
Vertical beam size at IP σ_y^* [nm]	692	486	48	62
Vertical beam-beam parameter ξ_y	0.0277	0.0186	0.088	0.081
Luminosity L [$\mathrm{cm}^{-2}\mathrm{s}^{-1}$]	2.62×10^{33}		8×10^{35}	

the predecessor of SuperKEKB, the vertical collimators had a jaw only on either the top or bottom side and the horizontal collimators only on the inner side of the main ring. The beams were not collimated from the outer side to prevent the synchrotron radiation from heating the collimators. However, effective suppression of the Touschek background requires the beam collimation also from the outer side. Since the Touschek background is enhanced by the nano-beam scheme, new collimators with jaws on both sides were developed for SuperKEKB and were added to the existing KEKB collimators. In Phase 2, the HER has sixteen KEKB collimators and three new ones, while the LER has five new ones.

3.2.2 Nano-beam scheme

SuperKEKB adopts a nano-beam scheme to achieve high luminosity. This scheme is characterized by a large beam crossing angle and extremely small vertical beam sizes.

The luminosity is given by

$$L = \frac{\gamma_\pm}{2er_e}\left(1 + \frac{\sigma_y^*}{\sigma_x^*}\right)\frac{I_\pm \xi_{y\pm}}{\beta_y^*}\frac{R_L}{R_{\xi_{y\pm}}} \tag{3.1}$$

Here $+$ and $-$ denote positrons and electrons respectively, γ is the Lorentz factor, r_e is the classical electron radius, $\sigma_{x,y}^*$ are the horizontal and vertical beam sizes at the IP, I is the beam current, ξ_y is the vertical beam-beam parameter, β_y^* is the vertical beta function at the IP, and R_L, R_{ξ_y} are the reduction factors for the luminosity and the beam-beam parameters. We assume that electron and positron beams have the same beam sizes and beta function at the IP. According to Eq. (3.1), a smaller beta function leads to a higher luminosity. However, if the beta function becomes as small as the bunch length, further squeezing does not increase the luminosity due to a beam-beam effect. In the nano-beam scheme, we collide the beams with a

large half crossing angle of 41.5 mrad (=ϕ), resulting in a small effective bunch length.

$$\sigma^*_{z,eff} = \frac{\sigma^*_x}{\sin\phi} \tag{3.2}$$

The small effective bunch length makes it possible to increase the luminosity avoiding the beam-beam effect. SuperKEKB squeezes the vertical beta function to 1/20 of that in KEKB. The beam currents are also doubled to achieve the forty-fold higher luminosity.

3.2.3 Linac

The linac provides a 7 GeV electron beam and a 4 GeV positron beam to the main ring. At first, the low-emittance electron beam is produced by a photocathode RF gun and accelerated by the linac. The positrons are produced by colliding 3.5 GeV electrons onto a tungsten target in the middle of the linac. A thermionic electron gun is used for the production of the primary electrons because a high-current electron beam is required instead of a low-emittance one. We accelerate the positrons to 4 GeV with the same accelerating components for the electrons. En route, we circulate them in a 1.1 GeV damping ring to lower the emittance of the positron beam. In Phase 2, the thermionic gun was used for both rings in most cases. The linac is capable of injecting beam bunches at the frequency of 50 Hz while changing the parameters bunch by bunch.

3.2.4 Beam injection

We use two different injection schemes: "normal injection" and "continuous injection". Normal injection is used to accumulate a large amount of beam current. Since we do not turn on the Belle II detector during normal injections, we can perform wilder injections without risking detector damage. After accumulating beam current by normal injections, we start beam collisions and record physics data with the Belle II detector turned on. At this stage, continuous injection is used to continuously accumulate smaller amount of the beam current in parallel with the data acquisition so that the beam currents are kept at the maximum values. This is also known as "top-up injection" or "trickle charge injection". Since we turn on the Belle II detector during continuous injections, more delicate injections are needed to protect detectors.

Keeping the maximum luminosity by continuous injection is essential for efficient data accumulation, because the beam lifetime is as short as several minutes at SuperKEKB. In Phase 3 operation, we will perform continuous injection at 50 Hz while alternately switching the beam species: thus, 25 Hz injections for each ring. In Phase 2, continuous injection was not performed during physics runs and the Belle II detector was turned off at every injection. As an exception, we once measured background rates during LER injections with the Belle II detector on in order to confirm the feasibility of continuous injection (see Section 7.5).

3.3 Belle II detector

The Belle II detector is a general-purpose detector surrounding the IP. Figure 3.2 shows the cross-sectional top view of the detector. It detects final state particles of e^+e^- collisions with seven subdetectors: PXD (Pixel Detector), SVD (Silicon Vertex Detector), CDC (Central Drift

Chamber), TOP (Time of Propagation counter), ARICH (Aerogel Ring Imaging Cherenkov counter), ECL (Electromagnetic Calorimeter), and KLM (K_L^0 and μ detector).

We define the Belle II coordinate system as a right-handed Cartesian system whose origin is at the interaction point. As shown in Fig. 3.3, the z-axis is defined as the median line of the HER and LER beams, and the +Z direction points toward the HER direction. According to the direction toward which the center-of-mass system is boosted because of the asymmetric beam energies, the positive and negative z-directions are called Forward (FWD) and Backward (BWD), respectively. The y-direction points along the vertically upper direction. Consequently, the x-axis points toward the outside of the main ring. The polar angle θ and the azimuthal angle ϕ are defined as $\theta = \arccos(z/\sqrt{x^2+y^2+z^2}), \phi = \arctan(y/x)$. In this thesis, we define the radii of the detectors as $r = \sqrt{x^2+y^2}$.

Because of the asymmetric beam energies, the structure of the Belle II detector is also asymmetric in the polar angle acceptance of $17° < \theta < 150°$.

3.3.1 Subdetectors

The innermost subdetectors are the PXD and the SVD, forming the Vertex Detector (VXD) together. The PXD forms the inner two layers with DEPFET (DEpleted P-channel Field Effect Transistor) pixel sensors, while the SVD forms the outer four layers with double-sided silicon strip sensors. They measure the positions of the charged tracks to reconstruct their production vertices. Because of the small beam pipe radius of 10 mm at the IP, the innermost layer is only 14 mm apart from the IP. Being closer to the IP is advantageous for the high-precision vertex reconstruction, but the background environment becomes severe. Thus, the inner PXD has finer channels of 8 million pixels in total with a typical pixel size of 50×50–$80\,\mu\text{m}^2$. The SVD covers much larger volume with 223,744 strips with 50–240 µm pitches. We describe the SVD in detail in Section 3.4.

The CDC is a drift chamber that has 14,336 sense wires, filled with the gas mixture of 50 % He and 50 % C_2H_6. It measures the trajectories and energy losses of the charged particles for three purposes: measurement of the momenta of the tracks from their curvatures and polar angles, trigger generation by using the track information, and particle identification using the energy-loss rates. The particle identification is important for low-momentum tracks that do not reach the TOP and ARICH.

The TOP and ARICH counters are built for the particle identification of $\pi^\pm$ and $K^\pm$ in the barrel and the forward endcap, respectively. Both reconstruct Cherenkov ring images from the particles to measure their velocities. The TOP counter uses quartz bars as the radiator and detects the Cherenkov photons that propagate to the end of the bars by MCP (Micro-Channel Plate) PMTs. The timing and position information of the hits on the MCP-PMTs are used for the reconstruction. The MCP PMTs have timing resolution better than 50 ps, enabling the TOP to provide good timing triggers. The ARICH counter uses silica aerogel as the radiator and directly reconstructs the ring images detected by HAPDs (Hybrid Avalanche Photon Detectors).

The ECL consists of CsI(Tl) scintillation crystals and PIN photodiodes. It measures the energies and angular coordinates of photons and identifies electrons. The information from the ECL is used for trigger generation and luminosity measurement.

All the detectors up to the ECL are surrounded by a superconducting solenoid. It applies

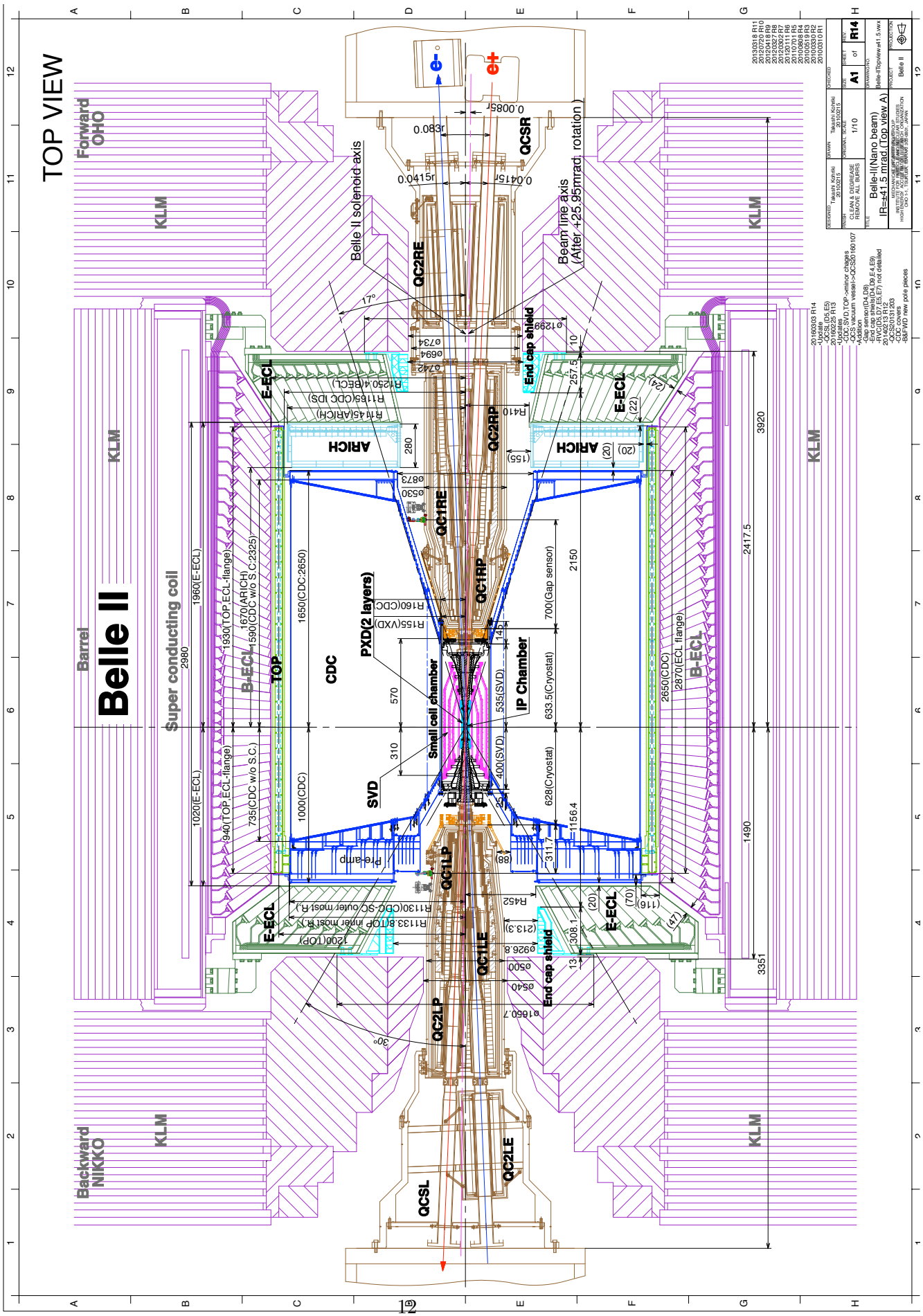

Figure 3.2: The cross-sectional top view of the Belle II detector.

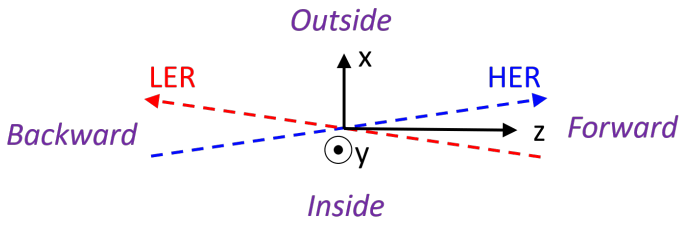

Figure 3.3: The top view of the Belle II coordinate system.

Table 3.2: The estimated cross sections and trigger rates from various physics processes at the $\Upsilon(4S)$ resonance. The Bhabha and $\gamma\gamma$ rates are prescaled by a factor of 1/100. [7]

Process	σ [nb]	Rate [Hz]
$\Upsilon(4S)$	1.2	960
$q\bar{q}$	2.8	2200
$\mu^+\mu^-$	0.8	640
$\tau^+\tau^-$	0.8	640
Bhabha ($\theta_{lab} \geq 17°$)	44	350
$\gamma\gamma$ ($\theta_{lab} \geq 17°$)	2.4	19
Two-photon ($\theta_{lab} \geq 17°$, $p_t \geq 0.1\,\mathrm{GeV}/c$)	∼80	∼15000
Total	∼130	∼20000

the magnetic field of 1.5 T along the z-axis.

The KLM detects K_L^0 mesons and muons. The endcap sections have a sandwich structure of fourteen iron plates and fourteen plastic scintillator layers. The barrel part has fourteen iron plates and fifteen detector layers of RPCs (Resistive Plate Chambers) and plastic scintillators. Muons are identified with hits in the KLM associated with the CDC tracks. K_L^0 mesons are detected as isolated KLM hit clusters. The KLM is the only subdetector outside the superconducting solenoid. The iron plates work as the return yoke of the magnetic field.

3.3.2 Target trigger rate in Belle II

In Belle II, the CDC, ECL, TOP, and KLM provide information for trigger generation [7]. The entire trigger system consists of the four subdetector trigger inputs and the global decision logic (GDL), which makes the final decision.

One of the requirements for the trigger system is to keep the maximum average trigger rate less than 30 kHz. The event rates from main physics processes are listed in Tab. 3.2. Since the total trigger rate from the physics processes amounts to 2/3 of the maximum rate, background suppression is essential to meet the requirement.

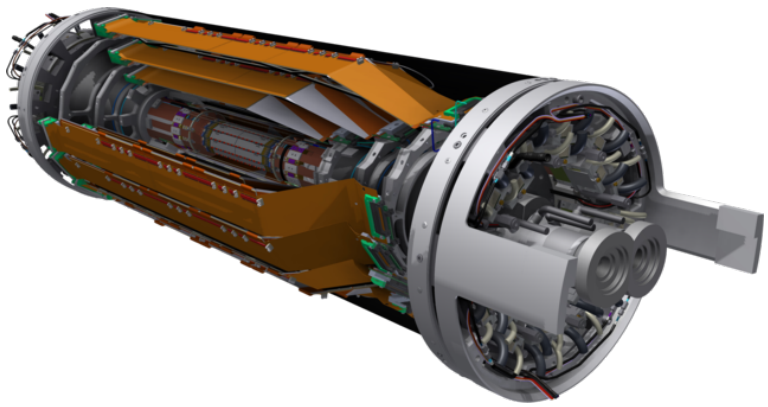

Figure 3.4: The Vertex Detector

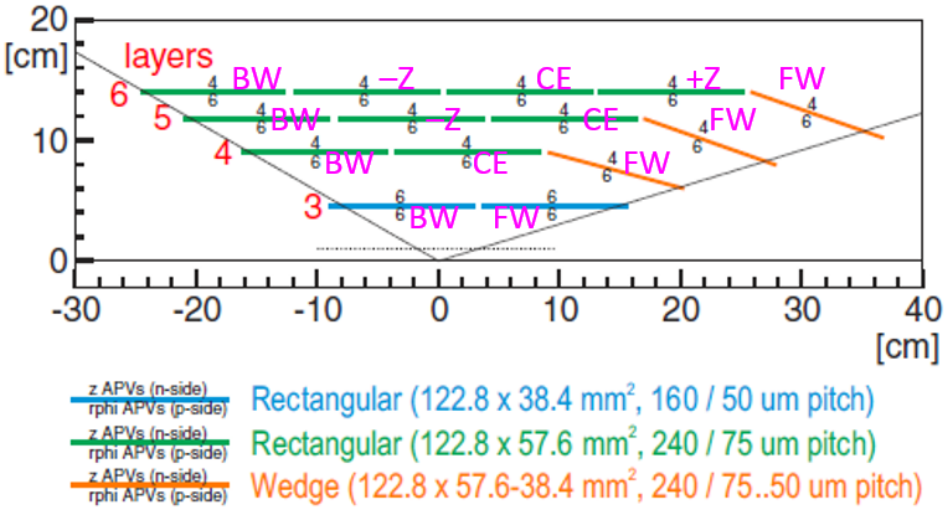

Figure 3.5: Schematic view of the SVD ladders. [8]

3.4 SVD

3.4.1 Structure of the SVD

The SVD consists of four cylindrical layers located at 39 mm, 80 mm, 104 mm, and 135 mm from the z-axis, respectively. The whole VXD structure is shown in Fig. 3.4. The four SVD layers are called L3–6 (Layer 3–6). Layers 1 and 2 correspond to the two PXD layers. Each SVD layer is composed of ladders of 2–5 DSSD (double-sided silicon strip detector) sensors. Ladders in the outer layers have more sensors to cover the wider acceptance region. The sensors are named FW, +Z, CE, -Z, or BW according to their positions on the ladder as shown in Fig. 3.5. To effectively cover the asymmetrically wide acceptance in the forward side, most forward (FW) sensors in L4–6 ladders are slanted. The ladders are placed in a windmill shape to make the edges overlap as shown in Fig. 3.6. Each ladder is labeled by the layer number and ladder number along the ϕ direction, which is shown in Fig. 3.6.

We apply a bias voltage of 100 V on the sensors to deplete them. When an ionizing particle

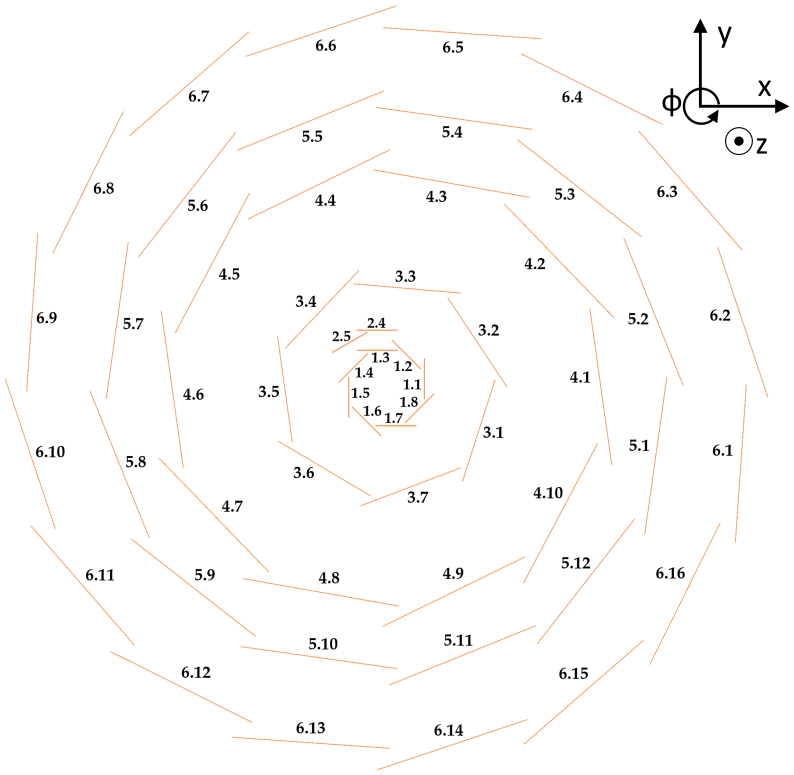

Figure 3.6: The cross section of the VXD in the X-Y plane [9]. The ladder number is shown beside each ladder. In the first year of Phase 3, two L2 ladders are installed out of twelve.

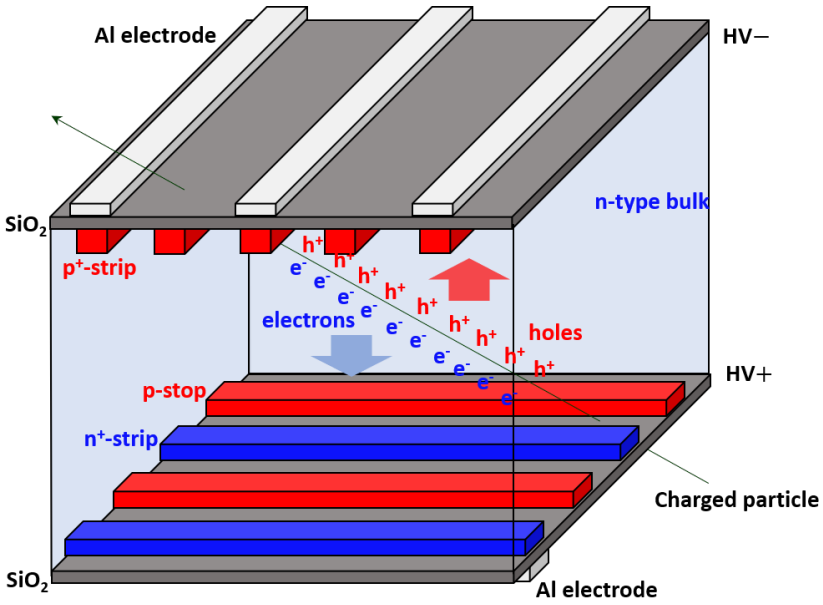

Figure 3.7: The working principle of the DSSD sensor.

traverses the sensor, it produces electron-hole pairs in the depletion region as shown in Fig. 3.7. The carriers are separated to each side of the sensor by the electric field and collected in the strips. The electric signals can be read out from the strips on both sides through Al electrodes.

The strips on each side of the sensor are called P and N strips, according to the types of silicon. As shown in Fig. 3.8, P and N strips measure the r-ϕ and z coordinates, respectively. We define (u,v,w) coordinate on each sensor as shown in Fig. 3.8 so that u- (v-)coordinate increases along the z- (phi-)direction. P (N) strips are also called U (V) strips since they measure u- (v-)coordinates.

Three different sensors are used to form the ladders depending on the position (Tab. 3.3). There are two types of rectangular sensors of different sizes and strip pitches. The smaller sensors are for L3 and the larger ones for L4–6. The other type of sensor is the trapezoidal one for the slanted forward position.

3.4.2 Readout

Figure 3.9 shows the readout chain for the SVD data. We read out the signals from DSSD sensors with frontend ASICs named APV25 [10]. For the sensors at the forward and backward ends of ladders, the APV25 chips are mounted on the rigid printed circuit boards outside the acceptance region. For the other sensors, the APV25 chips are mounted on the flex printed circuit boards which are glued on the DSSD sensors with insulating material in between.

The FADCs[2] control the APV25 and receive the data from them. They are responsible for the analog-to-digital conversion and low-level data processing such as reordering of the data samples and zero suppression. Each FADC can handle data from 48 APV25 chips.

[2]Flash Analog-to-Digital Converters

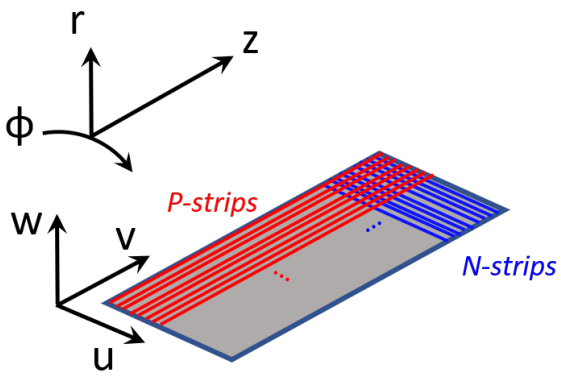

Figure 3.8: (u,v,w) coordinate system on a barrel sensor.

Table 3.3: The parameters of the three types of DSSD sensors [8].

Parameter	Small	Large	Trapezoidal
Location	L3	L4–6 (except FW)	L4–6 (FW)
# P-strips	1535	1535	1535
# Readout P-strips	768	768	768
# N-strips	1535	1023	1023
# Readout N-strips	768	512	512
Pitch (P-side) [µm]	25	37.5	25–37.5
Readout pitch (P-side) [µm]	50	75	50–75
Pitch (N-side) [µm]	80	120	120
Readout pitch (N-side) [µm]	160	240	240
Length [mm]	124.88	124.88	125.58
Width [mm]	40.43	59.6	41.02–60.63
Area [mm^2]	5048.90	7442.85	6382.60
Active area [mm^2]	4737.80	7029.88	5890.00
Thickness [µm]	320	320	300
Manufacturer	Hamamatsu Photonics		Micron Semiconductor

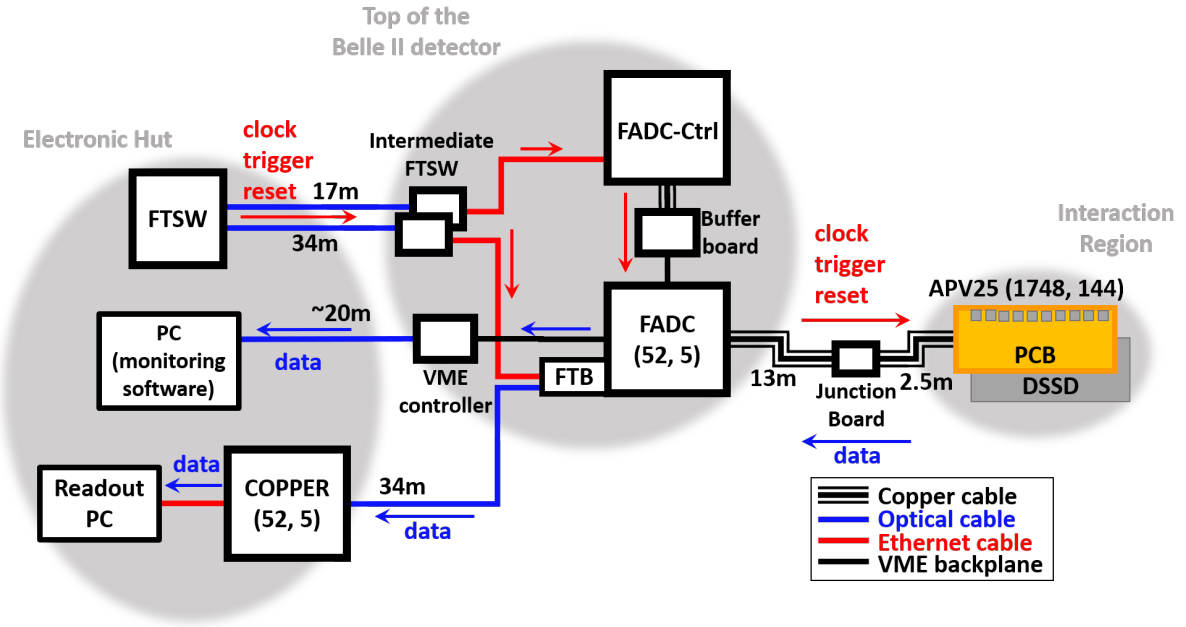

Figure 3.9: The readout chain of the SVD data. Two numbers in parentheses that follow a module name are the number of modules in phase 3, and the number in phase 2, respectively. The readout modules are placed on the top of the Belle II detector and in an "electronic hut" beside the detector.

The electrical signals from the FADCs are transferred with the FTBs[3] via high-speed serial communication over optical data links. They are sent to COPPERs[4], which are the common interface to the central Belle II DAQ.

The trigger signals issued by the GDL and reset signals at the start of every data acquisition run are distributed by the FTSW[5], which also provides a 127 MHz clock to the readout system. We operate the APV25 chips with the system clock of 31.8 MHz which is generated by dividing the 127 MHz clock by four. The FADC-Ctrl[6] encodes the trigger and reset signals to the APV25 format with the 31.8 MHz clock.

The APV25 was originally developed for the CMS silicon strip tracker [10]. The APV25 has 128 input channels, each of which has a preamplifier, a shaper with the shaping time of 50 ns, and an analog pipeline with 192 cells. Figure 3.10 shows the block diagram of analog signal processing in the APV25. We operate the APV25 chips with 31.8 MHz clock and trigger signals. After being amplified and shaped, signals from a DSSD are sampled at the clock rate and recorded in the pipeline. The APV25 outputs three consecutive samples from 192 pipeline cells for reception of a single trigger pulse. We usually send two trigger pulses per each Belle II trigger to the APV25 to read out six consecutive samples for a Belle II trigger (6-sample mode). When the trigger timing resolution is as good as O(ns), three data samples will be good enough to determine the pulse height and the hit timing. In order to reduce the average event size and

[3]Finesse Transmitter Boards
[4]COmmon Pipelined Platform for Electronics Readout
[5]Frontend Timing SWitch
[6]FADC-Controller

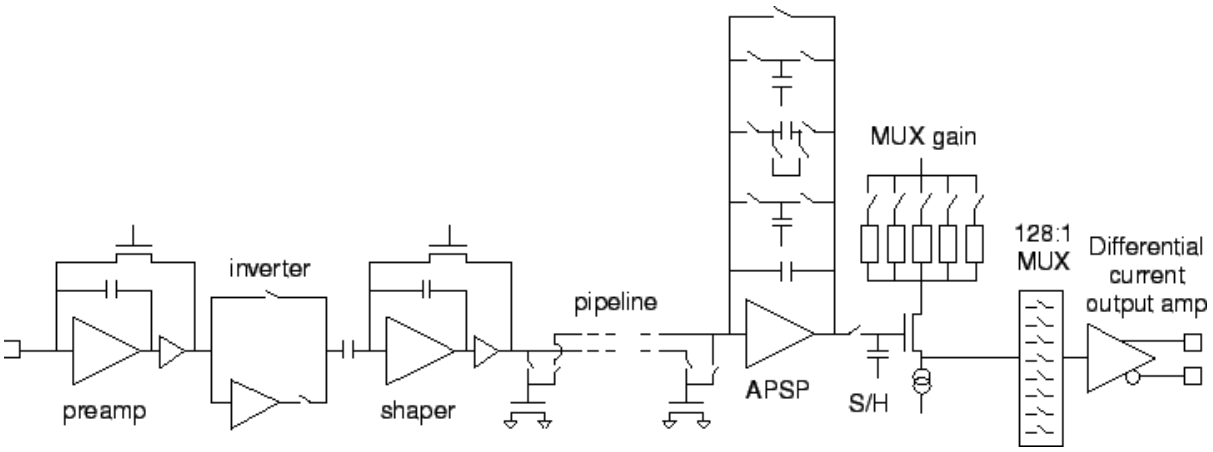

Figure 3.10: Block diagram of the APV25 [11]

hence reduce the SVD dead time (see Section 4.4), we plan to implement a mixed mode, in which we basically read out six samples, but we read out only three samples for the event when the trigger timing is determined by the TOP counters. We focus on the 6-sample mode without explicit expressions from this point and "a trigger" means two trigger pulses that result in a readout of six samples from each strip.

In the zero suppression process in the FADC, we set a threshold to classify the strips into fired and unfired ones. A strip is classified as unfired if all the six samples on the strip are below the threshold, or fired if any of the samples are above the threshold. Data samples on the unfired strips are discarded and not recorded, while the samples on the fired strips are regarded as signal and recorded. The threshold is set to the product of the strip noise and a common signal-to-noise ratio (SNR) factor. The noise is evaluated for each strip as the fluctuation (RMS) of the pedestal ADC values, and the SNR threshold is common for all the strips of the SVD.

While taking data, monitoring software analyzes a part of the data to monitor variables such as occupancy and hit map. The online-monitored variable of interest is occupancy, which is the fraction of fired strips in a sensor. In Phase 2, we record most of the data by the zero suppression with the SNR threshold of 3, while the online occupancy was calculated with the SNR threshold of 5.

The APV25 data output for one sample consists of a serialized 12-bit digital header and sequential 128 analog values of 128 DSSD strip signals as shown in Fig. 3.11. The header contains three high bits, an 8-bit pipeline address and an error bit. Therefore the output of one sample takes 140 clock cycles in total, corresponding to 4.4 μs. In the 6-sample mode, one trigger requires 26.4 μs for readout, limiting the maximum trigger rate for the APV25 to 37.9 kHz. The pulses seen at the edges of Fig. 3.11 are the synchronization pulses called "tick marks". The APV25 issues tick marks every 35 clock cycles[7] when no data is pending. The data output always starts when the tick mark is issued. The length of the data output frame amounts to four tick mark cycles.

Since the analog pipeline cells are overwritten every clock cycle, the 192-cell pipelines can

[7]In the CMS experiment, the APV25 is operated with 40 MHz system clock and 20 MHz readout frequency, which results in a different tick mark period, 70 clock cycles.

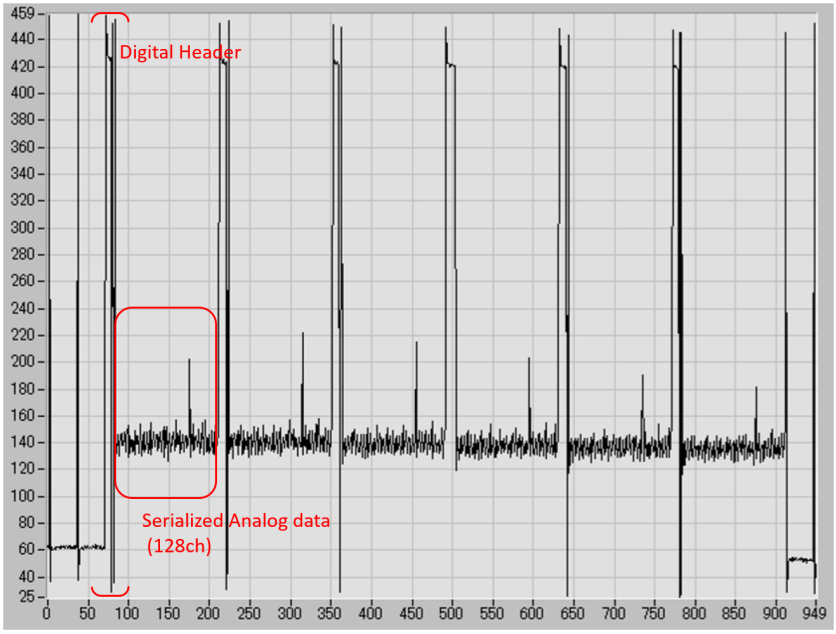

Figure 3.11: Output data frames from the APV25 [8]. The horizontal axis shows time using 31.8 MHz clock as the unit.

only keep the most recent 6.0 µs of data. In order to prevent overwriting samples to be read out before the completion of the readout, the APV25 contains a 32-depth FIFO (First-In-First-Out memory). The procedure is the following:

1. When the APV25 receives a trigger, it applies overwrite-protection on the pipeline cells that contain the triggered samples.
2. The pipeline addresses of the samples are pushed into the FIFO.
3. The samples at the first address in the FIFO are sent out from the APV25.
4. The address is popped out from the FIFO. The cell at the address is released from the protection.

However, if multiple triggers are sent to the APV25 in a short period, a FIFO overflow can happen. The FIFO overflow error is informed by the error bit in the data frames. Once the error occurs, the output data become nonsense unless the chip is reset.

3.4.3 Offline signal reconstruction by basf2

The stored data are analyzed by basf2 (Belle II Analysis Software Framework) [12]. We apply additional hit selections and form clusters with spatially continuous hits. In Phase 2, we usually took data with the zero suppression of SNR = 3 in order not to discard too much data, allowing many noise hits. Thus, offline analysis of the stored data requires additional hit selection to cut off the noise. The energy deposit of a cluster is calculated as the sum of the energies of the contained hits. The typical cluster energy spectrum estimated by Monte Carlo simulation

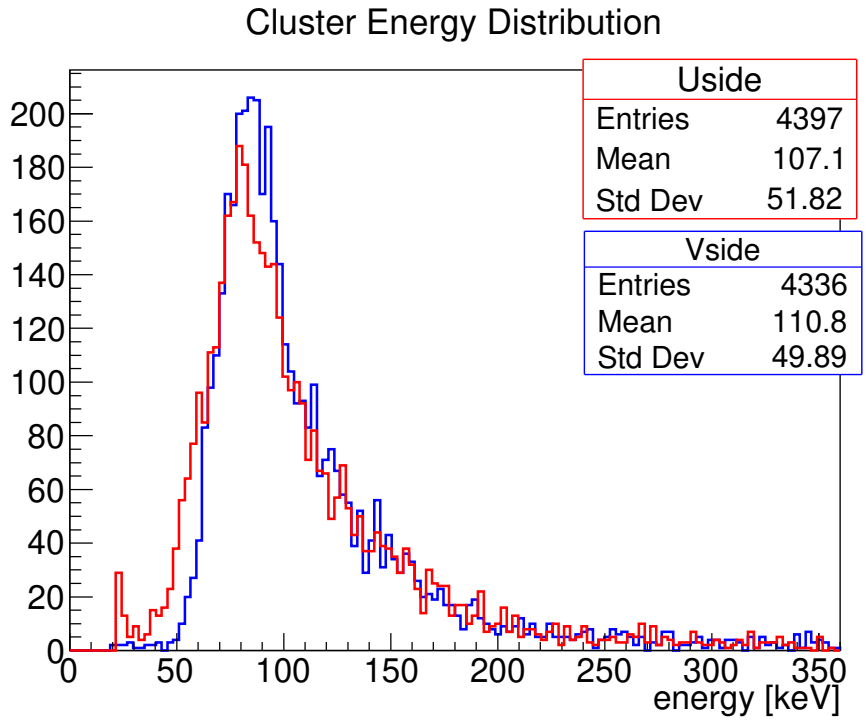

Figure 3.12: Simulated cluster energy distributions on L3BW sensor. The red (blue) line denotes U (V) side clusters. 1 GeV muons from the IP are assumed in the simulation.

is shown in Fig. 3.12. The size of a cluster is defined as the number of the strips contained in the cluster.

3.4.4 Phase 2 SVD cartridge

In Phase 2, we installed the SVD cartridge shown in Fig. 3.13 instead of the full detector. The cartridge contains one ladder for each layer. The ladders are aligned up straight in the +X direction (the outward direction of the SuperKEKB main ring) where the highest background rate is predicted by the MC simulation.

3.4.5 Diamond detector

The radiation monitoring system for the VXD uses $(4.5 \times 4.5 \times 0.5)$ mm^3 single-crystal diamond detectors. Figure 3.15 shows the diamond detector. The single-crystals are artificially grown by the chemical vapor decomposition (CVD) technique. Diamond is a suitable material for a radiation monitor at Belle II because of its radiation resistivity and negligible temperature dependence. [13]

In Phase 3, 28 diamond sensors in total are installed around the SVD: six sensors each on the FWD and BWD sides of SVD support structure, four each on the FWD and BWD side of the beam pipe, and four each on the bellows pipes at the FWD and BWD ends of the beam pipe. In Phase 2, eight sensors were installed on the beam pipe: four on the FWD side and four on the BWD side as shown in Fig. 3.14. Each sensor is labeled by the side (FWD or BWD) and

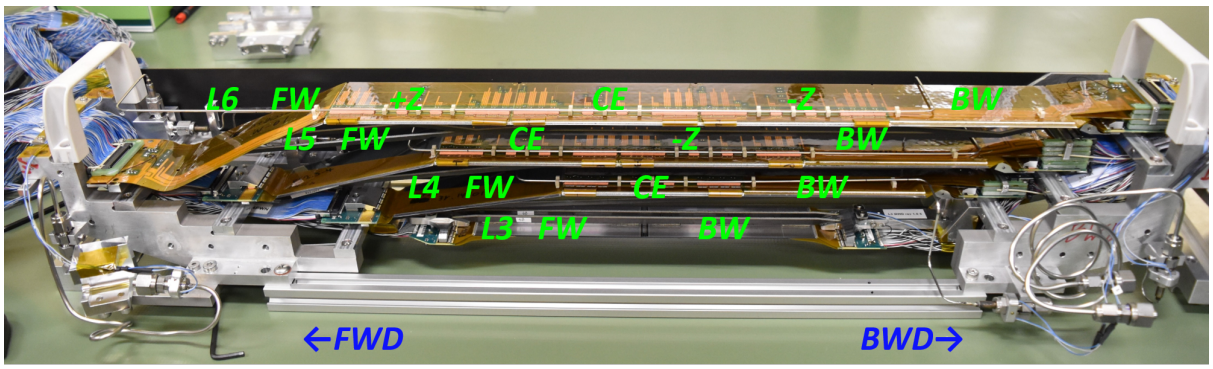

Figure 3.13: The SVD cartridge for Phase 2 commissioning

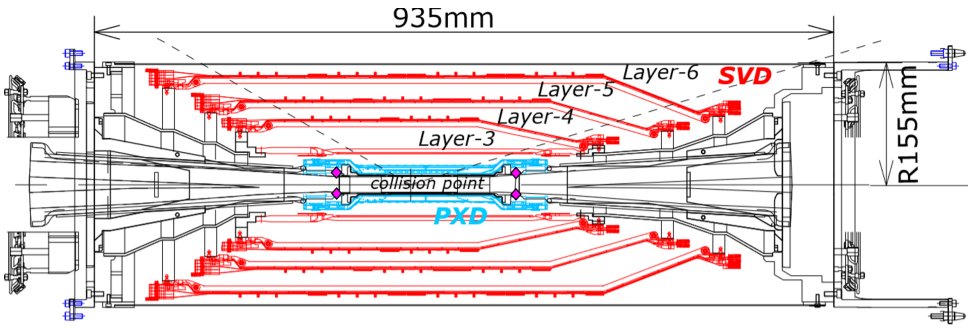

Figure 3.14: The diamond sensors are located at ⋄ in Phase 2. Twelve sensors are added on the conical structure supporting the SVD in Phase 3.

by the channel number (ch0–3) or the azimuthal angle where it is located (ϕ = 55, 125, 235, 305°). Figure 3.16 shows the positional relations of the Phase 2 VXD sensors and diamonds.

The diamond sensors are responsible for the continuous measurement of the instantaneous and integrated radiation doses. To protect the VXD from severe irradiation, they provide beam abort signals to the accelerator at the moment when the radiation dose amount in a short time interval reaches a certain threshold. The measurable radiation range can be selected. Since providing the abort signal requires a larger range at the sacrifice of precision, we alternately used the sensors on one side for beam abort and those on the other for precise measurement in Phase 2.

3.5 Key research subjects in this thesis

The Belle II experiment is intended to acquire data of 50 ab^{-1} integrated luminosity in a decade, which requires a much higher rate of triggers and larger beam backgrounds than the Belle experiment. For the SVD, this requirement causes two major challenges. Firstly, the required average trigger rate of 30 kHz is close to the maximum readout rate of the APV25 in the 6-sample mode, leading to the dead times of the APV25. We describe the issue and countermeasures to it in Chapter 4. Secondly, the accelerator upgrade increases the beam background particles by a

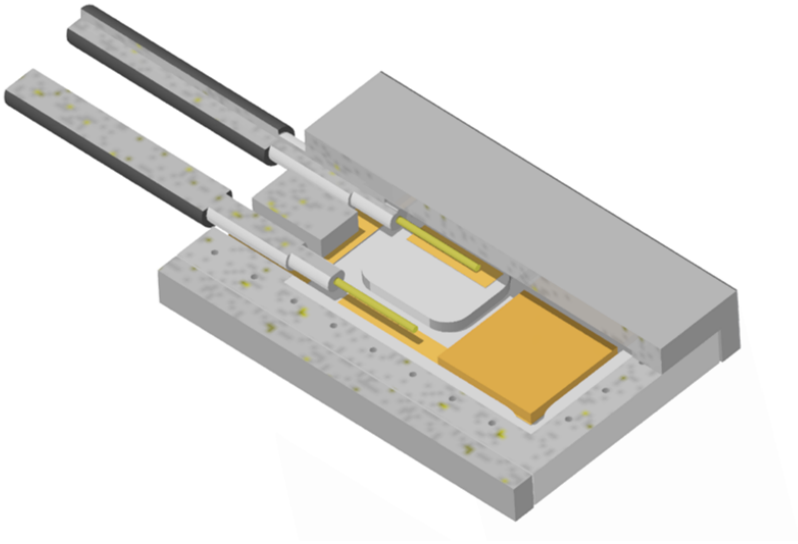

Figure 3.15: The diamond detector.

factor of about 30 [8], leading to the deterioration of tracking performance due to fake hits and radiation damage on the detector. In Chapter 5, we explain the effect of the beam background on the SVD and the origins of them. The beam background studies in Phase 2 are described in Chapters 6 and 7.

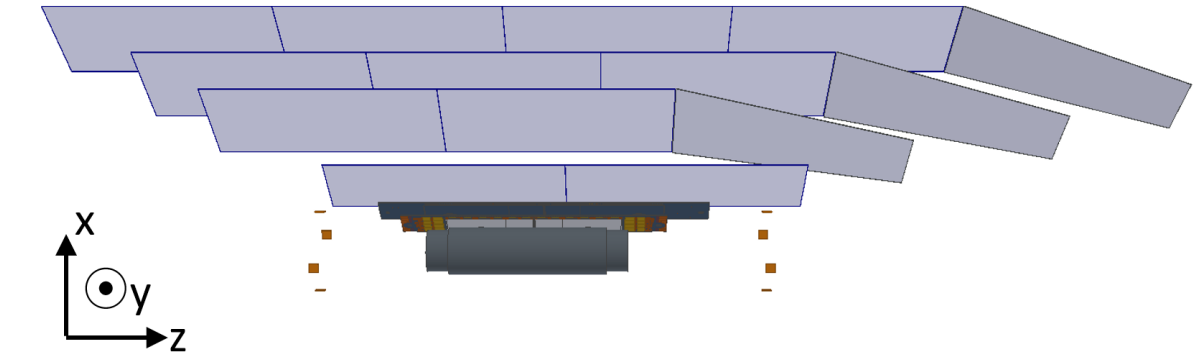

(a) 3-D view

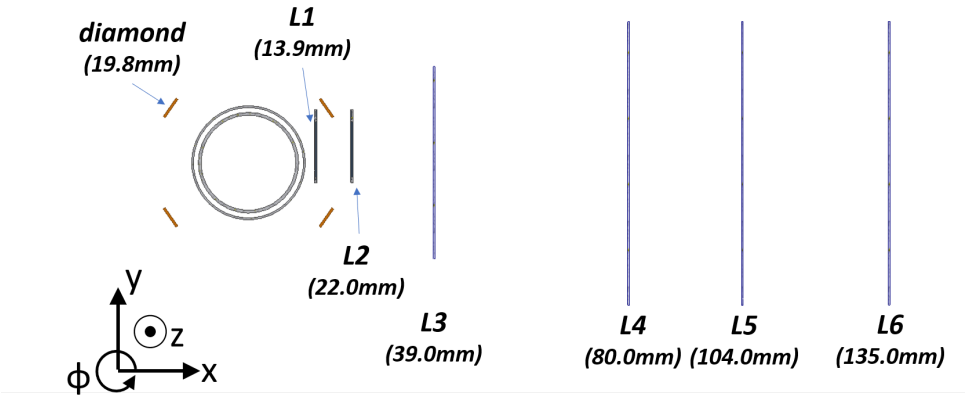

(b) X-Y projection

Figure 3.16: The 3-D view (a) and the projection onto the X-Y plane (b) of the VXD sensors, the diamonds, and the beam pipe in Phase 2. Only the DSSD sensors and the diamond crystals are shown out of the SVD and diamond sensors. In (b), the distance from the z-axis is shown in the parenthesis for each detector.

Chapter 4

Trigger veto

In order to meet the requirement of the average trigger rate of 30 kHz, we need to deal with the APV25 dead time. We developed a firmware module named "APV25-FIFO emulator" [14] as a countermeasure. The stability of the module and the resulting dead time are evaluated. We explain the necessity of the APV25-FIFO emulator in Section 4.1, the concept of the module in Section 4.2, performance evaluation in Section 4.3, and future prospects in Section 4.4.

4.1 Issue on trigger-veto for SVD

Since the FIFO depth of the APV25 is finite, the FIFO overflow can happen by an instantaneous increase of the trigger rate.[1] If we send 30 kHz trigger without any limitation, the APV25 suffers the FIFO overflow in about 3 ms and needs to be reset for resuming data taking. Since the recovery takes a considerable time in which SVD becomes inactive, the FIFO overflow leads to huge DAQ inefficiency. Therefore, it is essential to prevent the overflow by vetoing the triggers that would cause the FIFO overflow.

Since the event reconstruction is supposed to be done for every trigger with the data from all the Belle II subdetectors, vetoing the excessive triggers only in the SVD readout system would stop the event reconstruction. Therefore, the trigger-veto system should be implemented in the master FTSW, which distributes triggers to each subdetector.

The easiest way of avoiding the overflow is to apply a veto after every accepted trigger until its readout is completed (26.4 µs after every trigger). However, we lose 44 % of triggers with this method if we assume 30 kHz random triggers. A more optimized trigger-veto system is necessary for high-speed data acquisition in Belle II.

The most optimal trigger-veto is to reject triggers only when they would cause overflow on an almost full FIFO. Such a trigger-veto scheme requires information of the FIFO occupancy for the veto decision. However, the APV25 does not provide such information until the overflow actually happens. Thus, we need to estimate the occupancy by using input signals of the APV25. For that purpose, we investigated the behavior of the APV25 on a test bench to construct a model which describes how the APV25 processes data. Here we placed importance

[1] The FIFO depth is 32 samples while one trigger occupies six samples and one sample takes 4.4 µs to be read out. For example, six triggers (36 samples) coming in 17.6 µs (i.e. before four samples are read out) causes the overflow.

on the simplicity of the model, as it leads to simple implementation and conservation of FPGA resources.

We developed a trigger-veto firmware module (APV25-FIFO emulator) based on the model, which emulates the FIFO occupancy to prevent overflow with minimal vetoes.

4.2 Design of the APV25-FIFO emulator

The development of the APV25-FIFO emulator requires the simple model which predicts the timing and error bits of the APV25 output. We observed the behavior of the APV25 with the dedicated setup described in Section 4.2.1 to construct the model. In Section 4.2.2, we introduce the model, based on which the firmware module was developed. The implementation of the module in the FTSW requires two additional features to compensate two gaps between the FTSW and the FADC-Ctrl about the clock frequency and the reset timing. These features are described in Sections 4.2.3 and 4.2.4.

4.2.1 Development test bench for the APV25-FIFO emulator

The critical information for the APV25-FIFO emulator is the occurrence condition of the FIFO overflow. We investigated the condition by observing the output signal sequences to known input signal sequences on a dedicated setup shown in Fig. 4.1(a). A photograph of the test bench is shown in Fig. 4.2. The setup contains an FTSW, an FADC-Ctrl, an FADC, and a flexible circuit board designed for L6 +Z sensors with ten APV25 chips on it. We can generate reset and trigger signals at arbitrary timing with the FADC-Ctrl. The output signals to the inputs are observed through digitization in the FADC or directly from the flexible board by an oscilloscope. The tick mark timing, the start timing of the data frames, and the error bits in the data frames are checked. The waveforms of reset, trigger, tick marks and data output signals which are observed by the oscilloscope are shown in Fig. 4.3.

We can test the functionality of the developed firmware module with the same setup as shown in Fig. 4.1(b). Triggers are either generated by the FTSW itself, or are generated by an external trigger generator and sent to the FTSW. The firmware module is loaded in the FTSW, and the triggers are examined by the module before being sent out from the FTSW. We can monitor a part of the data digitized by the FADC. By sending high rate triggers and checking the error bits by the monitoring software, the functionality of the APV25-FIFO emulator was tested (see Section 4.3.1).

4.2.2 APV25 data processing model

The APV25 data processing model aims to predict the FIFO occupancy by emulating the timing of the tick marks and data output with the timing of the input trigger and reset signals. We assumed the model as below and measured the three parameters in the model at the test bench shown in Fig. 4.1(a). The model assumes:

- The reset signal determines the phase of tick marks which are issued at every 35 clock cycles. The first tick mark in the new cycle is issued after *18 clock cycles* from the reset signal as shown in Fig. 4.4.

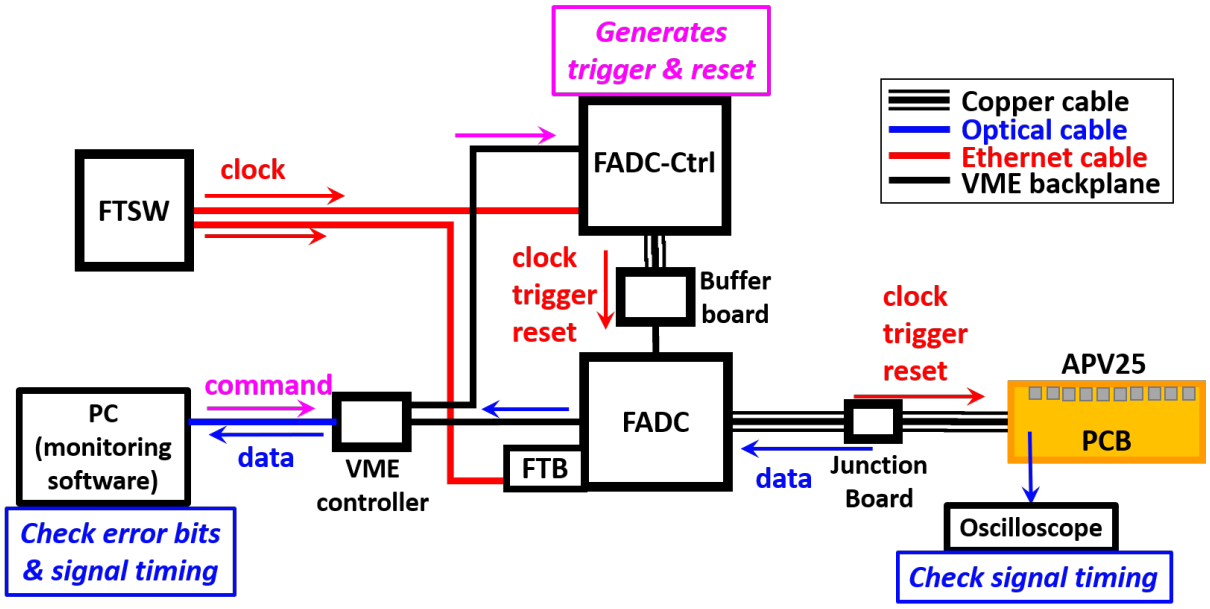

(a) Setup for APV25 behavior study

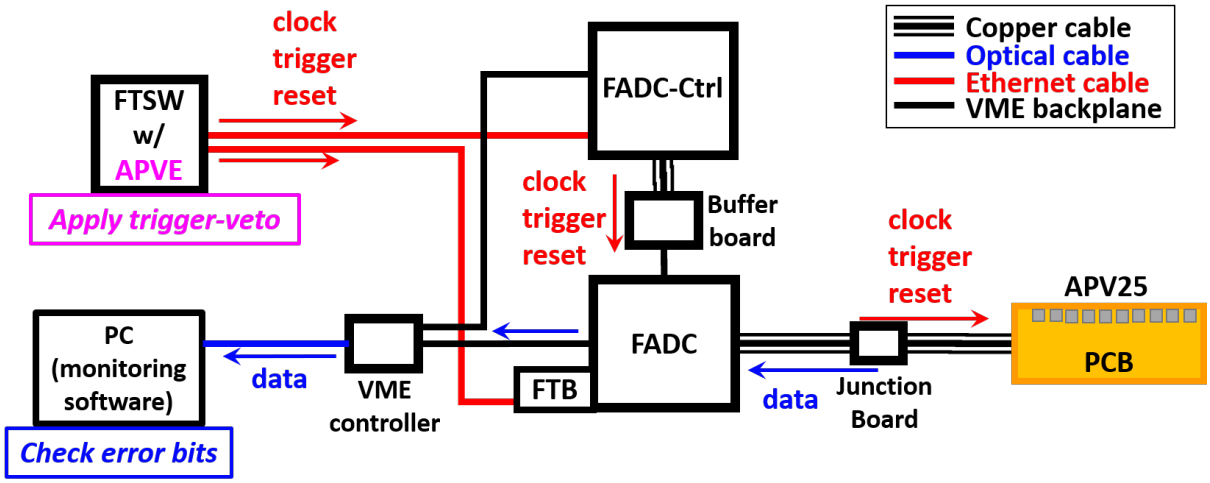

(b) Setup for the firmware module test

Figure 4.1: The test bench for the investigation of the APV25 behavior (a) and the performance evaluation of the APV25-FIFO emulator (b). The setup is a simplified version of the SVD readout chain shown in Fig. 3.9 without DSSD sensors and COPPERs. The reset and trigger signals are sent from the FTSW or are generated in the FADC-Ctrl. The data from the APV25 chips are digitized in the FADC and a part of them is read out by the monitoring software.

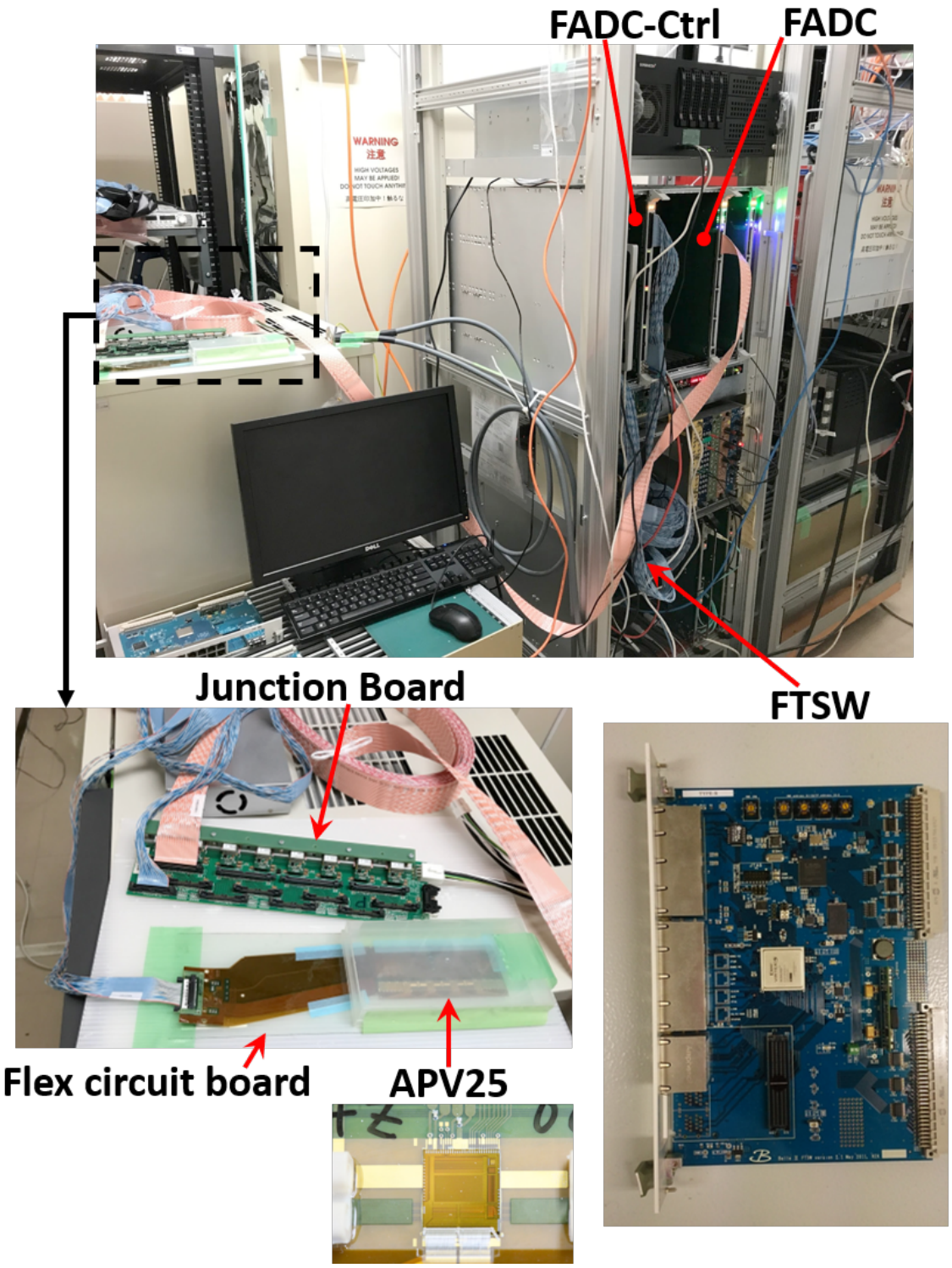

Figure 4.2: The photograph of the test bench. The 9U VME boards in the upper crate of the upper photograph are the FADC-Ctrl and FADC boards. The 6U VME board shown in lower right is the FTSW.

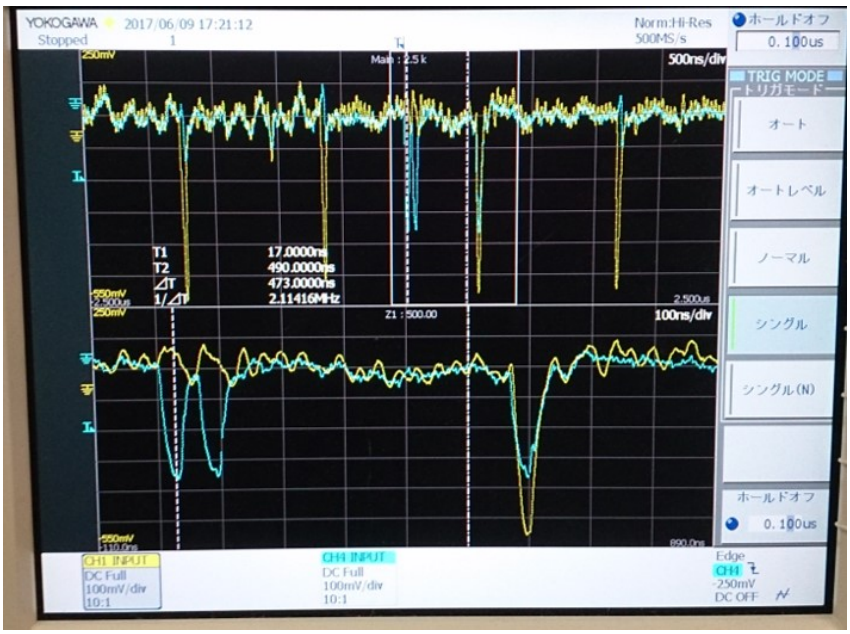

(a) Input trigger line and tick marks

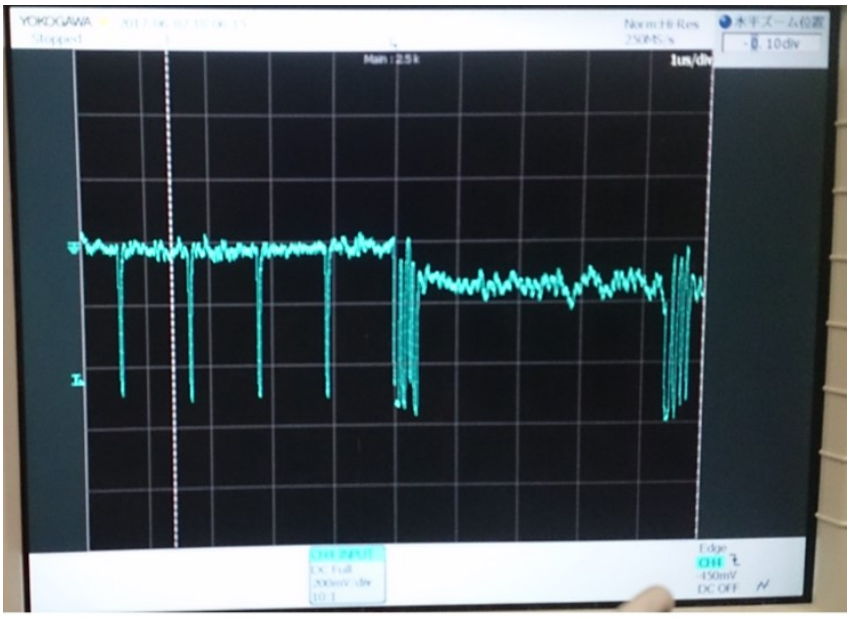

(b) Output signal

Figure 4.3: Input and output signals of the APV25 are observed by an oscilloscope. They are read out from the negative lines of the LVDS lines and hence inversely polarized. Since we read them out from the connector of the printed board using the probes of the oscilloscope, the signals are distorted. (a) shows the input line to the APV25 in blue and the output line in yellow. Reset and trigger signals are transmitted as 3-bit sequences via the single input line, reset corresponding to "101" and trigger "100". In (a), a reset and a trigger signal are being sent. We can see the periodic tick marks on the output line. The output signal is shown in (b). Tick marks are followed by data output frames, which consist of a 12-bit digital header and 128-bit analog strip signals.

- When the APV25 receives a trigger, it needs some time to start sending out the data frames. The data output starts at the first tick mark after a delay of *116 clock cycles* from the trigger signal as shown in Fig. 4.5, when no earlier data are pending. When there are pending data, the new data sample is sent out consecutively after the earlier ones.
- When a trigger is sent to the APV25, the pipeline addresses of the triggered 3 or 6 samples immediately occupy the FIFO. When the output of a data frame starts, the corresponding pipeline address is dequeued from the FIFO after *24 clock cycles* from the start of the data header. Therefore, when the data sample of 27th address in the FIFO is being read out, the next trigger causes a FIFO overflow only if it comes earlier than 24 clock cycles after the start of the data output. Figure 4.6 illustrates the timing chart of the FIFO occupancy and ideal veto signal resulting from this assumption.

The measured parameters are indicated by italic characters in the above assumptions. For the measurement, we chose the FADC-Ctrl as the trigger source. By scanning the timing of trigger signals, the delay parameters were found at the critical points where the output signal drastically changes.

The assumptions above enable us to determine when the trigger should be vetoed as long as we know the input signal sequence, that is, the timing of the reset and trigger signals to the APV25. According to the first assumption, the reset timing determines the tick mark timing. Then, based on the second assumption, the trigger timing identifies tick mark cycles in which the triggered data frames are sent out. By subtracting the number of output data frames from that of input triggers times six[2], the number of the pending data samples (the FIFO occupancy) is obtained. The third assumption determines the exact timing relative to the timing of data output when the FIFO occupancy is decreased. Triggers are acceptable when the occupancy is 26 or less[3]; otherwise, they would cause a FIFO overflow.

4.2.3 Clock frequency gap between the FTSW and the APV25

Based on the model described above, the core module of the APV25-FIFO emulator is designed. This module receives 31.8 MHz clock, trigger, and reset signals as the input and provides the trigger-veto signal as the output. We show the conceptual diagram of the module in Fig. 4.7.

However, the trigger and reset signals are synchronized with the 127 MHz system clock in the FTSW. To compensate the clock frequency difference, the FADC-Ctrl generates 31.8 MHz clock by counting the input 127 MHz clock and latch the input signals with the divided clock. In the same way, we need to convert the input signal sequence on the 31.8 MHz clock basis before using them for the APV25-FIFO emulation. There is a fourfold ambiguity which we have to resolve in the phase of the 31.8 MHz clock generated in the FADC-Ctrl since there is no function to deliver the clock phase back to the FTSW. If the 31.8 MHz clock phase is different between the APV25-FIFO emulator and the APV25, the timing of the translated 31.8 MHz trigger and reset signals can be different as shown in Fig. 4.8, which leads to the wrong emulation.

To deal with the phase ambiguity, we implement four identical emulator submodules whose input clock phases are different from each other as shown in Fig. 4.9. By taking the OR of the

[2]Six data samples are read out per trigger in 6-sample mode.
[3]The FIFO depth (32) minus the number of data samples per trigger (6).

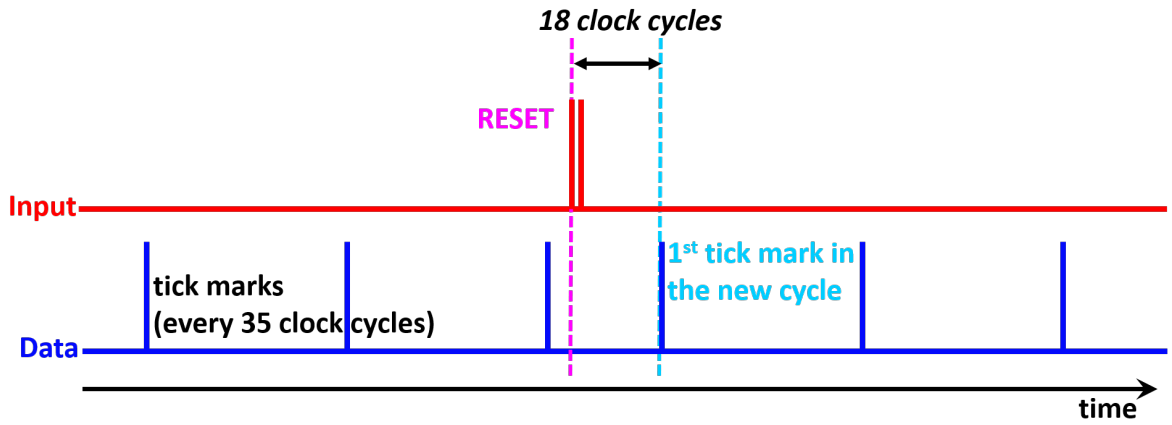

Figure 4.4: Reset signals for the APV25 also reset the tick mark cycle. The first tick mark in the new cycle is issued after 18 clock cycles from the reset signal. A reset signal is expressed as 101 signal on the input trigger line.

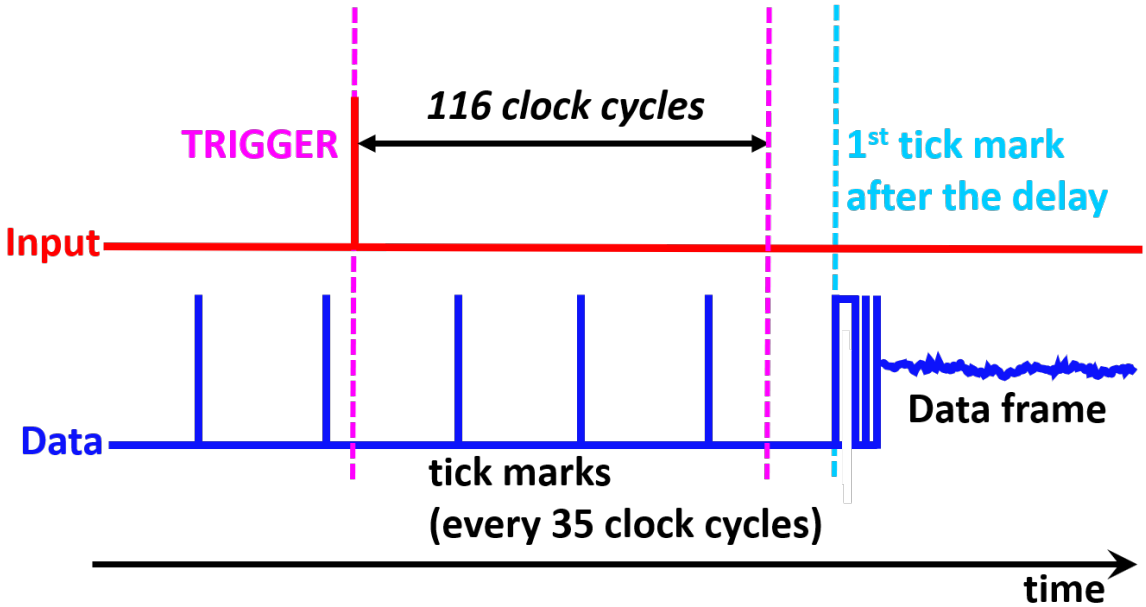

Figure 4.5: After reception of a trigger, the APV25 needs 116 clock cycles to become ready for sending out data frames. After the interval, the output starts at the first timing when the tick mark would stand.

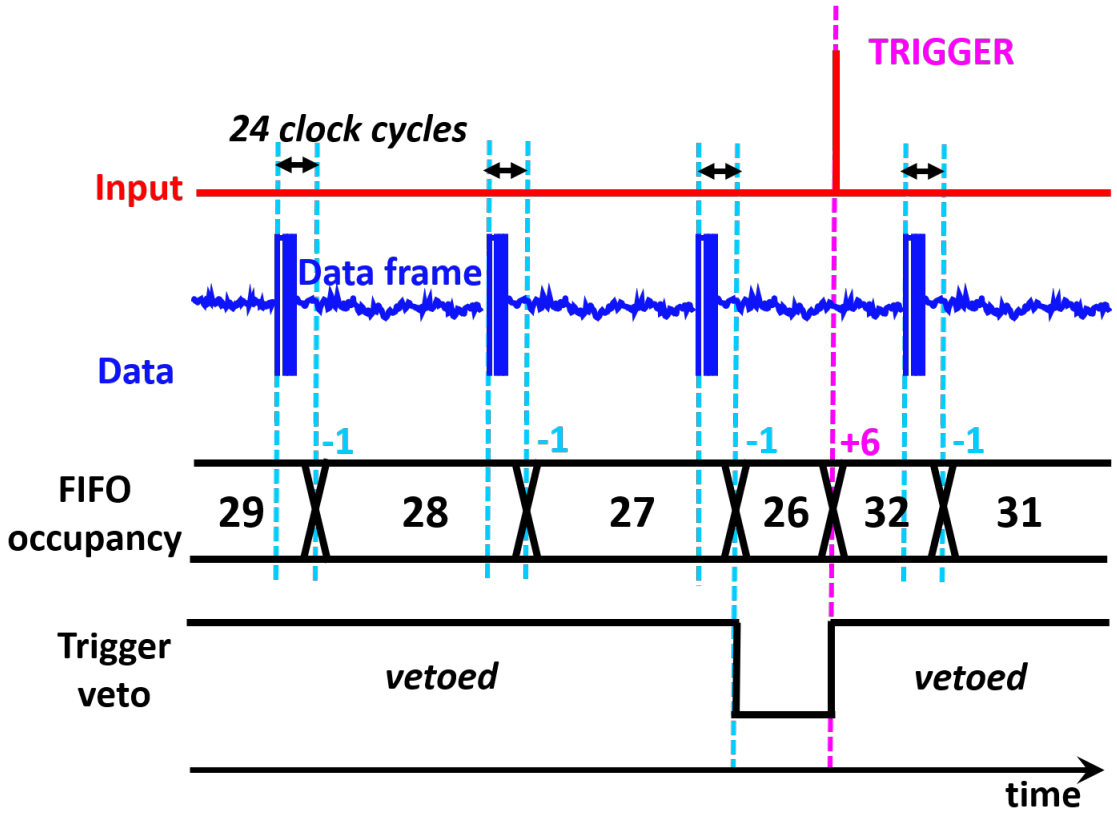

Figure 4.6: The FIFO is occupied by pipeline addresses immediately after reception of a trigger. Once a data frame starts to be sent out, the corresponding pipeline address is dequeued from the FIFO after 24 clock cycles. These assumptions enable us to estimate the FIFO occupancy. When the FIFO occupancy is larger than 26 (the FIFO depth (32) minus the number of data samples per trigger (6)), accepting another trigger signal causes the FIFO overflow.

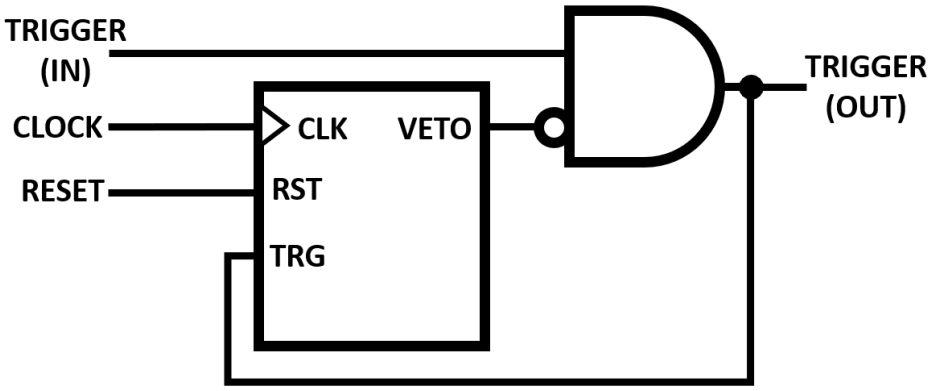

Figure 4.7: The conceptual diagram of the core module of the APV25-FIFO emulator. It receives 31.8 MHz system clock, the reset and trigger signals for the APV25 as input. The reset and trigger signals are latched by the system clock. The module is also reset by the reset signal for the APV25. It calculates the FIFO occupancy every clock, and asserts veto signal at the next clock when the occupancy is 27 or more. We apply the veto to the trigger before inputting it to the module so that the vetoed triggers are not recognized by the module.

four veto signals from these submodules, we can prevent the FIFO overflow no matter which clock phase is adopted in the FADC-Ctrl. Since 3 out of the 4 veto signals are redundant, this OR solution increases the trigger dead time. However, as they have almost same veto timing, the increase of the dead time is negligible $\sim O(10^{-3}\%)$.

4.2.4 Reset timing gap between the FTSW and the FADC-Ctrl

While the trigger signals must be delivered as fast as possible to minimize the trigger latency, the transfer of the reset signal is not as urgent. For this reason, the propagation times of the trigger signal (short) and the reset signal (long) from FTSW to FADC-Ctrl are different. Therefore, the reset timing relative to the triggers is different between the FTSW and on the FADC-Ctrl. The APV25-FIFO emulator needs to know the delay difference.

We implemented counters in the FTSW and the FADC-Ctrl to count the interval between a reset and the first trigger after the reset. The delay of the reset signal was measured by the counters and found to be a constant value. Since the emulation should be done with the delayed reset signal, we implemented a shift register in the APV25-FIFO emulator to delay the reset signal by the constant value. Figure 4.10 shows the final diagram of the APV25-FIFO emulator.

Based on the concepts described above, we implemented the firmware module for the use in the FTSW. We left the three delay parameters described in Section 4.2.2 changeable via VME interface.

4.3 Performance evaluation

The APV25-FIFO emulator firmware module was designed based on the concept described in Section 4.2. We tested the module with the test bench used for the development and the Phase 2 setup.

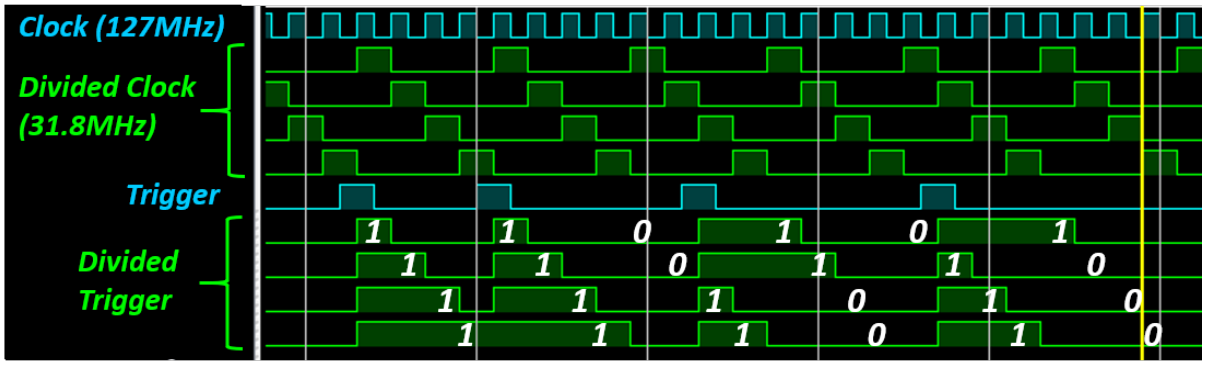

Figure 4.8: If we divide 127 MHz clock to produce 31.8 MHz clock, there are four possibilities about the phase of the divided clock. When triggers (blue) synchronized with 127 MHz clock are latched by four 31.8 MHz clocks with different phases, the timing of the latched triggers is different depending on the phase.

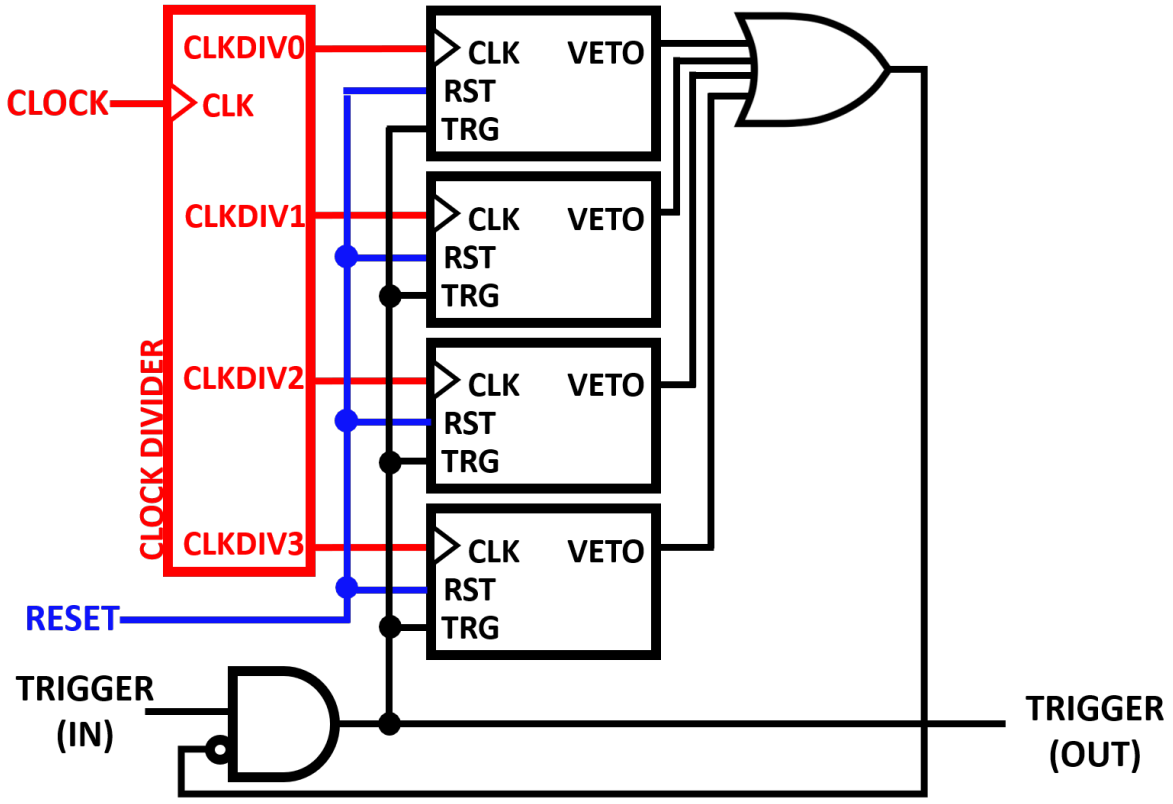

Figure 4.9: We use four core modules to deal with the ambiguity of the 31.8 MHz clock phase. The clock divider (essentially a 2-bit counter) uses input 127 MHz trigger to produce four 31.8 MHz clocks (CLKDIV1–4) whose phases are different by 1/4 clock cycle from each other. The four submodules use the clocks with different phases to latch the same trigger and reset signals, and send out veto signals based on the same logic. By using the OR of the four veto signals, we can safely veto the potentially excessive triggers.

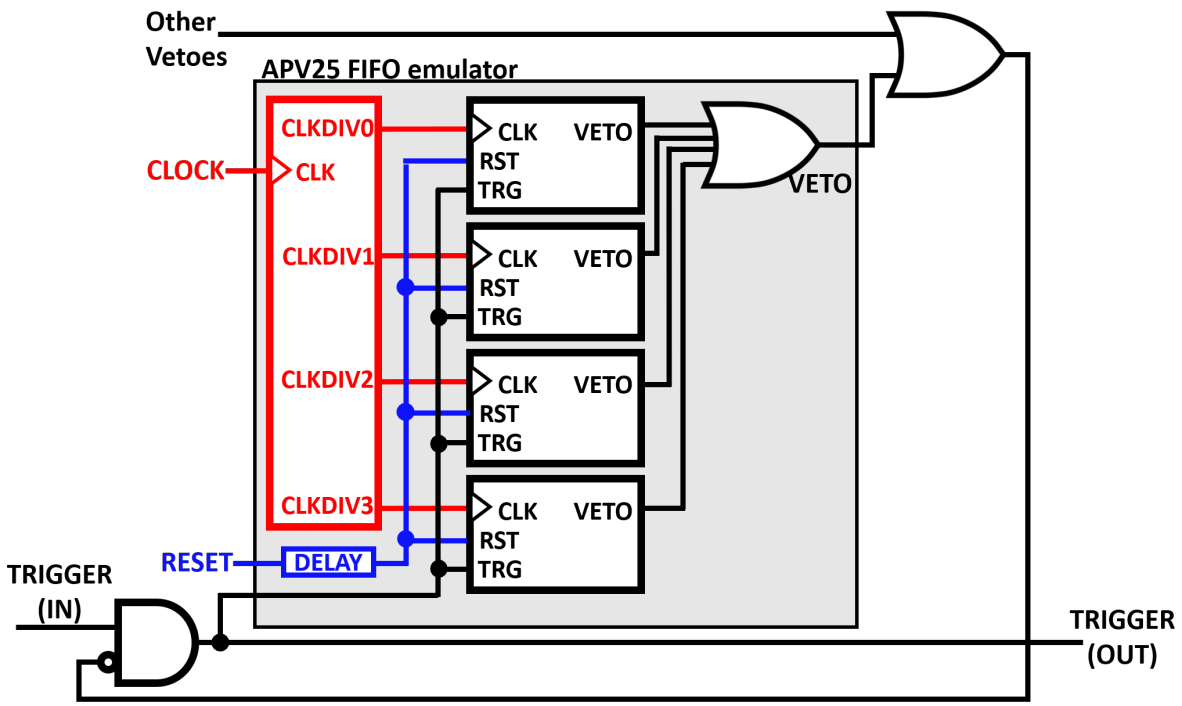

Figure 4.10: The conceptual diagram of the APV25-FIFO emulator. In addition to Fig. 4.9, the input reset signal is delayed for the compensation of the reset-trigger timing gap between the FTSW and the FADC-Ctrl. The veto signal from the emulator is OR-ed with the other veto signals in the FTSW.

4.3.1 Operation check in the test bench

The firmware module was tested in the test bench shown in Fig. 4.1(b). In the setup, the APV25-FIFO emulator is implemented on the FPGA of the FTSW. We can generate pseudo-random triggers of an arbitrary frequency by using 32-bit pseudorandom numbers generated by the Mersenne Twister [15] (MT triggers). The triggers are sent to the FTSW through the external input and examined by the APV25-FIFO emulator module. Triggers which are not vetoed by the emulator module are distributed to the APV25 chips. We read out a part of the data via the VME bus to check the error bits. The maximum readout rate with the software is about 1 kHz.

60 kHz MT triggers were generated and sent to the emulator module. The output triggers from the emulator module were sent to the 6 APV25 chips. The output trigger rate from the FTSW was about 37 kHz. After 15 hours of operation, we observed four error bits and three failures of detecting the data header in total. However, we consider that the presence of the errors does not mean the failure of the trigger veto system for the two reasons below. Firstly, if errors truly happen, the error bits should remain until they are cleared by reset. In that case, the number of error bits increases at every trigger. Considering the trigger rate and the operation time, the observed number of the error bits is strangely small. Secondly, since the six APV25 chips are supposed to work in synchronization, the number of error bits should be a multiple of six in principle. The number of the error bits not being a multiple of six, they do not originate from the designed behavior of the APV25. Therefore, we suspect the observed error bits are due to bit flips. The header detection failures can also be explained by bit flips. From the observation, we consider the APV25-FIFO emulator prevented the FIFO overflow error at least for fifteen hours at the maximum possible rate.

We also tried running the system while changing the input parameters described in Section 4.2.2. Sending 30 kHz MT triggers, we observed that the error bits appeared when the parameters were changed from the designed values to the critical side. This validates the reasonability of the assumed data processing model.

4.3.2 Trigger loss rate

The trigger loss rate, the fraction of the vetoed triggers, is the most important observable that shows the performance of the trigger-veto module. It is defined as

$$\frac{\#\text{vetoedTriggers}}{\#\text{inputTriggers}} = \frac{\#\text{inputTriggers} - \#\text{outputTriggers}}{\#\text{inputTriggers}} \tag{4.1}$$

where #inputTriggers is the number of the triggers going into the FTSW, #outputTriggers is the number of the triggers going out from the FTSW, #vetoedTriggers is the number of the triggers vetoed by the APV25-FIFO emulator. We measured the trigger loss rate as the function of the input trigger rate in the test bench in Fig. 4.1(b). We sent the MT triggers for ten minutes to count the triggers before and after the FTSW.

In addition, we wrote a C-program to estimate the trigger loss rate by simulating the APV25-FIFO emulator. The program generates triggers by itself with the Mersenne Twister and applies vetoes to them on the same logic as the APV25-FIFO emulator. The trigger loss rate is calculated by counting the vetoed triggers.

The observed and simulated trigger loss rates are shown in Fig. 4.11. The measured trigger

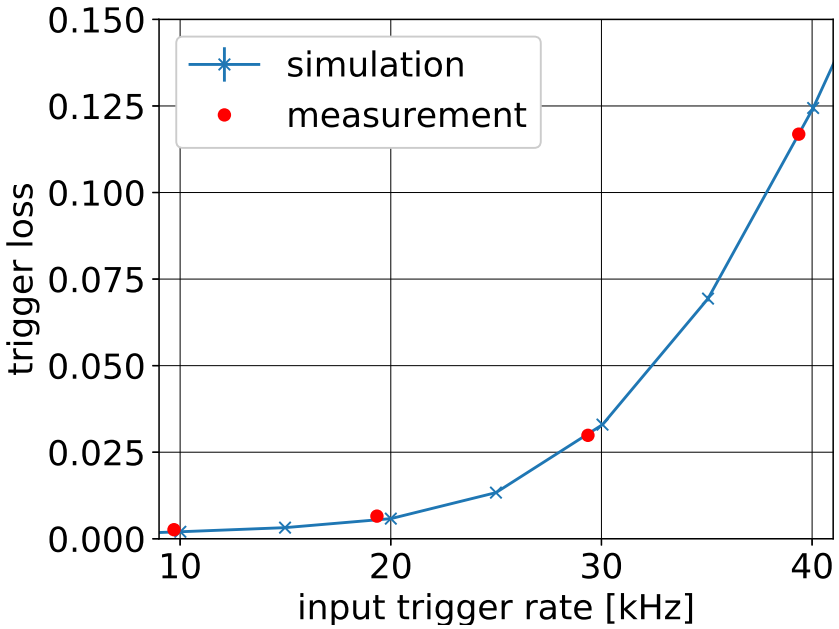

Figure 4.11: The trigger loss rate due to the veto by the APV25-FIFO emulator is shown as the function of the input trigger rate. The triggers were generated by the Mersenne Twister individually for the measurement and the simulation. We generated 100,000 triggers in each simulation. In each measurement, we took data for about ten minutes.

loss rate shows good agreement with the simulation, which indicates the developed emulator module works as expected. The loss rate is about 3 % assuming the input trigger rate of 30 kHz as required in the Belle II experiment. This is a significant improvement compared with the easiest trigger-veto scheme (see Section 4.1) which loses 44 % of 30 kHz triggers.

4.3.3 High trigger rate test in the Phase 2 setup

Before Phase 2 operation, the stability of the trigger-veto system was tested in the Phase 2 setup shown in Fig. 3.9. All the components were in place for the use in Phase 2. We generated pseudorandom triggers in the FTSW (FTSW triggers) and sent them to the 144 APV25 chips on the Phase 2 SVD cartridge. We checked all the error bits in the data from the SVD cartridge by using the readout PC.

We sent 50 kHz FTSW triggers for ten hours while monitoring the number of the error bits in the readout PC. The output trigger rate was about 35 kHz. After ten hours, no error bits were observed except for one APV25 chip. The chip had eighteen error bits in total, discontinuously increasing the number as shown in Fig. 4.12. For the same reasons described in Section 4.3.1, we assume the error bits were caused by bit flips. In other tests with shorter run times, this phenomenon was observed in several chips.

The stability test was conducted well before the start of Phase 2, and the SVD was ready for high rate data acquisition in Phase 2. However, the trigger rate during Phase 2 was as

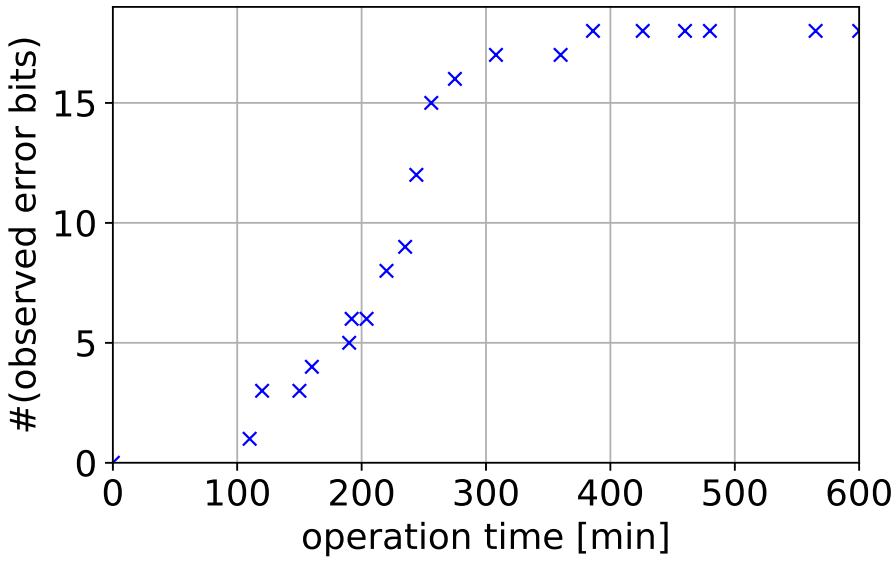

Figure 4.12: The time evolution of the error-bit count during the stability test in the Phase 2 setup. The error bits arose from the same APV25 chips.

low as 1 kHz due to limitations from the other subdetector systems and the low luminosity. Therefore, the APV25-FIFO emulator was not intensively utilized, although it was implemented and functioning.

4.4 Further improvement in trigger loss rate due to trigger with good timing resolution

We plan to apply the APV25 data processing model to the mixed mode (see Section 3.4.2) when the trigger with good timing resolution (3-sample trigger) becomes available. We assume the fraction of the 3-sample triggers R_3 and estimate the trigger loss rate by the C-program. Figure 4.13 shows the estimated trigger loss rate as the function of the input trigger rate. Assuming R_3=0.5 as was in the Belle experiment[4], the trigger loss rate becomes less than 1 % for the 30 kHz trigger.

[4]In the Belle experiment, the timing of roughly half the triggers was decided by the barrel PID detectors. [16].

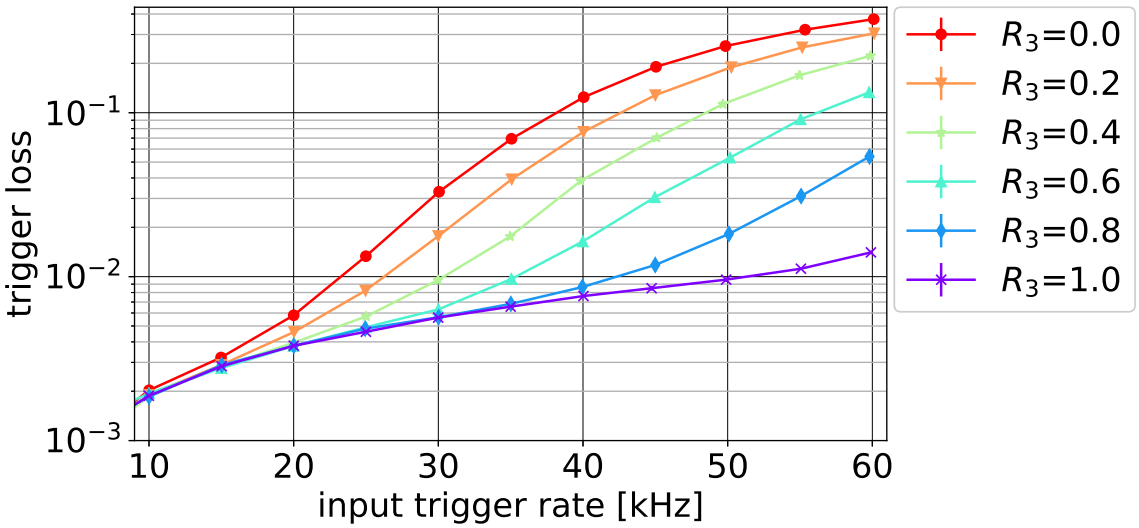

Figure 4.13: The simulated trigger loss rate in the mixed mode is shown as the function of the input trigger rate. Each simulation assumes a fixed input trigger rate and a fixed fraction of the 3-sample trigger out of all the input trigger, R_3. For each simulation, 1,000,000 triggers and their types (3- or 6-sample) are generated pseudorandomly by the Mersenne Twister based on the assumed rate and R_3. The legend denotes the assumed R_3.

Chapter 5

Beam backgrounds

Beam particles sometimes deviate from the ideal orbit and produce electromagnetic showers by hitting the wall of the beam pipe. If the beam particles are lost near the detectors, the resulting showers can hit the detectors. They are called beam background and the detectors are affected by fake hits and their associated radiation damage. Fake hits transiently deteriorate the detector performance such as tracking efficiency, momentum resolution, etc. They also cause dead time by occupying a large amount of the DAQ bandwidth. Furthermore, the accumulation of the radiation damage leads to permanent degradation of the performance. For example, the radiation damage increases noise in semiconductor devices, degrades the quantum efficiency of photoelectric surfaces of photodetectors, and decreases light output of scintillation crystals.

In Section 5.1, we explain the background tolerance of the SVD and the purpose of the beam background studies performed in Phase 2. We describe the sources of the beam backgrounds and their properties in Section 5.2. We introduce a model which describes the single-beam background rate in Section 5.3.

5.1 Background tolerance of the SVD and purpose of study

We consider the effect of beam backgrounds on the SVD from two aspects: the degradation of tracking performance due to fake hits, and radiation damage on the sensors. The effect of fake hits is quantified as occupancy, that is, the percentage of fired strips in all the strips. The latter effect is quantified as total ionizing dose (TID) and non-ionizing energy loss (NIEL).

5.1.1 Occupancy

We define the occupancy as the fraction of fired strips in a sensor. Thus, the occupancy is defined for each side of a DSSD sensor. We classify a strip as fired if it survives the zero suppression or hit selection with the threshold of SNR=5 in this thesis. Under background conditions which result in occupancy of 3 % for the L3 sensors, the SVD standalone tracking exhibits a tracking efficiency of 94 % and a fake rate of 14 % in Monte Carlo simulation [17]. Since $B\overline{B}$ events produce 11 tracks on average, the 94 % efficiency means a full reconstruction efficiency of 50 %. We define the occupancy of 3 % as the limit for the acceptable degradation of the tracking performance.

5.1.2 Radiation damage to silicon sensors

Radiation incident on silicon sensors interacts with the electron cloud or nuclei in the crystal lattice [18]. Interactions with nuclei cause displacement of the lattice atoms, generating interstitials (atoms between regular lattice sites) and vacancies (empty lattice sites). These unstable defects grow into stable defect complexes, which change the electrical properties of the sensor by the following mechanisms:

- They capture and emit electrons and holes as recombination-generation centers. Defects that introduce energy levels at the center of the band gap can alternatively emit electrons and holes, which increases the reverse-bias current if it happens in the depletion region.
- They change the charge density in the depletion region. This causes type inversion and eventually increases the full depletion voltage of the sensor.
- They trap the charge carriers and release them after some delay. This prevents efficient charge collection and leads to signal reduction.

Interactions with nuclei are mainly caused by heavy particles. The effect of the NIEL is evaluated as the equivalent fluence of 1 MeV neutrons.

In the surface region, the displacement of the atoms does not have a significant effect since the material structure is already irregular. On the other hand, ionizing radiation in the form of photons and charged particles causes damage to the oxide insulator. Because electrons have several orders of magnitude larger mobility than holes in SiO_2, electrons quickly diffuse out of SiO_2 while holes are captured. This ends in the positive charge-up of the insulator, reducing the high voltage stability of the sensor.

5.1.3 Radiation tolerance for Belle II SVD

From the experience of the Belle experiment, the Belle II SVD is required to tolerate the TID of 10 Mrad. That value is obtained by scaling the radiation dose in Belle by the luminosity (4.5 Mrad) and multiplying it by a safety factor about two [8].

Beam tests showed that irradiation of 10 Mrad does not significantly degrade the signal-to-noise ratio of the DSSD sensors [19]. Regarding the APV25, they observed almost no degradation after 10 Mrad irradiation [10]. Araldite 2011 [20], the adhesive used in the SVD, is also confirmed to have enough radiation hardness [21]. We define 10 Mrad as the limit of acceptable TID over a decade of operation.

The significant effect on the SVD due to the NIEL damage is type inversion, which changes the n-type bulk substrate of the DSSD into effectively p-type and prevents signal readout from the p-type strips. We define the acceptable limit of $10^{13}\,\mathrm{cm}^{-2}$ 1 MeV neutron equivalent fluence as the maximum NIEL damage before type inversion, based on the observation of the ATLAS SCT group [22].

5.1.4 Purpose of Phase 2 beam background study

The Monte Carlo simulation of the beam background in the designed SuperKEKB condition predicts about 1 % occupancy and about 0.1 Mrad/smy[1] irradiation on the SVD (see Chapter 6).

[1] An approximation of the total operation time in a year. 1 smy (snowmass year) = 10^7 s

These values are within the limits described above. However, we should be careful because the simulation of the beam-induced backgrounds has a large uncertainty due to the difficulty in simulating all the details of the accelerator complex, such as beam dynamics, vacuum pressure measurements, etc. Indeed, in Phase 1, some BEAST II detectors observed background rates which are one to three orders of magnitude higher than simulation [4]. Judging from the values above, keeping good tracking performance is the more pressing issue for the SVD.

For the installation of the full SVD, we aim to verify three points by estimating the background level in Phase 3. Firstly, the occupancy should be low enough for the SVD to achieve good tracking performance in the first year of Phase 3. Secondly, after the design luminosity is achieved, the integrated dose over Phase 3 and the occupancy should stay within the limits. Finally, the correlation of the background rates between the SVD and diamonds should be confirmed so that we can use diamonds as a beam abort sensor to keep the SVD safe.

5.2 Beam background sources

In the SuperKEKB storage ring, it is expected that beam backgrounds arise from the following sources.

5.2.1 Touschek scattering

Touschek scattering is a scattering process between two beam particles within the same bunch, which causes an energy transfer from one to the other. If the energies get out of the dynamic aperture of the ring, the beam particles are no longer stable and start to deviate from the design orbit. After hundreds of turns, they are eventually lost by hitting the beam pipe wall and produce electromagnetic showers. Showers due to beam losses near the IR, or their secondary showers might hit the detector.

The Touschek background rate is proportional to

$$\frac{I^2}{\sigma_y n_b E^3}, \tag{5.1}$$

where I is the beam current, σ_y is the vertical beam size, n_b is the number of bunches and E is the beam energy [8]. Due to its beam size dependence, it is predicted to be the major background source at SuperKEKB, which adopts the nano-beam scheme. Also, it is more serious for the LER due to its beam energy dependence. Touschek background rate also depends on the horizontal beam size, but we focus on the vertical. In the nano-beam scheme, where vertical beam size is extremely small, dependence on the vertical beam size is more important. To reduce the Touschek background, movable collimators are installed along the beam pipes (see Section 3.2.1). These collimators stop the particles deviating widely from the nominal orbit before they produce showers near the IR.

5.2.2 Beam-gas scattering

Beam-gas scattering is a process where beam particles are scattered by residual gas molecules, due to Coulomb scattering. It changes the directions of beam particles and leads to immediate

beam losses at the beam pipe wall. Bremsstrahlung also happens as a higher order effect. It reduces the energies of the beam particles, producing beam background similarly to the Touschek background. Because the bremsstrahlung event rate is low and beam particles with lower energies are stopped by horizontal collimators before hitting the beam pipe, the beam-gas background is mainly due to Coulomb scattering. The beam-gas scattering rate is proportional to the beam current and the pressure inside the beam pipe.

5.2.3 Synchrotron radiation

Synchrotron radiation (SR) is a process where beam particles emit photons when they are bent by magnets. In SuperKEKB, beam particles emit low energy photons ranging from a few keV to tens of keV [4]. Its contribution in detector background is predicted to be negligible by Monte Carlo simulation. Moreover, background particles due to SR are hard to detect for the SVD because their energy deposits are so small relative to the noise of the SVD. The difficulty of detecting the SR makes it difficult to evaluate its contribution to the radiation dose. The power of SR is proportional to beam energy squared and magnetic field strength squared. Thus, the HER mainly contributes to this beam background, and we consider only the SR from HER in the simulation study described in Section 6.1. The SR background rate is also proportional to the beam current.

5.2.4 Luminosity backgrounds

We define luminosity backgrounds as the beam background components induced by beam collisions. For the SVD, the largest contribution comes from two-photon process $e^+e^- \to e^+e^-e^+e^-$, where the e^+e^- collisions produce low momentum electron-positron pairs at the interaction point. The magnetic field by the Belle II solenoid makes these tracks with low momenta spiral inside the SVD volume leaving multiple hits on the sensors. The second largest contribution is due to radiative Bhabha process, where electrons and positrons scatter with small angles, producing photons along the beam axis. The emitted photons hit the material downstream to produce showers and neutrons. The beam particles whose energy are taken by two-photon or radiative Bhabha process are overbent by the magnetic field of the solenoid and QCS magnets after the interaction point to hit the beam pipe. Bhabha scattering with a small scattering angle also produces such background. Since the rates of these backgrounds are proportional to the luminosity, they are predicted to dominate beam backgrounds at the design luminosity of SuperKEKB ($8 \times 10^{35}\,\mathrm{cm^{-2}s^{-1}}$). However, they are hard to detect at the luminosity of a few $\times 10^{33}\,\mathrm{cm^{-2}s^{-1}}$ in Phase 2.

5.2.5 Injection background

As described in Section 3.2.4, in Phase 3, we will take physics data while repeating continuous injections at 50 Hz continuously to maintain high luminosity. For a few milliseconds just after an injection, the SVD suffers harsh beam background. In order to not take data during this period, we apply a trigger veto for several milliseconds after every injection. Therefore, the duration in which the SVD cannot take data due to the injection background should be investigated to determine the veto duration. Also, since the radiation damage from the injections is accumulated

in the SVD, it is important to confirm that the radiation dose is at a safe level for the SVD operation. We used only the normal and continuous injections in Phase 2.

5.3 Single-beam background model

Most of the beam background measurements in Phase 2 were devoted to the investigation of the single-beam backgrounds. We introduce a model which describes the single-beam background rate. If we assume the beam background rate from a single beam is dominated by Touschek and beam-gas Coulomb scatterings and may ignore other background sources, the background rate is parametrized as

$$\mathcal{O} = T \cdot \frac{I^2}{\sigma_y n_b} + B \cdot PI \tag{5.2}$$

where $\mathcal{O}$ is background rate such as SVD occupancy and dose rate on diamond sensors, I is the beam current, σ_y is the vertical beam size at the location of the beam size monitor, n_b is the number of bunches, P is the average pressure over the ring, and coefficients T, B are the quantities of Touschek and beam-gas components, which are independent of other parameters. The Touschek component also depends on the beam energy, the horizontal beam size, and the bunch length as described in Section 5.2.1. However, since we did not change these parameters in the measurements, we show only the parameters of our interest in Eq. (5.2).

The beam-gas component is also proportional to the second power of the effective atomic number of the residual gas, but we do not take this dependence into account in this thesis. Instead, the averaged value is absorbed in B. Empirically, the pressure is approximated by a linear function of the beam current:

$$P = P_0 + k \cdot I \tag{5.3}$$

where P_0 is the base pressure without the beam stored and k is a constant. The background rate in Eq. (5.2) is characterized by a quadratic function of the beam current in a beam study run because the beam size and the number of bunches do not change significantly during a usual run.

Chapter 6

Beam background simulation

In this chapter, we describe the Monte Carlo simulation of the various beam background sources. Section 6.1 explains the simulation procedure and introduces the simulation campaigns covered in this thesis. The following sections describe each simulation campaign.

6.1 Beam background simulation

The beam background rates from following sources are estimated by Monte Carlo simulation: Touschek, beam-gas Coulomb, HER SR, two-photon, and radiative Bhabha scattering. Injection background is not included since the simulation is difficult. We consider the SR contribution only from the HER because the HER dominates the SR background owing to its larger beam energy.

Radiative Bhabha processes are classified depending on the scattering angles of $e^{\pm}$, $\theta_{e^{\pm}}$. "BHWideLargeAngle" (BHWide LA) events are defined as the event where both of $\theta_{e^{\pm}}$ are larger than 1° and at least one of them is larger than 10°. The events are classified as "BH-Wide" events if they are not BHWideLargeAngle events and both of $\theta_{e^{\pm}}$ are larger than 0.5°. The other events are classified as "RBB" events.

The event generation of each background is done by different methods. For the Touschek and beam-gas Coulomb scatterings, we use SAD (Strategic Accelerator Design) software [23] to simulate the propagation and loss of beam particles along the ring. The information of the lost particles is recorded. The SR events are simulated by Geant4. The two-photon events are generated by AAFH [24], RBB by BBBREM [25], BHWide and BHWide LA by BHWIDE [26]. We take these events as the input of detector simulation by Geant4 to calculate energy deposits in the detectors. The radiation dose and NIEL damage on the SVD are estimated by the energy deposits. The radiation dose is calculated as the energy deposit per sensor mass. We calculate the NIEL damage as the equivalent fluence of 1 MeV neutron, assigning a conversion factor to each particle according to its species and kinetic energy.

Since the background events do not happen in sync with triggers[1], these energy deposits are randomized in the time axis according to the assumed background rate. The time-randomized energy deposits in the SVD are processed by a dedicated digitizer module in basf2 [12] to sim-

[1] In the designed condition, the beam bunch crossing period is 4 ns while the trigger rate is 30 kHz. The bunch crossing is approximately continuous.

ulate the signal propagation inside the sensors. As a result, the hit information equivalent to the APV25 output is produced for each event. The occupancy and the clusters on the SVD are reconstructed from the information.

There have been several background simulation campaigns. We divide them into three categories: Phase 2 and Phase 3 design simulation, Phase 2 realistic simulation, and HER SR simulation.

Before Phase 2 started, the Phase 2 and Phase 3 design simulation was done assuming the designed machine condition in Phase 2 and 3, respectively. Here, the Touschek and beam-gas backgrounds are simulated with the design optics and collimator setting which is optimized for the optics by simulation. The luminosity backgrounds are simulated with the event rate calculated from the assumed luminosity.

A series of the Phase 2 realistic simulations was made for the reference of the single-beam background studies in Phase 2. For important beam size scans, we produced the Touschek and beam-gas background samples by reflecting the beam optics and collimator setting during each study in the SAD simulation.

These campaigns do not include the SR background because the previous simulations predicted negligible SR contribution. The SR simulation was done separately, motivated by an unexpected peak in the energy distribution measured by some detectors in Phase 2. We consider only the HER SR simulation in this thesis.

In the following sections in this chapter, we describe each simulation campaign.

6.2 Simulation for Phase 2 and Phase 3 design optics

MC simulations for beam backgrounds are performed under assumptions of the accelerator settings designed for Phase 2 and Phase 3 individually. The assumed machine parameters are listed in Tab. 6.1. The collimator setting is optimized by simulation for the background mitigation in the assumed beam optics. The Touschek, beam-gas and luminosity backgrounds are simulated. For each background species, we estimate the radiation dose, NIEL damage, and occupancy on the sensors.

Figures 6.1 and 6.2 show the estimated dose, NIEL, and occupancy averaged over the sensors in each layer. We can see that the main contribution in Phase 3 is from the luminosity backgrounds, especially the two-photon. In contrast, the single-beam backgrounds are dominant in Phase 2, where forty times smaller luminosity is assumed. The background variables in Figs. 6.1 and 6.2 do not show the radial dependence of $1/r^2$, since the background particles do not necessarily come from the IP.

The azimuthal angle dependence of the radiation dose in Phase 3 is shown in Fig. 6.3. We can see that the ladders in the horizontal plane suffer more intense background condition. One reason is that the particles with wrong energies arising from the Touschek scattering are lost in the horizontal plane. The two-photon and radiative Bhabha backgrounds are also more intense in the +X direction since the center-of-mass system is slightly boosted toward the +X direction owing to the finite crossing angle. We show the ϕ dependence plots of each background species in Appendix B. In Phase 2, we cannot study the ϕ dependence because the SVD cartridge covers only the +X direction.

From the Phase 2 simulation result, we calculate the ratio of the radiation dose to the

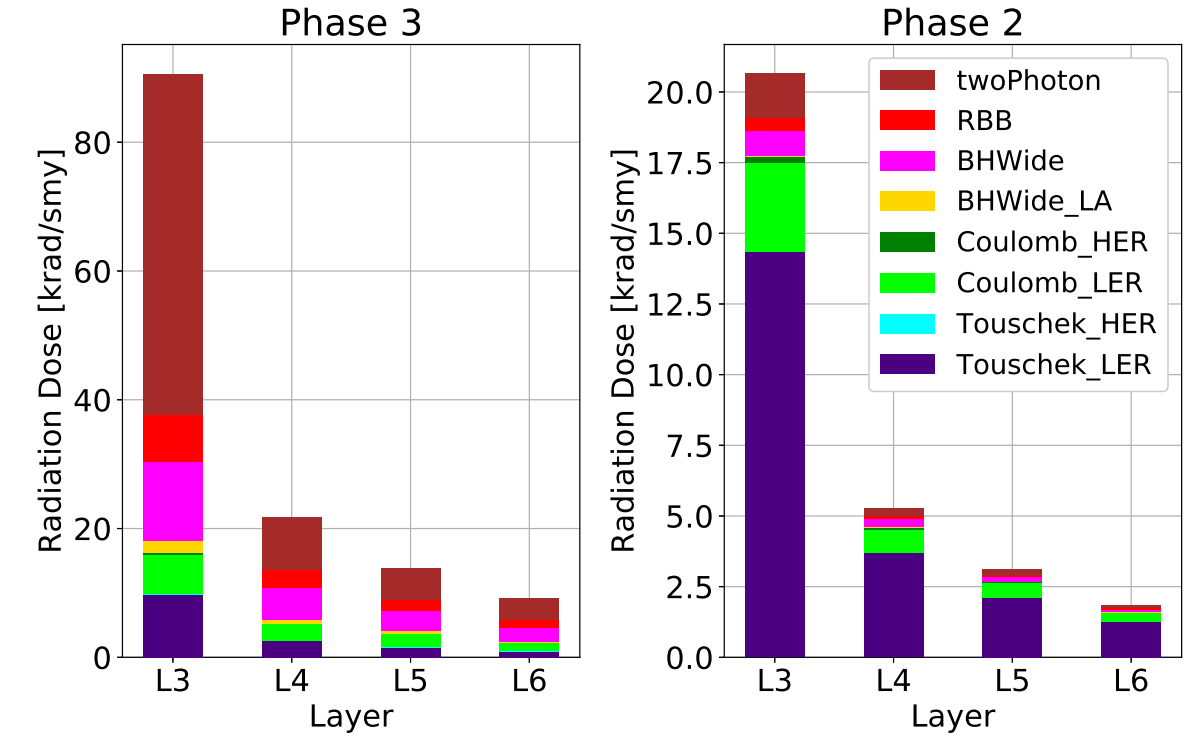

(a) Radiation dose

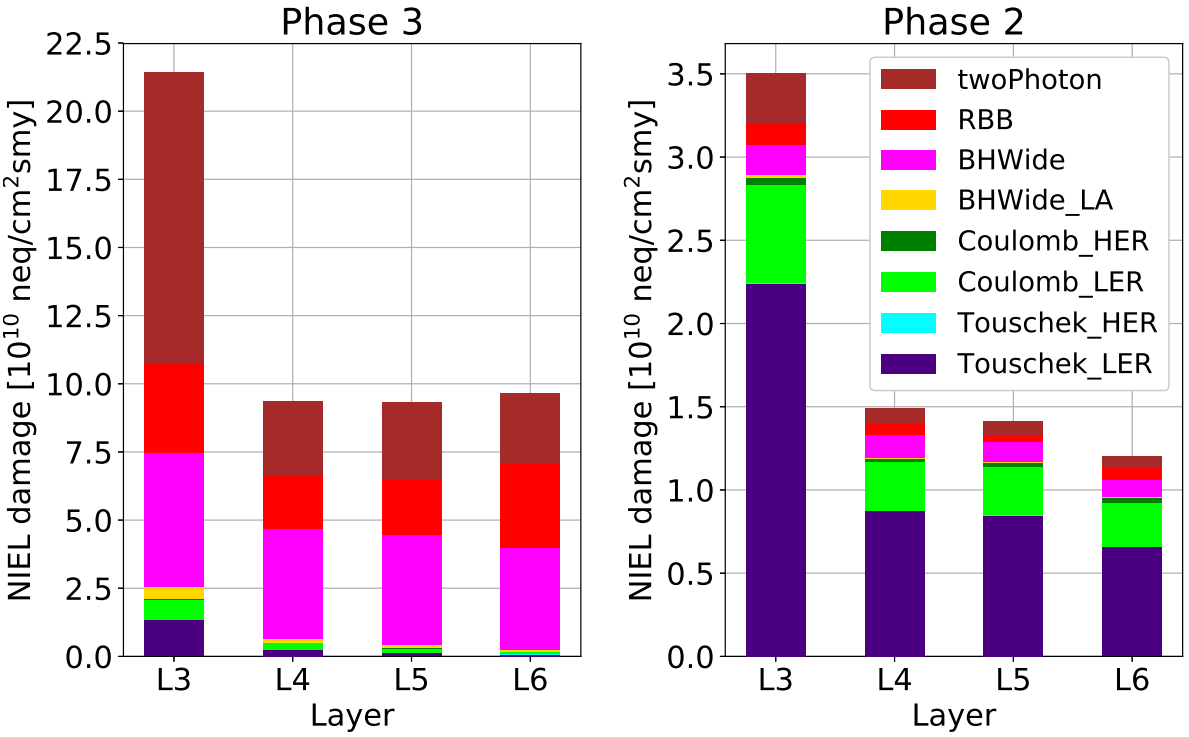

(b) NIEL damage

Figure 6.1: The radiation dose (a) and NIEL damage (b) to the SVD are estimated by the simulation assuming the accelerator setting designed for Phase 2 and 3. The variables are averaged over the sensors in each layer. The contributions from different background species are plotted in different colors as shown in the legend. The NIEL damage is expressed as the equivalent fluence of 1 MeV neutron.

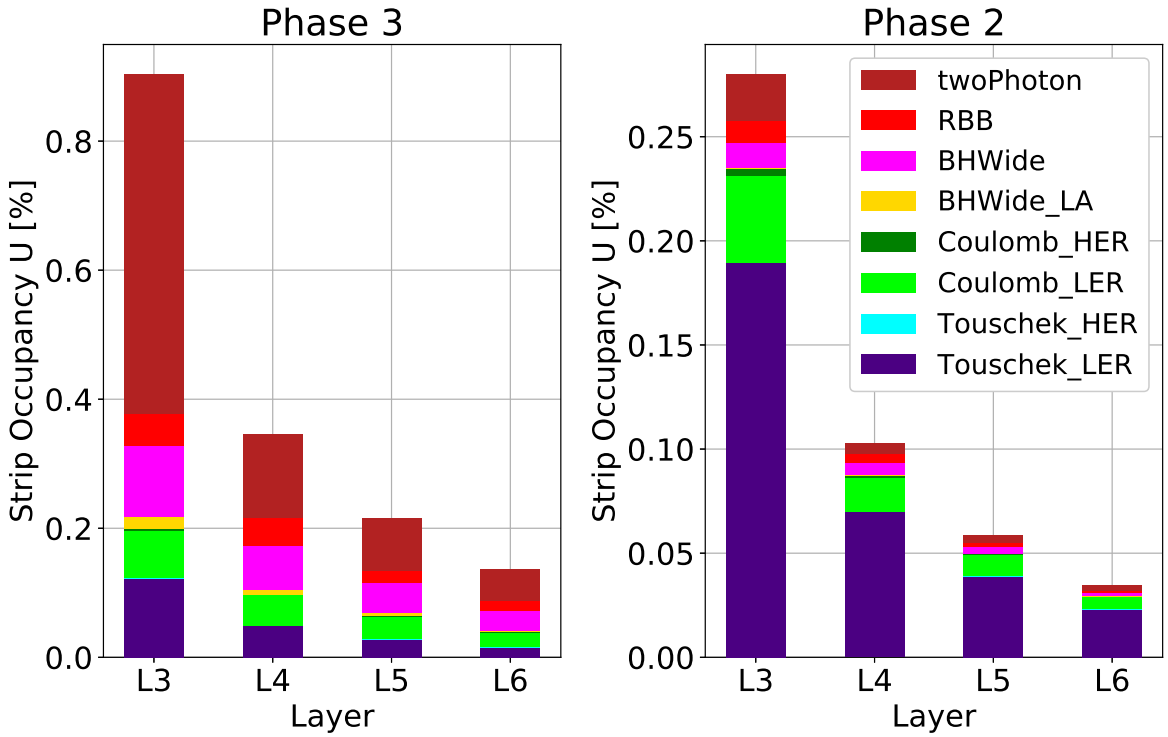

(a) Occupancy (U side)

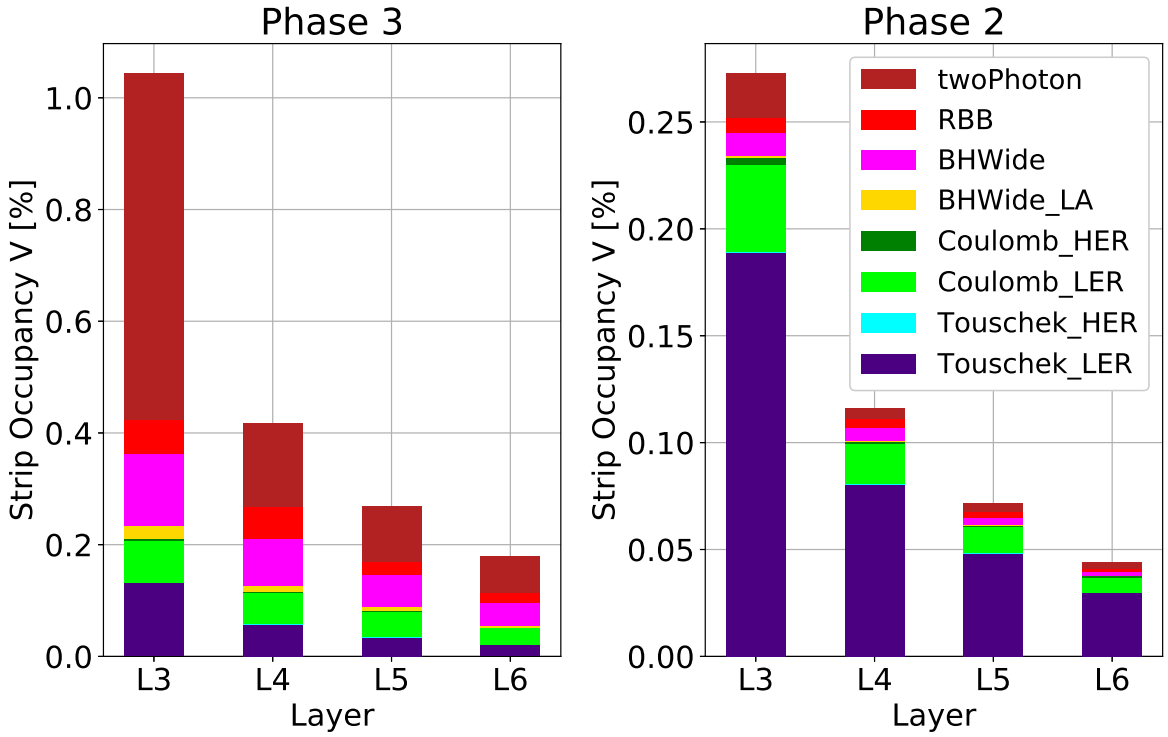

(b) Occupancy (V side)

Figure 6.2: The SVD occupancies on the U side (a) and the V side (b) are estimated by the simulation assuming the accelerator setting designed for Phase 2 and 3. The occupancies are averaged over the sensors in each layer. The contributions from different background species are plotted in different colors as shown in the legend.

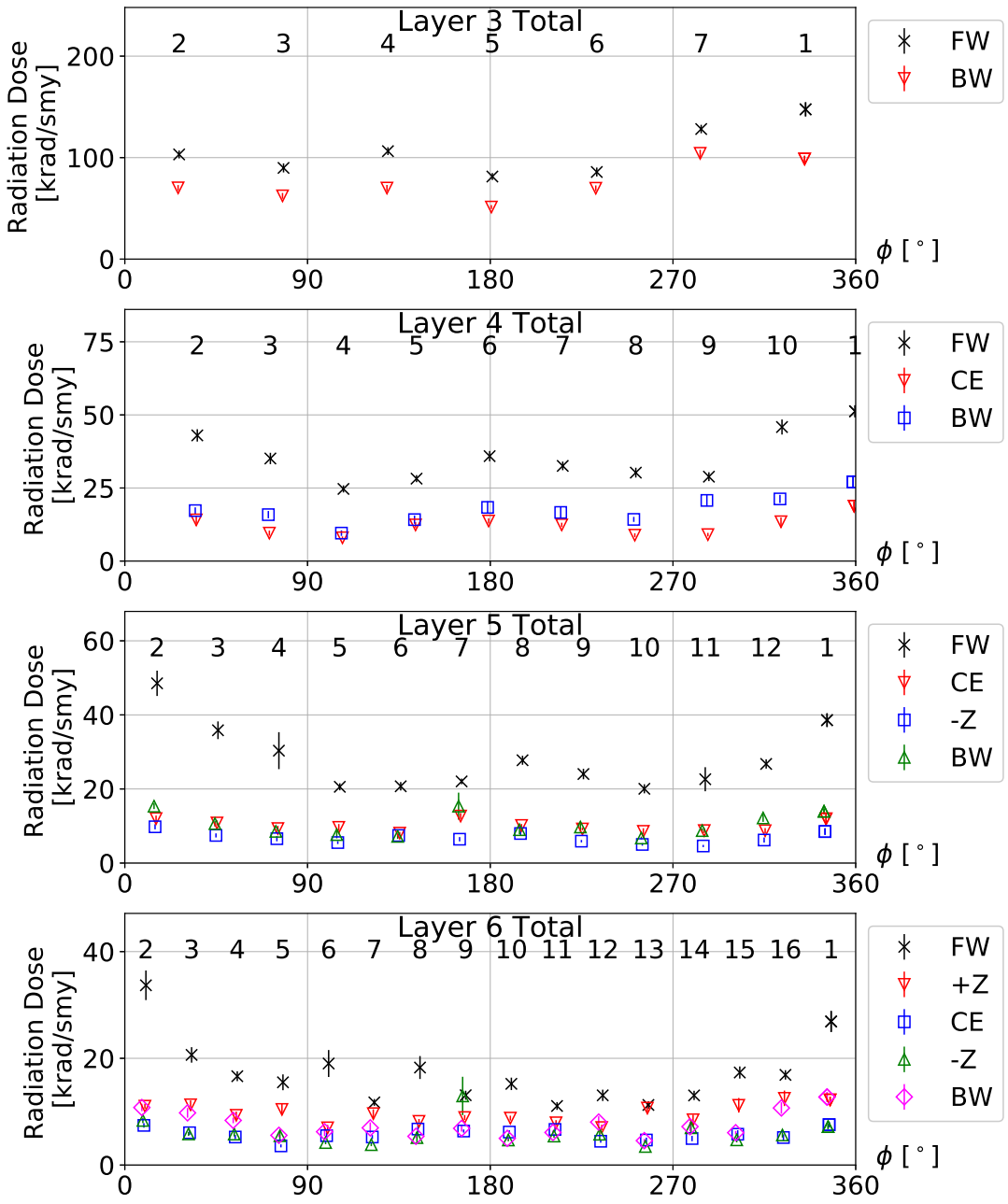

Figure 6.3: The azimuthal angle dependence of the radiation dose in the Phase 3 simulation. The total dose from all the background components is shown for each sensor. The plots are separated by the layers. For each layer, the x-axis shows the azimuthal angle of the center of the sensor. The ladder numbers are shown above the data points. Markers denote the sensor position on the ladder.

Table 6.1: Machine parameters in the Phase 2 and Phase 3 designed simulation. The pressure is assumed to be uniform in the ring. Vertical beam sizes are the ones at the location of the beam size monitor.

	Phase 2		Phase 3	
Parameter [unit]	LER	HER	LER	HER
Beam current [mA]	1000	800	3600	2600
Number of bunches	1576	1576	2500	2500
Bunch current [mA]	0.63	0.51	1.44	1.04
Horizontal beta function at IP [mm]	128	100	32	25
Vertical beta function at IP[mm]	2.16	2.4	0.27	0.3
Vertical beam size [μm]	42	44	10	24
Pressure [10^{-8} Pa]	13.3	13.3	13.3	13.3
Luminosity [$\mathrm{cm}^{-2}\mathrm{s}^{-1}$]	2×10^{34}		8×10^{35}	

occupancy on each SVD sensor. The ratios for each background component and each sensor are shown in Fig. 6.4. In Fig. 6.4, we categorize the sensors according to their shape (see Tab. 3.3). The ratios of the same sensor type show similar results even though the background sources are different, except for the radiative Bhabha and HER Touschek backgrounds with poor statistics. This is assumed to be because the distribution of the energy deposits from each background source is similar and hence the energy deposit per hit is similar. Therefore, while taking data with the SVD, we can estimate the radiation dose rate on the SVD from the measured occupancy without distinguishing the background sources. Sensors with different shapes show different ratios. This is because signal charges are differently distributed and zero-suppressed by different thresholds owing to the difference of the capacitance between the strips and differing noise levels.

The dose rates on the diamond sensors are estimated from the same Phase 2 simulation sample. We calculate the ratio of radiation dose between the SVD and diamond in Phase 2 as shown in Fig. 6.5. To see the correlation, we focus on the SVD L3 sensors, which are nearest to the diamond sensors. Although the L3 sensors and diamonds at ϕ=55, 305° are only several centimeters apart, we can see that the ratios from different backgrounds do not coincide. This indicates the spatial distribution is different between the background sources. The calculated ratio enables us to make a very rough estimation of the dose rate on the SVD sensor from the diamond dose rate.

6.3 Phase 2 realistic simulation

In Phase 2, we performed beam size scans to estimate the contributions from the beam-gas and Touschek backgrounds, B and T in Eq. (5.2) (see Section 7.2). We estimate B^{MC} and T^{MC} by the simulation for comparison. For important beam size scans in Phase 2, we take the beam optics and collimator setting during each study as the input to produce the Phase 2 realistic simulation. The machine parameters used in each simulation are listed in Tab. 6.2.

For each simulation, we estimate the SVD occupancy. The beam-gas and Touschek contri-

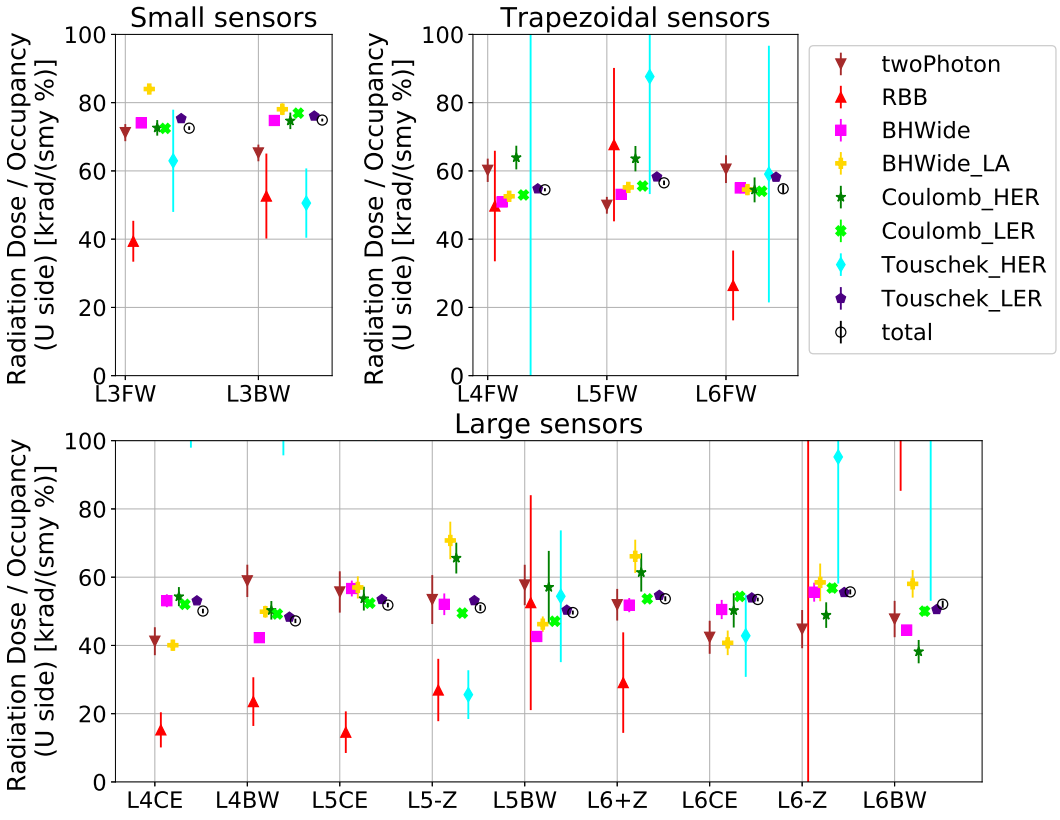

(a) U side

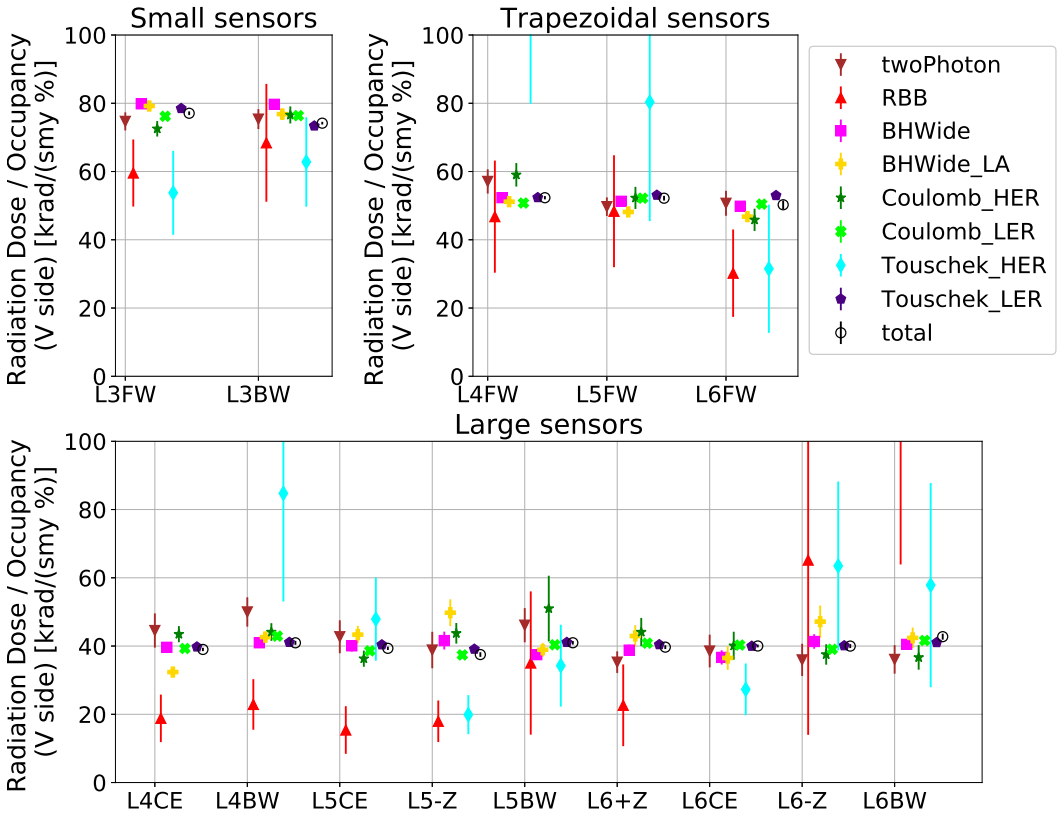

(b) V side

Figure 6.4: The ratio of radiation dose to occupancy on the SVD sensors in the simulation assuming the accelerator setting designed for Phase 2. The plots are made for the U side occupancy (a) and the V side (b). The x-axis denotes the sensor names. The ratio is calculated for each background species as shown by the legend. We separate the plot areas by the sensor shape (see Tab. 3.3).

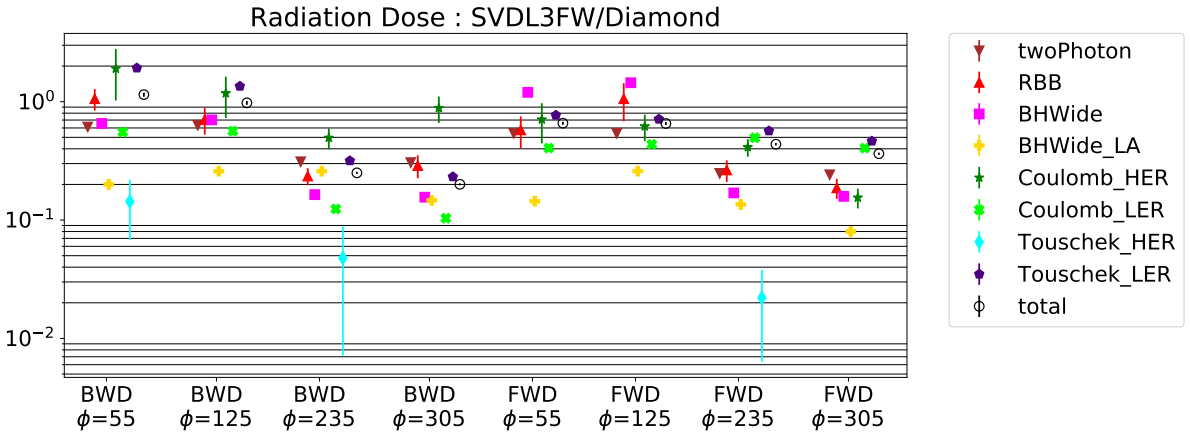

(a) SVD L3FW sensor vs Diamonds

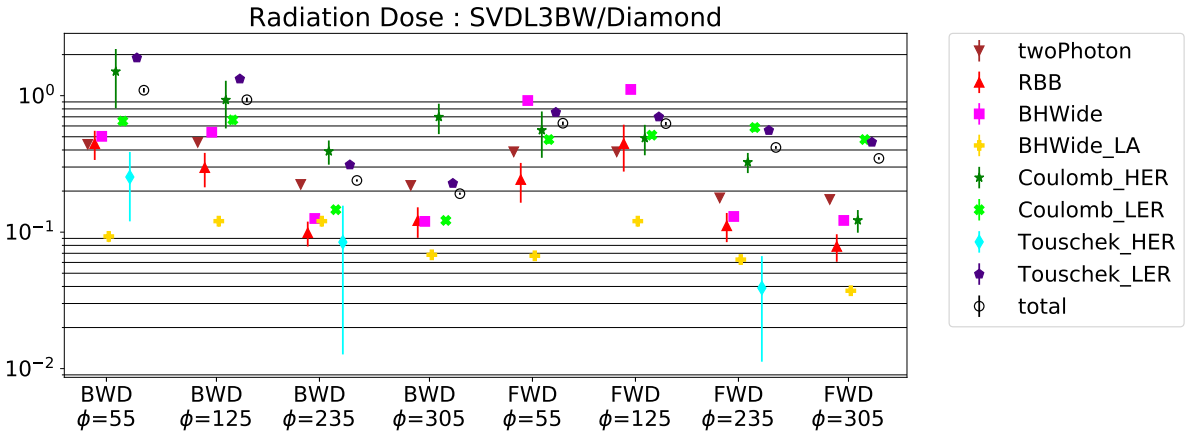

(b) SVD L3BW sensor vs Diamonds

Figure 6.5: The ratio of the dose rate between the SVD L3 sensors and diamonds in the simulation assuming the accelerator setting designed for Phase 2. The x-axis denotes the diamond sensor to which the ratio is taken. The ratio is calculated for each background species shown in the legend. The HER Touschek is missing in many places since corresponding diamond sensors had no hits due to poor statistics.

Table 6.2: Machine parameters in the Phase 2 realistic simulation. The pressure is assumed to be uniform in the ring. Vertical beam sizes are the ones at the location of the beam size monitor. The experiment names are the ones set for each beam size scan in Section 7.2.

Experiment	H-A	H-C	L-A	L-B
Ring	HER	HER	LER	LER
Date	June 11th	July 16th	June 12th	July 16th
Beam current I [mA]	287	251	341	302
Number of bunches n_b	789	789	789	789
Bunch current I/n_b [mA]	0.36	0.32	0.43	0.38
Horizontal beta function at IP β_x^* [mm]	200	100	200	200
Vertical beta function at IP β_y^* [mm]	3	3	3	3
Vertical beam size σ_y^* [μm]	36	36	38	38
Pressure P [10^{-8}Pa]	13.3	13.3	13.3	13.3

butions, B^{MC} and T^{MC}, are given by

$$\mathcal{O}_{beam\text{-}gas} = B^{MC} \cdot PI \tag{6.1}$$

$$\mathcal{O}_{Touschek} = T^{MC} \cdot \frac{I^2}{\sigma_y n_b} \tag{6.2}$$

where $\mathcal{O}_{beam\text{-}gas}, \mathcal{O}_{Touschek}$ are the occupancies estimated in the beam-gas and Touschek simulation. The beam parameters are fixed at the values in Tab. 6.2, unlike the actual measurement where the parameters are scanned for the decomposition of the two background sources. The occupancy and background contributions are estimated for each sensor. We compare B^{MC}, T^{MC} with the measured B, T in Section 7.2.6.

6.4 HER SR simulation

We consider two patterns of beam tail structure in the HER SR simulation because the beam tail structure has a large effect on the SR background. Three types of simulation samples are generated: the Gaussian-distributed core part (BeamCore), the Gaussian-distributed tail part (GausTail), and the uniformly distributed tail part (FlatTail) [27]. We evaluate the SR background by summing up the contributions from the common core part and either tail part: BeamCore+GausTail or BeamCore+FlatTail.

The horizontal (vertical) width of the GausTail Gaussian is $5\sigma_{x\text{-core}}$ ($15\sigma_{y\text{-core}}$) where $\sigma_{x\text{-core}}$ ($\sigma_{y\text{-core}}$) is the horizontal (vertical) width of the BeamCore Gaussian. FlatTail is distributed over $[-18\sigma_{x\text{-core}}, +18\sigma_{x\text{-core}}]$ in the X direction and $[-54\sigma_{y\text{-core}}, +54\sigma_{y\text{-core}}]$ in the Y direction. The tail distributions are scaled so that the number of particles beyond $10\sigma_{x\text{-core}}$ and $30\sigma_{y\text{-core}}$ are equal to 10^{-5} of that of the BeamCore population.

In addition to the occupancy, we formed clusters from the hits (see Section 3.4.3) to evaluate the cluster energies and cluster sizes. Figure 6.6 shows the estimated SR occupancies from an HER single beam. L3 FW sensor receives the largest contribution from the SR background. Scaled by the beam current, the simulated SR occupancy amounts to about 10 % of the total occupancy measured during the SR study on July 13th (see Section 7.3).

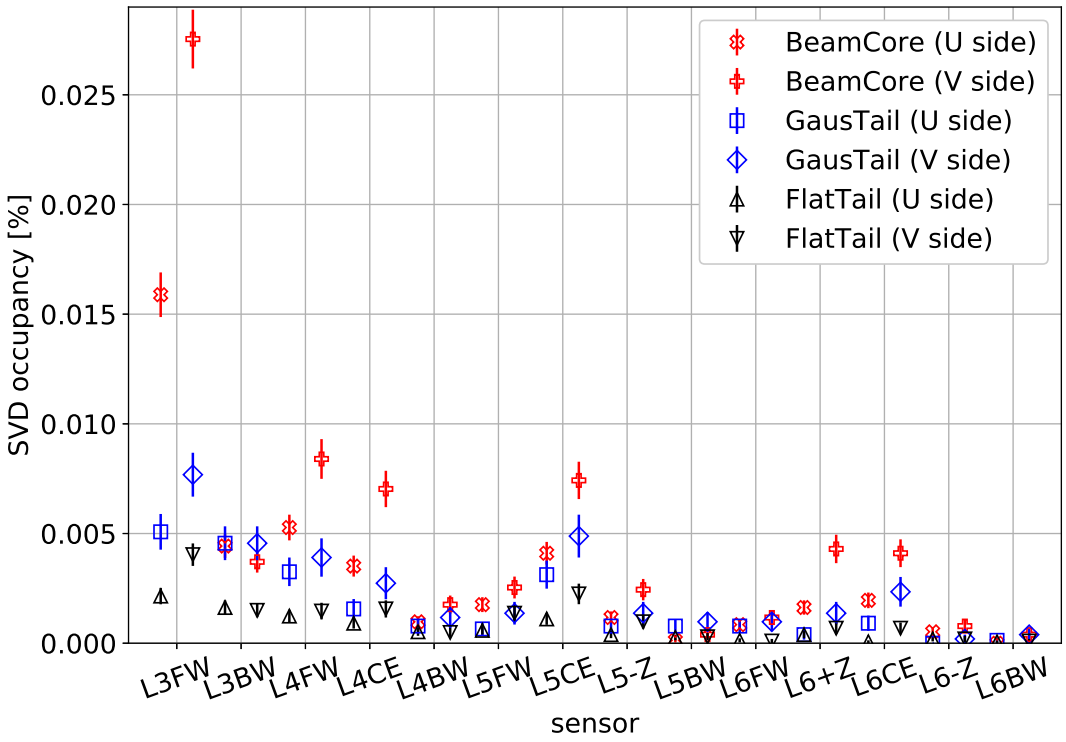

Figure 6.6: Estimated occupancy from the three SR components in the HER SR simulation. The beam current of 800 mA is assumed. The occupancies are calculated for each sensor based on the zero suppression cut of SNR=5. The x-axis denotes the sensor names. U and V side occupancies adopts different markers.

The energy spectra of the reconstructed SR clusters are shown in Fig. 6.7. For comparison, we show the energy spectra in the HER beam-gas and Touschek simulation in Fig. 6.8. We can see almost all the SR clusters have the energy deposit below 50 keV unlike the beam-gas and Touschek backgrounds. This is useful information for extracting the SR contribution from the measured background rate. We set the energy threshold of the SR study to 50 keV (see Section 7.3.1) based on the simulation.

The averaged cluster size on the L3 sensors is close to one, as shown in Tab. 6.3. This is expected because the low energy photons stop at the surface of the silicon sensor and they do not have enough energies to make hits over multiple strips. We use the information in Section 7.3 to translate the number of the SR clusters into the occupancy.

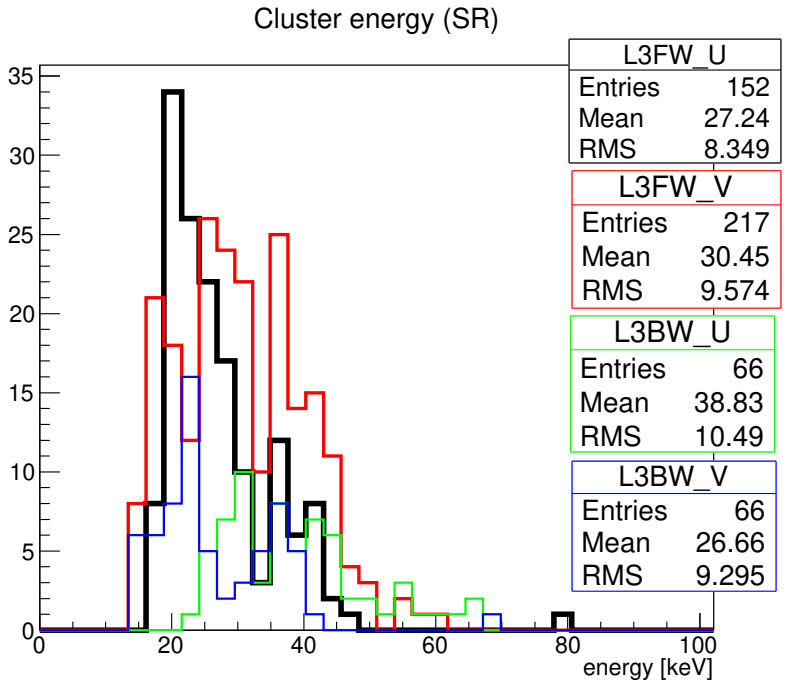

(a) BeamCore+GausTail

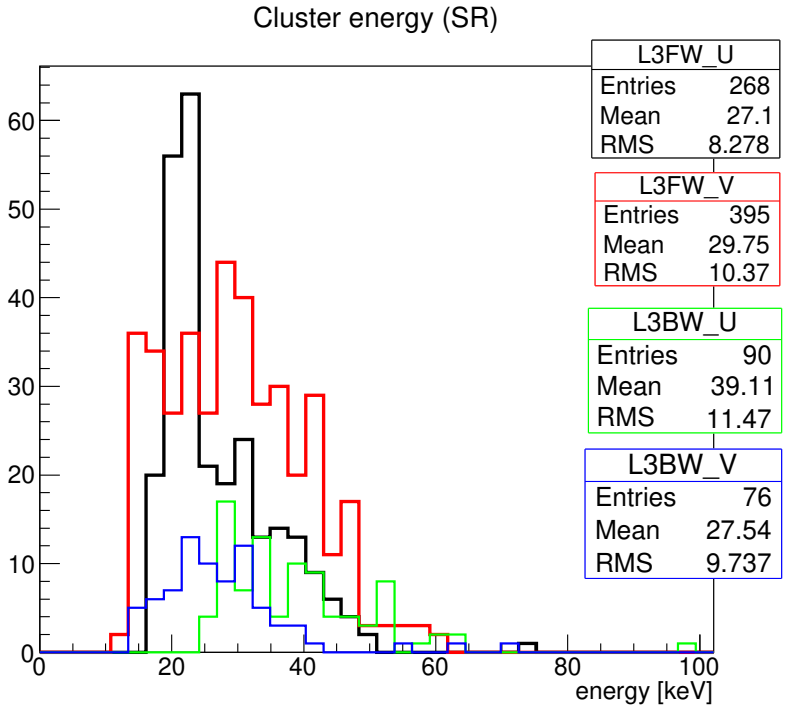

(b) BeamCore+FlatTail

Figure 6.7: Cluster energy distributions on the L3 sensors in the HER SR simulation. The clusters from the BeamCore and one of the beam tail components are summed up: BeamCore and GausTail (a), BeamCore and FlatTail (b). The black line corresponds to the U side of L3 FW sensor, red the V side of L3 FW sensor, green the U side of L3 BW sensor, blue the V side of L3 BW sensor.

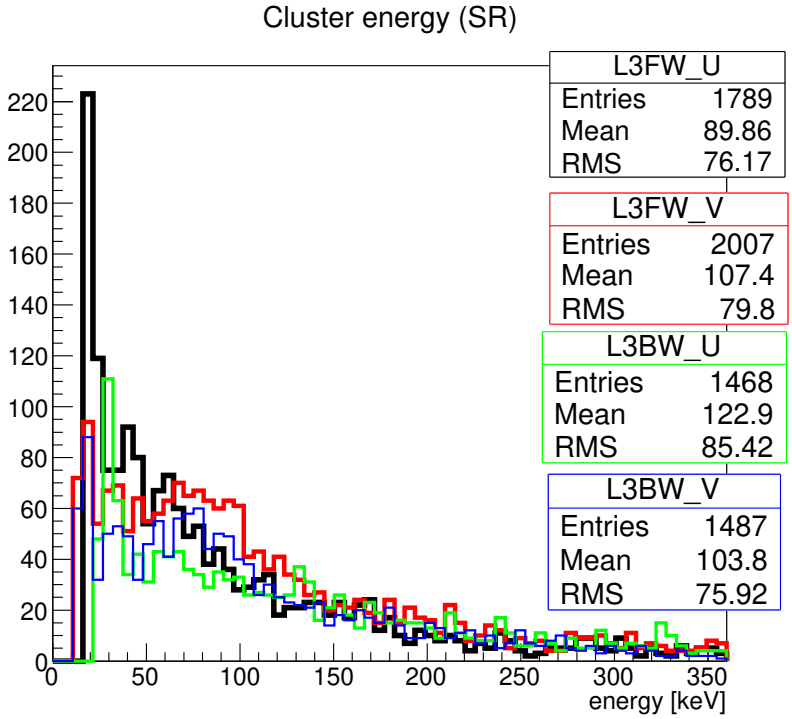

(a) HER beam-gas

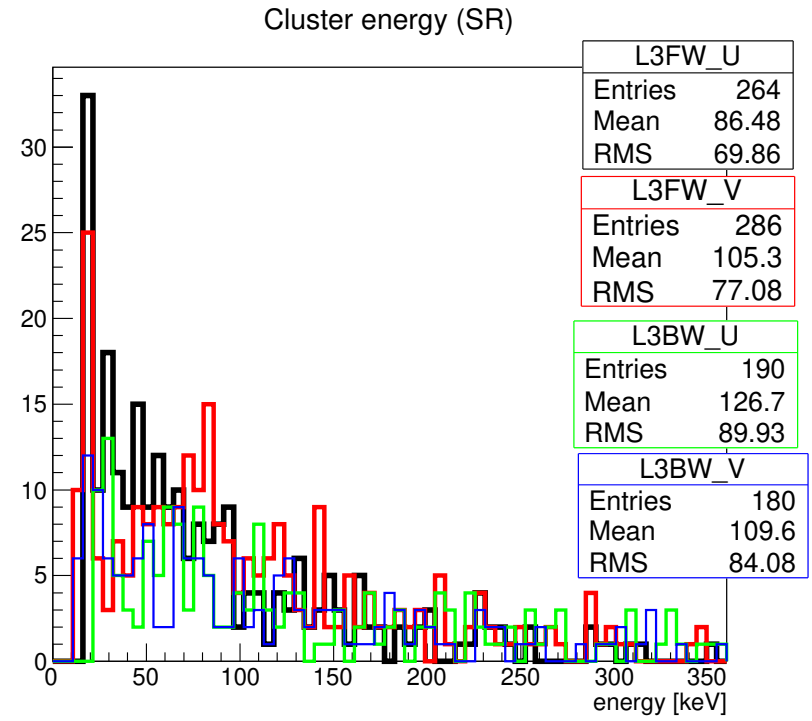

(b) HER Touschek

Figure 6.8: Cluster energy distributions on the L3 sensors in HER beam-gas (a) and HER Touschek (b) simulations. The black line corresponds to the U side of L3 FW sensor, red the V side of L3 FW sensor, green the U side of L3 BW sensor, blue the V side of L3 BW sensor. The y-axis scales are arbitrary.

Table 6.3: Cluster sizes on L3 sensors in the SR simulations. Each value is followed by the standard error. For FlatTail component on the U side of L3 FW (BW) sensor, the 68 % C.L. upper limit is calculated since all the 33 (25) clusters reconstructed in the simulation are single-strip clusters. The upper limit calculation assumes that the cluster size is either one or two and follows the binomial distribution.

sensor	side	BeamCore	FlatTail	GausTail
L3FW	U	1.04 ± 0.01	1.00 + 1.03	1.05 ± 0.04
L3FW	V	1.23 ± 0.02	1.19 ± 0.06	1.18 ± 0.05
L3BW	U	1.05 ± 0.03	1.00 + 1.04	1.06 ± 0.04
L3BW	V	1.04 ± 0.03	1.10 ± 0.07	1.09 ± 0.05

Chapter 7

Analysis of the beam background data

During the Phase 2 commissioning, which was held March–July 2018, several beam background measurements were done. We list the measurements mentioned in this section in Tab. 7.1. Regarding the important measurements, the strip charts during the measurements are shown in Appendix A.

Table 7.1: The list of beam background measurements. Beam size scans, SR studies, luminosity scan, and injection background study are respectively mentioned in Section 7.2, 7.3, 7.4, and 7.5.

date	beam	HER β_x^*/β_y^* [mm]	LER β_x^*/β_y^* [mm]	note
April 30th	HER	200/8	–	
May 1st	LER	–	200/8	
May 8th	HER	200/8	–	
May 10th	LER	–	200/8	
May 21st	HER	200/8	–	
May 21st	Collision	200/8	200/8	
May 24th	HER	200/6	–	
May 24th	LER	–	200/6	
June 11th	HER	200/3	–	Beam size scan (H-A)
June 12th	LER	–	200/3	Beam size scan (L-A)
July 12th	Collision	100/3	200/3	Luminosity scan
July 13th	LER	–	200/3	LER injection background study
July 13th	LER	–	200/3	
July 13th	HER	100/3	–	Beam size scan (H-B), SR study
July 14th	–	–	–	HER vacuum leak
July 16th	LER	–	200/3	Beam size scan (L-B), SR study
July 16th	HER	100/3	–	Beam size scan (H-C)

In the first section of this chapter, we explain the long-term evolution of the single-beam background rates. In the following sections, we describe dedicated analyses for the beam background sources introduced in Section 5.2. We close the chapter by confirming the correlation between the SVD and diamond and estimating the Phase 3 background rate, which are the goals of our beam background study.

7.1 Beam background evolution over Phase 2

In Phase 2, collision tuning started with the optics of (β_x^*[mm], β_y^*[mm]) = (200, 8) for both rings. As the beta functions were progressively squeezed in stages, we measured the single-beam background rate. Figure 7.1 shows the long-term evolution of the beam background seen in the SVD. The occupancy on the V side of L3 FW (BW) sensor is shown for the HER (LER) because the sensor suffers the largest occupancy from the HER (LER) background.

In general, smaller beta functions make the beams narrower, which leads to more backgrounds due to the Touschek effect. However, it is not always true for Fig. 7.1, because the background rate also depends largely on the optics and collimator condition.

- The HER background rate on June 11th ($\beta_x^* = 200\,\mathrm{mm}$) is higher than July 13th and 16th ($\beta_x^* = 100\,\mathrm{mm}$) despite its larger β_x^*. We suppose this is because June 11th was right after the optics setting was changed to a new one and the collimator setting was not yet optimized to mitigate the background.
- The higher background rate on July 16th compared to July 13th in both rings is also due to the collimator setting. Since the study on July 16th was the reference for the luminosity background study on a different day, we opened the collimators to make the collimator setting the same as the previous study[1].
- The difference in the LER background between June 12th and July 13th is also due to the collimator condition. Since a vertical collimator in LER, which is the only one, was damaged at the end of June, the beam background is less mitigated by the collimator in July.

7.2 Decomposition of Touschek and beam-gas components

7.2.1 Method

To disentangle the two major backgrounds, Touschek and beam-gas components, we performed several "beam size scans" in Phase 2. In a beam size scan, we monitor the beam parameters and the background rates on the detectors via EPICS [28] as shown in Fig. 7.2. They are measured as the beam current decays and the measurement is repeated with different beam sizes σ_y and also different numbers of bunches n_b.

Since only the Touschek component depends on the beam size and the number of bunches, the difference of the background rates between the measurements arises from Touschek effect assuming the same beam current. The result of a beam size scan is analyzed by plotting $\mathcal{O}/IP$

[1] On July 12th, when we performed the luminosity study, poor injection conditions forced us to open the collimators widely to allow beam injection, leading to higher background rate from the stored beam

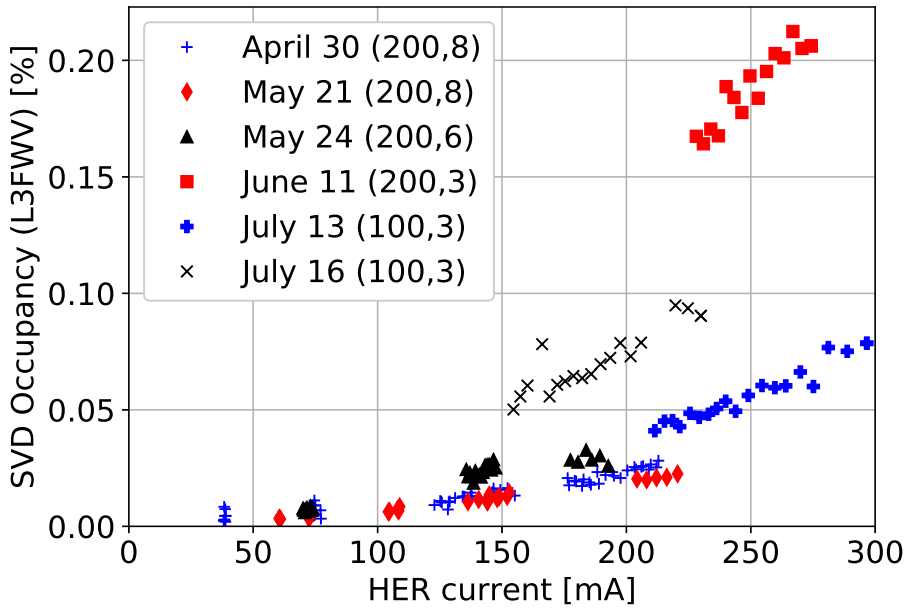

(a) HER

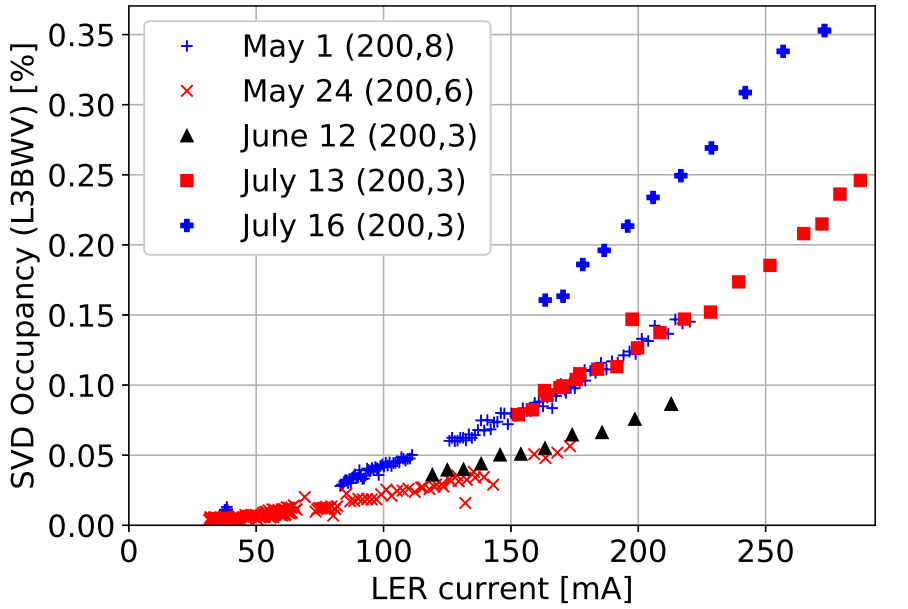

(b) LER

Figure 7.1: The long-term evolution of the single-beam backgrounds of the HER (a) and the LER (b). The SVD occupancy is shown as a function of the beam current. The legend denotes (β_x^*[mm], β_y^*[mm]) together with the dates of the measurements. The background rates are measured with the nominal beam size of each optics, and by 1 kHz pseudorandom trigger.

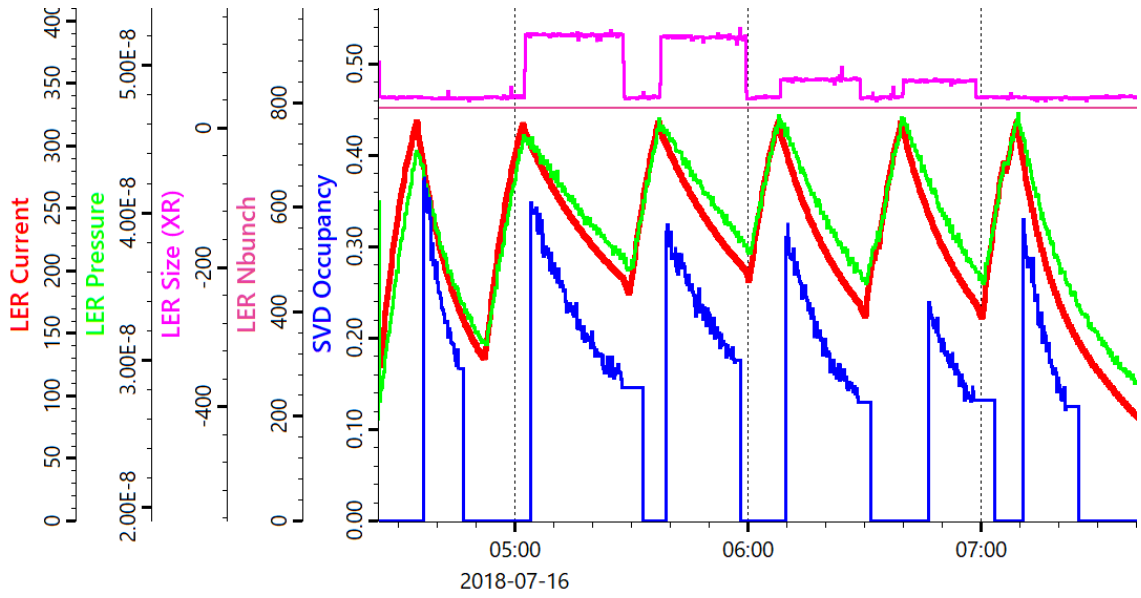

Figure 7.2: Strip chart showing SVD occupancy and beam parameters during a beam size scan (L-B). The LER parameters (I, P, σ_y, n_b) and the SVD occupancy (averaged over L3 sensors) are shown as function of time. We inject the beam to the maximum current and take data as the current decays. The procedure is repeated for each beam size setting. The SVD occupancy is recorded only when the Belle II DAQ is running and the last value is kept when the DAQ is stopped. It goes to the default value when the system is configured for a new run.

values as a function of $I/P\sigma_y n_b$. This "heuristic plot" is a convenient way to confirm the validity of our model described in Section 5.3, because another form of Eq. (5.2)

$$\frac{\mathcal{O}}{IP} = T \cdot \frac{I}{P\sigma_y n_b} + B \tag{7.1}$$

indicates that $\mathcal{O}/IP$ should be a linear function of $I/P\sigma_y n_b$ with an offset of B and a slope of T. Only sweeping with the beam current is not enough to determine B and T, since I/P does not change drastically in Eq. (7.1) due to the linearity of P to I.

7.2.2 Beam size scans in Phase 2

Table 7.2 shows the list of beam size scans performed in Phase 2. Two different methods were used to change the beam size: the vertical steering method and the x-y coupling method. In the vertical steering method, we locally introduce the vertical shift in the beam orbit with bending magnets. This leads to the vertical dispersion and increases the beam size. In the x-y coupling method, we increase the x-y coupling of the beam by changing the strength of a skew quadruple magnet. Since the horizontal beam size is larger than the vertical one, the x-y coupling increases the vertical beam size. The latter method enables us to increase the beam size without affecting the beam orbit, and is the preferred method. The beam orbit shift by the vertical steering method might cause an unexpected effect on the beam background rate. The vertical steering method was used in H-B due to miscommunication between the accelerator

Table 7.2: The list of beam size scans. n_b is the number of bunches, σ_y is the vertical beam size at the location of the beam size monitor, I is the maximum beam current right after the beam injection. In L-A, the SVD data are available only for n_b=789.

exp	date	ring	method	n_b	σ_y [μm]	I [mA]
H-A	June 11th	HER	x-y coupling	789, 1576	35, 50, 85	285
L-A	June 12th	LER	x-y coupling	789(, 1576)	35, 85, 165	320
H-B	July 13th	HER	vertical steering	789	40, 50, 80, 135	320
L-B	July 16th	LER	x-y coupling	789	45, 70, 130	320
H-C	July 16th	HER	x-y coupling	789	40, 60, 70	240

and detector groups.

For H-A, H-C, L-A, and L-B, we prepared the dedicated beam background simulations, which reflect the beam optics and collimator settings during the studies. In this section, we aim to determine the Touschek and beam-gas contributions in these studies and to compare them with the simulations.

7.2.3 Pressure correction

Since the CCGs (see Section 3.2.1) are located near the sputter ion pumps outside the beam pipe, they do not directly measure the pressure in the beam pipe. Because of the finite conductance between the beam pipe and the pumps, the dynamic pressure becomes lower around the CCGs. In the Phase 1 analysis [4], the dynamic pressure measured by each CCG is considered to be three times lower than the one in the beam pipe according to simulations:

$$P_{CCG} = P_0 + k \cdot I \tag{7.2}$$

$$P_{beam} = P_0 + 3k \cdot I \tag{7.3}$$

where, P_{CCG} and P_{beam} are the pressures around the CCGs and inside the beam pipe respectively, P_0 is the base pressure, and $k \cdot I$ is the dynamic pressure proportional to the beam current. In this thesis, we take the factor for the dynamic component to be an unknown parameter c.

$$P_{beam} = P_0 + ck \cdot I \tag{7.4}$$

Therefore, the pressure in the beam pipe is given by

$$P_{beam} = c \cdot P_{CCG} - (c-1) \cdot P_0. \tag{7.5}$$

P_0 is determined as the pressure which has become stable after several hours without the beam stored in the ring. When there is not such a period near the background measurement, we determined it by fitting the measured pressure and the beam current with a linear function.

For the LER, we optimize c so that the measured diamond dose rates fit the single-beam background model (see Section 5.3) the best. We use the dose rates on the four BWD diamond sensors during L-A for the optimization. The LER base pressure is determined to be $P_0 = 1.8 \times 10^{-8}$ Pa from the pressure measured without the beam as shown in Fig. 7.3. For each

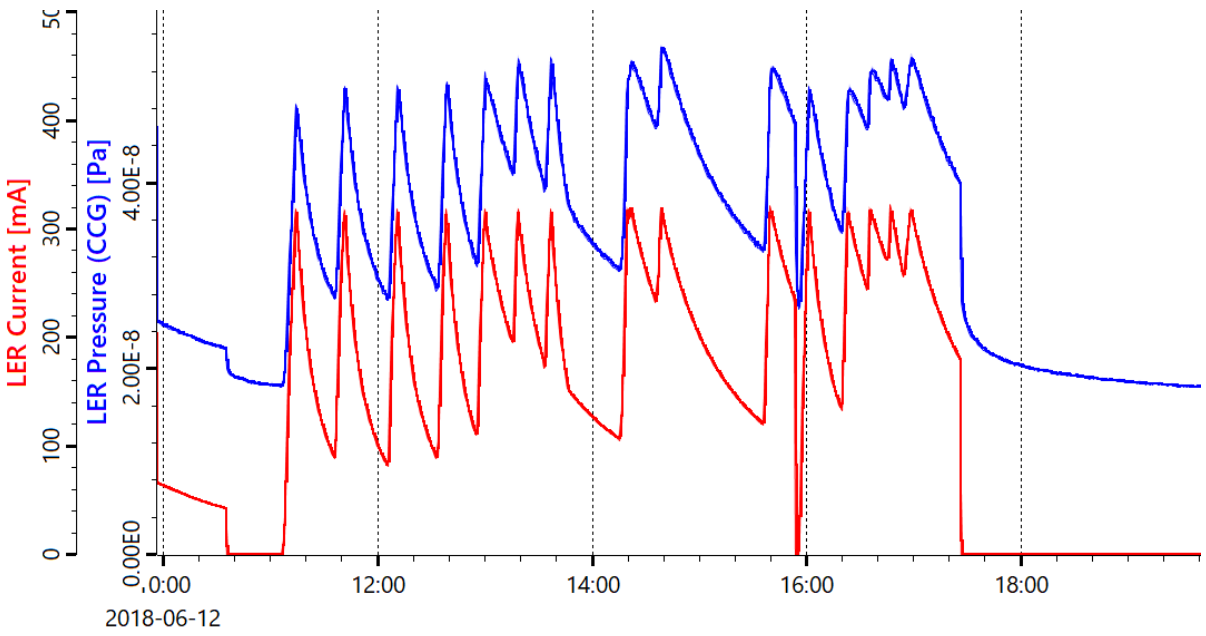

Figure 7.3: The LER pressure and current during L-A. The pressure after a few hours without stored beam is taken as the base pressure $P_0 = 1.8 \times 10^{-8}$ Pa.

diamond sensor, we fit the dose rate and the beam parameters with Eq. (5.2) to determine B, T, and c. Figure 7.4 shows the heuristic plots (see Section 7.2.1) for the diamond sensors with the optimized c. In contrast to Fig. 7.5 where no or old correction is applied, Fig. 7.4 shows good linearity and hence good agreement with the model.

The optimized parameter c is listed in Tab. 7.3. The parameter does not agree across the different channels of diamonds. We speculate this is because we use the average pressure over the entire ring in the fit though the pressure is an order of magnitude different depending on the location. The probability that the beam-gas background particles hit each detector also depends on the beam loss position. In order to take these things into account, we should use all the pressures measured along the ring and assign the beam-gas contribution B to each of them, which corresponds to weighting CCGs according to their contributions as was done in the Phase 1 analysis [4]. In this thesis, we use only the average pressure to avoid introducing too many fitting parameters.

The parameter c for the SVD sensors may also differ from the ones for the diamonds, but as an approximation, we use the average of the values in Tab. 7.3, $c = 1.7$, for the LER pressure correction from this point. Another BEAST II detector at the same radius as the SVD also shows $c = 1.7$ [29].

For the HER, we do not determine c from the data, because the data do not match the model because of the unknown background component (see Section 7.2.6). Thus, we assume $c = 3$ for the HER and estimate the systematic uncertainty from c later.

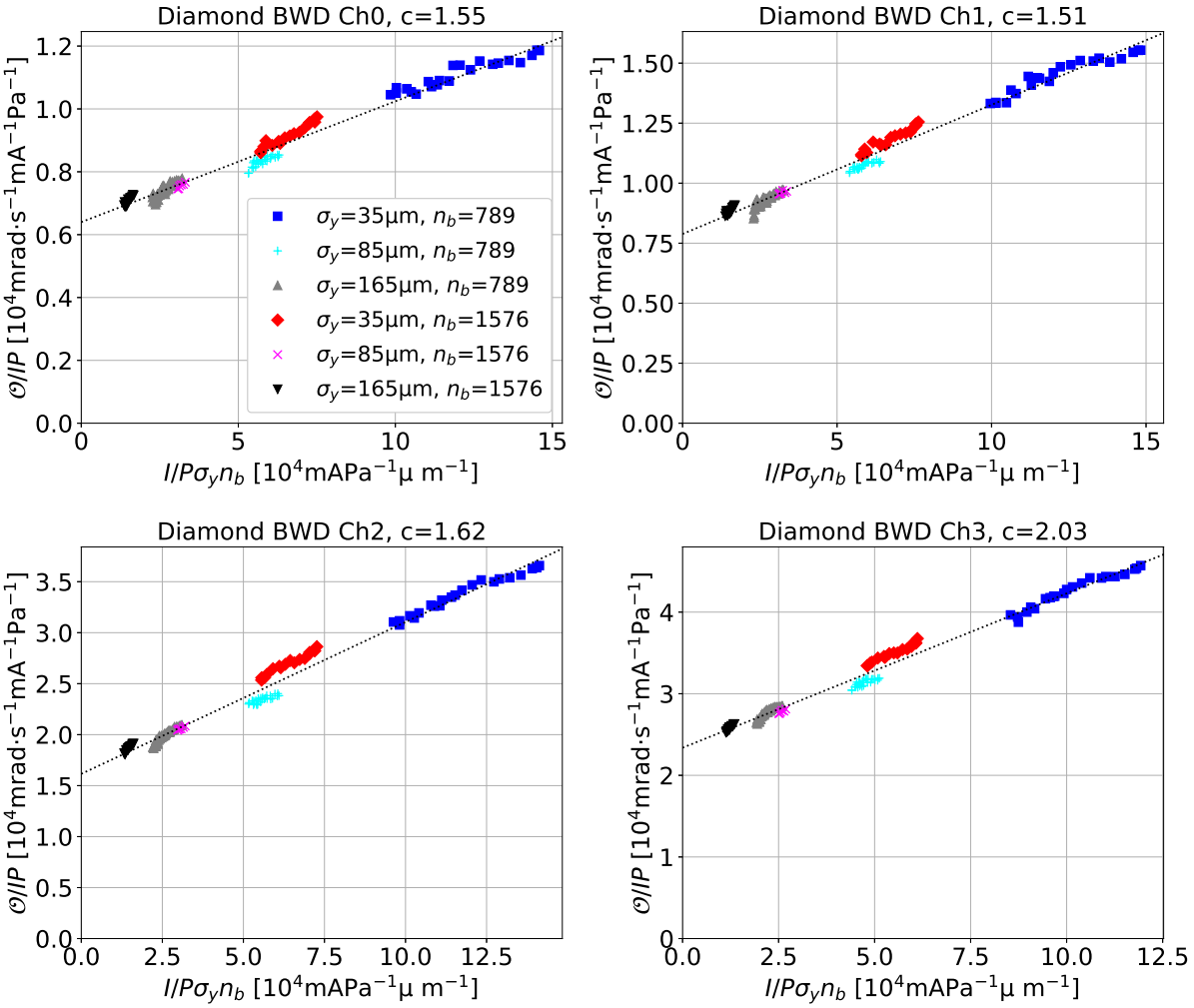

Figure 7.4: Heuristic plots with the optimized pressure correction for the four BWD diamond sensors in L-A. The x-axis and y-axis represent $I/P\sigma_y n_b$ and $\mathcal{O}/PI$ respectively, where $\mathcal{O}$ is the diamond dose rate, I is the beam current, n_b is the number of bunches, σ_y is the vertical beam size. The pressure is given by $P = c \cdot P_{CCG} - (c-1) \cdot P_0$. The data from six measurements with different σ_y, n_b shown in the legend are plotted. In each plot, c is determined by fitting data with the single-beam background model. The fitted line is drawn in each plot.

Table 7.3: The optimized pressure correction parameter c for the BWD diamond sensors. c is determined by fitting the diamond dose rate and beam parameters with the single-beam background model Eq. (5.2). The minute-by-minute averages of the measured values are used in the fit and the uncertainties are determined as described in Section 7.2.4.

diamond	c	χ^2/ndf
ch0 ($\phi = 55$)	1.54 ± 0.02	51/151
ch1 ($\phi = 125$)	$1.51^{+0.02}_{-0.01}$	45/151
ch2 ($\phi = 235$)	$1.62^{+0.01}_{-0.02}$	85/151
ch3 ($\phi = 305$)	2.03 ± 0.02	43/151

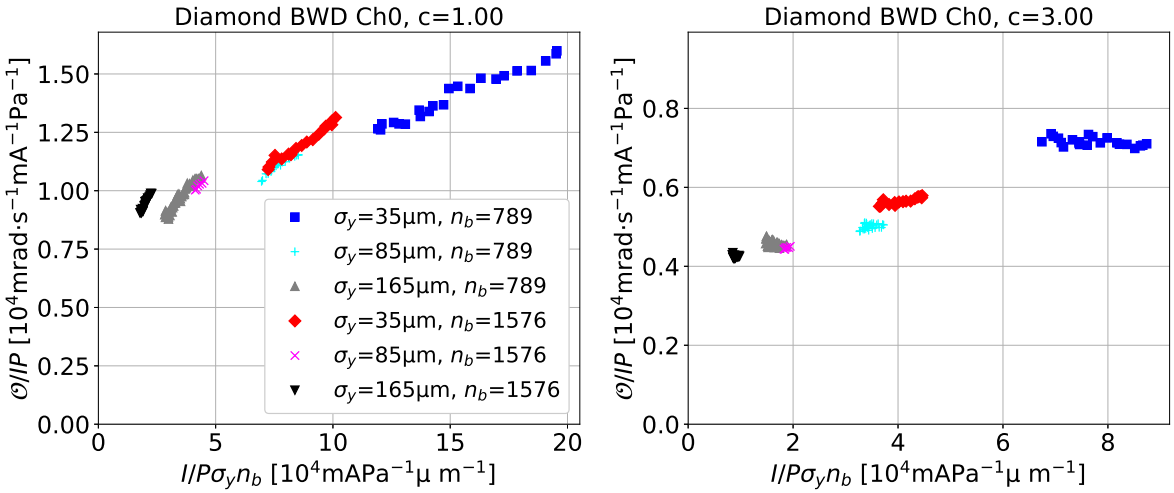

Figure 7.5: Heuristic plots for a BWD diamond sensor (ch0) in L-A, with no or old pressure correction. The x-axis and y-axis represent $I/P\sigma_y n_b$ and $\mathcal{O}/PI$ respectively, where $\mathcal{O}$ is the diamond dose rate, I is the beam current, n_b is the number of bunches, σ_y is the vertical beam size. The pressure is given by $P = c \cdot P_{CCG} - (c-1) \cdot P_0$. The plotted data are same as Fig. 7.4 except for the pressure correction factor c. The left plot assumes $c = 1$ (no correction) and right $c = 3$ (naive correction).

7.2.4 Errors of the variables

We use the minute-by-minute averages of the beam parameters and the SVD occupancies provided by EPICS for the decomposition analysis. An example is shown in Fig. 7.6. For each variable, we separate all the data points into subsets by timestamp to calculate the average. The error of the SVD occupancy is estimated as the standard error of the mean $\overline{x}$,

$$\sigma_{\overline{x}} = \sqrt{\frac{\sum_{i=1}^{n}(x_i - \overline{x})^2}{n(n-1)}} \tag{7.6}$$

for each subset x_i $(i = 1...n)$. We conservatively assume the errors of σ_y and P to be 5 % of the center value. Since the standard deviation of the beam current monitored by the DCCT is negligibly small[2] compared to other variables, we ignore the error of the beam current.

7.2.5 Noise subtraction

When a DSSD sensor does not have particle hits, it still has the finite occupancy of about 10^{-3} % due to electrical noise (assuming the zero suppression threshold of SNR = 5). We measured the noise occupancy without the beam stored before or after each beam background study. The noise is subtracted in our analysis. However, since the occupancy from beam background is $O(0.1\,\%)$, the noise component does not have a significant effect on the total occupancy.

[2] 0.01 mA for the LER and 0.007 mA for the HER [30].

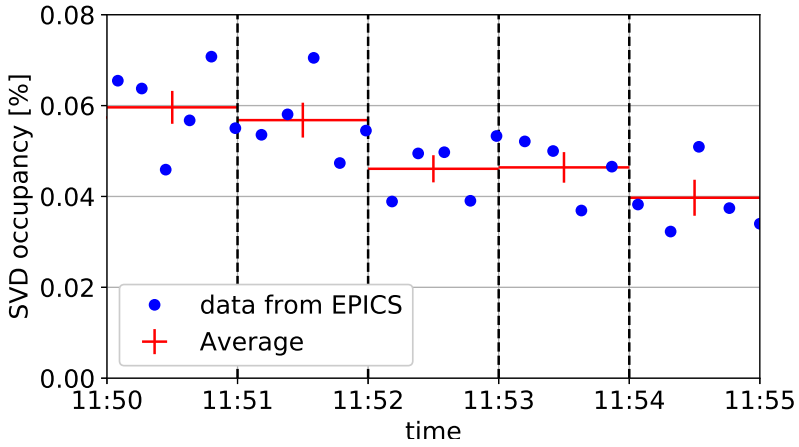

Figure 7.6: The occupancy of the U side of L3 FW sensor as the function of time during a beam background measurement. The blue dots show the occupancy which is calculated by the monitoring software and provided via EPICS. The data points are separated on a minute-by-minute basis. The average and the standard error of each subset are shown in red.

7.2.6 Heuristic analysis

(1) HER

Figures 7.7 and 7.8 show the heuristic plots for the HER beam size scans, H-A, H-B, and H-C. We use the occupancy of the V side of L3 FW sensor in the plots because the sensor has the largest occupancy from HER. We can see that data points are not in a linear relation indicated by the single-beam background model represented as Eq. (7.1). As clearly seen in Fig. 7.7(b), when we increase the beam size from the smallest point (the nominal size in the optics), the SVD occupancy slightly decreases at first but increases significantly at larger beam sizes. The decrease is explained by the Touschek component, but the increase indicates the existence of an unexpected background component which is not involved in the model. We call this unexpected component X. The X component positively correlates with the beam size, in contrast to the Touschek component.

The dependence of the X component on the other beam parameters is seen in Fig. 7.7(a). On June 11th, we measured the beam background rate with three different σ_y and two different n_b. If we group the six datasets into three groups by vertical beam size σ_y, we can draw three lines each of which goes through each dataset. Figure 7.9 shows the offsets and slopes of these lines. They have similar offsets B as shown in Fig. 7.9(a). Assuming the offsets are common, Eq. (5.2) can be extended as

$$\mathcal{O} = T \cdot \frac{I^2}{\sigma_y n_b} + B \cdot PI + X(\sigma_y)\frac{I^2}{n_b} \tag{7.7}$$

where $X(\sigma_y)$ is the function describing the beam size dependence of the X. If σ_y is fixed, $\mathcal{O}/PI$ is still a linear function of $I/P\sigma_y n_b$ but the slope of the line is modified as $T + \sigma_y X(\sigma_y)$.

As shown in Fig. 7.9(b), the lines for $\sigma_y = 35, 50\,\mu\text{m}$ in Fig. 7.7(a) have the almost same slope $T + \sigma_y X(\sigma_y)$, which is much different from $\sigma_y = 85\,\mu\text{m}$. This means that the X contribution

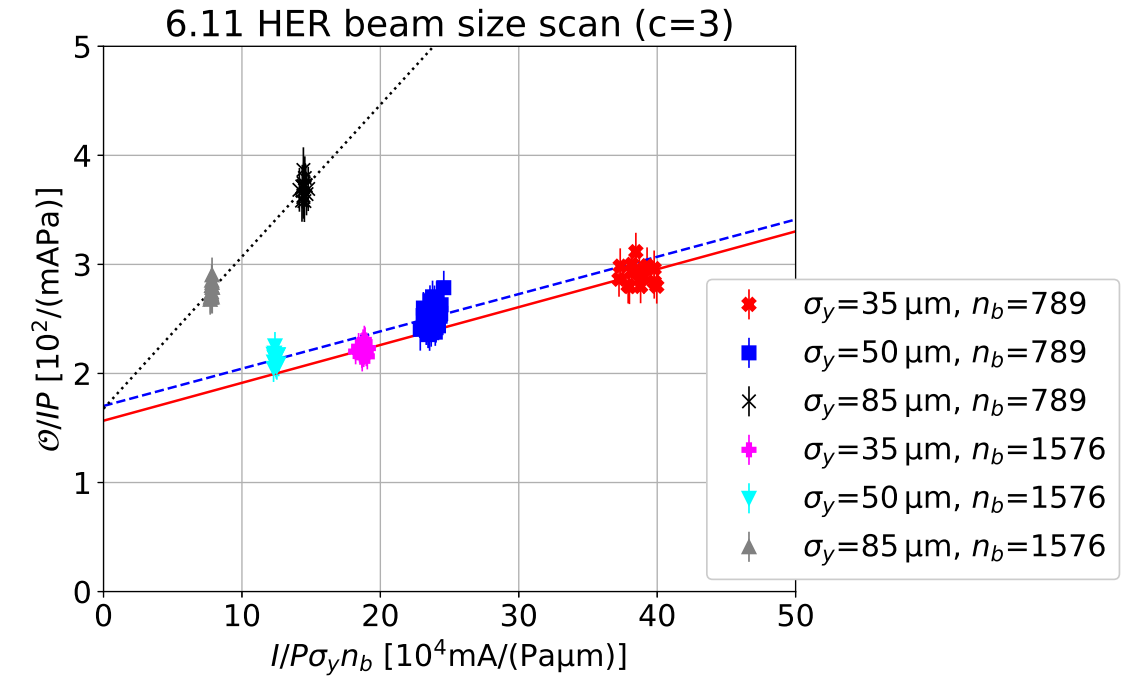

(a) H-A

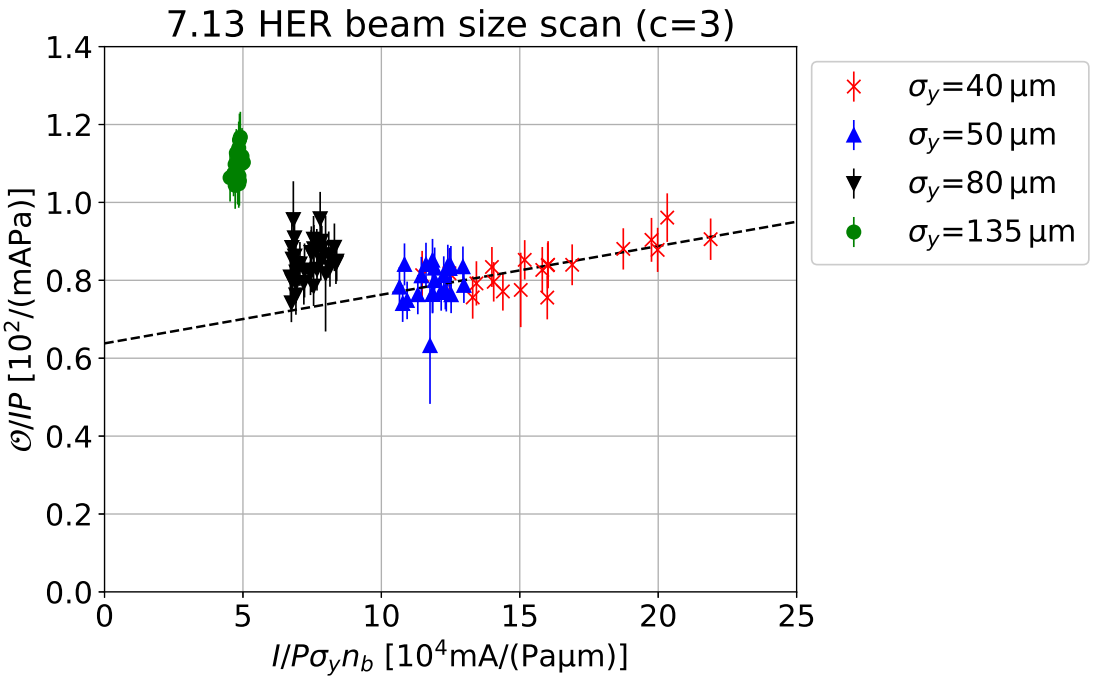

(b) H-B

Figure 7.7: Heuristic plots for two HER beam size scans: H-A (a), H-B (b). The x-axis and y-axis represent $I/P\sigma_y n_b$ and $\mathcal{O}/PI$ respectively, where $\mathcal{O}$ is the occupancy of the V side of L3 FW sensor, I is the beam current, P is the pressure, n_b is the number of bunches, σ_y is the vertical beam size. The SVD occupancy was measured by 1 kHz pseudorandom trigger. The legend denotes rough σ_y (and n_b for (a)) during each measurement. The three lines in (a) respectively fit the data points with σ_y=35, 50, 85 μm. χ^2/ndf of the fitted lines are 12.2/30, 33.5/45, and 7.9/27, respectively. The line in (b) fits the data points with σ_y=40, 50 μm. χ^2/ndf of the fitting is 21.2/40.

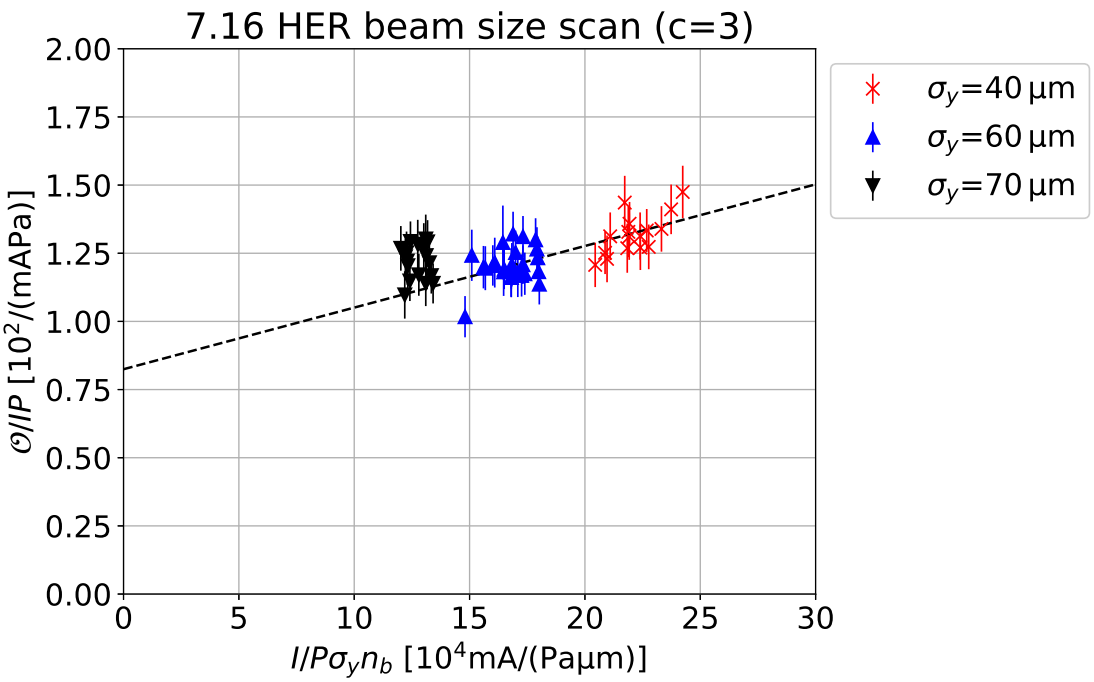

Figure 7.8: Heuristic plots for the HER beam size scan H-C. The x-axis and y-axis represent $I/P\sigma_y n_b$ and $\mathcal{O}/PI$ respectively, where $\mathcal{O}$ is the occupancy of the V side of L3 FW sensor, I is the beam current, P is the pressure, n_b is the number of bunches, σ_y is the vertical beam size. The SVD occupancy was measured by 1 kHz pseudorandom trigger. The legend denotes rough σ_y during each measurement. The line fit the data points with σ_y=40, 60 μm. χ^2/ndf of the fitting is 28.1/41.

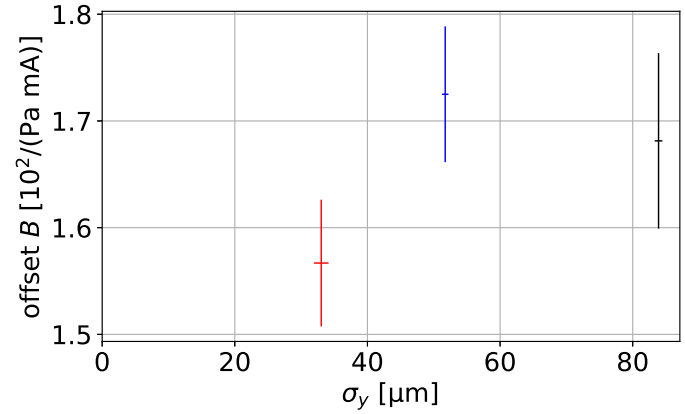

(a) offset

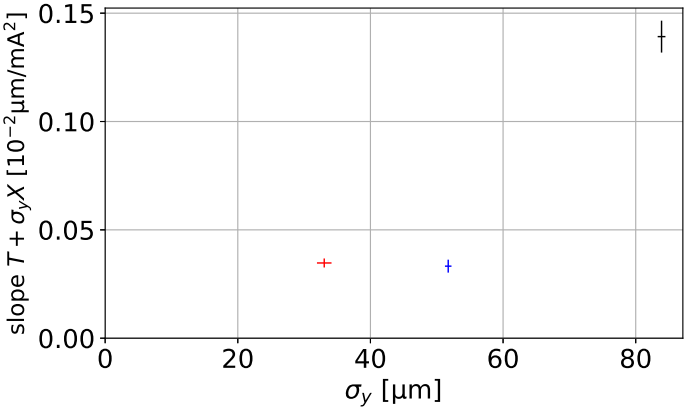

(b) slope

Figure 7.9: The offsets (a) and slopes (b) of the three lines drawn in Fig. 7.7(a). Each line fits the data points with the same beam size in Fig. 7.7(a). The x-axis shows the vertical beam size that is averaged over the data points used in each fit. The error bar shows the standard deviation of the beam size. The errors of the offsets and slopes originate from the errors of the parameters used in the fit (see Section 7.2.4).

Table 7.4: The uncertainty of the fitted background contributions B, T due to the pressure correction factor c. For each experiment, B and T are obtained assuming $c = 1$ or $c = 3$. $\frac{x_{c=1}}{x_{c=3}} - 1 (x = T, B, BP)$ are averaged over the sensors and are listed in the table.

	H-A	H-B	H-C
T	$-0.5\,\%$	$+1.0\,\%$	$+15\,\%$
B	$+62\,\%$	$+65\,\%$	$+35\,\%$
BP	$-3.4\,\%$	$-4.5\,\%$	$-24\,\%$

$X(\sigma_y)$ is small around the nominal beam size but increases drastically when the beam size is too large. We assume the X contribution is negligible at $\sigma_y = 35,\ 50\,\mu\text{m}$ and determine the beam-gas and Touschek contribution B, T by fitting Eq. (7.1) to these data. Similarly, we choose $\sigma_y = 40,\ 60\,\mu\text{m}$ runs in Fig. 7.8 to determine B, T in H-C. We estimate B, T for each sensor and compare them with the simulation. Figure 7.10 shows $B^{data}/B^{MC}, T^{data}/T^{MC}$ for each sensor. The measured background contributions are larger than the simulated ones by two or three orders of magnitude. Uncertainties originate from the errors of the parameters used in the fits (see Section 7.2.4) and the statistical error of the simulation.

We have been using $c = 3$ for the pressure correction so far, but since the smaller value (1.5–2.0) for c is favored in the LER (see Section 7.2.3), we estimate the systematic uncertainties of B and T due to c. For that purpose, we compare B and T determined with $c = 1$ and $c = 3$. If we set c smaller, the corrected pressure becomes smaller and the beam-gas contribution B will be larger. In order to compensate for this obvious effect, we also compare the beam-gas contributions multiplied by the corrected pressure[3] $B \cdot P$. The Touschek contributions are compared as they are. The effect of changing c is shown in Tab. 7.4. We can see that the effect on the decomposition is negligible in H-A and H-B, but rather large in H-C. During H-C, dynamic pressure was almost twice as high as H-B, because of a vacuum leak which happened between these experiments. We speculate this is the reason why the decomposition of H-C is sensitive to c.

(2) LER

Figure 7.11 shows the heuristic plots for the LER beam size scans, L-A and L-B. The occupancy of the V side of L3 FW sensor, which is most sensitive to the LER background, is used for the plots. The pressure correction factor is set to $c = 1.7$ as described in Section 7.2.3.

The heuristic plot for L-A Fig. 7.11(a) shows good linearity, indicating that the LER background is explained as the sum of the Touschek and beam-gas components. The X component that appears in the HER background is not present in the LER or at least not visible. The beam-gas and Touschek contributions in L-A are determined by simply fitting the model to all the data.

On the other hand, the result of L-B Fig. 7.11(b) is not easily explained by the model. In L-B, we measured the background rate at the nominal beam size twice, at the beginning and end of the study. The two measurements show different background rates, despite there being

[3]The pressure at $I = 300\,\text{mA}$ is used.

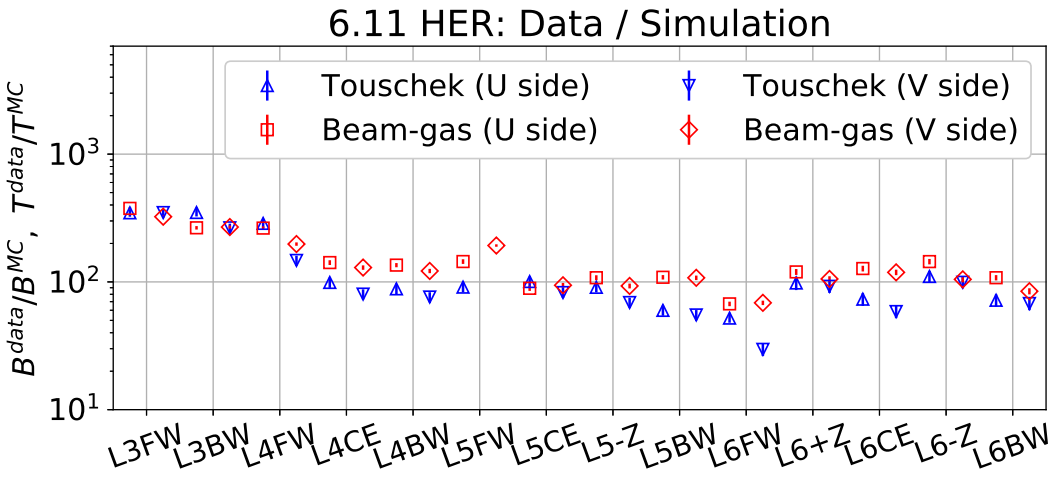

(a) H-A

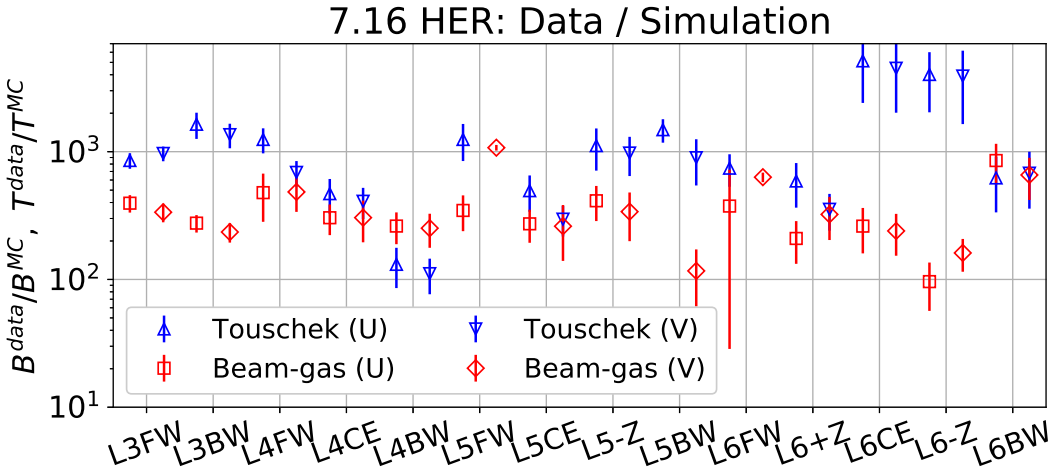

(b) H-C

Figure 7.10: The beam-gas and Touschek contributions in the HER background B, T are compared between the measurement and the simulation for each sensor. The comparison was done individually for H-A (a) and H-C (b). The x-axis denotes the sensor names. The triangles (inverted triangles) denote the Touschek component of the U (V) side occupancy. The squares (diamonds) denote the beam-gas component of the U (V) side occupancy.

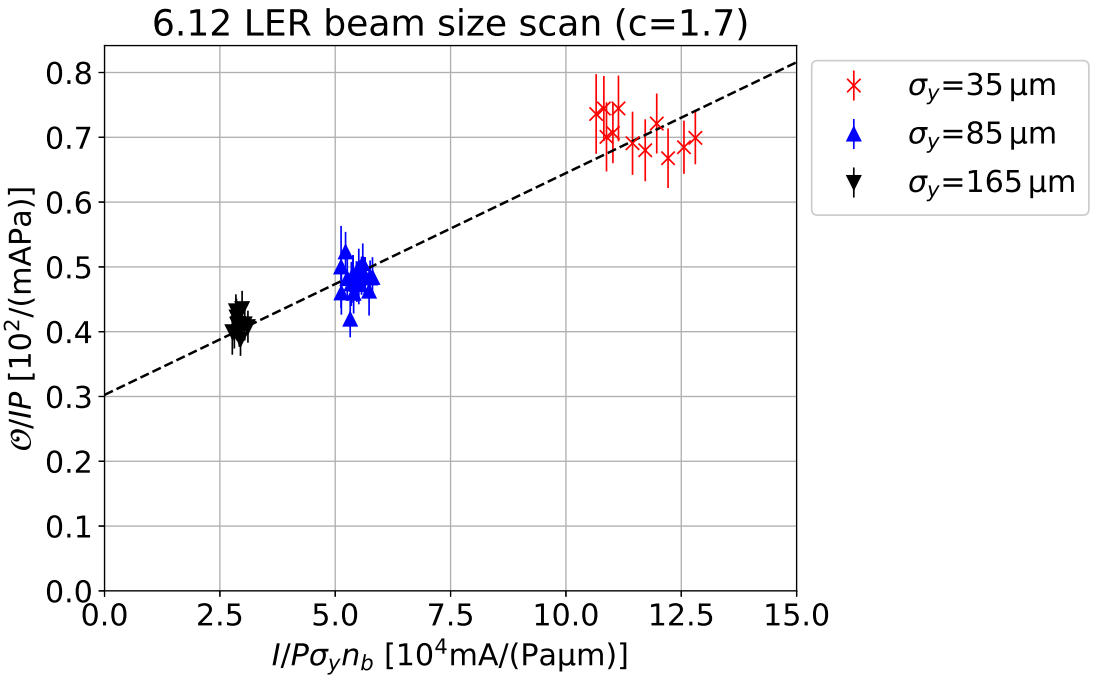

(a) L-A

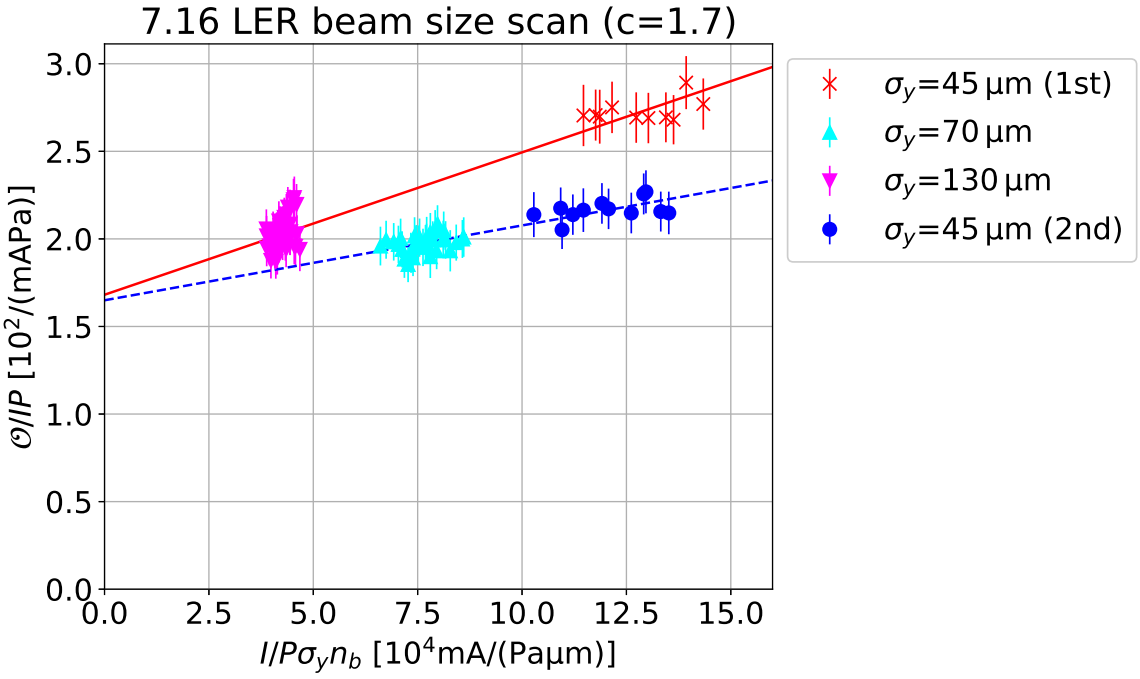

(b) L-B

Figure 7.11: Heuristic plots for the LER beam size scans: L-A (a) and L-B (b). The x-axis and y-axis represent $I/P\sigma_y n_b$ and $\mathcal{O}/PI$ respectively, where $\mathcal{O}$ is the occupancy of the V side of L3 BW sensor, I is the beam current, P is the pressure, n_b is the number of bunches, σ_y is the vertical beam size. The SVD occupancy was measured by 1 kHz pseudorandom trigger. The legend denotes rough σ_y during each measurement. The line in (a) fit all the data points in the plot. In L-B, six measurements where σ_y=45, 130, 130, 70, 70, 45 μ were done. The two lines in (b) individually fit the data points measured during the first and second halves of L-B. χ^2/ndf of the fitted lines are 32.3/40, 35.6/51, and 117/43, respectively.

Table 7.5: The uncertainty of the fitted background contributions B, T due to the pressure correction factor c. For each experiment, B and T are obtained assuming $c = 1.5, 1.7, 2.0$. $\frac{(BP)_{c'=1.5,2.0}}{(BP)_{c=1.7}} - 1$ and $\frac{T_{c'=1.5,2.0}}{T_{c=1.7}} - 1$ are averaged over the sensors and are listed in the table.

	L-A		L-B (1st half)		L-B (2nd half)	
c'	1.5	2.0	1.5	2.0	1.5	2.0
beam-gas	+0.5 %	-0.6 %	-0.3 %	+0.4 %	-1.3 %	+1.6 %
Touschek	-2.1 %	+2.6 %	-1.5 %	+1.9 %	+5.3 %	-6.2 %

no difference in accelerator conditions such as the beam current, pressure at each location of the ring, vertical and horizontal beam sizes, and effective atomic number of the residual gas. This difference was also seen in other subdetectors.

The background rate measured on July 12th, four days before L-B shows a similar inexplicable effect (see Section 7.4.2). Considering these observations, we conclude that the LER background was unstable for an as-yet-undetermined reason. One possible explanation is the vacuum leak that occurred two days before L-B in the HER. Since the leak was found in the HER beam pipe near the IP, it could have affected the LER vacuum condition near the IP, where there are no vacuum pumps or CCGs.

Assuming that the LER background follows our model in the short term, we divide L-B into halves and estimate the beam-gas and Touschek contributions B, T for each half. The halves show similar beam-gas contributions, whereas the Touschek contribution is doubled in the second half. This result does not support the above hypothesis that the instability was caused by the vacuum leak.

Figure 7.12 shows the comparison of the beam-gas and Touschek contributions between data and simulation. Uncertainties originate from the errors of the parameters used in the fits (see Section 7.2.4). Similarly to the HER, the measured background contributions are larger than the simulated ones, but the discrepancy is not as large as that seen in the HER. The discrepancy for the Touschek component is within one order of magnitude, while the beam-gas contributions differ by one or two orders of magnitude. We can see that B^{data}/B^{MC} and T^{data}/T^{MC} are flat in Fig. 7.12, which means the simulated spatial distribution is consistent with the measured one for each background species.

We estimate the systematic uncertainties of B and T due to the pressure correction factor c. Since c for the diamond sensors ranges from 1.5 to 2.0, we use these values to obtain B and T, and compare them with the ones obtained assuming $c = 1.7$. The result is shown in Tab. 7.5. The uncertainty is 6 % at most.

7.2.7 Gas composition

Up to this point, the effective atomic number of the residual gas Z_{eff} has not been discussed. Since the measured $Z_{eff}(\sim 2)$ is smaller than the one assumed in the simulation $Z_{eff}^{MC} = 7$, the simulated beam-gas contribution is overestimated about 9 times as shown in Tab. 7.6. Therefore, taking this into account, B^{data}/B^{MC} estimated above, which is $O(10^2)$ for the HER and $O(10)$ for the LER, becomes 9 times larger ($O(10^3)$ for the HER and $O(10^2)$ for the LER).

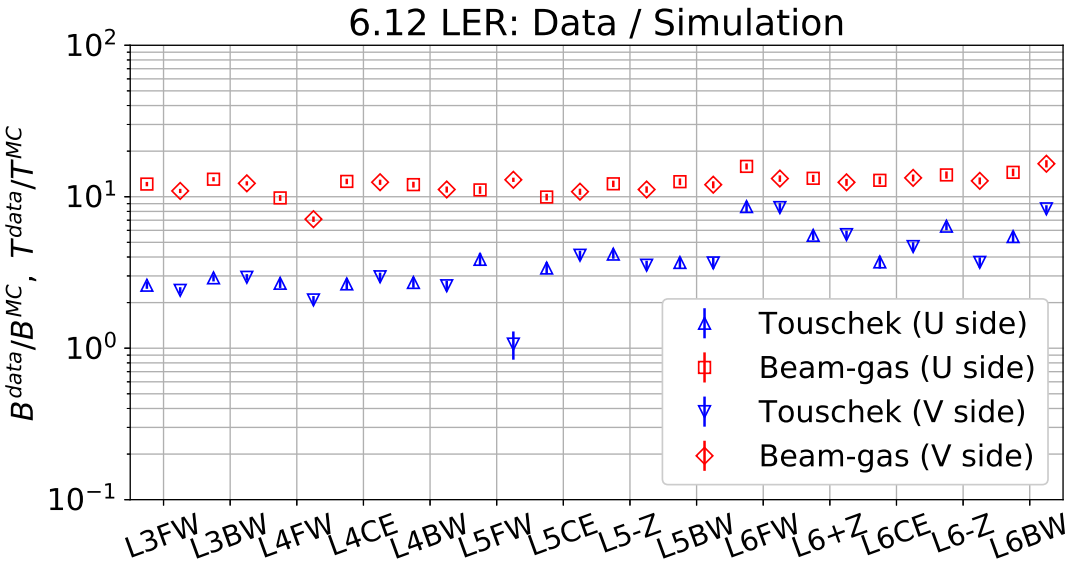

(a) L-A

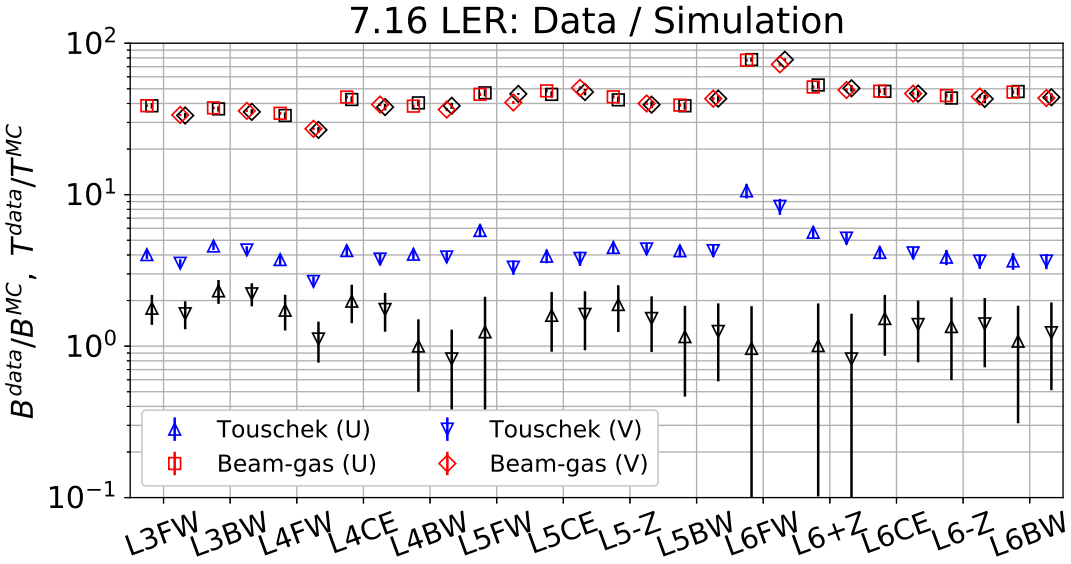

(b) L-B

Figure 7.12: The beam-gas and Touschek contributions in the LER background B, T are compared between the measurement and the simulation for each sensor. The comparison was done individually for L-A (a) and L-B (b). The triangles (inverted triangles) denote the Touschek component of the U (V) side occupancy. The squares (diamonds) denote the beam-gas component of the U (V) side occupancy. In (b), B^{data} (T^{data}) derived from the first half of the measurement is plotted in red (blue) markers and the ones derived from the second half are plotted in black markers.

Table 7.6: Effective atomic numbers which are measured or assumed in the simulation.

exp	Z_{eff}^{data}	Z_{eff}^{sim}	$\left(Z_{eff}^{sim}/Z_{eff}^{data}\right)^2$
H-A	2.265	7	9.55
L-A	2.265	7	9.55
L-B	2.314	7	9.15
H-C	2.314	7	9.15

7.3 Synchrotron radiation study

7.3.1 Method

We evaluate the SR background, which is considered to be a minor background component hidden by other backgrounds. Background hits from SR can be discriminated from beam-gas and Touschek backgrounds by their low energies and beam current dependence.

In Phase 2, we measured the background rate from single beams while the beam current decayed. Figure 7.13 shows the typical cluster energy distribution on the SVD, which was measured during the HER single-beam background measurement. We set a threshold of O(10 keV) for hit energies to separate the background hits into two classes. Since the Touschek, beam-gas, and SR rates are a quadratic or linear function of I, the background rates above and below the threshold, $H(I)$ and $L(I)$, are individually represented as quadratic functions.

$$H(I) = \int_{e>e_0} \frac{d\mathcal{O}}{de}(I,e)de = a \cdot I + b \cdot I^2 \tag{7.8}$$

$$L(I) = \int_{e<e_0} \frac{d\mathcal{O}}{de}(I,e)de = c \cdot I + d \cdot I^2 \tag{7.9}$$

Here, e is the hit energy and e_0 is the threshold. We set the threshold e_0 so that the SR contributes only to the low energy class $L(I)$. We assume that the energy spectra of SR and other backgrounds, $f_{SR}(e)$ and $f_{B+T}(e)$, do not depend on the beam current.

$$\frac{d\mathcal{O}}{de}(I,e) = \mathcal{O}_{B+T}(I) f_{B+T}(e) + \mathcal{O}_{SR}(I) f_{SR}(e) \tag{7.10}$$

Then, Eq. (7.8) becomes

$$L(I) = k \cdot H(I) + S \cdot I \tag{7.11}$$

where $k = \int_{e<e_0} f_{B+T}(e)de / \int_{e>e_0} f_{B+T}(e)de = d/b$ is a constant and $S \cdot I$ is the SR term proportional to the beam current. Therefore, the SR quantity S is given by

$$S = c - a \cdot \frac{d}{b} \tag{7.12}$$

where a to d are determined by fitting quadratic functions to measured $H(I)$ and $L(I)$.

7.3.2 Result

We estimated the SR contribution in the HER and LER backgrounds. The estimated contribution in the HER is compared with simulation. Since the estimated SR backgrounds are

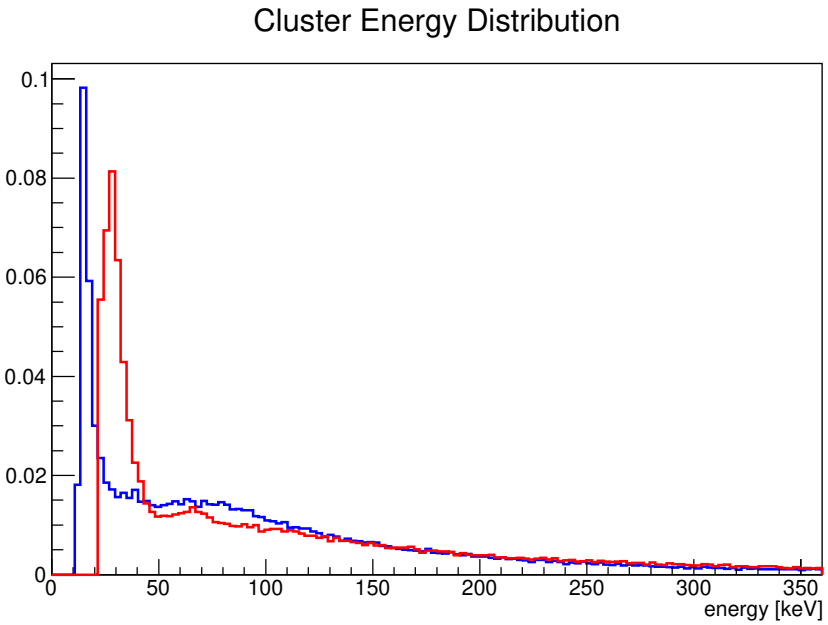

Figure 7.13: Cluster energy distributions on L3 BW sensor due to the HER beam background particles. The red (blue) line denotes U (V) side clusters.

Table 7.7: The SR studies. We measured the SVD occupancy with the nominal beam size and by the 1 kHz pseudorandom trigger while the beam current decays. n_b, σ_y, and I are the number of bunches, the vertical beam size at the location of the beam size monitor, and the beam current, respectively. We also took noise data before each measurement when no beam is stored in the ring for the noise subtraction.

ring	date	n_b	σ_y [µm]	I [mA]	time length [s]
HER	July 13th	789	40	300–217	1020
LER	July 16th	789	45	282–170	540

both consistent with zero as described below, the simulation studies are done only for the HER, which has larger SR background than the LER.

Table 7.7 shows the measurements for the SR studies. The SR contribution is estimated for the HER and LER individually.

In the offline analysis, we apply a hit selection with a threshold of SNR = 5 and reconstruct clusters from the fired strips. The clusters are classified according to an energy threshold of 50 keV, which is determined by the HER SR simulation. Assuming the simulation is true and also applicable for the LER, the SR contribution is present in only the class of lower energy clusters.

The data acquisition period is divided into six parts of equal length. For each period the averaged number of clusters in each class per event is calculated. After subtracting the noise, we fit the number of clusters with a function of the beam current. Figure 7.14 shows the fit results. The SR contribution in the number of clusters per event per beam current $SR_{cluster}$ is

Table 7.8: The SR occupancies in the measurement and simulation are shown for L3 sensors. The observed occupancy (data) assumes $\langle clsSize \rangle = 1$ and scaled to the final beam current of Phase 3 (I=2.6 [A] for HER, I=3.6 [A] for LER). The simulation was done only for the HER. The error of the observed occupancy arises from the fit. The simulated occupancy varies depending on the tail structure.

ring	sensor	side	data [10^{-3} %]	simulation [10^{-3} %] BeamCore+FlatTail	simulation [10^{-3} %] BeamCore+GausTail
HER	L3FW	U	-2.6 ± 3.4	58.5	68.3
HER	L3FW	V	-0.5 ± 1.5	102.4	114.4
HER	L3BW	U	-0.2 ± 3.1	19.5	29.3
HER	L3BW	V	-1.1 ± 7.0	16.9	27.0
LER	L3FW	U	-6.5 ± 17.0	–	–
LER	L3FW	V	-49.7 ± 14.4	–	–
LER	L3BW	U	-8.3 ± 15.2	–	–
LER	L3BW	V	-82.4 ± 16.6	–	–

determined by Eq. (7.12). It is translated into occupancy as

$$SR\text{occupancy}[\%] = SR_{cluster} \cdot I \cdot \langle clsSize \rangle \cdot \frac{100}{\#strips} \tag{7.13}$$

where I is the beam current of interest, $\langle clsSize \rangle$ is the averaged number of strips contained in an SR cluster, $\#strips$ is the total number of strips on the sensor. Since the SR cluster size is confirmed to be close to unity in the HER SR simulation, we assume $\langle clsSize \rangle = 1$ for simplicity. The calculated SR occupancies equivalent to $I = 800$ mA are listed in Tab. 7.8. The observed SR contributions are consistent with zero within errors for both rings. For the HER, the estimated contributions are systematically lower than the simulated ones.

7.4 Luminosity backgrounds

The evaluation of luminosity backgrounds requires a series of luminosity background studies. On July 12th, we performed a luminosity scan, where the HER and LER beams were stored in the rings and the luminosity was changed by vertically shifting the orbit of one beam at the IP. The background rate was measured while the beams were colliding and not colliding. However, only scanning the luminosity is not enough to extract luminosity backgrounds. Because the beam sizes increase during beam collisions, leading to the mitigation of Touschek backgrounds, we need to estimate the Touschek contribution separately to evaluate the luminosity component. To estimate the decrease of the Touschek component, beam size scans of each ring were performed on July 16th, on the same beam optics and collimator setting as the luminosity scan.

Originally, we planned to extract luminosity backgrounds by subtracting single-beam backgrounds estimated by the beam size scans from the background rate during collisions. However, this strategy was found to be not feasible this time because the single-beam background rates during the beam size scans and during the luminosity scan contradicted each other. Hence,

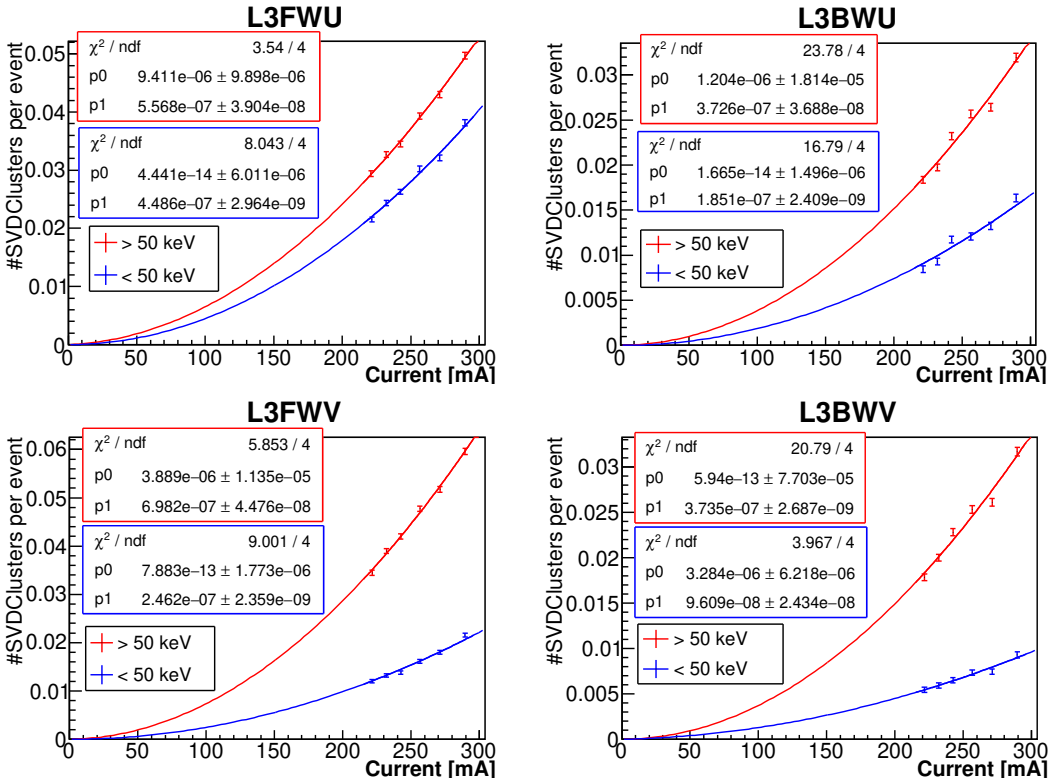

(a) HER

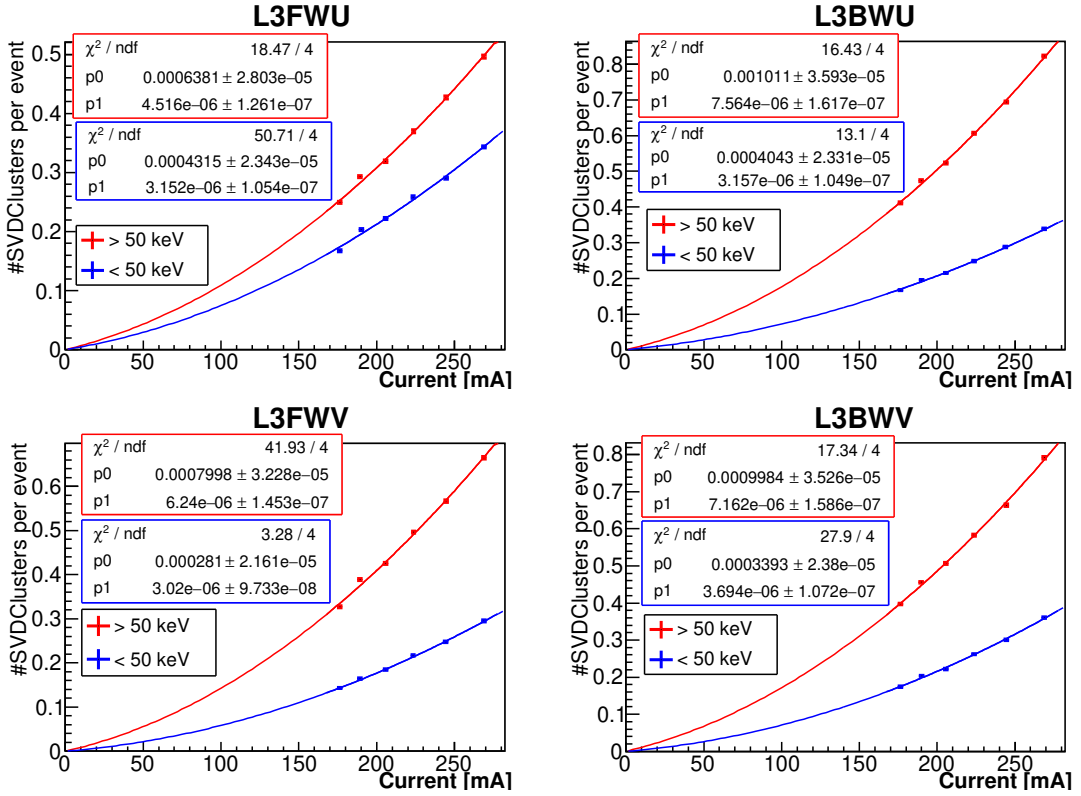

(b) LER

Figure 7.14: The number of clusters per event is plotted as a function of the beam current. The clusters are reconstructed from the HER (a) and the LER (b) single-beam background data. Each plot represents the clusters on one of the four sides of L3 sensors. The clusters are classified by the energy threshold: above 50 keV (red) and below 50 keV (blue). The solid lines are the fitting functions $\mathrm{p0} \cdot I + \mathrm{p1} \cdot I^2$.

subtracting the single-beam background rates from the rate during collision was no longer valid. We describe this issue in Section 7.4.2. Instead, we attempted to estimate the luminosity backgrounds by two different methods, described in Sections 7.4.3 and 7.4.4.

7.4.1 Sensitivity to the luminosity backgrounds

We can estimate the sensitivity to the luminosity backgrounds from the simulation. The sensitivity is defined as the ratio between the expected luminosity component and the total background:

$$\frac{\mathcal{O}_{lumi}^{MC} \cdot \mathcal{L}^{data}/\mathcal{L}^{MC}}{\mathcal{O}_{total}^{data}}. \tag{7.14}$$

Here, $\mathcal{O}_{lumi}^{MC}$ is the simulated occupancy due to the luminosity backgrounds, $\mathcal{L}^{data,MC}$ is the luminosity that is measured or assumed in the simulation, $\mathcal{O}_{total}^{data}$ is the measured occupancy. For the L3 FW sensor, where the luminosity backgrounds have the largest contribution in the simulation, the sensitivity is estimated to be about 1/40. The luminosity in Phase 2 was low and the single-beam background rates were unexpectedly high so that the luminosity backgrounds were hard to detect. Even though the expected sensitivity is low, the luminosity background will be visible if it shows a huge excess with respect to the simulation. Therefore, it is worthwhile to confirm it is not visible.

7.4.2 Instability of the single-beam backgrounds

We have problems in estimating both of the HER and LER single-beam backgrounds during the luminosity scan. Firstly, the LER single-beam background rate during the luminosity scan contradicts the one measured during the LER beam size scan on July 16th. Figure 7.15 shows the background rate measured during the LER beam size scan and non-collision run in the luminosity study. The optics and collimator settings for the LER are the same for both measurements. We measured the background rate twice with the nominal beam size during the beam size scan, and the results are inconsistent as noted in subsection (2) of section 7.2.6. Since the HER also contributes, the background rate during the non-collision run should be higher than the LER single-beam background rate. However, the LER background rates measured on July 16th exceed the background rate on July 12th. Therefore, the LER background rates are different between the three measurements despite the apparently identical accelerator conditions, which are three hours or four days apart from each other.

The HER displayed short-term instability. Figure 7.16 is the strip chart during one run of the luminosity scan, which shows the background rates measured by various subdetectors and the beam parameters as functions of time. The background rates show step-like deviation, which is synchronized with the horizontal betatron tune of the HER. This deviation was observed in both the collision and non-collision runs of the luminosity scan, but was not present in the beam size scans. The other parameters such as the horizontal or LER betatron tunes, beam currents, pressures, and horizontal and vertical beam sizes, did not show the deviation synchronized with the background rates. We suppose that the HER tune was close to an unstable resonance at that time and any subtle changes of the tune made a large difference in the background rate. It is practically impossible to take into account the effect of the unstable tune.

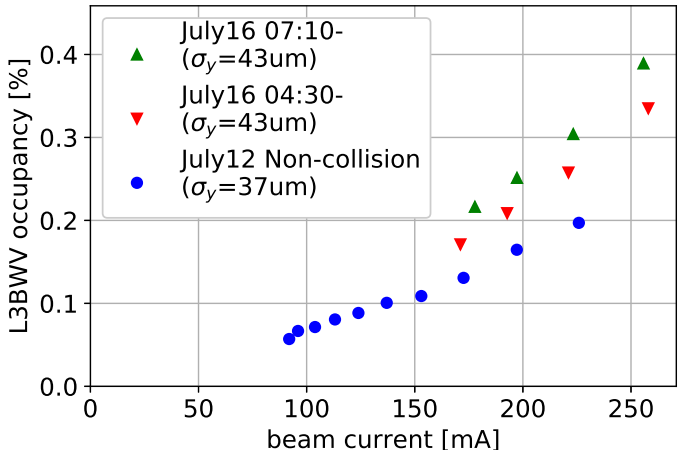

Figure 7.15: The background rates during the luminosity scan (July 12th) and the LER beam size scan (July 16th) as functions of the LER beam current. Despite including the HER component, the background rate during the luminosity scan is lower than the LER single-beam background rates.

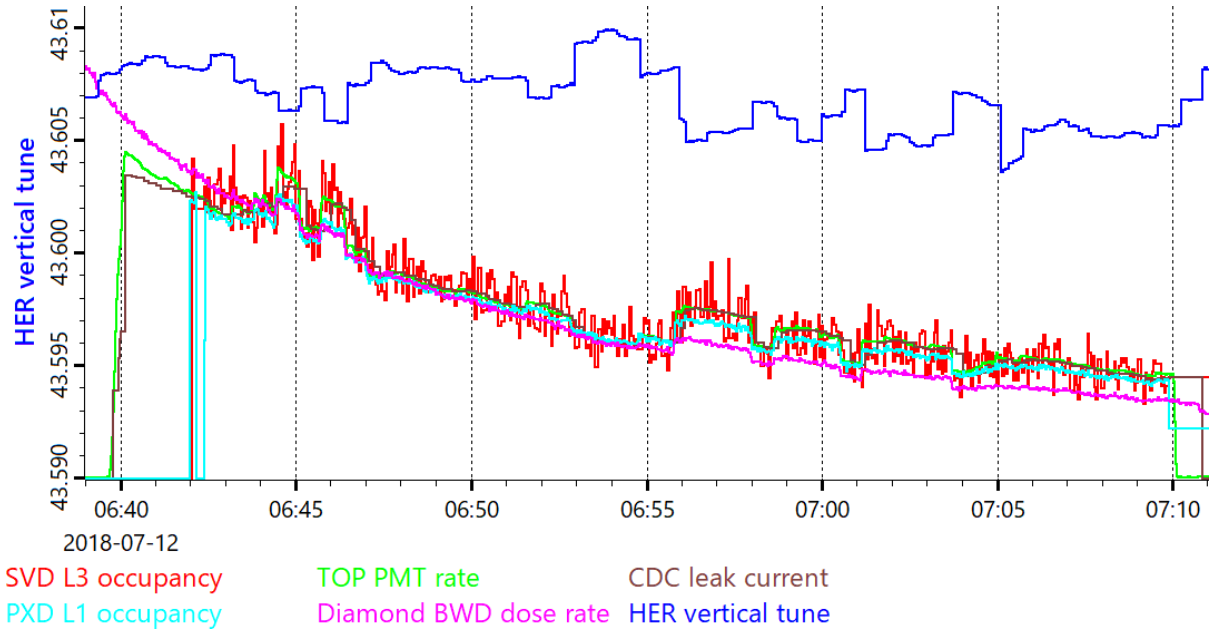

Figure 7.16: The strip chart during a non-collision run of the luminosity scan. The overlapped lines are the background rates measured by various subdetectors. The background rates show step-like deviation synchronized with the horizontal tune of the HER (the blue line).

7.4.3 SVD-TOP correlation

Instead of the original plan which found to be not feasible, we introduce two different methods to analyze the luminosity scan data. In these two methods, we assume the spatial distributions of the backgrounds were stable even though the background rate changed over time.

Firstly, we focus on low-momentum charged tracks due to the two-photon process, which dominates the luminosity backgrounds on the SVD. Due to their small radii, these tracks leave multiple hits on the SVD, but in contrast, do not reach outer detectors. We choose the TOP counters as a reference and study the correlation between the SVD and the TOP, with and without collisions.[4] The low-momentum components are evaluated as the difference of the SVD-TOP correlation between with and without collisions.

When we measure the SVD and TOP rates with and without collisions, the low-momentum contribution in the SVD, $SVD_{low\text{-}p_t}$, is approximately estimated as

$$SVD_{low\text{-}p_t} = SVD_{coll} - \left(\frac{SVD}{TOP}\right)_{non\text{-}coll} \cdot TOP_{coll} \tag{7.15}$$

where *coll* (*non-coll*) denotes the background rate measured with (without) collisions. Here, it is assumed that only the low-momentum component makes difference between collisions and non-collisions and the ratio SVD/TOP of the total single-beam backgrounds is conserved. However, since the ratio is the weighted sum of the ratio for each background component, it can vary as the percentage of each background component changes. In our case, the beam collisions make the beam sizes larger and Touschek backgrounds decrease. Hence the ratio depends on the beam size in general. In order to validate Eq. (7.15), we study the beam size dependence of the ratio.

We measured the ratio for the single beams during the beam size scans on July 16th. Figure 7.17 shows the ratio between the SVD occupancy averaged over each layer and the TOP MCP-PMT rate. We can see that the LER background ratio of the SVD L3, 4 and TOP depends on the beam sizes. The negative correlation indicates that the SVD-TOP ratio of the LER Touschek background is larger than that of the beam-gas. The presence of the beam size dependence does not allow us to use the ratio measured in non-collision runs as in Eq. (7.15).

In principle, the low-momentum background enhances the SVD-TOP ratio. The fact that the ratio during collisions is not larger than that without collisions implies that the low-momentum contribution, and hence the luminosity background itself, is small so that it is hidden by the Touschek effect.

7.4.4 Decomposition of background spatial distributions

The second method uses the spatial distribution of each beam background component to break down the background rate measured during collisions. We categorize the beam backgrounds into three components: luminosity backgrounds, HER single-beam backgrounds, and LER single-beam backgrounds. We estimate the spatial distribution of each component by the simulation or measurement. Fitting a superposition of the three spatial distributions to the one measured during collisions, the contribution of each background component is determined.

[4] According to simulation, the charged particles due to two-photon process have transverse momenta of $p_T = 4\,\mathrm{MeV/c}$ in average, while $p_T > 500\,\mathrm{MeV/c}$ ($18\,\mathrm{MeV/c}$) is required to reach the TOP counters (the SVD).

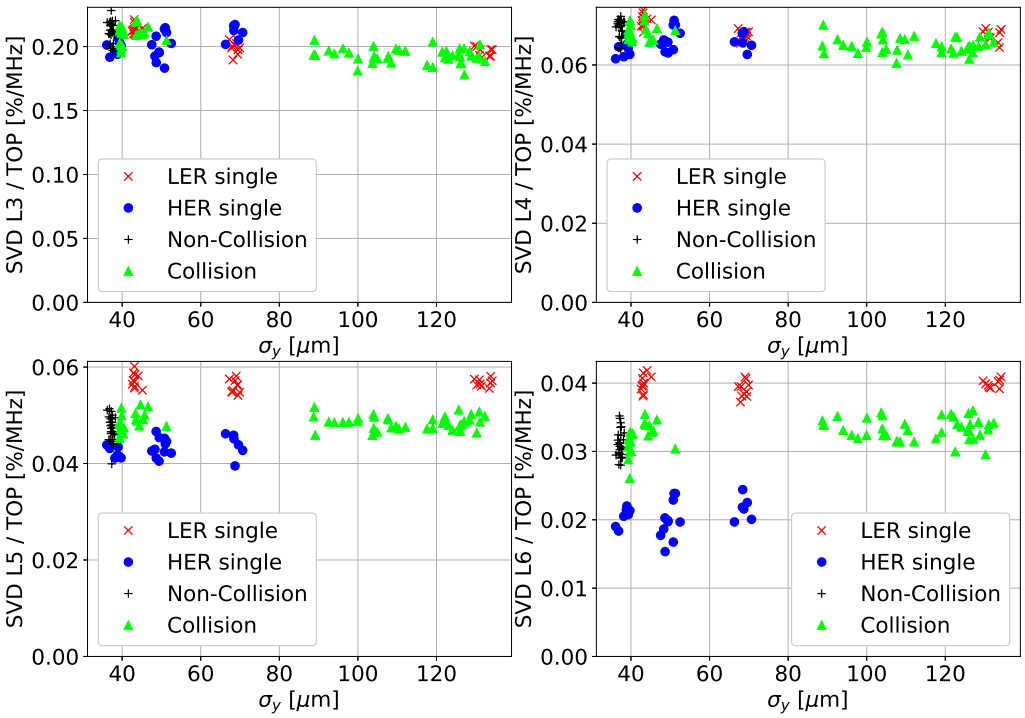

Figure 7.17: The ratio between the SVD and TOP background rates as a function of the beam size. The averaged occupancy of each SVD layer and the total scaler rate of the TOP MCP-PMT are used. The single-beam background rates were measured during the beam size scan on July 16th, when the same collimator setting was applied as the luminosity scan. Non-collision (Collision) denotes the background rate measured during non-collision (collision) runs in the luminosity scan. The x-axis is the HER vertical beam size for "HER single", otherwise the LER vertical beam size.

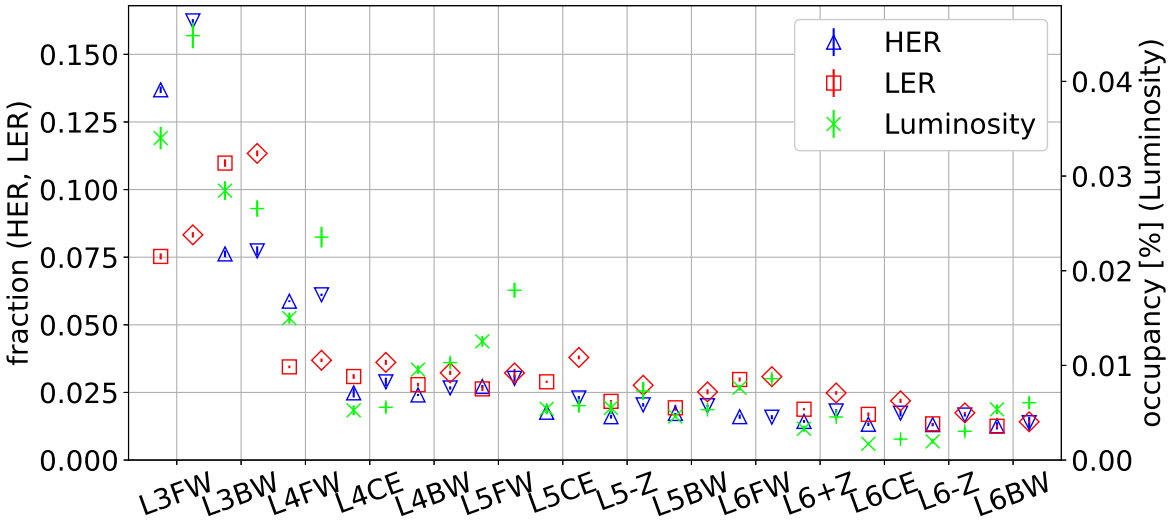

Figure 7.18: The spatial distributions of the single-beam and luminosity backgrounds. The measured single-beam background rates and simulated luminosity background rate are plotted for each sensor. $\triangle, \times, \square$ ($\triangledown, +, \diamond$) denote the U (V) side occupancy. The HER and LER distributions are normalized so that the sum of all the sensors becomes unity, while the luminosity background shows the absolute occupancy [%] assuming the luminosity of $2 \times 10^{34}\,\mathrm{cm}^{-2}\mathrm{s}^{-1}$. The HER (LER) distribution was measured on July 13th (16th).

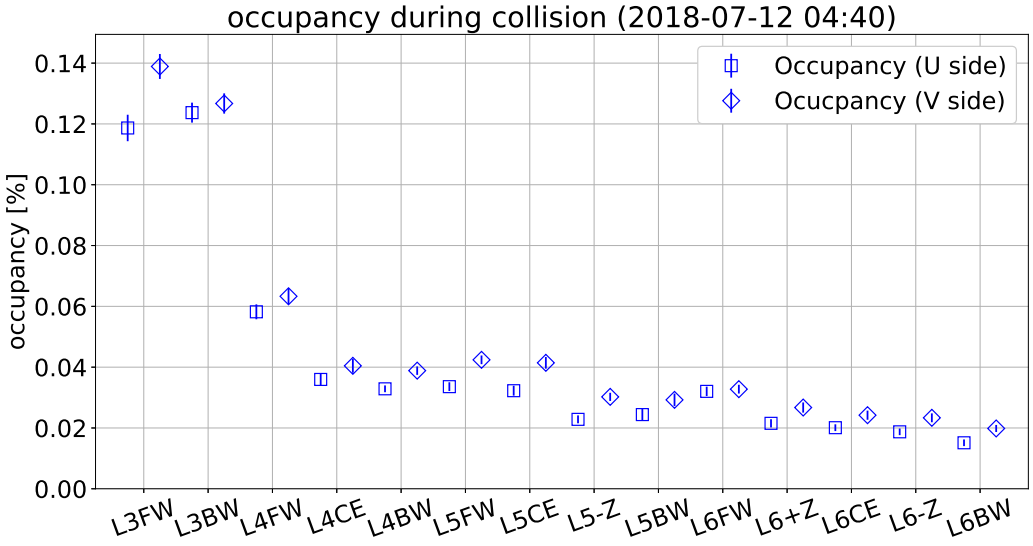

Figure 7.19: An occupancy spatial distribution averaged over one minute. $\square$ ($\diamond$) denotes the U (V) side occupancy. Measured during beam collisions.

Figure 7.18 shows the spatial distributions of the HER single beam, LER single beam, and luminosity backgrounds. The distribution is defined as the SVD occupancy calculated on each side of the sensors. The distributions for the single-beam backgrounds are measured during the beam size scans on July 16th, while the one for the luminosity backgrounds is taken from the simulation that assumes the designed accelerator settings in Phase 2.

To calculate the spatial distribution, the SVD occupancy measured during collisions is divided into one-minute periods. For each period, the distribution is given by the occupancies averaged over that period and the error is given by the standard error (see Section 7.2.4). Figure 7.19 shows a typical occupancy distribution during collisions.

The background spatial distributions measured during collisions are fitted by the superposition of the three distributions:

$$\mathcal{O}^i_{coll}[\%] = a \cdot \mathrm{HER}^i + b \cdot \mathrm{LER}^i + \frac{\mathcal{L}}{\mathcal{L}^{MC}} \cdot \mathrm{LUMI}^i[\%] \tag{7.16}$$

where i denotes each sensor, $\mathcal{O}_{coll}$ is the occupancy measured during collisions, HER, LER, LUMI are the measured single-beam background distributions and the simulated luminosity background distribution, $\mathcal{L}^{MC}$ is the luminosity assumed in the simulation, and $a, b, \mathcal{L}$ are the fit parameters. The luminosity during the collision run is estimated as $\mathcal{L}$ by the fit. Figure 7.20 shows the fit result of one period. The measured background distribution is well fitted by the superposition.

The fitted luminosity is determined in each period as shown in Fig. 7.21. We can see that the sensitivity of the fit is not good enough to see such low luminosity. Since there is not an excess of the fitted luminosity, assuming the simulated distribution is true, the luminosity backgrounds are not much larger than the simulation. The reasonability of the luminosity background simulation is confirmed within the large error.

We note that the fitted luminosity tends to be negative at the beginning of each run in Fig. 7.21. Since the LER lifetime is smaller than the HER, the largest change of the spatial distribution between the beginning and end of the run would be the fraction of the LER components. Assuming the negative luminosity is explained by the fraction of the LER component, it appears that the LER distribution used for the fit is slightly wrong and the error is compensated for by the negative luminosity component.

7.5 Injection background

In order to confirm the feasibility of continuous injection in Phase 3, we turned on the SVD and measured the background rate during LER injections on July 13th. Before the measurement, the injection background rate was confirmed to be low, judging from the dose rates on the diamond sensors. We checked the online-monitored SVD occupancy and the offline-analyzed one to observe the instantaneous increase due to the injection background.

The background rate was not measured with the SVD during the HER injections since the diamond dose rates were too high to ramp up the SVD high voltage. In the middle of July, when the injection background measurement was done, the injection conditions were unstable because a large temperature deviation had changed the length of the accelerating tube. Before that, when the HER injection was well controlled, the HER injection background was observed to be as low as the LER. Therefore, we consider the background measurement during the HER

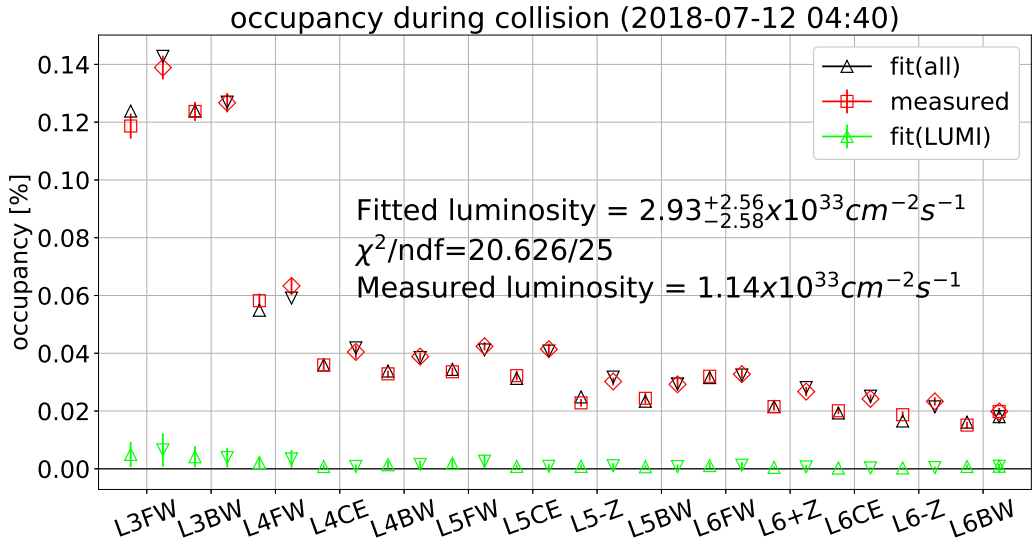

Figure 7.20: A fit result of the occupancy spatial distribution. The distribution measured during collisions is fitted with the superposition of the distributions of single beam backgrounds and luminosity background. The luminosity is determined to be $2.93^{+2.56}_{-2.58} \times 10^{33}\,\mathrm{cm}^{-2}\mathrm{s}^{-1}$, while the measured luminosity is $1.14{\times}10^{33}\,\mathrm{cm}^{-2}\mathrm{s}^{-1}$. The contribution from the fitted luminosity background is plotted in green. $\triangle$ and $\square$ ($\triangledown$ and $\diamond$) denote the U (V) side occupancy.

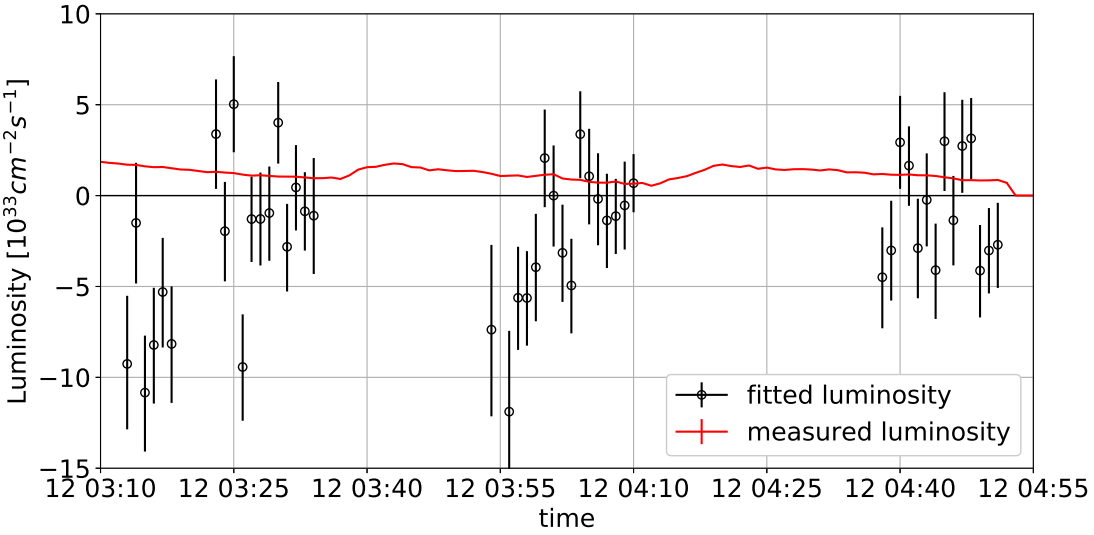

Figure 7.21: The fitted and measured luminosity during collisions are plotted as functions of time. The fitted luminosity is estimated by fitting the occupancy spatial distribution on a minute-by-minute basis.

injection is also possible under more favorable conditions and should be conducted in Phase 3.

Figure 7.22 is the strip chart describing the LER injection background measurement. During the measurement, the LER maximum beam current was set to 125 mA and the LER was topped up as soon as 0.5 % of the current was lost. Accordingly, the injection was performed by alternating between injection periods of about 20 seconds with an injection rate of 0.5 Hz, and non-injection periods of about 30 seconds. The HER beam current of about 100 mA was also stored in the ring without injections, though not shown in the chart. The SVD occupancy and diamond dose rate were measured over the alternating injection and non-injection periods. The SVD occupancy in the chart is calculated online from part of the data taken by pseudorandom 1 kHz trigger. The diamond dose rate is sampled by 500 MHz clock and averaged every second.

We note that the period of the harsh background condition after each injection lasts for a few milliseconds according to a measurement with a background monitor. Therefore, the effect of the injection background is diluted to about $O(10^{-3})$[5]. Despite the dilution, we can see periodic increases in the diamond dose rate synchronized with the 0.5 Hz injections during injection periods in Fig. 7.22. On the other hand, the online SVD occupancy does not show any concurrent increase. Since the SVD time window is as short as $O(100\,\text{ns})$, the trigger was not synchronized with the injection, and the trigger rate was as low as 1 kHz, each injection background event was rarely captured by the SVD time window. This would be one reason why the injection background on the SVD is not visible in the strip chart in spite of the same dilution as the diamonds.

We further investigate the effect of the injection backgrounds on the SVD occupancy in the offline analysis. Figure 7.23 shows the histogram of the occupancy calculated on an event-by-event basis. We can see that high-occupancy events tend to happen in the injection periods and the average occupancy is about 1 % higher during injections. The effect on the SVD occupancy is much smaller than the diamond dose rate, which increases by about 10 % in average during injection as shown in Fig. 7.22.

One possible explanation for the difference is that the injection background particles are more likely to hit the diamonds than the SVD because of their spatial distribution. Since the correlation between the SVD and diamonds is confirmed for the backgrounds from the storage beam (see Section 7.6), this is a remarkable feature of the LER injection background.

This observation indicates that at least the background from the 0.5 Hz LER injections has a negligible effect on the tracking performance, while 25 Hz continuous injection is planned in Phase 3. The effect of higher injection rates and the HER injection background should be investigated in Phase 3. Since the SVD cartridge is only installed in the +X direction, attention should be paid to the injection backgrounds in the other directions in Phase 3.

7.6 SVD-Diamond correlation

A large number of background hits arriving in a short period can destroy the APV25 chips due to large currents on input channels. Thus, before ramping up the high voltage on the DSSD sensors, we need to estimate the beam background rate on the SVD. Since the diamond sensors always monitor the background level on the beam pipe near the SVD, we think about estimating the SVD background conditions with the diamonds. The correlation between the

[5] a few milliseconds times the injection rate, 0.5 Hz.

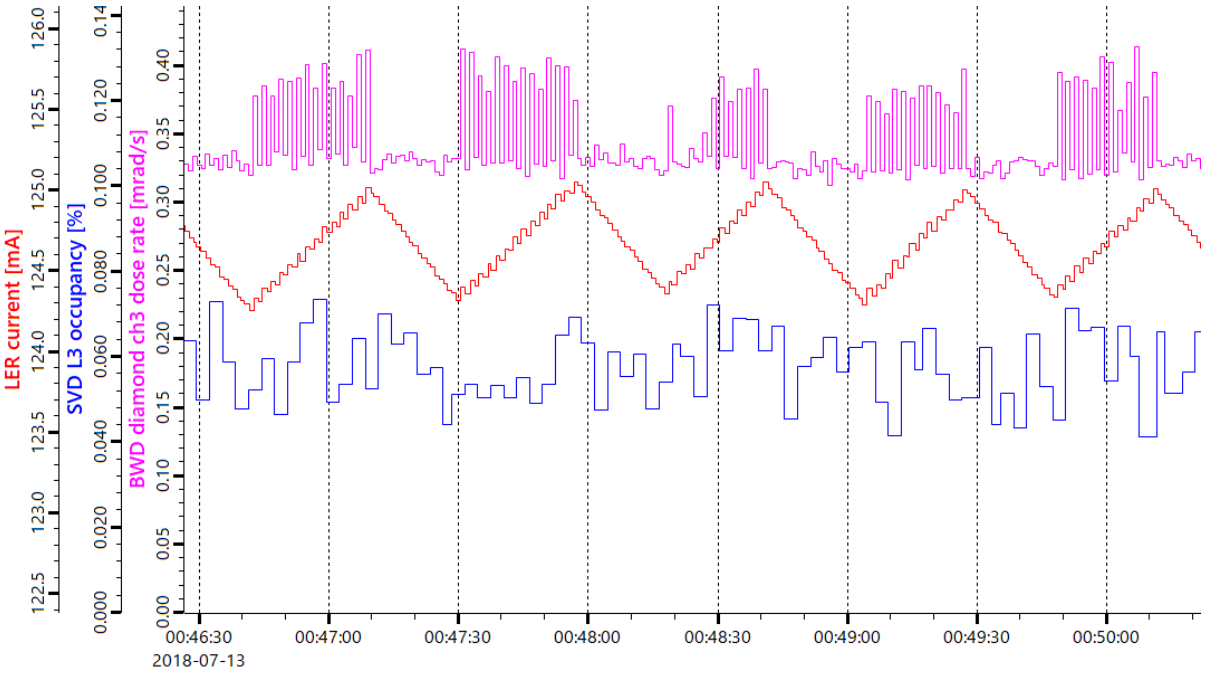

Figure 7.22: The strip chart during the LER injection background measurement. The LER current (red) is topped-up by injections as soon as it loses 0.5 % of the current. The diamond dose rate (magenta) shows instantaneous increases synchronously with the 0.5 Hz injection while the SVD occupancy (blue) does not.

SVD and diamond background rate is studied for that purpose. The correlation also ensures that a beam abort by the diamonds can protect the SVD from the excessive radiations.

The measurements in Phase 2 are separated into three categories according to the stored beam species: HER, LER, and HER+LER. For each category, we show the correlation between the SVD L3 occupancy and BWD (FWD) Diamond dose rate in Fig. 7.24 (7.25). Figure 7.25 does not include the HER+LER case because we did not measure the background rate with both beams while the FWD diamonds had sensitive measurable range. In the plots, only the occupancy on the U side of the sensors and the dose rate on the diamond sensor at $\phi = 305$ (ch3) are used. This is because the occupancies on the U and V sides of a sensor is well correlated, and the ch3 diamond sensor is one of the nearest sensors to the SVD and has the largest dose rate among four diamond sensors on each side.

In each scatter plot, we can see the clear correlation between the SVD and diamond rates. The correlation is stable even though the measurements are weeks or months apart from each other. Therefore, it enables us to make robust estimation of the SVD occupancy without actually ramping up the SVD high voltage.

For each set of SVD sensor and diamond, the scatter plots in Fig. 7.24 and 7.25 are overlaid and shown in Fig. 7.26. We can see that the correlation largely depends on the positions of the sensors of interest and which ring stores the beam. This is due to the position distribution of the backgrounds (the HER background is harder on the FWD side, the LER on the BWD side).

Table 7.9 shows the ratio between the SVD occupancy and the diamond dose rate calculated from Fig. 7.26. For comparison, we show the ratio estimated by the simulation assuming the

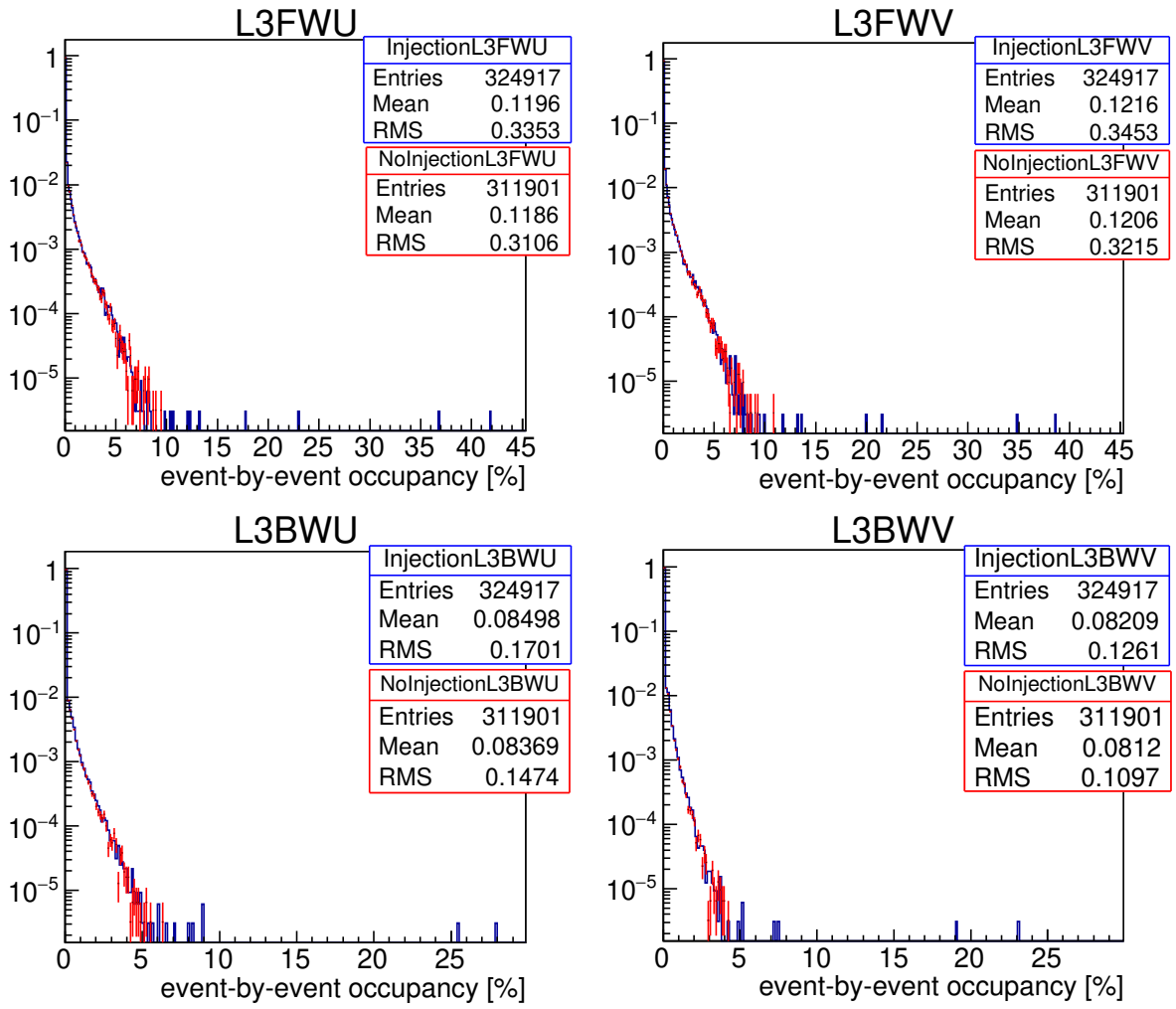

Figure 7.23: Histograms of event-by-event occupancy on the L3 sensors. The blue lines are the occupancies during injection periods, the red lines during non-injection periods.

Table 7.9: The ratio between the U side occupancy of L3 sensors and the dose rate on diamond sensors at ϕ=305 [%/(mrad/s)]. Calculated from the Fig. 7.26. The standard deviation of each distribution is shown in the parentheses.

SVD / diamond	HER	LER	HER+LER
L3FW / BWD	0.55(16)	0.10(2)	0.17(5)
L3BW / BWD	0.37(12)	0.15(3)	0.16(3)
L3FW / FWD	0.10(2)	0.30(4)	–
L3BW / FWD	0.07(1)	0.43(6)	–

Table 7.10: The ratio between the U side occupancy of L3 sensors and the dose rate on diamond sensors at ϕ=305 [%/(mrad/s)]. Estimated by the Phase 2 simulation (see Section 6.2). The ratio for the single beam backgrounds are shown except for the HER Touschek which has no hit on the diamond sensors owing to poor statistics.

	HER	LER	
SVD / diamond	beam-gas Coulomb	beam-gas Coulomb	Touschek
L3FW / BWD	0.12(3)	0.0143(5)	0.0308(8)
L3BW / BWD	0.09(2)	0.0158(6)	0.0299(7)
L3FW / FWD	0.021(4)	0.056(3)	0.062(2)
L3BW / FWD	0.016(3)	0.062(4)	0.060(2)

design optics of Phase 2 in Tab. 7.10. The measured ratios are several times higher than the simulated ones. This indicates the discrepancy is smaller for the diamonds while the measured SVD background shows large excess with respect to the simulation.

7.7 Estimation of the Phase 3 beam background

One goal of the Phase 2 beam background studies is to estimate the beam background rate in Phase 3. The difficulty is that the simulation of the beam-induced backgrounds is not reliable. As described in Section 7.2, we assumed the single-beam background model (see Section 5.3) and estimated the beam-gas and Touschek contributions B and T. However, simply substituting the obtained B, T and the expected beam parameters in Phase 3 into Eq. (5.2) does not give a reasonable result, because B and T will be changed in Phase 3 due to the difference in the beam optics and the collimator settings. To take account of both the measured background rate in Phase 2 and the optics and collimators in Phase 3, we correct the result of Phase 3 simulation by

$$\mathcal{O}_{corr} = \frac{T^{data}_{ph2}}{T^{MC}_{ph2}} \cdot \mathcal{O}^{Touschek}_{ph3MC} + \frac{B^{data}_{ph2}}{B^{MC}_{ph2}} \cdot \mathcal{O}^{beam\text{-}gas}_{ph3MC} \tag{7.17}$$

for each ring. Here, $T^{data}_{ph2}, T^{MC}_{ph2}$ are the Touschek contributions measured in Phase 2 and calculated in Phase 2 simulation, and similarly for the beam-gas contributions. $\mathcal{O}^{Touschek(beam\text{-}gas)}_{ph3MC}$ is the Touschek (beam-gas) background rate in the Phase 3 simulation. By this method, we

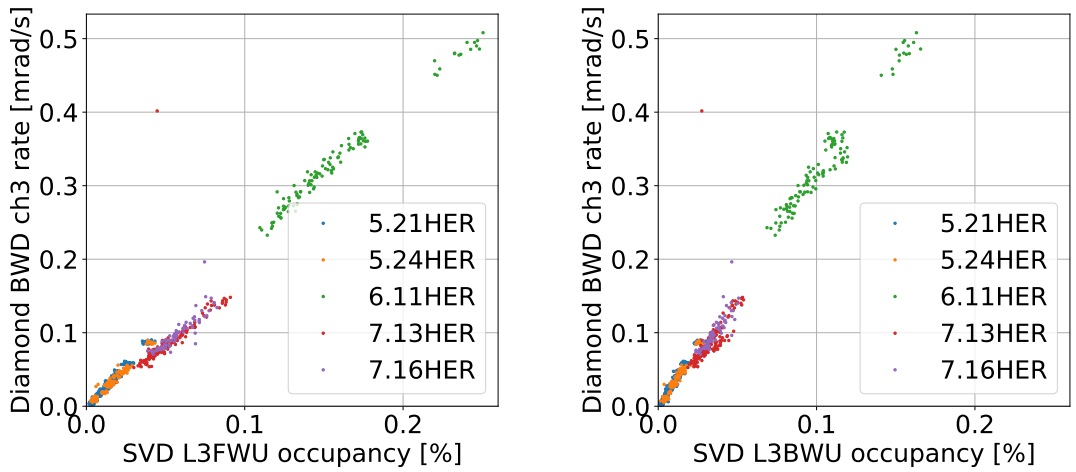

(a) HER

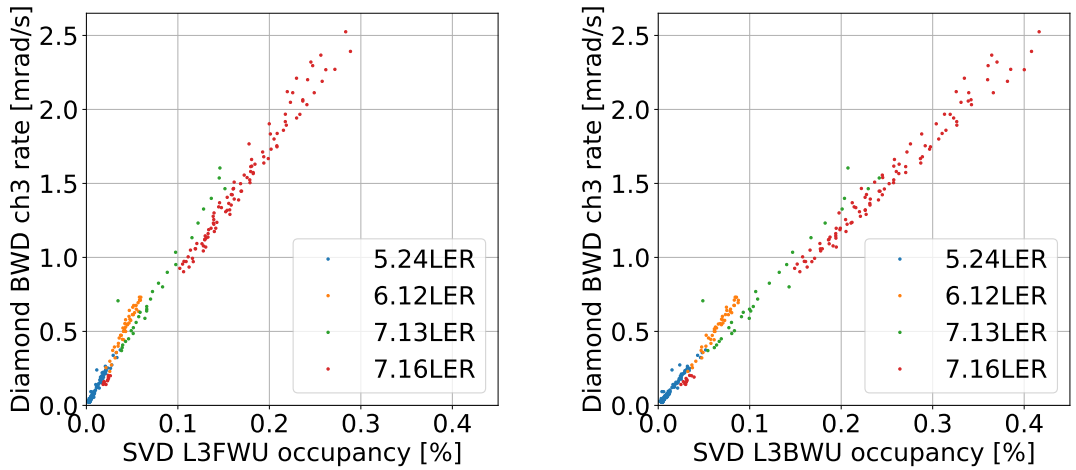

(b) LER

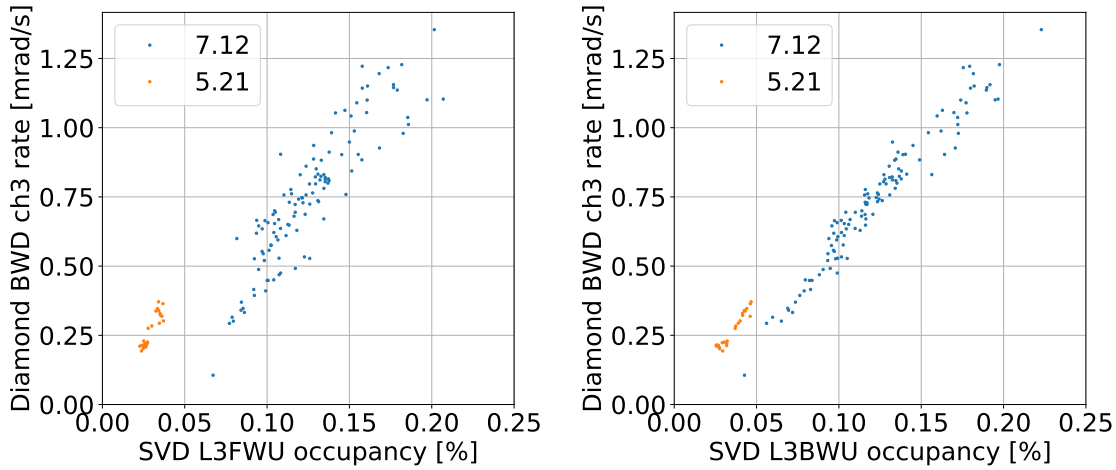

(c) HER+LER

Figure 7.24: The correlation between the SVD and the BWD diamond. The x-axis shows the occupancy on the U side of the SVD L3 FW or BW sensor and the y-axis shows the dose rate on the BWD diamond (ch3). The background is from the HER single beam (a), the LER single beam (b), or HER and LER beams (c). Each point corresponds to the one-minute averaged background rates. The legend denotes the dates of the measurements.

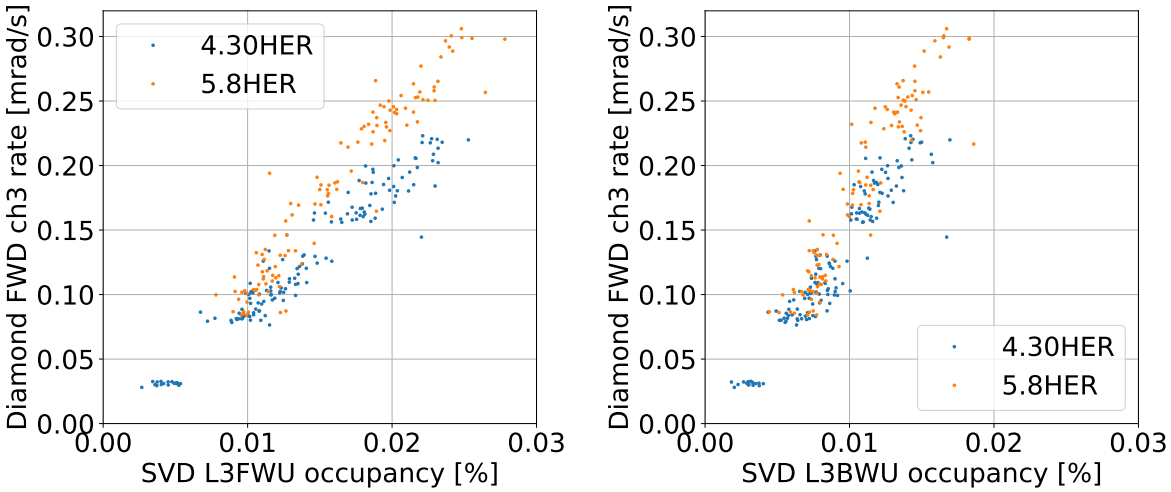

(a) HER

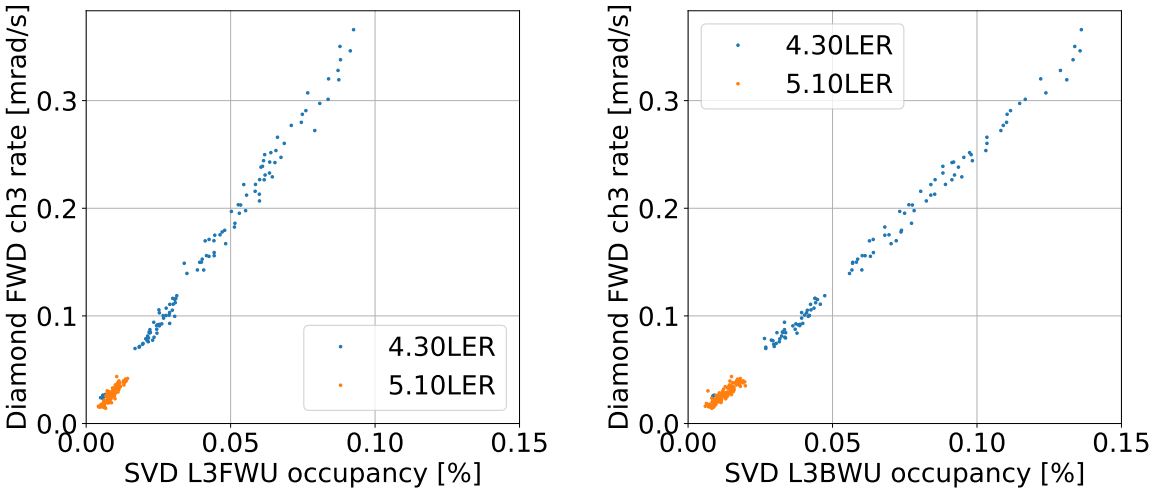

(b) LER

Figure 7.25: The correlation between the SVD and the FWD diamond. The x-axis shows the occupancy on the U side of the SVD L3 FW or BW sensor and the y-axis shows the dose rate on the FWD diamond (ch3). The background is from the HER single beam (a) or the LER single beam (b). Each point corresponds to the one-minute averaged background rates. The legend denotes the dates of the measurements.

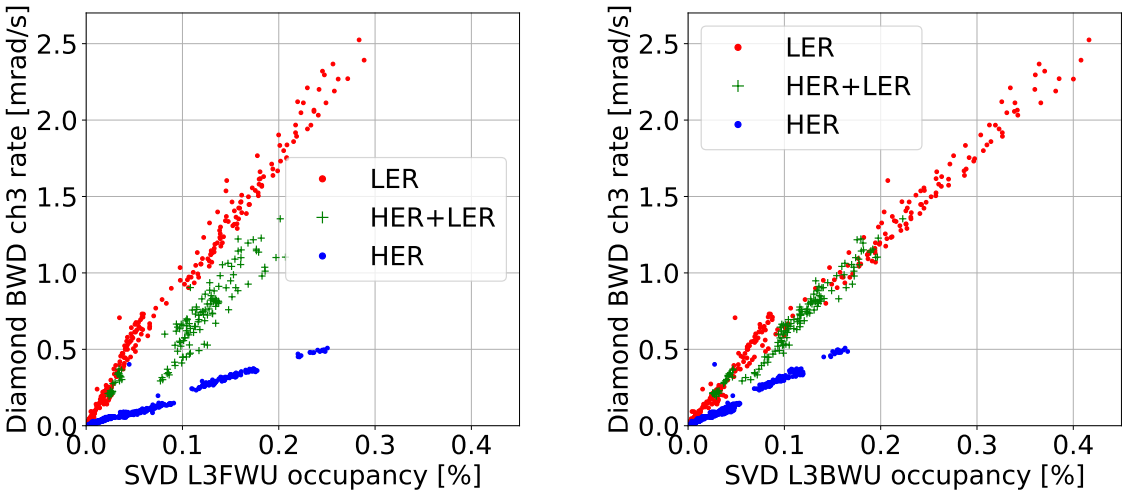

(a) SVD vs BWD diamond

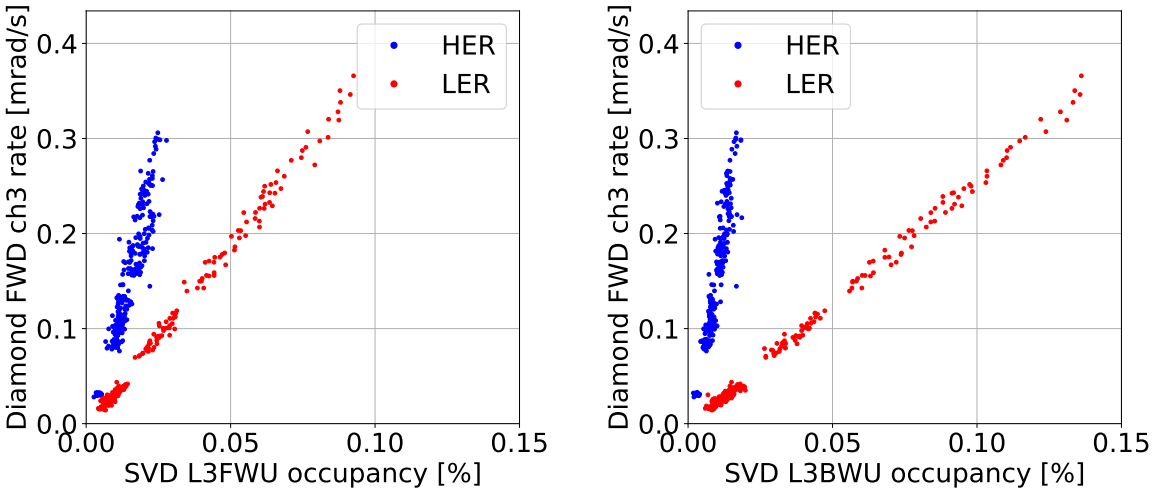

(b) SVD vs FWD diamond

Figure 7.26: The correlation between the SVD and the BWD diamond (a) or the FWD diamond (b). The x-axis shows the occupancy on the U side of the SVD L3 FW or BW sensor and the y-axis shows the dose rate on the FWD or BWD diamond (ch3). The scatter plots in Fig. 7.24 and 7.25 are overlaid for each set of the SVD and diamond sensors. Each point corresponds to the one-minute averaged background rates. The legend denotes the beams stored during the measurements.

Table 7.11: The scale factors used for the estimation of the Phase 3 single-beam backgrounds.

	Touschek	Coulomb
HER	1700	610
LER	4.6	39

scale the Phase 3 simulation results by the observed discrepancy between measurements and simulations in Phase 2, assuming the actual background rate in Phase 3 will show a similar discrepancy from the simulation as observed in Phase 2.

So far, we have simulated the beam backgrounds in Phase 2 and Phase 3 (see Section 6.2), and compared the single-beam backgrounds between the measurements and simulation in Phase 2 (see Section 7.2.6). The estimated Phase 3 beam background rates on the L3 sensors are shown in Figs. 7.27, 7.29, and 7.31.[6] In these plots, we scale the Touschek and beam-gas Coulomb backgrounds according to Eq. (7.17), while the luminosity backgrounds are not scaled because no large excess is found in the luminosity background study (see Section 7.4.4). The SR background is not included because the observed SR contribution was consistent with zero (see Section 7.3). The shown errors include only the statistical error of the Phase 3 simulation result and the errors of the scale factors are not considered. The background rates averaged over the sensors in each layer are shown in Figs. 7.28, 7.30, and 7.32. The occupancies exceed the limit from tracking performance. Assuming the luminosity backgrounds are irreducible, the mitigation of the beam backgrounds by an order of magnitude is required to take good-quality data within the limit. The radiation dose rate is still within the limit of 10 Mrad in a decade for all the L3 sensors, but we note that the injection backgrounds are not included in the plot. The estimated NIEL damage exceeds the limit for some L3 sensors in the horizontal plane. It will reach acceptable level after the background mitigation required from the viewpoint of occupancy.

In the first year of Phase 3, the plan is to keep the beam currents less than half of the designed values. This will make the single-beam backgrounds roughly four times smaller than the final condition. Since the planned beam sizes in the period are also 7–9 times larger, the Touschek backgrounds will be even smaller and the luminosity will be 1/20 of the design. Considering the reduction, the occupancy due to the backgrounds will be acceptable at the beginning of Phase 3 and the SVD will be operational with good performance. In order to proceed with Phase 3, we will mitigate the backgrounds by tuning the beam optics and collimator settings, improving the vaccum condition, and adding collimators.

[6] The background rates on the other layers are shown in Appendix C.

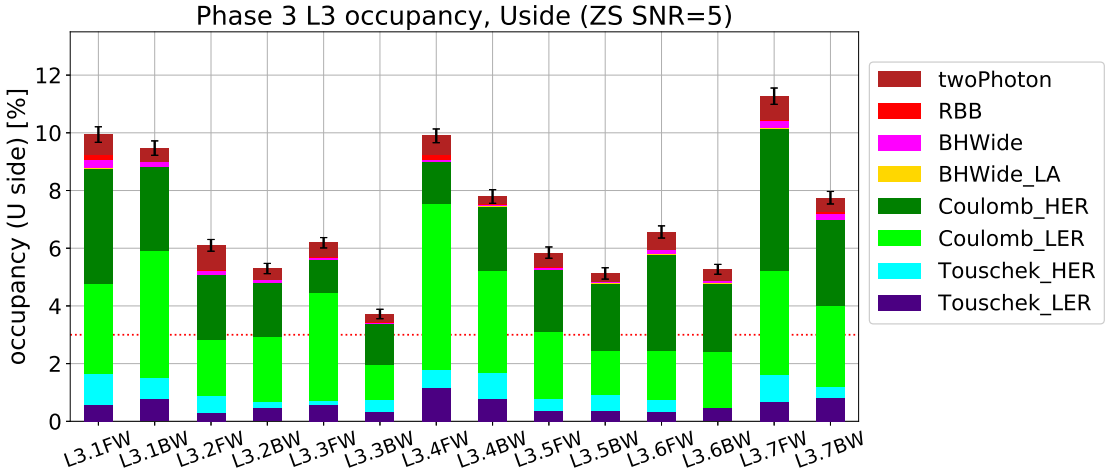

(a) U side

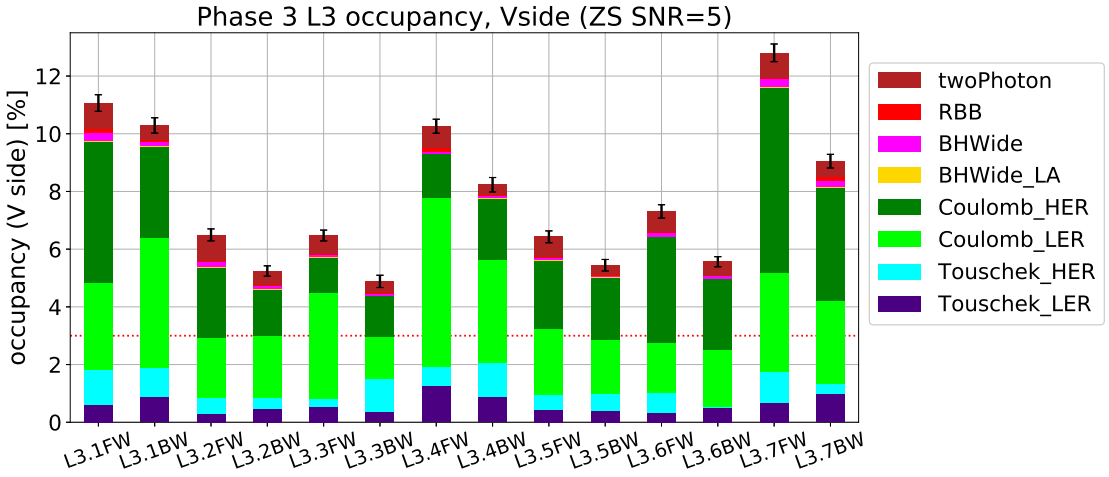

(b) V side

Figure 7.27: The estimated occupancies on U sides (a) and V sides (b) of the L3 sensors in the final Phase 3 condition. The result of the Phase 3 simulation is rescaled considering the Phase 2 observation. The contributions from different background sources are plotted in different colors denoted by the legend. The x-axis denotes the sensor names. The red dotted line is the detector limit of 3 % from tracking performance (see Section 5.1.1). The errors of the scale factors are not considered.

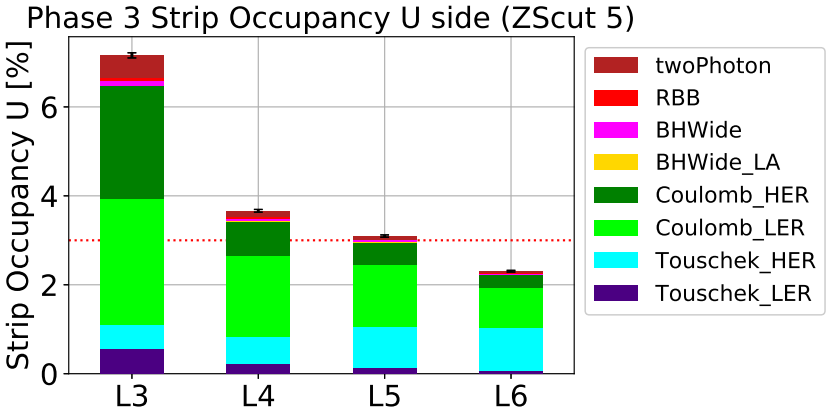

(a) U side

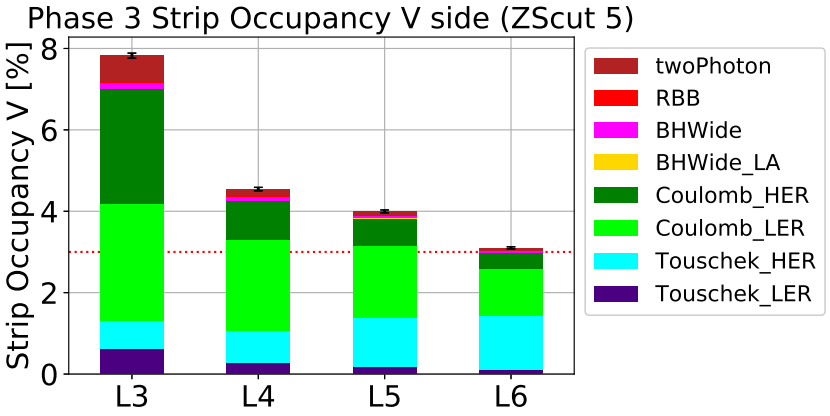

(b) V side

Figure 7.28: The estimated occupancies on U sides (a) and V sides (b) in the final Phase 3 condition. The occupancy is averaged over the sensors in each layer. The result of the Phase 3 simulation is rescaled considering the Phase 2 observation. The contributions from different background sources are plotted in different colors denoted by the legend. The x-axis denotes the layer number. The red dotted line shows the limit of 3 % from tracking performance (see Section 5.1.1). The errors of the scale factors are not considered.

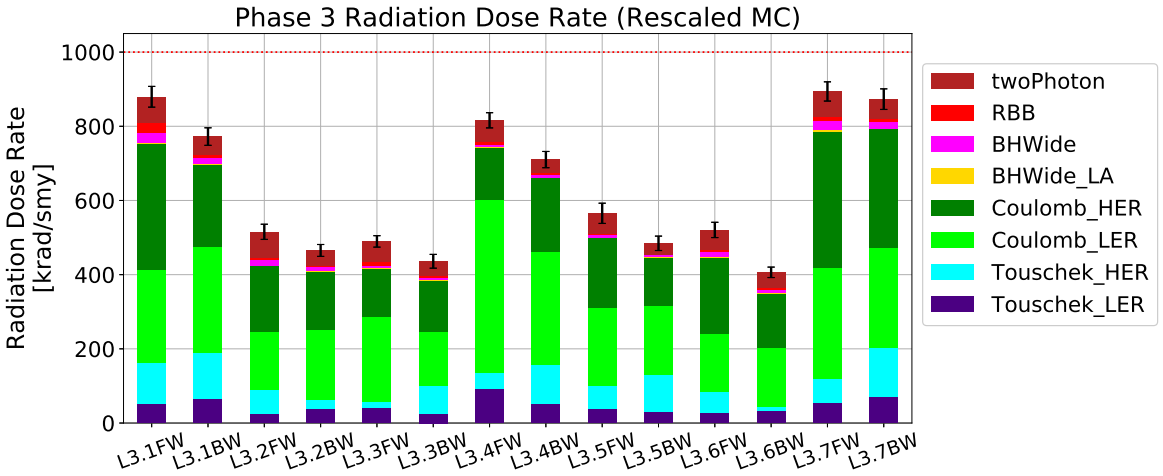

Figure 7.29: The estimated radiation dose on the L3 sensors in the final Phase 3 condition. The result of the Phase 3 simulation is rescaled considering the Phase 2 observation. The contributions from different background sources are plotted in different colors denoted by the legend. The red dotted line shows the limit of 1 Mrad/smy (see Section 5.1.3). The errors of the scale factors are not considered.

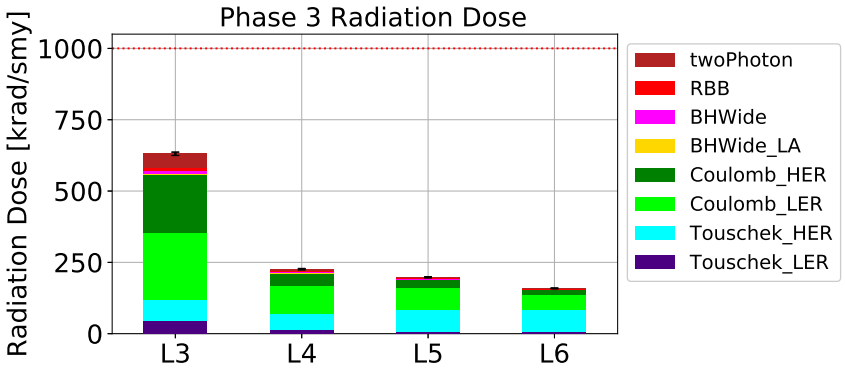

Figure 7.30: The estimated radiation dose rate on the SVD in the final Phase 3 condition. The dose rate is averaged over the sensors in each layer. The result of the Phase 3 simulation is rescaled considering the Phase 2 observation. The contributions from different background sources are plotted in different colors denoted by the legend. The x-axis denotes the layer number. The red dotted line shows the limit of 1 Mrad/smy (see Section 5.1.3). The errors of the scale factors are not considered.

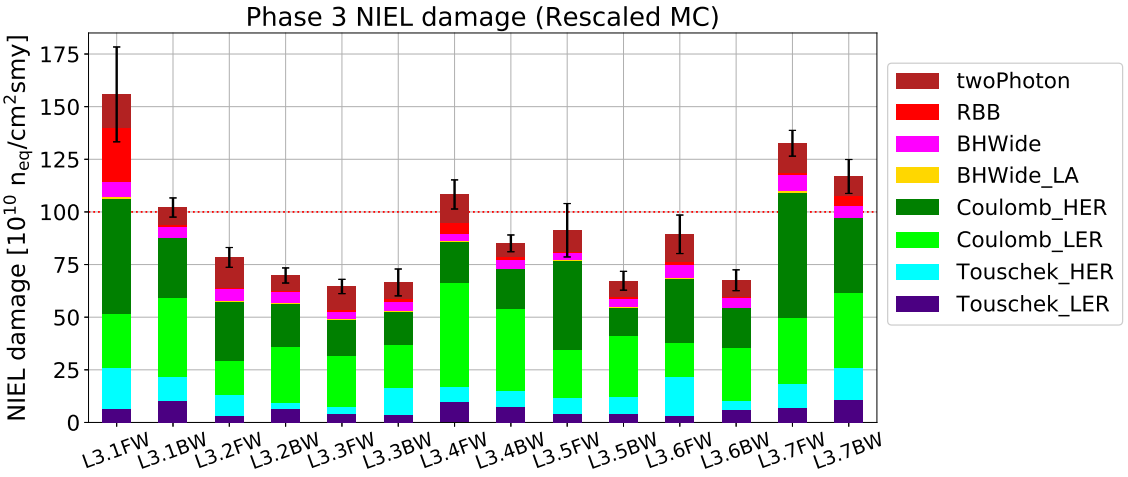

Figure 7.31: The estimated NIEL damage on the L3 sensors in the final Phase 3 condition. The result of the Phase 3 simulation is rescaled considering the Phase 2 observation. The contributions from different background sources are plotted in different colors denoted by the legend. The red dotted line shows the limit of $10^{12}\,\mathrm{cm}^{-2}\mathrm{smy}^{-1}$ 1 MeV neutron equivalent fluence (see Section 5.1.3). The errors of the scale factors are not considered.

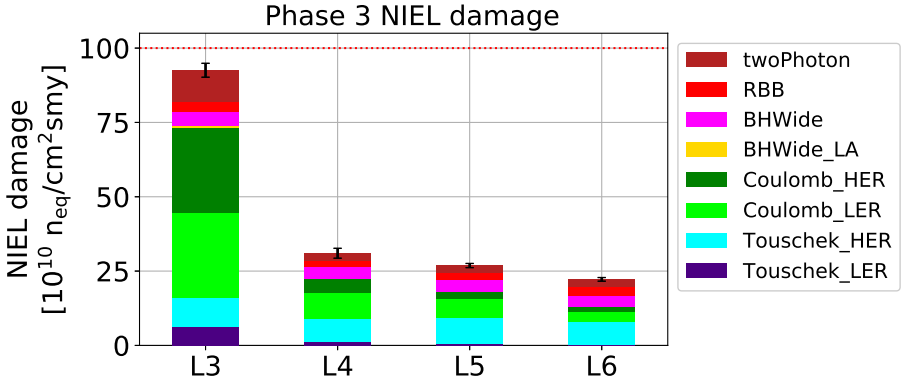

Figure 7.32: The estimated NIEL damage on the SVD in the final Phase 3 condition. The NIEL damage is averaged over the sensors in each layer. The result of the Phase 3 simulation is rescaled considering the Phase 2 observation. The contributions from different background sources are plotted in different colors denoted by the legend. The x-axis denotes the layer number. The red dotted line shows the limit of $10^{12}\,\mathrm{cm}^{-2}\mathrm{smy}^{-1}$ 1 MeV neutron equivalent fluence (see Section 5.1.3). The errors of the scale factors are not considered.

Chapter 8

Conclusion

8.1 Achievements

Although the SM successfully explains most of the phenomena in the particle physics, there remain many unexplained mysteries: the matter-antimatter asymmetry in the universe, the number of the fermion generations, the source of the neutrino mass, the existence of dark matter, the fine-tuning of the Higgs mass, etc. Many new physics models beyond the SM are suggested to explain these mysteries. The Belle II experiment, an intensity frontier experiment, probes the new physics scenarios by precisely measuring the deviations from SM predictions.

The essence of the Belle II experiment is to accumulate 50 times more data than its predecessor with more intense beam collisions and a higher DAQ rate. For these improvements, the SVD faces two challenges: the harsh beam background environment resulting from the intense beam collisions and the dead time of the readout ASIC due to the high trigger rate.

The APV25, the readout ASIC for the SVD, needs a trigger-veto system to prevent FIFO overflow. However, the conventional trigger-veto scheme results in a large dead time of the APV25 at the trigger rate of 30 kHz. Therefore there is a need for a more sophisticated trigger-veto system (the APV25-FIFO emulator) that prevents the FIFO overflow with minimal dead time.

At a test bench setup, we investigated how the APV25 reacts to given input signals. Based on the observation, we constructed a simple model to estimate the FIFO occupancy, in order to develop the APV25-FIFO emulator which provides the most efficient trigger-veto. We implemented the developed APV25-FIFO emulator in the FTSW firmware. We confirmed that trigger loss rates due to the APV25-FIFO emulator are consistent with expectations from simulation at various input trigger rates. The trigger loss rate for 30 kHz input triggers is about 3 %, which is a significant improvement from the conventional trigger-veto scheme. We verified its performance to prevent the FIFO overflow at high trigger rate by using the Phase 2 setup. The development of the APV25-FIFO emulator was an essential achievement for the 30 kHz DAQ of the SVD.

Since the harsh beam background environment leads to the degradation of the detector performance and radiation damage, it is necessary to confirm that the background level in Phase 3 is appropriate for SVD operation. The installation of the full SVD should happen after the confirmation of the following three items: The strip occupancy on every SVD sensor should

be low enough to achieve good tracking performance; the radiation dose rate should be low enough to ensure acceptable levels of radiation damage on the SVD when accumulated for a decade; the diamond sensors should be well correlated to the SVD for effective protection from instantaneous excessive background.

We had several simulation campaigns of the beam backgrounds in Phase 2 and 3, and several beam background measurements during Phase 2 operation. We decomposed the measured beam backgrounds according to their beam parameter dependency, energy distribution, and spatial distribution. For each background species, we compared the measurement and simulation. We confirmed large excesses of the observed Touschek and beam-gas backgrounds especially in the HER, while there was no measurable excess of the observed synchrotron radiation and luminosity backgrounds. Considering the observed excess of beam backgrounds, we scaled the Phase 3 simulation results to make a realistic estimation of the background rate in Phase 3. We concluded that the background level is low enough to allow for acceptable tracking performance assuming moderate accelerator conditions in the first years of Phase 3, but long-term operation requires the mitigation of single-beam backgrounds by an order of magnitude. We also observed a good correlation between the diamond dose rate and the SVD occupancy. Based on these results, the installation of the SVD in the Belle II detector was finally completed in November of 2018, anticipating the background will be mitigated in the first years of Phase 3.

8.2 Remaining studies

In order to achieve the design performance of the Belle II experiment, some topics in the SVD remain to be studied in the Phase 3 operation. We list them below:

- We have already confirmed that the APV25-FIFO emulator functions for short periods in the Phase 3 setup[1]. The long-term stability of the trigger veto system with the APV25-FIFO emulator should be confirmed in the Phase 3 operation with a high rate trigger.
- The mixed mode of the APV25-FIFO emulator should be implemented and tested.
- In the first year of Phase 3, beam background mitigation by tuning the accelerator and collimator settings will be the first priority. We should perform beam size scans to update the estimate of the final Phase 3 background. This will be an important input to decide the operation plan.
- The properties of the unknown background X in the HER should be investigated. In addition to the beam size scans, scanning the number of bunches will be an important approach to disentangle it from other backgrounds.
- We should investigate the source of the discrepancy between the measured and simulated single-beam background rates. By correcting the simulation, we should make the estimation for the final Phase 3 more reliable.
- The beam-gas background model is approximated in this thesis. We should consider the gas composition and local difference of pressure to make the model more realistic.
- Since the SVD is not sensitive to the SR background, it can damage the SVD without being recognized. Therefore, the SR background should be carefully estimated. We should

[1]The data from the full SVD were read out without the FIFO overflow for at least 50 minutes with 10 kHz FTSW pseudorandom trigger, and at least 27 minutes with 30 kHz pseudorandom trigger.

investigate it with a more sensitive approach to the low energy photons.

- In Phase 2, the machine luminosity was too low to measure the luminosity backgrounds, which are predicted to be dominant in the Phase 3 simulation. We should redo the luminosity background study in stable accelerator condition with higher luminosity.
- The LER continuous injection background was barely visible to the SVD in Phase 2, unlike the diamonds. The reason and the background from the HER injections should be investigated.
- In Phase 3, the full SVD covering the entire azimuthal angle will be available. The ϕ distribution of the beam backgrounds should be investigated and utilized for the comparison to the simulation.

Appendix A

The strip charts during beam background measurements

In this chapter, we show the strip charts for important beam background measurements, the beam size scans and luminosity scan. In each chart, the beam parameters (current, pressure, vertical beam size, number of bunches, and luminosity) and the background rates (SVD occupancy averaged over the L3 sensors, diamond dose rate averaged over the BWD diamond sensors, and total PMT rate of the TOP counters) are shown as functions of time.
While pseudorandom trigger was used in the most of the measurements, we took data by "physics trigger" during some runs in the beam size scans H-A and L-A. Due to the short time window of the SVD, the SVD occupancy measured by the physics trigger is biased to be higher than pseudorandom trigger. The bias can be seen by comparing the SVD occupancy with the diamond and TOP background rate which are measured independently of the trigger.
In the physics data taking, the physics trigger should be sensitive to only the collision events and beam background events are observed as random events superimposed on the collision events. Therefore, we are interested in the beam background rate measured by the pseudorandom trigger. Physics trigger runs are not included in the analysis in this thesis.

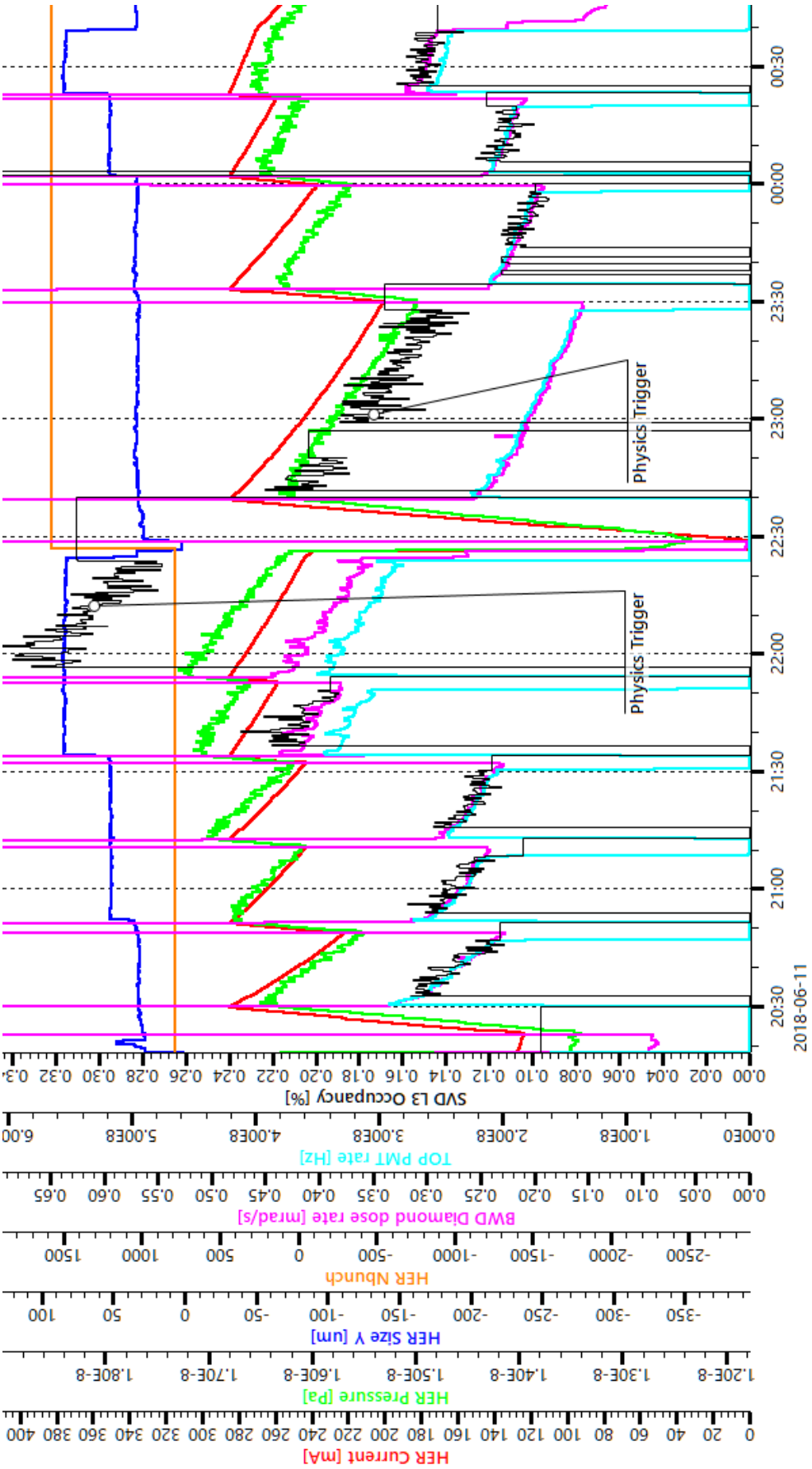

Figure A.1: HER beam size scan on June 11th, H-A.

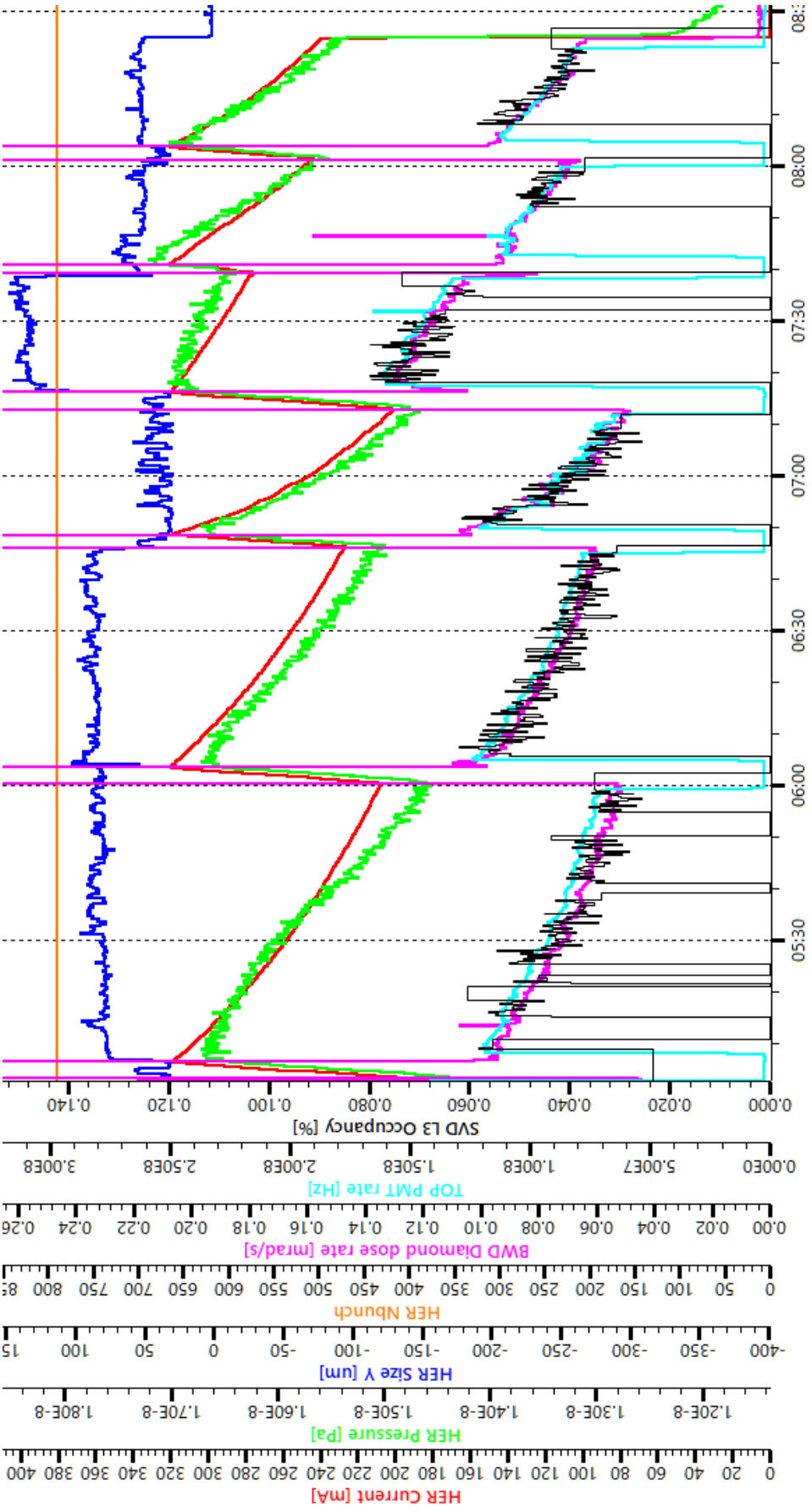

Figure A.2: HER beam size scan on July 13th, H-B.

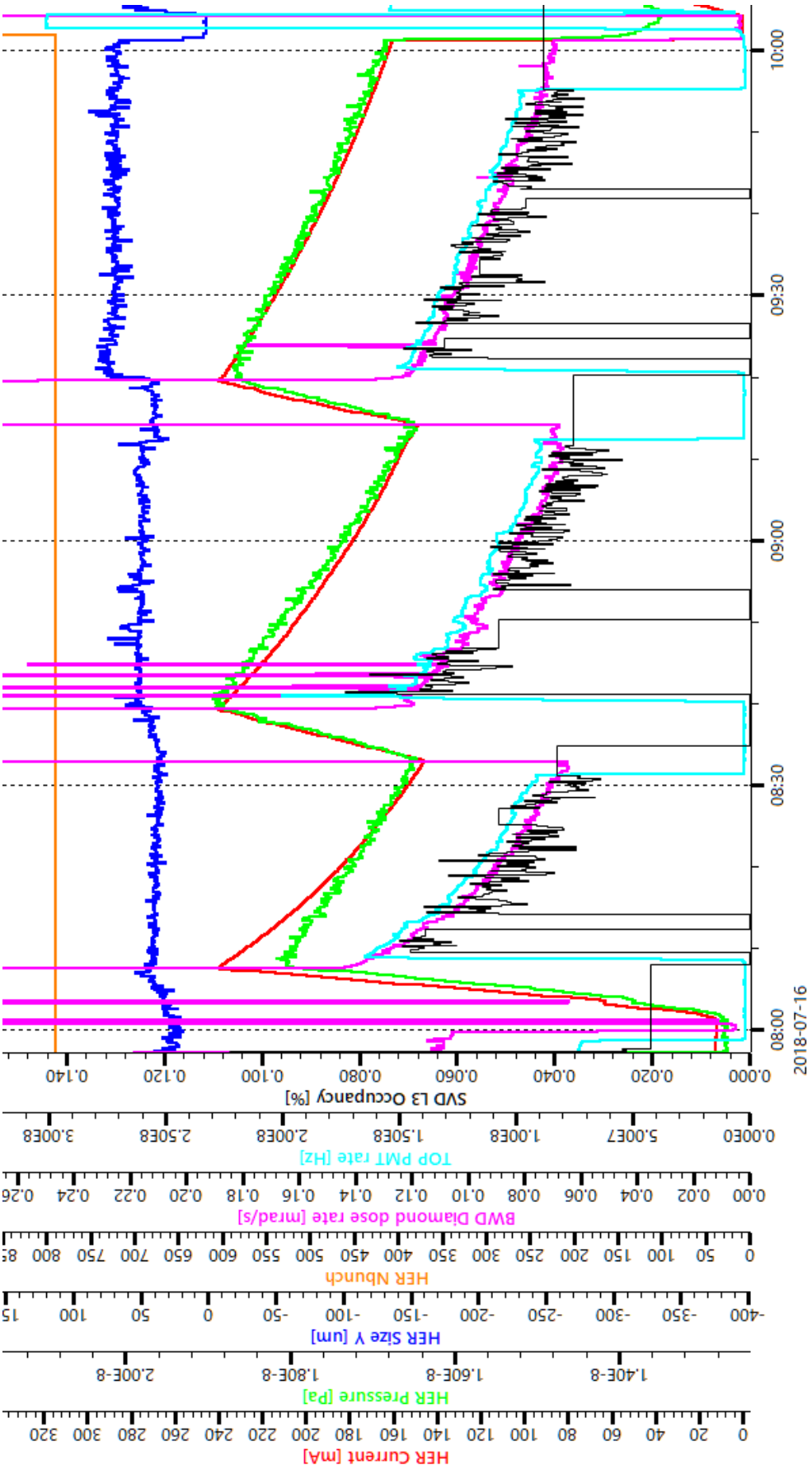

Figure A.3: HER beam size scan on July 16th, H-C.

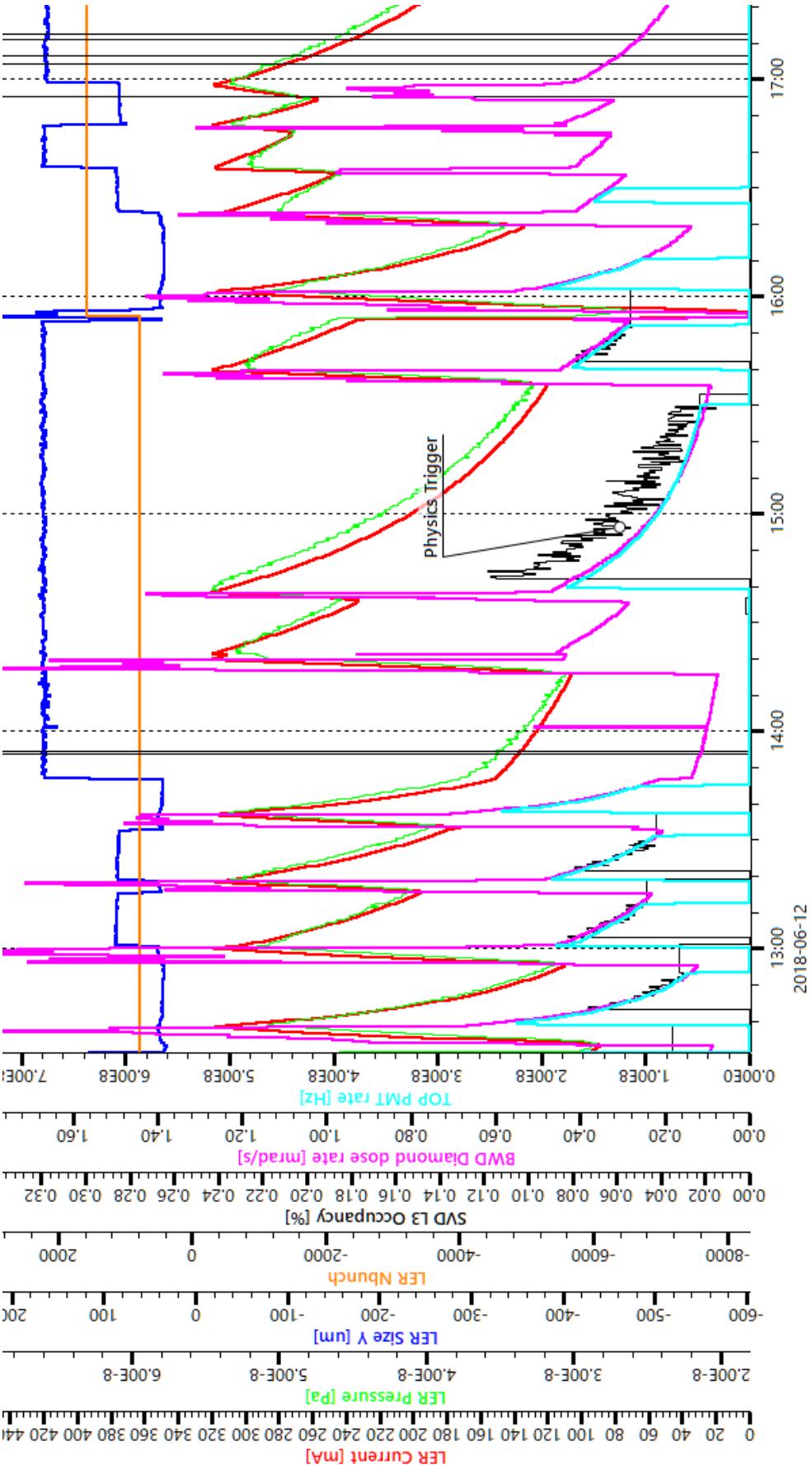

Figure A.4: LER beam size scan on June 12th, L-A.

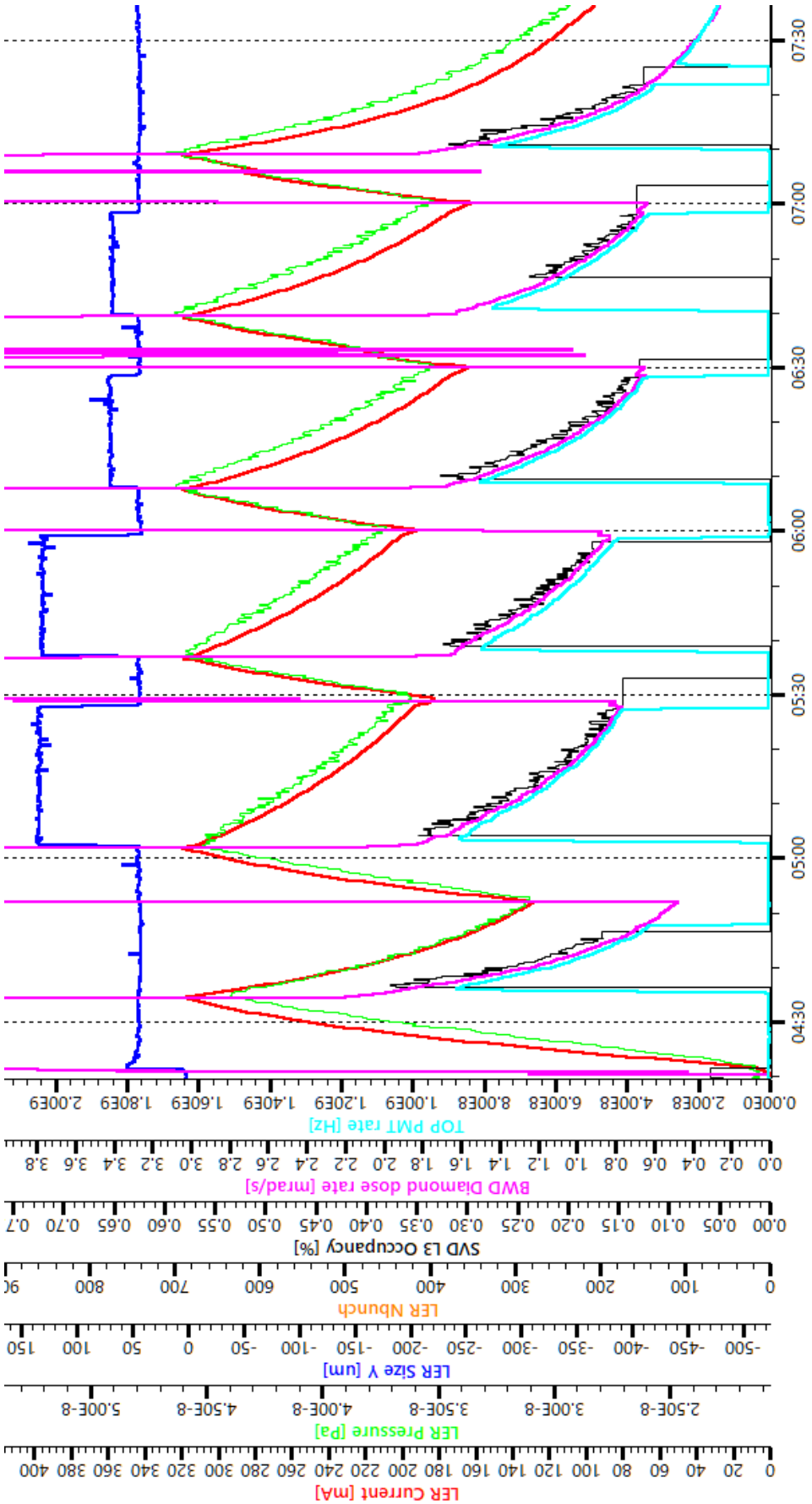

Figure A.5: LER beam size scan on July 16th, L-B.

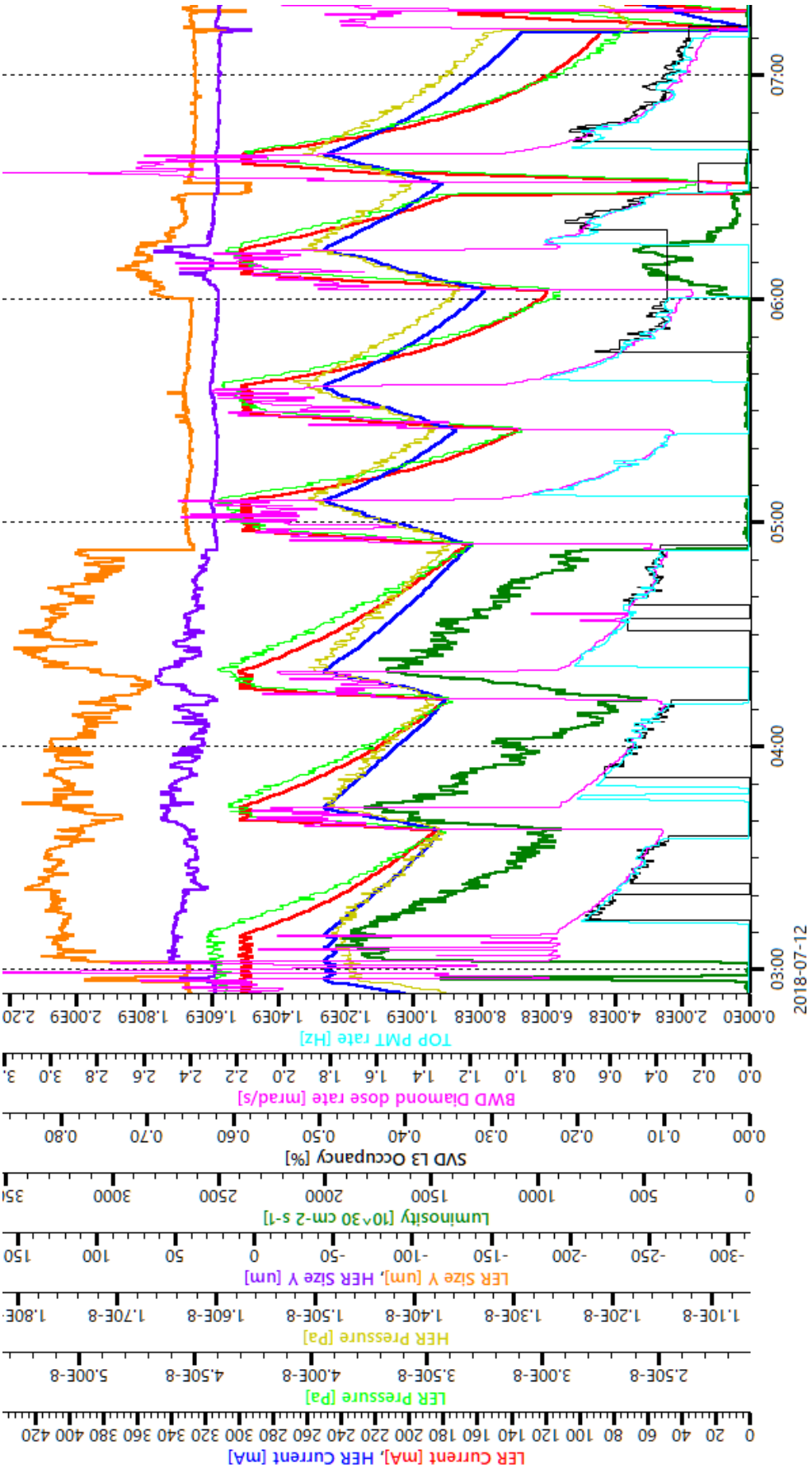

Figure A.6: Luminosity scan on July 12th. The number of bunches is 789 for both rings.

Appendix B

The result of the Phase 3 beam background simulation

We show the detailed result of the Phase 3 background simulation in this chapter. The following plots show the background rate (occupancy on U and V sides, radiation dose, and NIEL damage) on each SVD sensor due to various background sources (two-photon, RBB, BHWide, BHWide LA, HER Coulomb, LER Coulomb, HER Touschek, LER Touschek, and total of them), in addition to Fig. 6.3. Each plot is separated by the layers. The x-axis shows the azimuthal angle of the center of the sensor.[1] The ladder numbers are shown above the data points. Markers denote the sensor position on the ladder.

[1] In the plots, the FW sensors are adjusted to the azimuthal angle and the other sensors are slightly shifted for visibility.

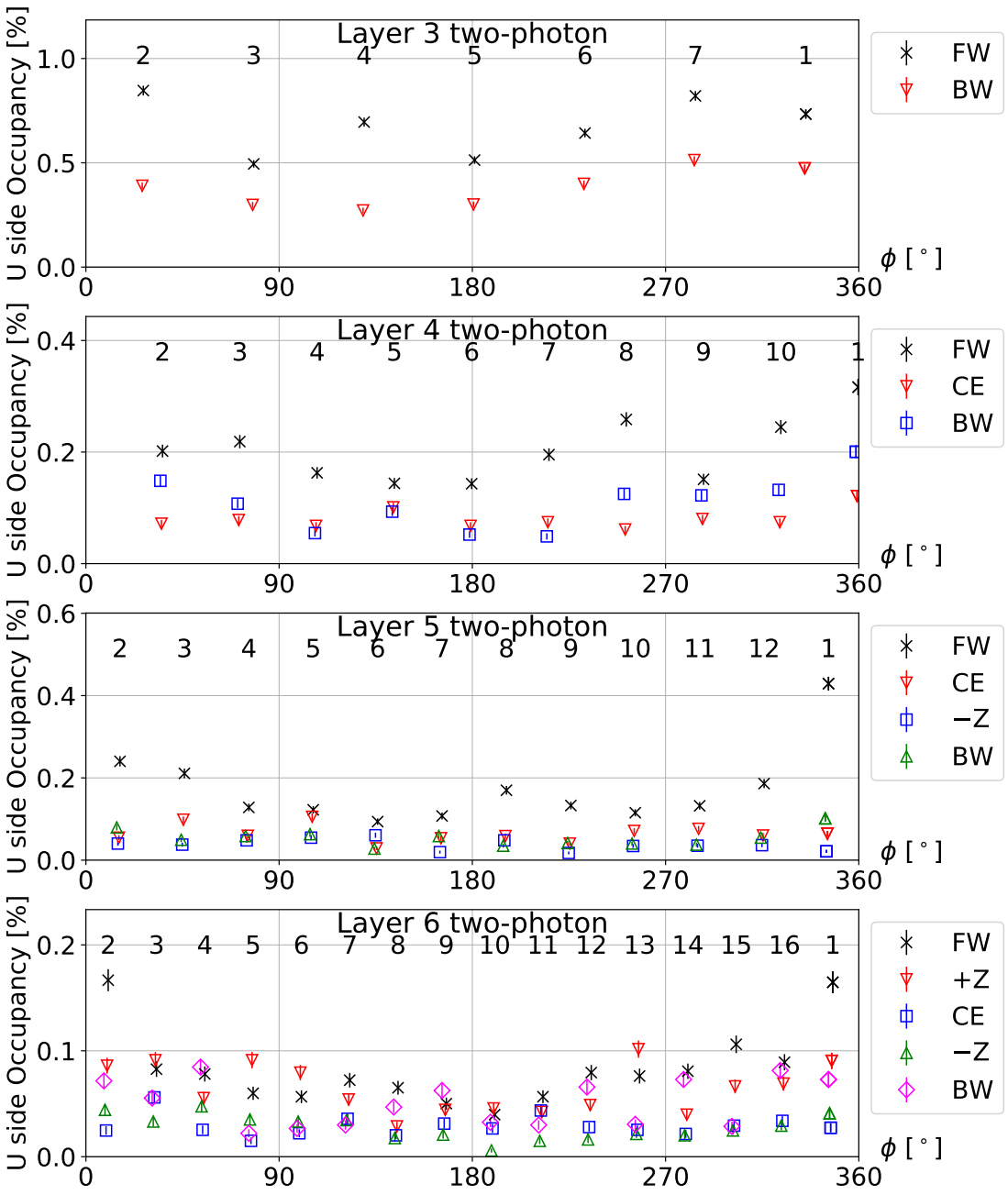

Figure B.1: The azimuthal angle dependence of the U side occupancy in the Phase 3 simulation. The U side occupancy from two-photon background is plotted for each SVD sensor. The plots are separated by the layers. For each layer, the x-axis shows the azimuthal angle of the center of the sensor. The ladder numbers are shown above the data points. Markers denote the sensor position on the ladder.

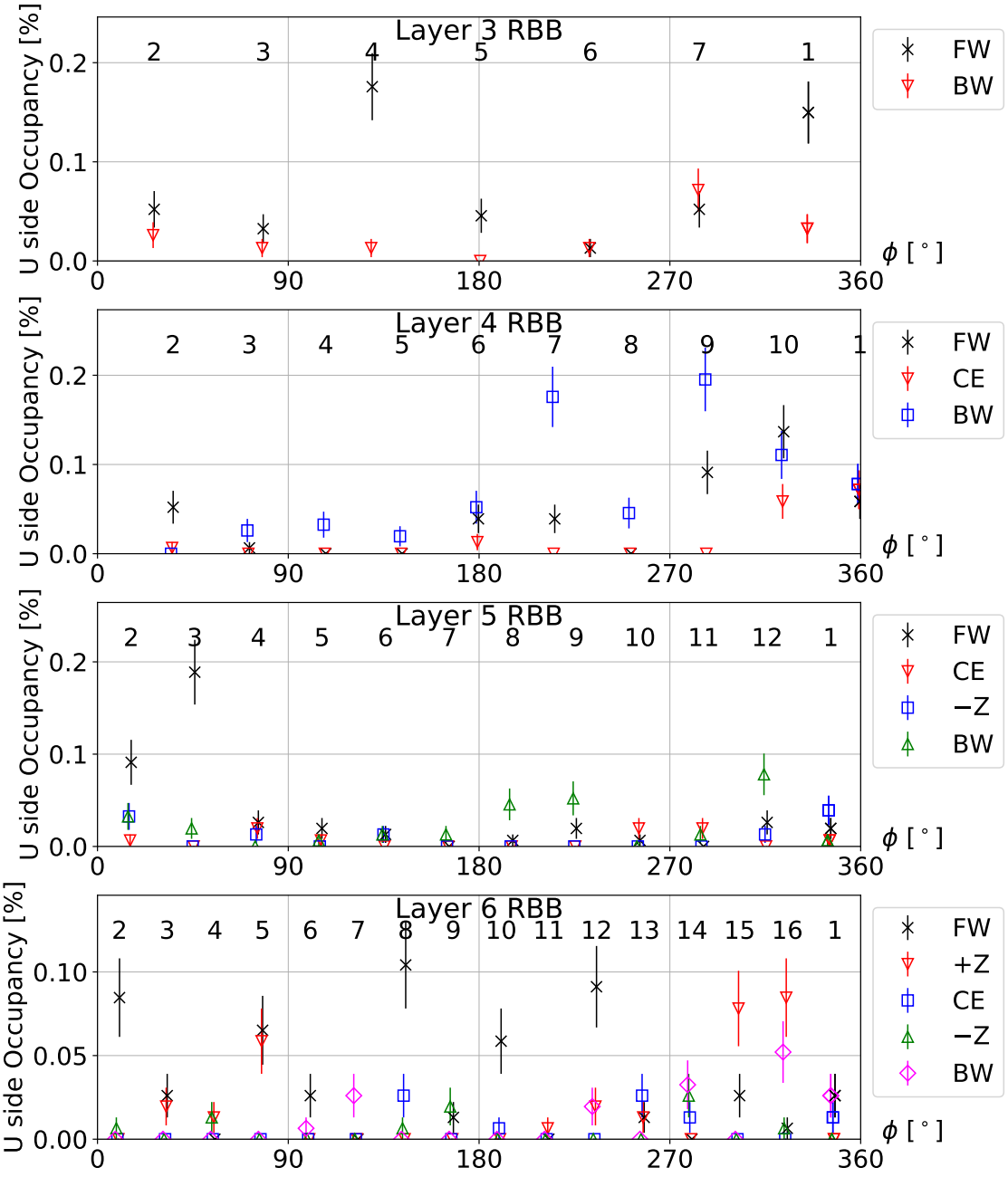

Figure B.2: The azimuthal angle dependence of the U side occupancy in the Phase 3 simulation. The U side occupancy from RBB background is plotted for each SVD sensor. The plots are separated by the layers. For each layer, the x-axis shows the azimuthal angle of the center of the sensor. The ladder numbers are shown above the data points. Markers denote the sensor position on the ladder.

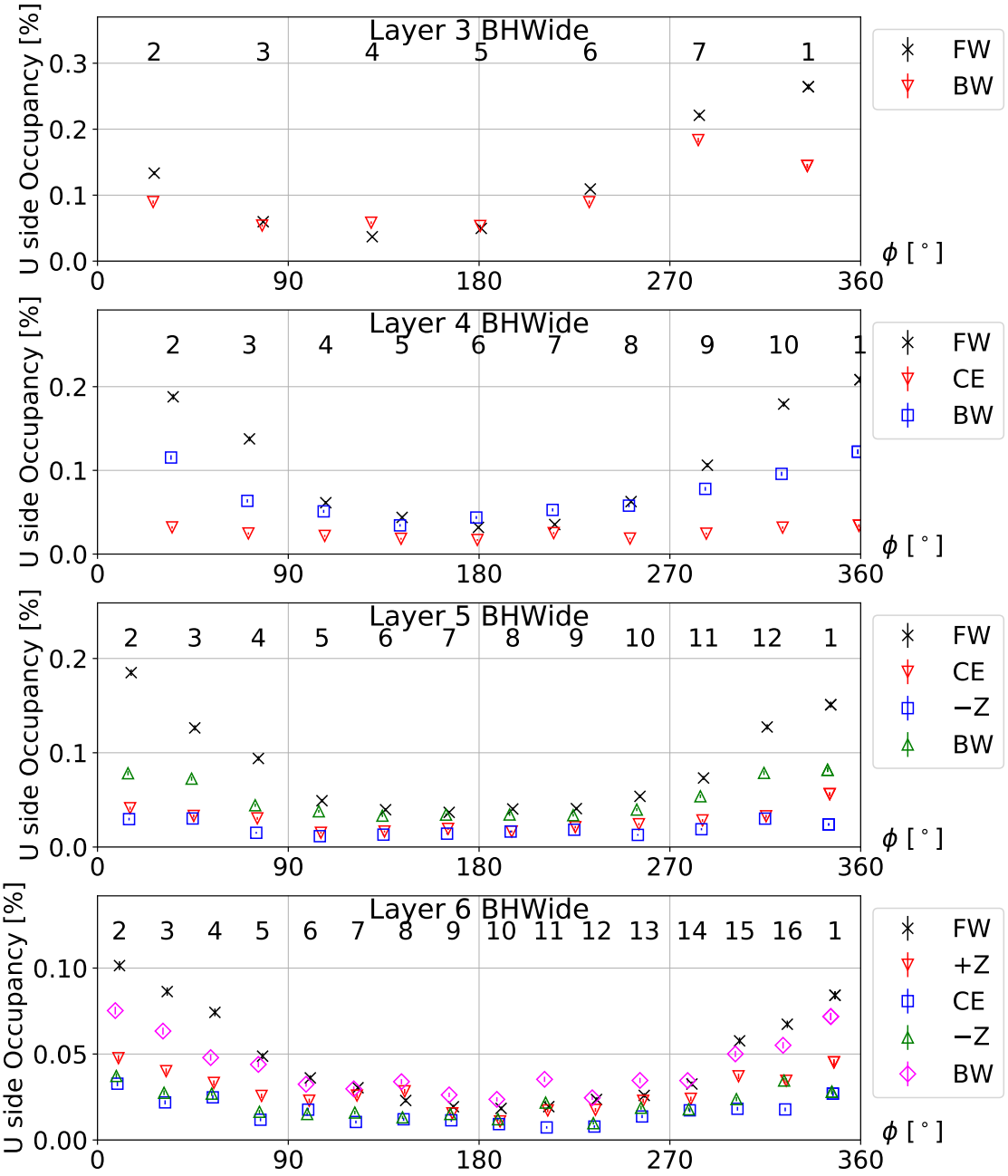

Figure B.3: The azimuthal angle dependence of the U side occupancy in the Phase 3 simulation. The U side occupancy from BHWide background is plotted for each SVD sensor. The plots are separated by the layers. For each layer, the x-axis shows the azimuthal angle of the center of the sensor. The ladder numbers are shown above the data points. Markers denote the sensor position on the ladder.

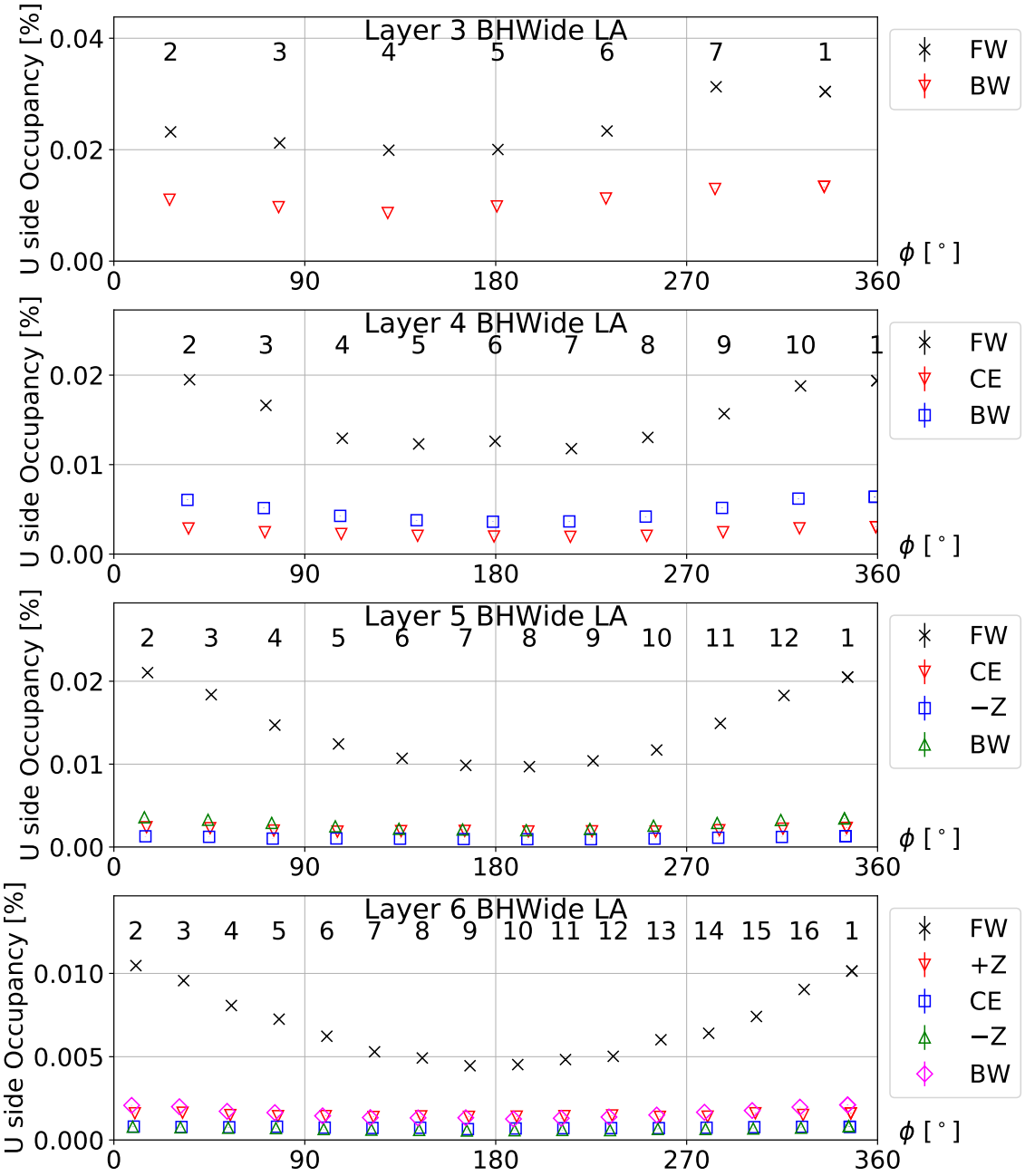

Figure B.4: The azimuthal angle dependence of the U side occupancy in the Phase 3 simulation. The U side occupancy from BHWide LA background is plotted for each SVD sensor. The plots are separated by the layers. For each layer, the x-axis shows the azimuthal angle of the center of the sensor. The ladder numbers are shown above the data points. Markers denote the sensor position on the ladder.

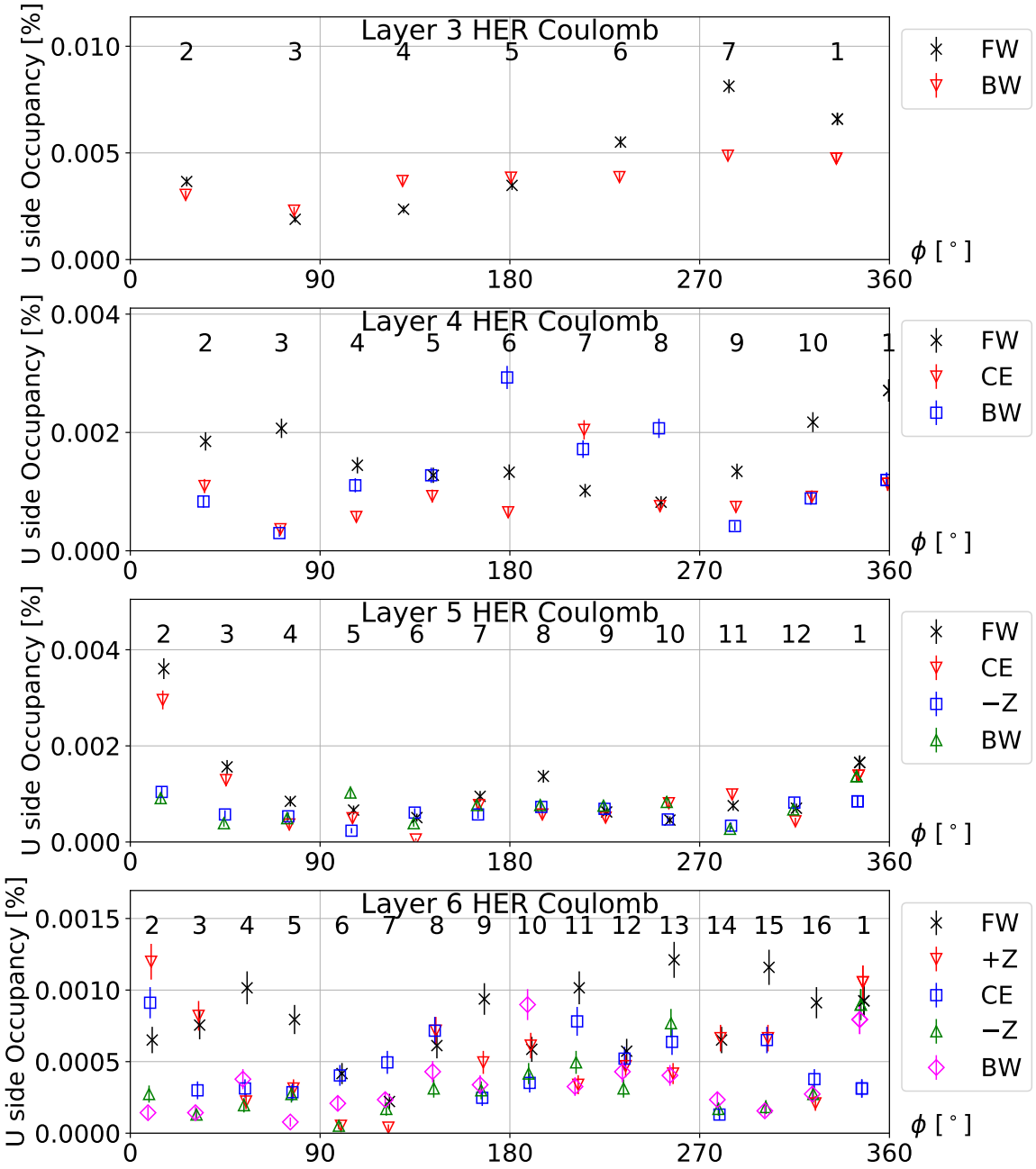

Figure B.5: The azimuthal angle dependence of the U side occupancy in the Phase 3 simulation. The U side occupancy from HER Coulomb background is plotted for each SVD sensor. The plots are separated by the layers. For each layer, the x-axis shows the azimuthal angle of the center of the sensor. The ladder numbers are shown above the data points. Markers denote the sensor position on the ladder.

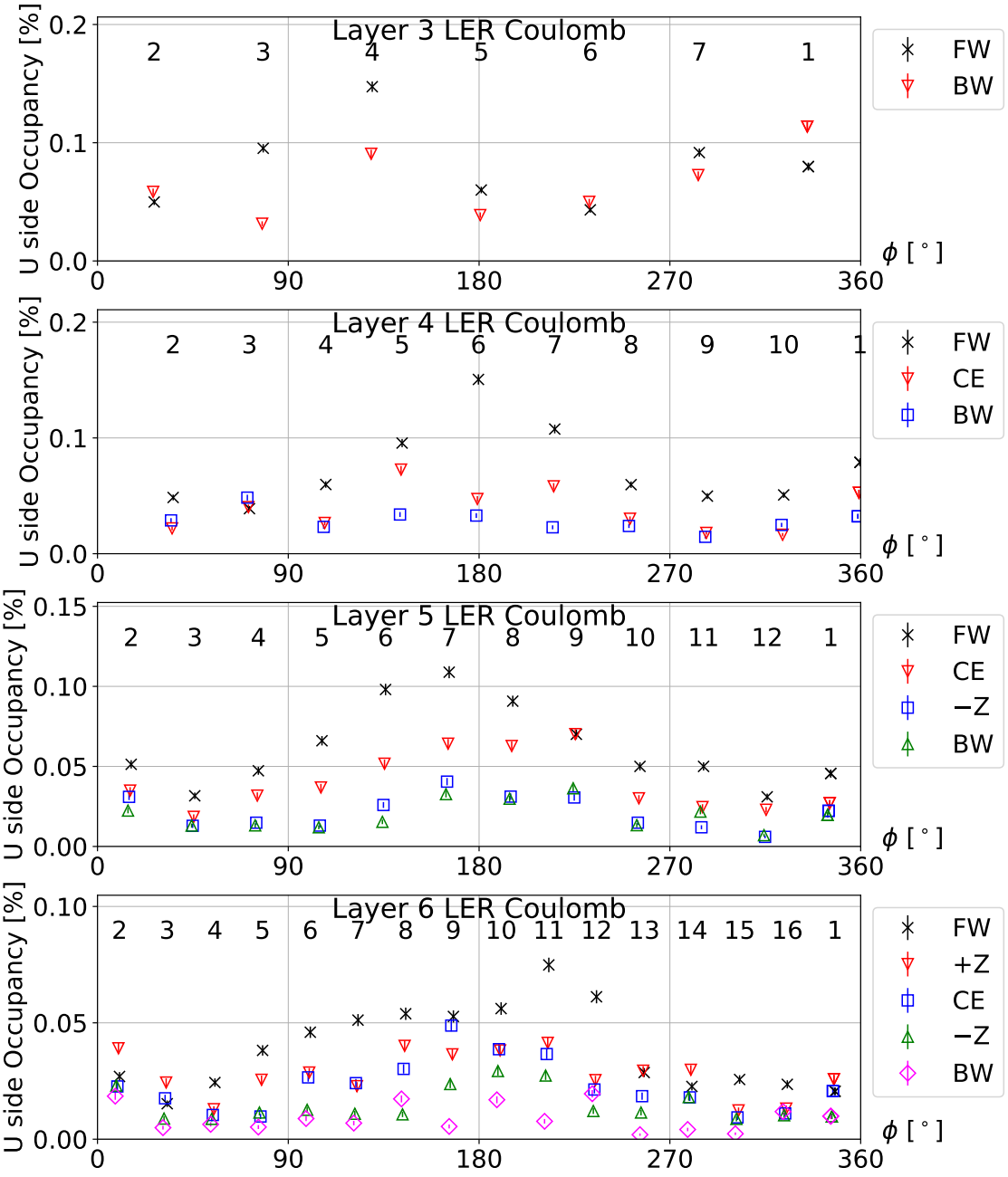

Figure B.6: The azimuthal angle dependence of the U side occupancy in the Phase 3 simulation. The U side occupancy from LER Coulomb background is plotted for each SVD sensor. The plots are separated by the layers. For each layer, the x-axis shows the azimuthal angle of the center of the sensor. The ladder numbers are shown above the data points. Markers denote the sensor position on the ladder.

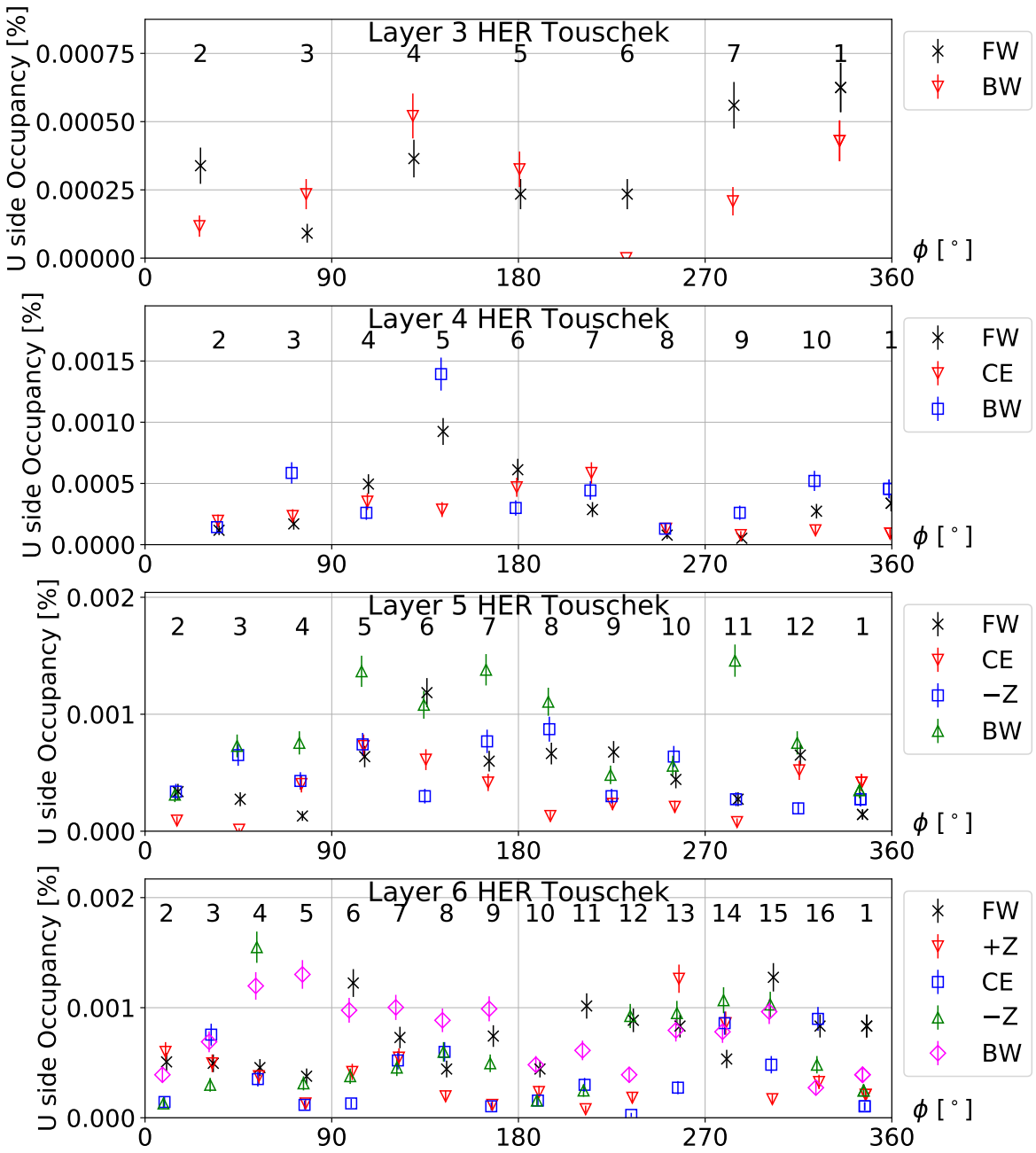

Figure B.7: The azimuthal angle dependence of the U side occupancy in the Phase 3 simulation. The U side occupancy from HER Touschek background is plotted for each SVD sensor. The plots are separated by the layers. For each layer, the x-axis shows the azimuthal angle of the center of the sensor. The ladder numbers are shown above the data points. Markers denote the sensor position on the ladder.

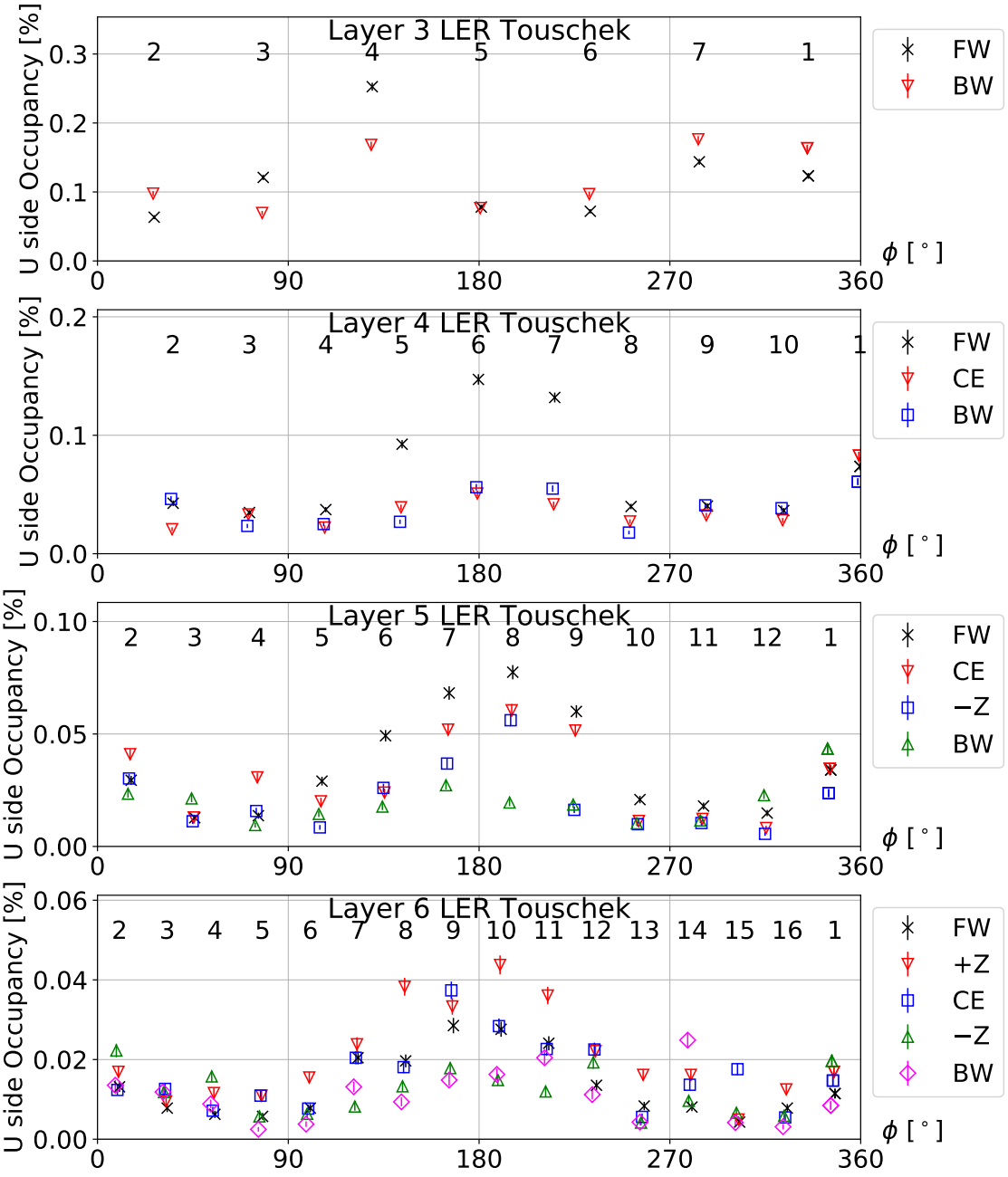

Figure B.8: The azimuthal angle dependence of the U side occupancy in the Phase 3 simulation. The U side occupancy from LER Touschek background is plotted for each SVD sensor. The plots are separated by the layers. For each layer, the x-axis shows the azimuthal angle of the center of the sensor. The ladder numbers are shown above the data points. Markers denote the sensor position on the ladder.

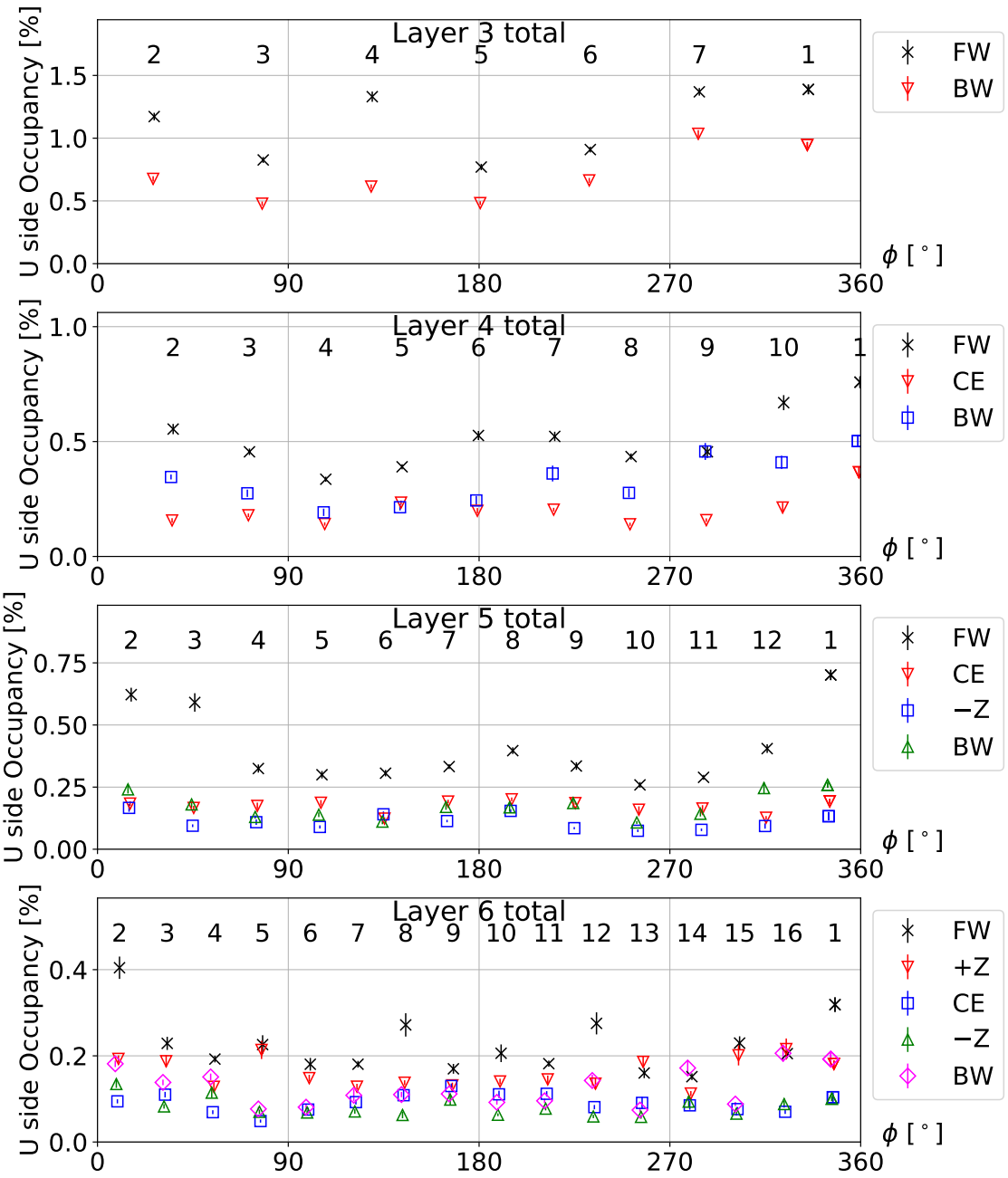

Figure B.9: The azimuthal angle dependence of the U side occupancy in the Phase 3 simulation. The total U side occupancy is plotted for each SVD sensor. The plots are separated by the layers. For each layer, the x-axis shows the azimuthal angle of the center of the sensor. The ladder numbers are shown above the data points. Markers denote the sensor position on the ladder.

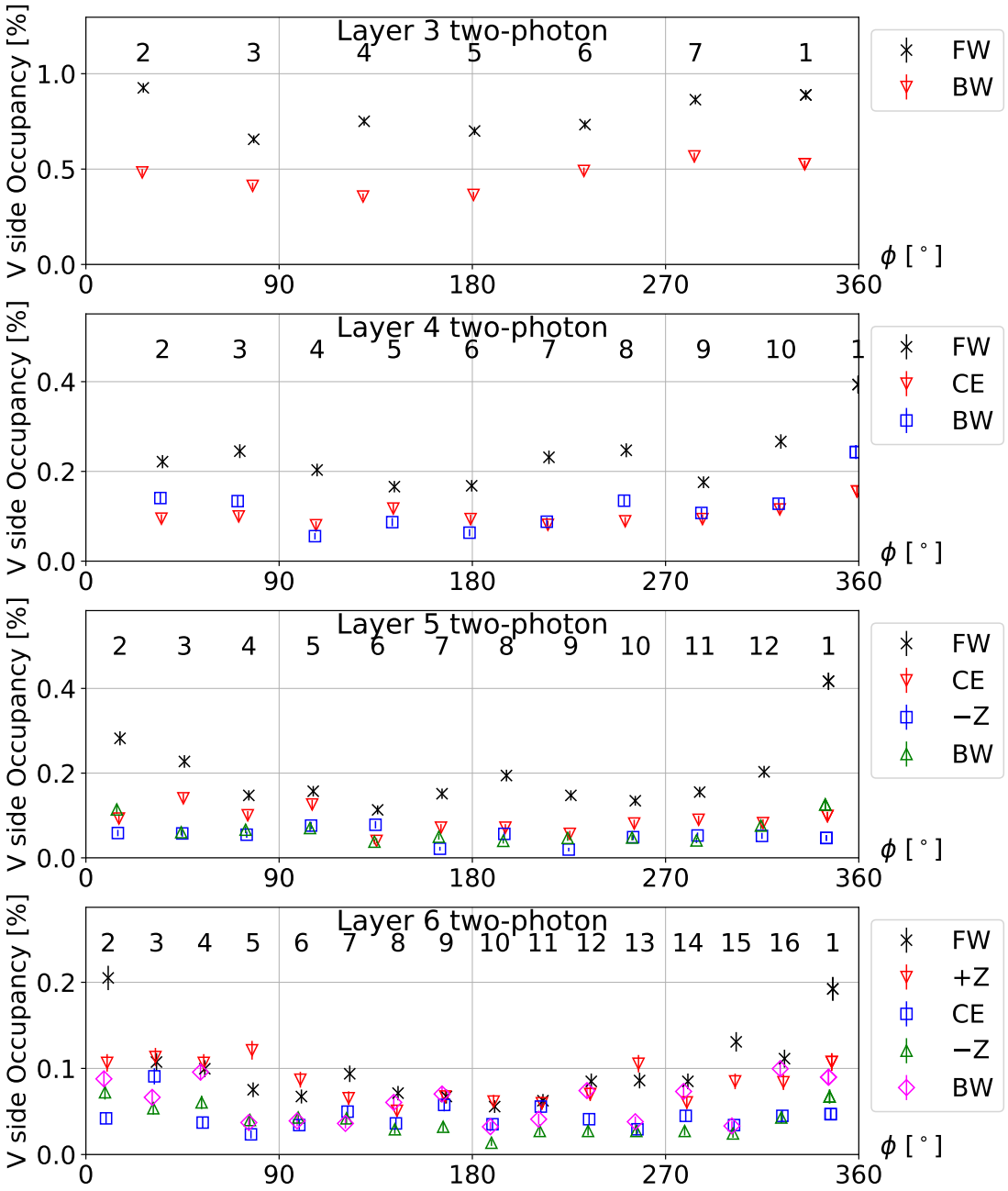

Figure B.10: The azimuthal angle dependence of the V side occupancy in the Phase 3 simulation. The V side occupancy from two-photon background is plotted for each SVD sensor. The plots are separated by the layers. For each layer, the x-axis shows the azimuthal angle of the center of the sensor. The ladder numbers are shown above the data points. Markers denote the sensor position on the ladder.

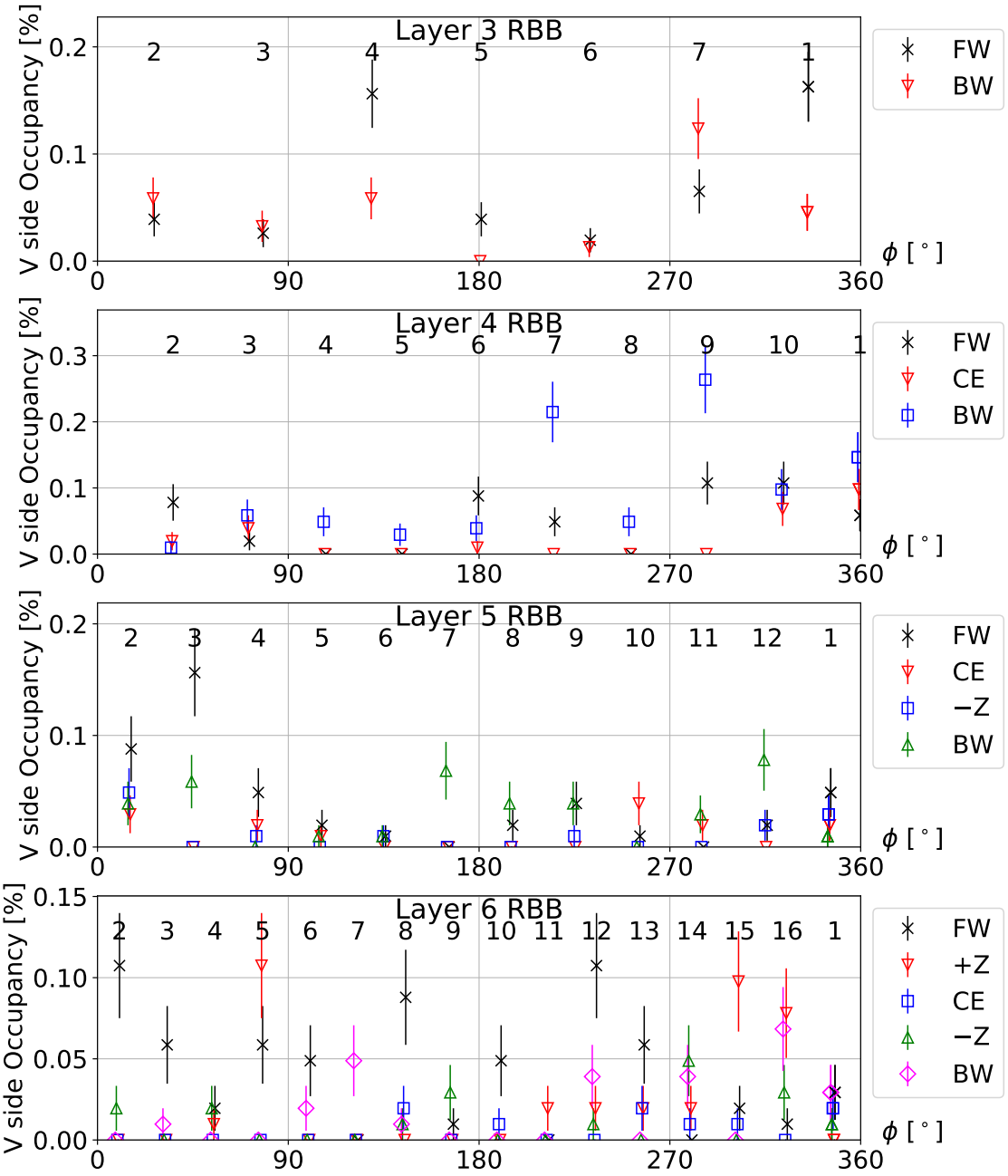

Figure B.11: The azimuthal angle dependence of the V side occupancy in the Phase 3 simulation. The V side occupancy from RBB background is plotted for each SVD sensor. The plots are separated by the layers. For each layer, the x-axis shows the azimuthal angle of the center of the sensor. The ladder numbers are shown above the data points. Markers denote the sensor position on the ladder.

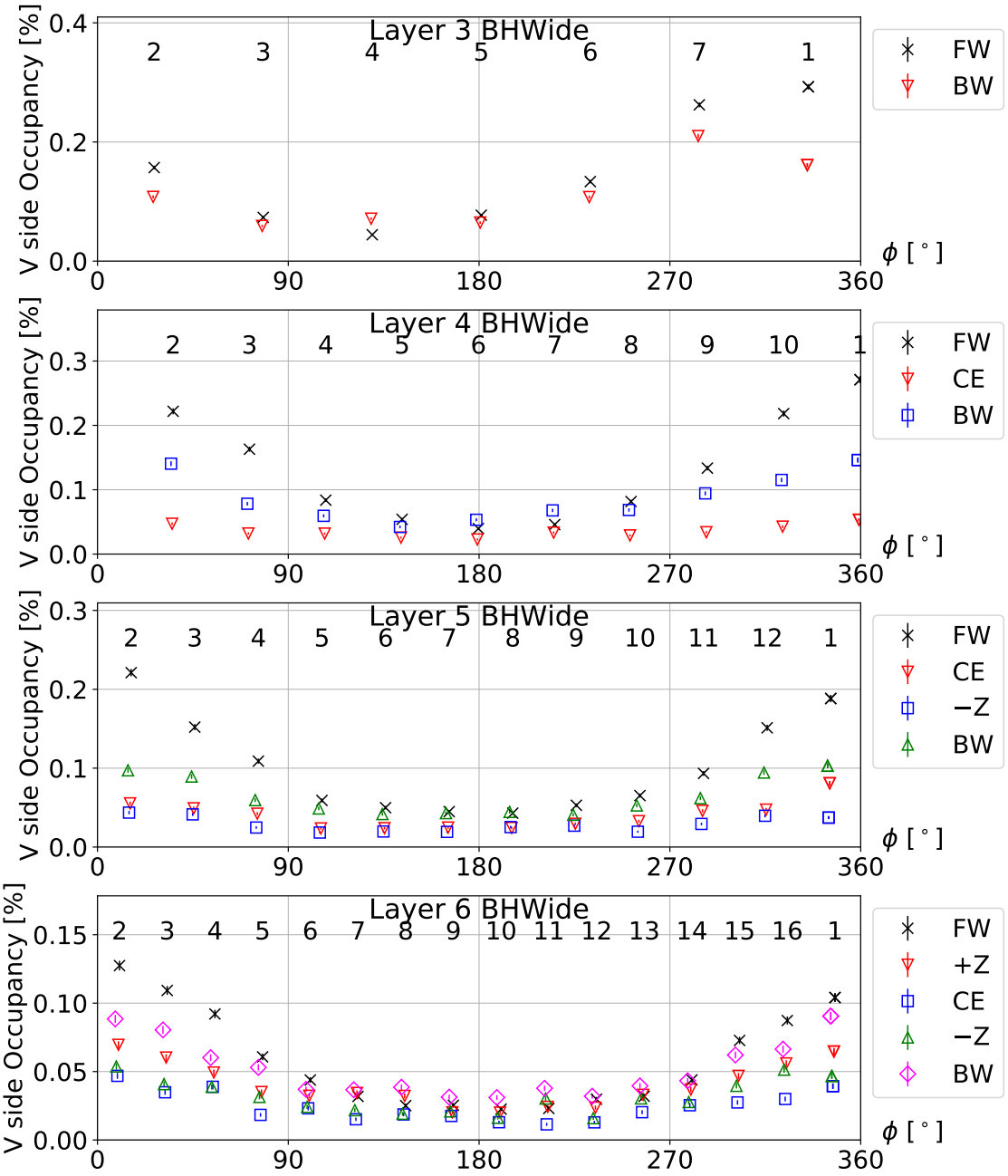

Figure B.12: The azimuthal angle dependence of the V side occupancy in the Phase 3 simulation. The V side occupancy from BHWide background is plotted for each SVD sensor. The plots are separated by the layers. For each layer, the x-axis shows the azimuthal angle of the center of the sensor. The ladder numbers are shown above the data points. Markers denote the sensor position on the ladder.

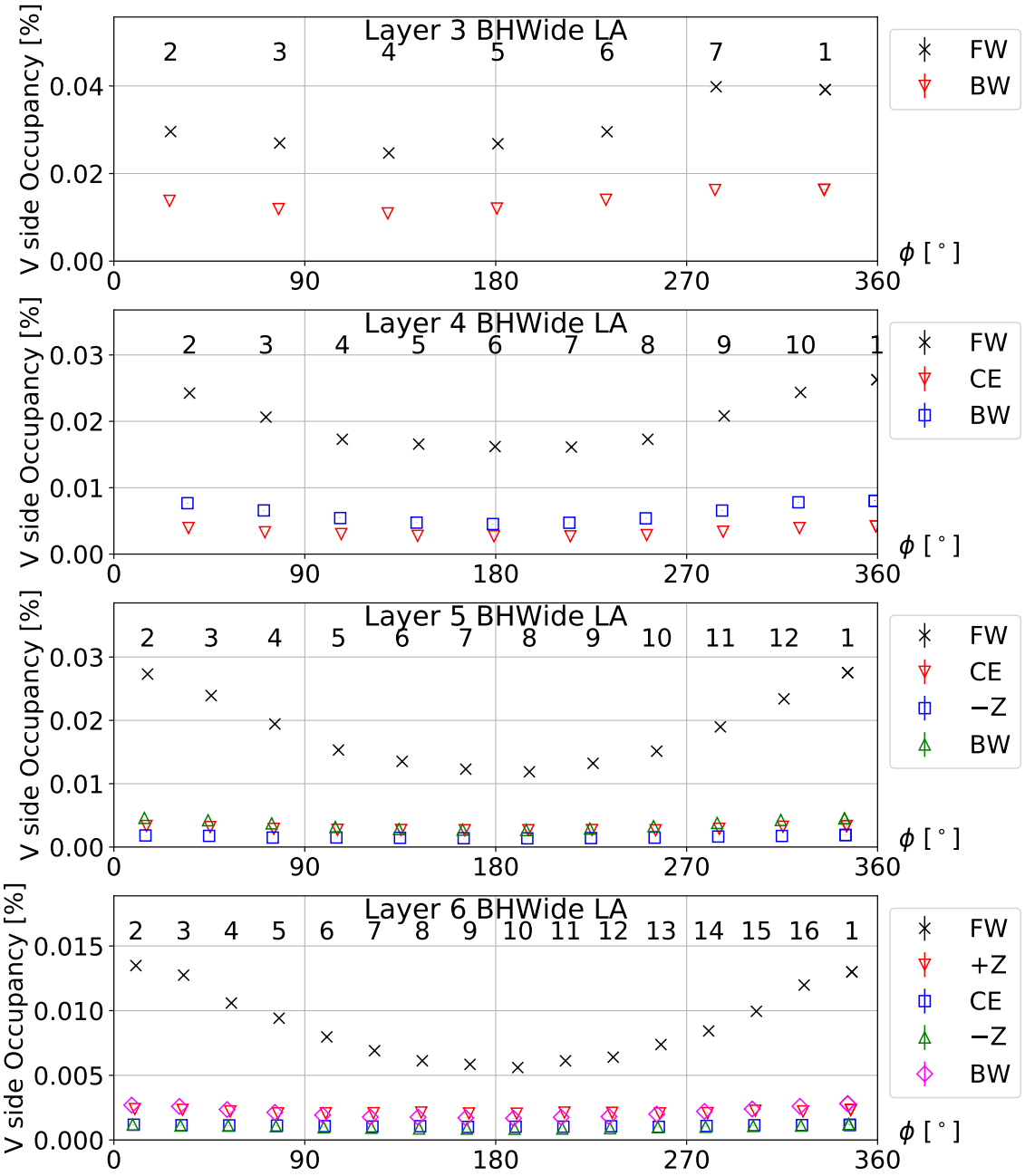

Figure B.13: The azimuthal angle dependence of the V side occupancy in the Phase 3 simulation. The V side occupancy from BHWide LA background is plotted for each SVD sensor. The plots are separated by the layers. For each layer, the x-axis shows the azimuthal angle of the center of the sensor. The ladder numbers are shown above the data points. Markers denote the sensor position on the ladder.

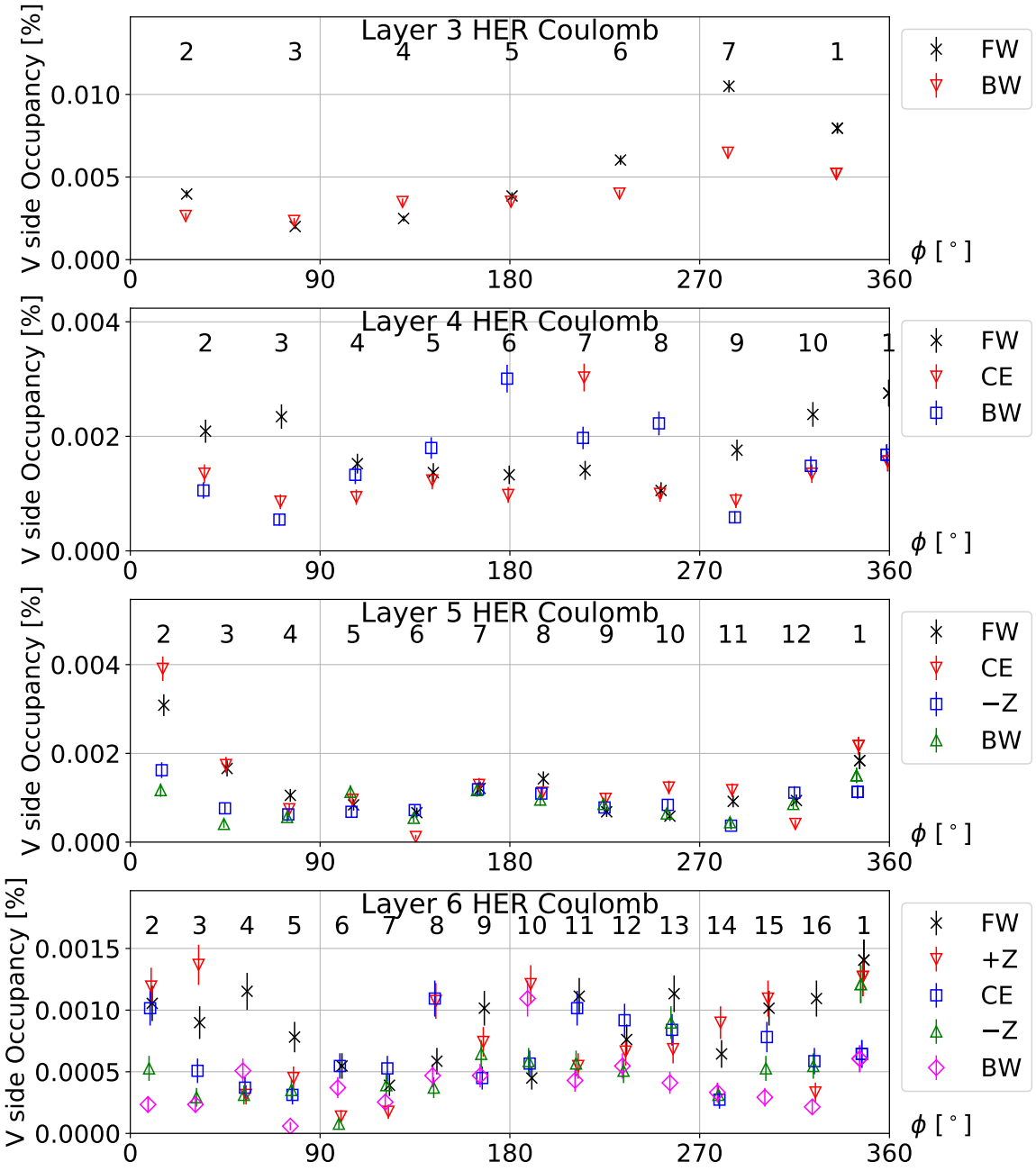

Figure B.14: The azimuthal angle dependence of the V side occupancy in the Phase 3 simulation. The V side occupancy from HER Coulomb background is plotted for each SVD sensor. The plots are separated by the layers. For each layer, the x-axis shows the azimuthal angle of the center of the sensor. The ladder numbers are shown above the data points. Markers denote the sensor position on the ladder.

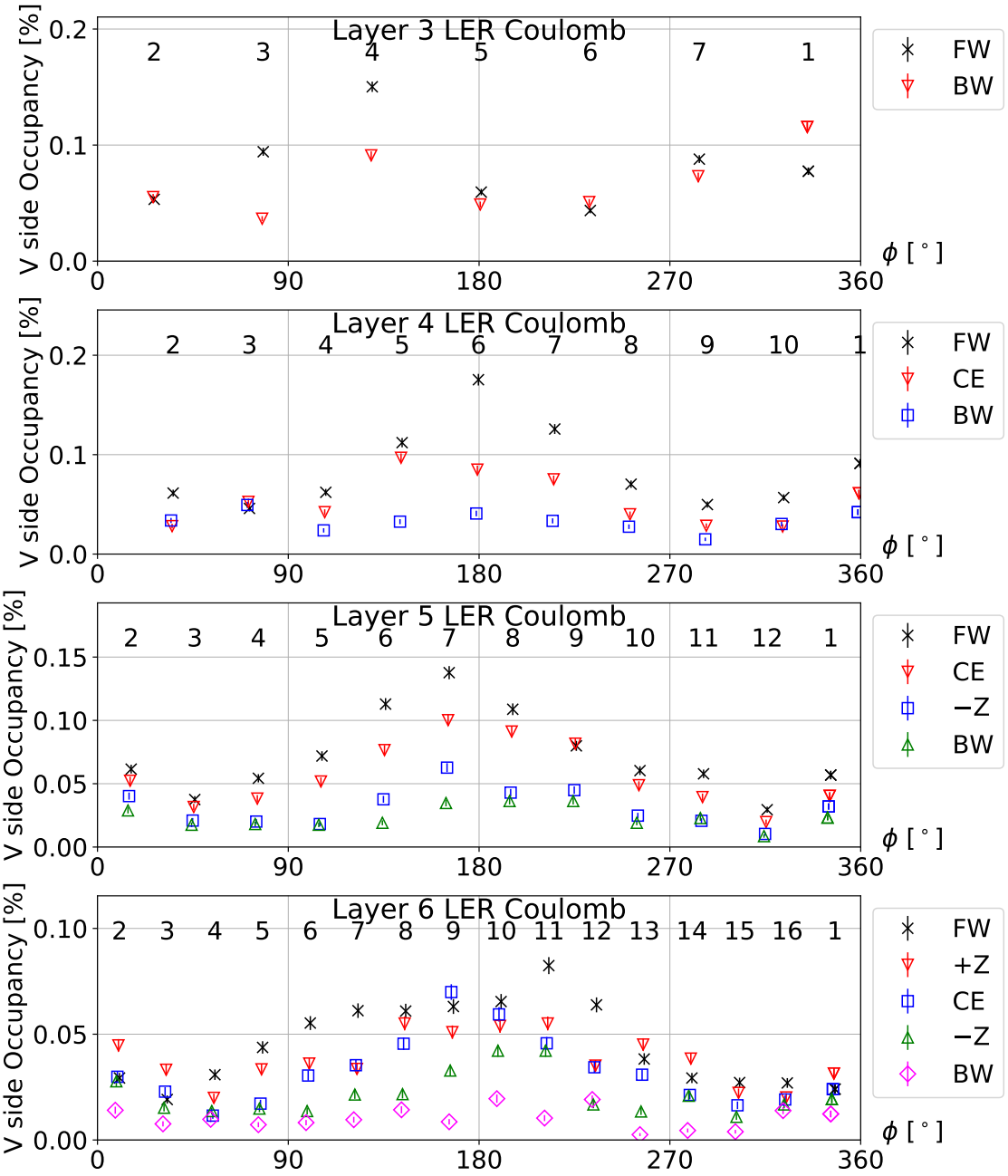

Figure B.15: The azimuthal angle dependence of the V side occupancy in the Phase 3 simulation. The V side occupancy from LER Coulomb background is plotted for each SVD sensor. The plots are separated by the layers. For each layer, the x-axis shows the azimuthal angle of the center of the sensor. The ladder numbers are shown above the data points. Markers denote the sensor position on the ladder.

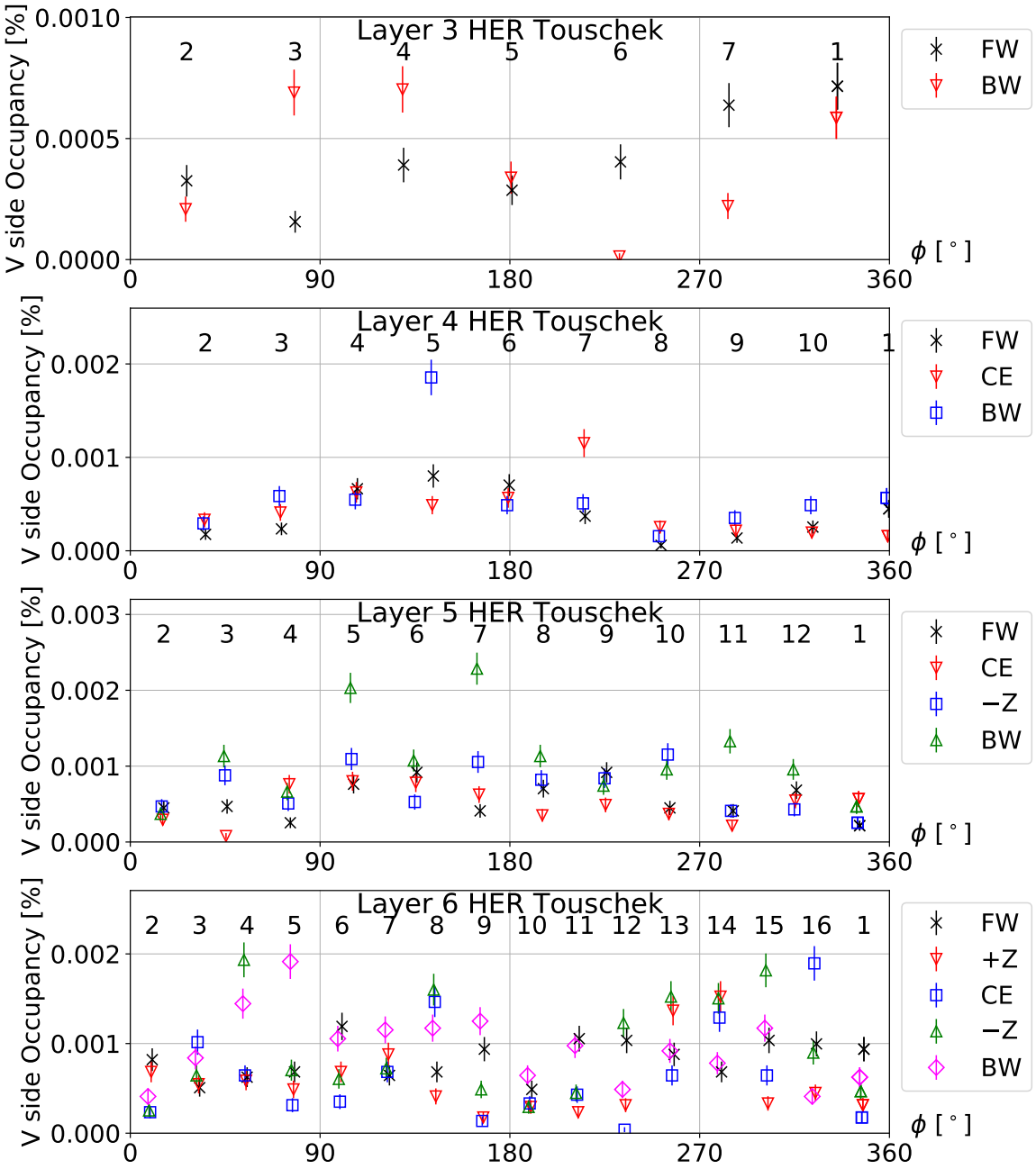

Figure B.16: The azimuthal angle dependence of the V side occupancy in the Phase 3 simulation. The V side occupancy from HER Touschek background is plotted for each SVD sensor. The plots are separated by the layers. For each layer, the x-axis shows the azimuthal angle of the center of the sensor. The ladder numbers are shown above the data points. Markers denote the sensor position on the ladder.

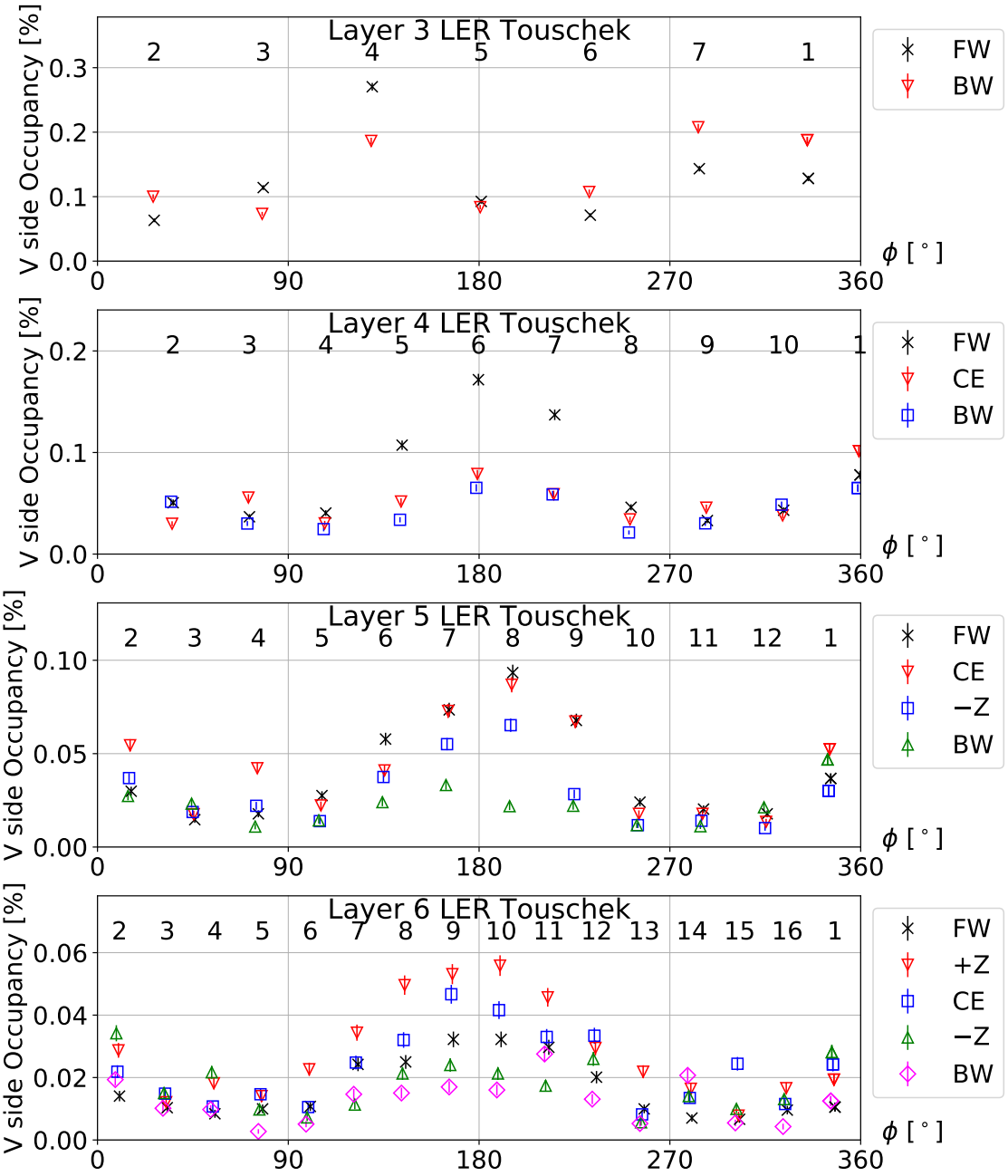

Figure B.17: The azimuthal angle dependence of the V side occupancy in the Phase 3 simulation. The V side occupancy from LER Touschek background is plotted for each SVD sensor. The plots are separated by the layers. For each layer, the x-axis shows the azimuthal angle of the center of the sensor. The ladder numbers are shown above the data points. Markers denote the sensor position on the ladder.

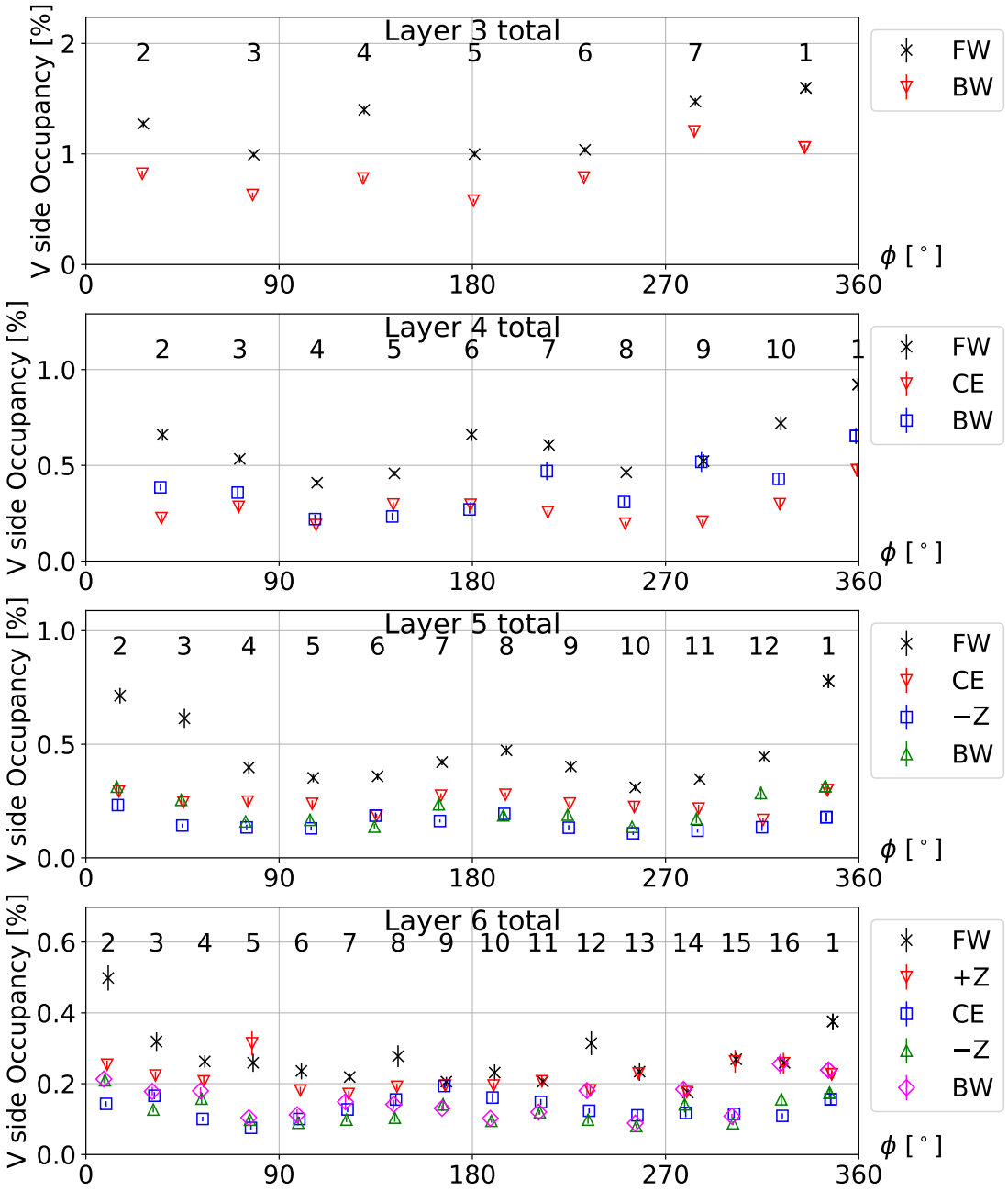

Figure B.18: The azimuthal angle dependence of the V side occupancy in the Phase 3 simulation. The total V side occupancy is plotted for each SVD sensor. The plots are separated by the layers. For each layer, the x-axis shows the azimuthal angle of the center of the sensor. The ladder numbers are shown above the data points. Markers denote the sensor position on the ladder.

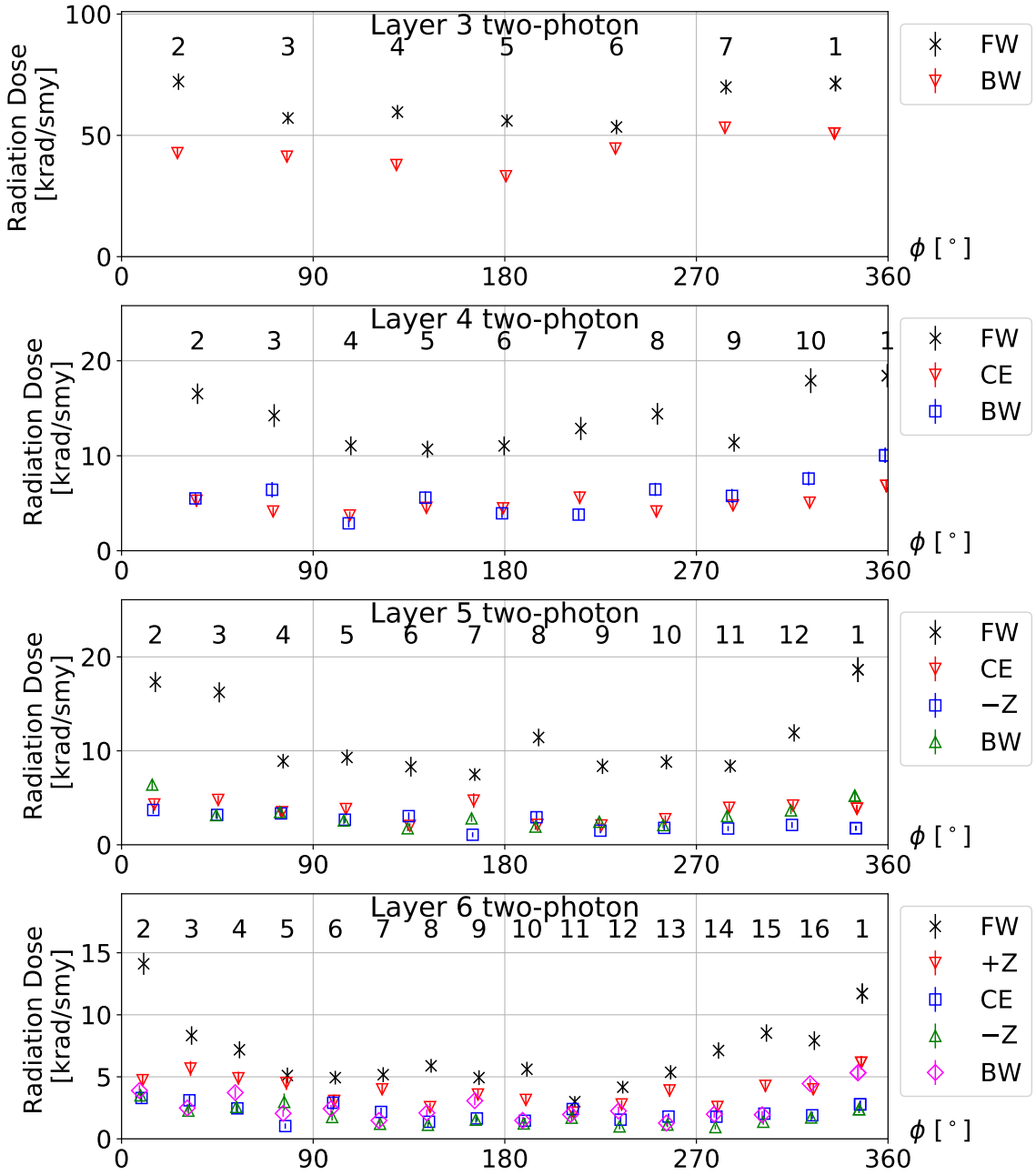

Figure B.19: The azimuthal angle dependence of the radiation dose in the Phase 3 simulation. The radiation dose from two-photon background is plotted for each SVD sensor. The plots are separated by the layers. For each layer, the x-axis shows the azimuthal angle of the center of the sensor. The ladder numbers are shown above the data points. Markers denote the sensor position on the ladder.

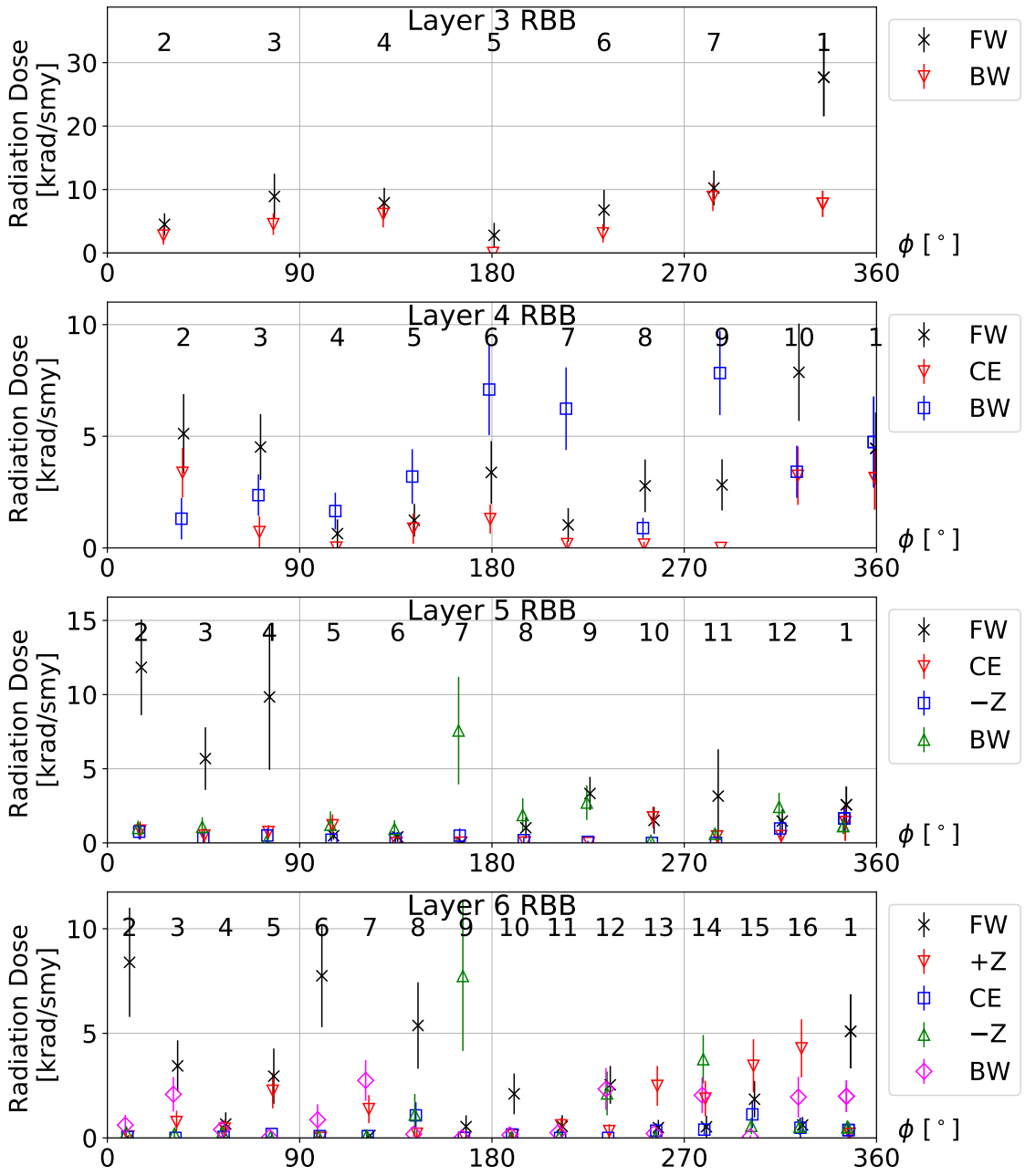

Figure B.20: The azimuthal angle dependence of the radiation dose in the Phase 3 simulation. The radiation dose from RBB background is plotted for each SVD sensor. The plots are separated by the layers. For each layer, the x-axis shows the azimuthal angle of the center of the sensor. The ladder numbers are shown above the data points. Markers denote the sensor position on the ladder.

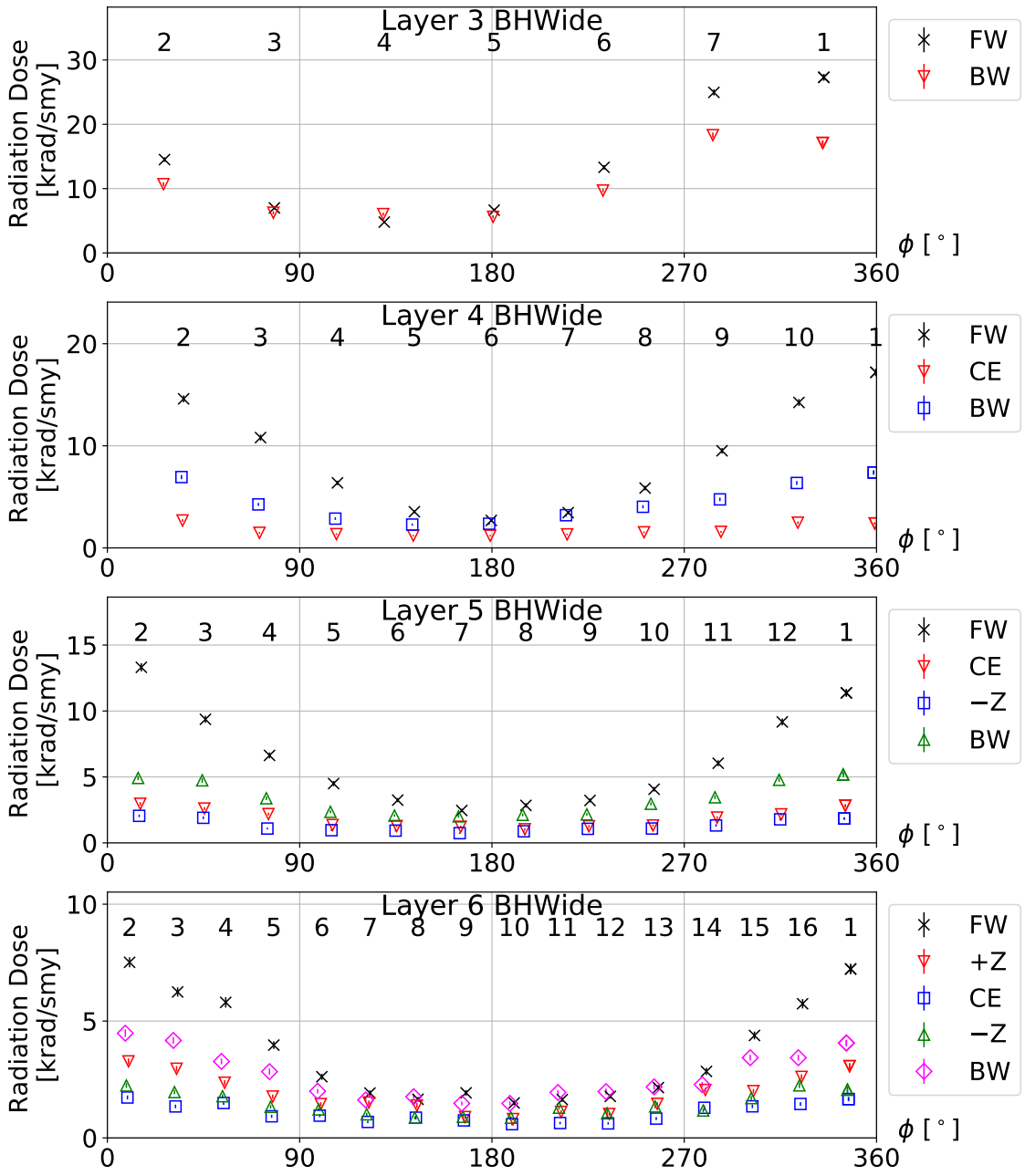

Figure B.21: The azimuthal angle dependence of the radiation dose in the Phase 3 simulation. The radiation dose from BHWide background is plotted for each SVD sensor. The plots are separated by the layers. For each layer, the x-axis shows the azimuthal angle of the center of the sensor. The ladder numbers are shown above the data points. Markers denote the sensor position on the ladder.

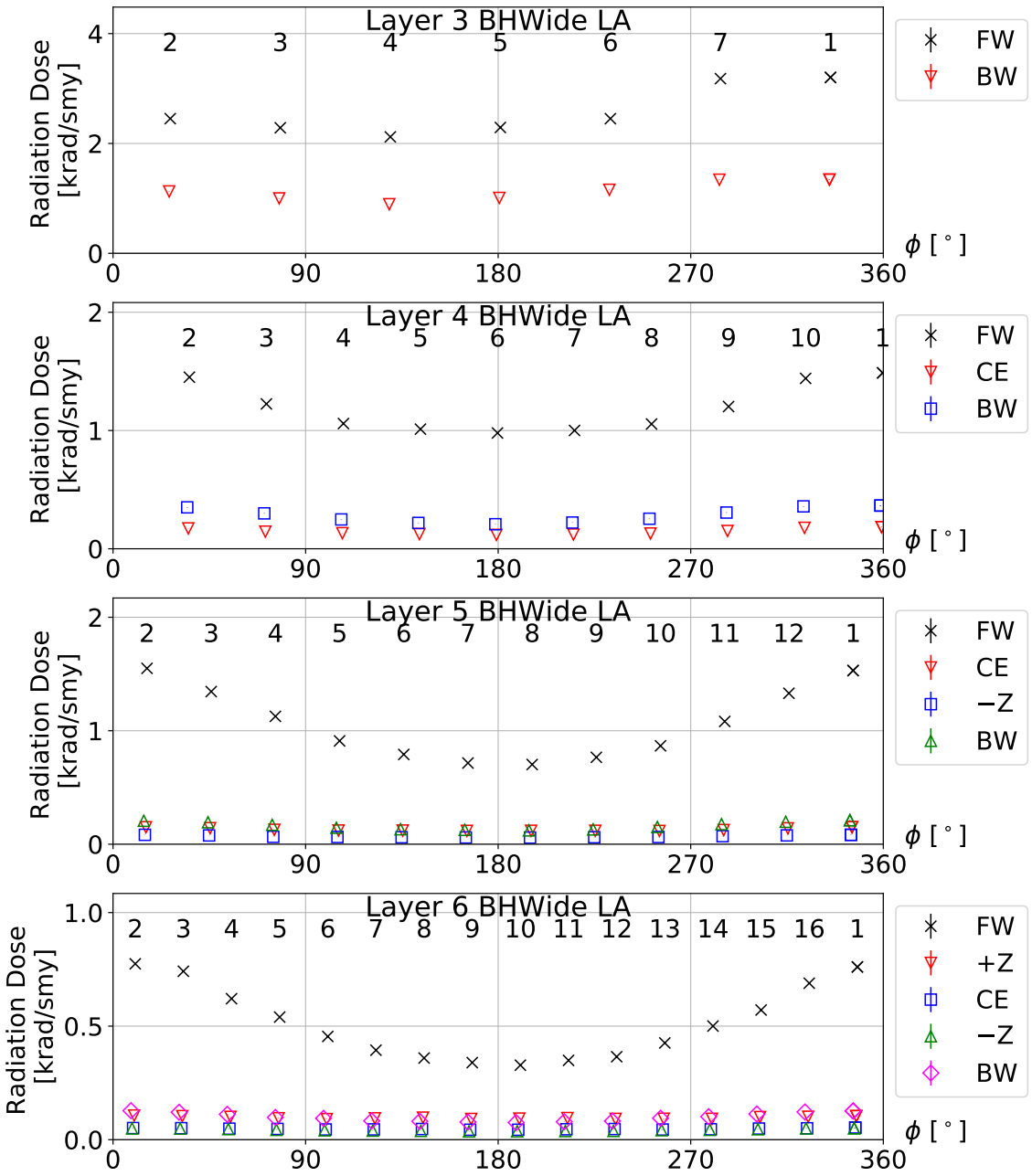

Figure B.22: The azimuthal angle dependence of the radiation dose in the Phase 3 simulation. The radiation dose from BHWide LA background is plotted for each SVD sensor. The plots are separated by the layers. For each layer, the x-axis shows the azimuthal angle of the center of the sensor. The ladder numbers are shown above the data points. Markers denote the sensor position on the ladder.

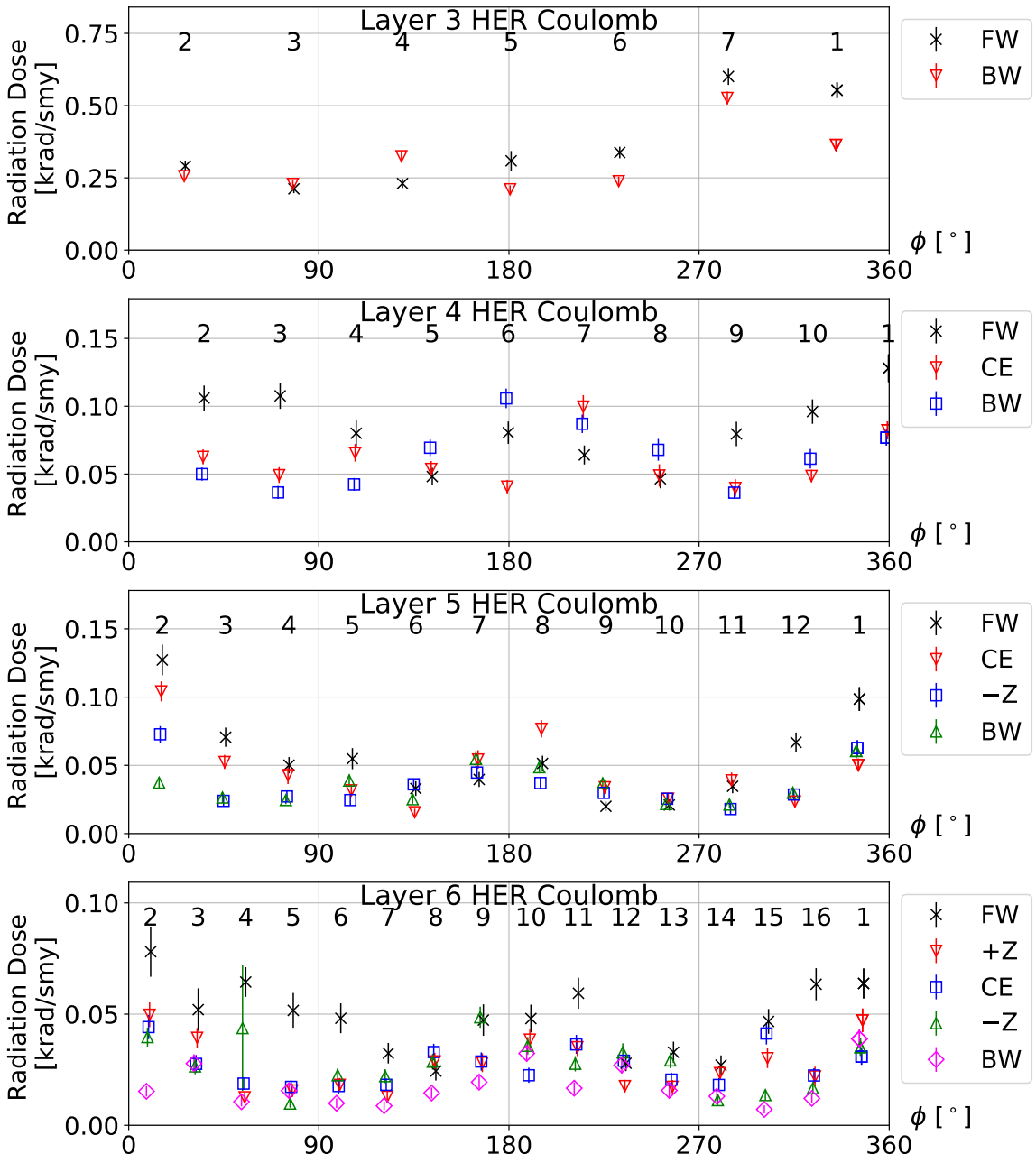

Figure B.23: The azimuthal angle dependence of the radiation dose in the Phase 3 simulation. The radiation dose from HER Coulomb background is plotted for each SVD sensor. The plots are separated by the layers. For each layer, the x-axis shows the azimuthal angle of the center of the sensor. The ladder numbers are shown above the data points. Markers denote the sensor position on the ladder.

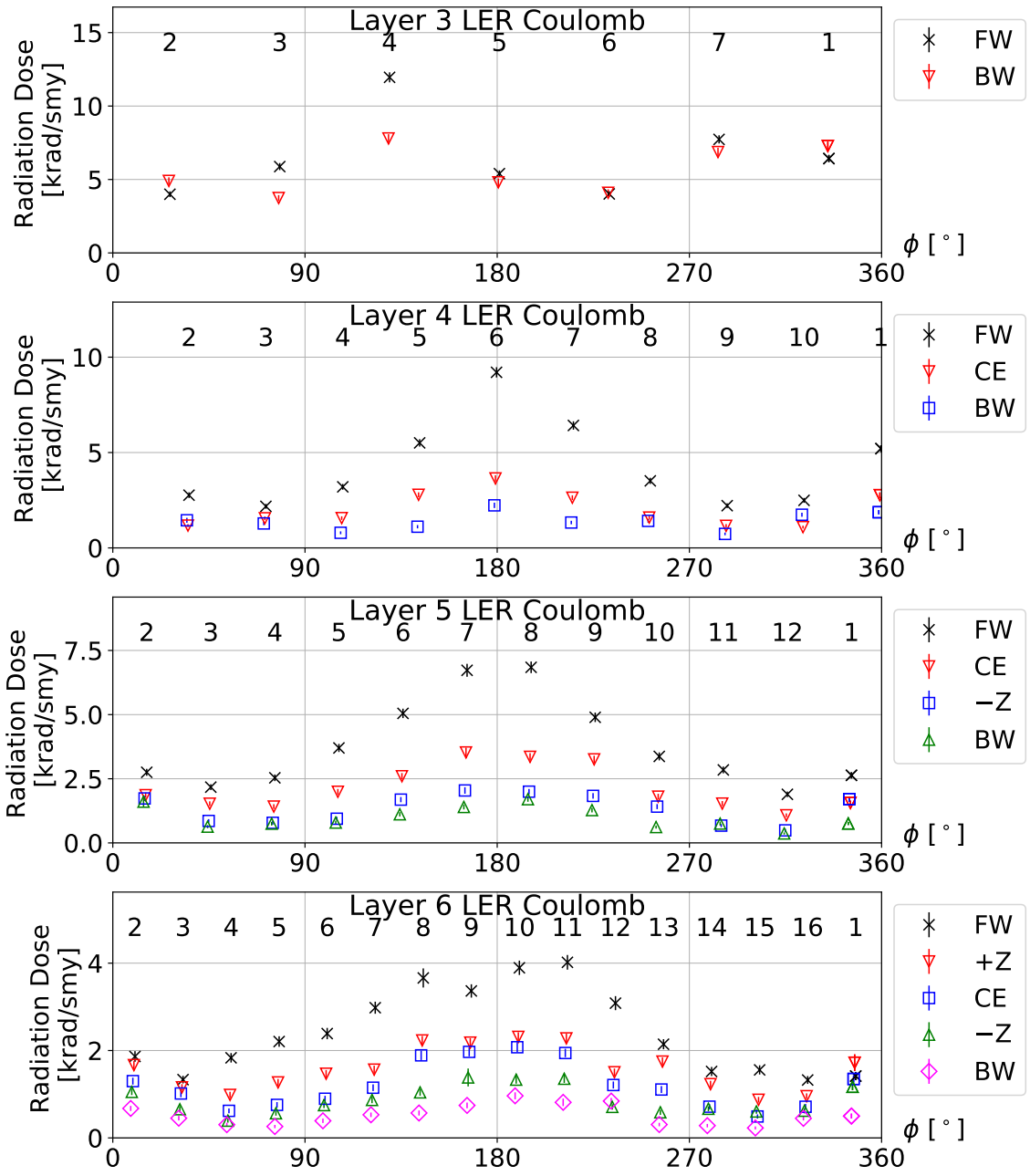

Figure B.24: The azimuthal angle dependence of the radiation dose in the Phase 3 simulation. The radiation dose from LER Coulomb background is plotted for each SVD sensor. The plots are separated by the layers. For each layer, the x-axis shows the azimuthal angle of the center of the sensor. The ladder numbers are shown above the data points. Markers denote the sensor position on the ladder.

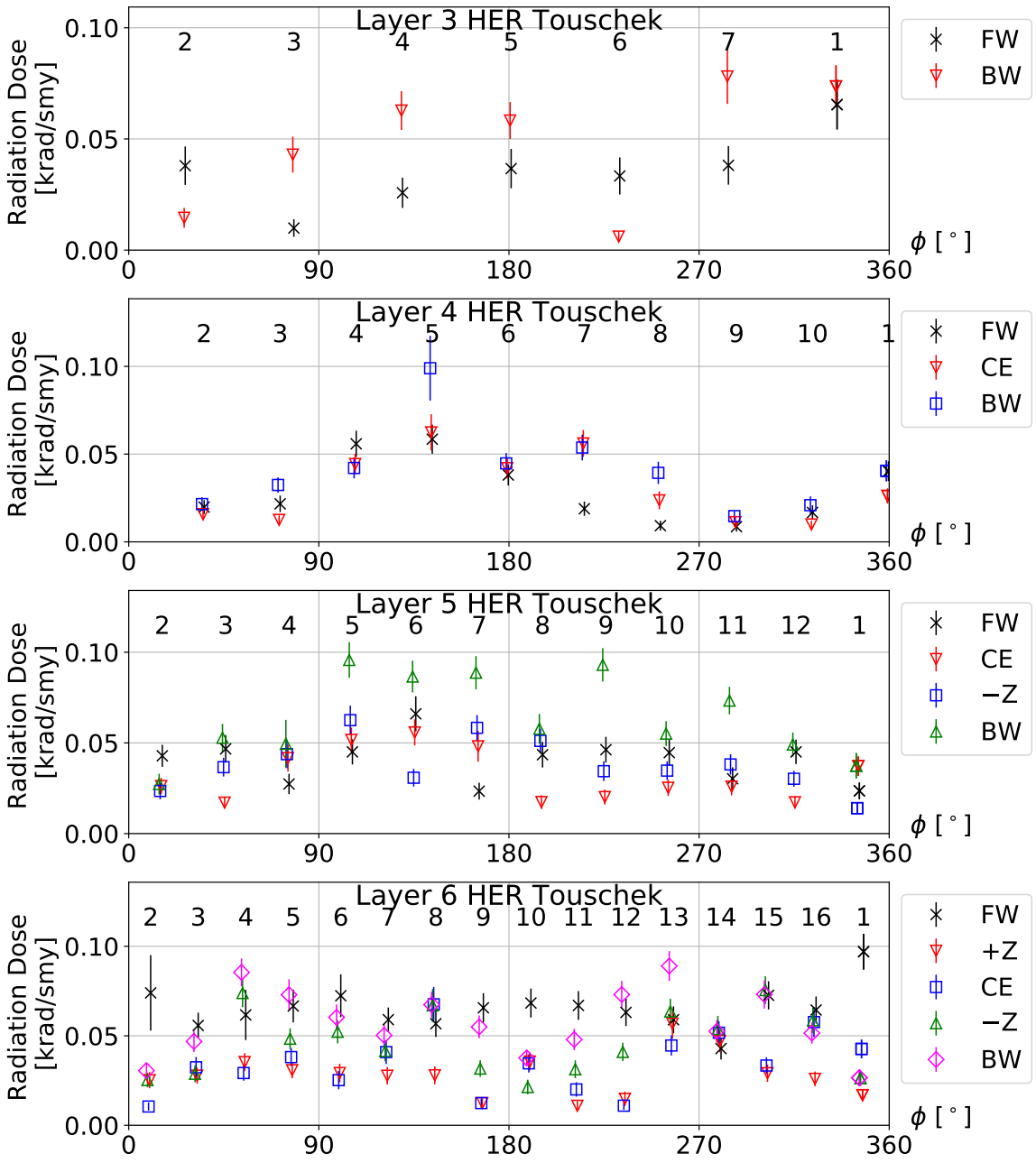

Figure B.25: The azimuthal angle dependence of the radiation dose in the Phase 3 simulation. The radiation dose from HER Touschek background is plotted for each SVD sensor. The plots are separated by the layers. For each layer, the x-axis shows the azimuthal angle of the center of the sensor. The ladder numbers are shown above the data points. Markers denote the sensor position on the ladder.

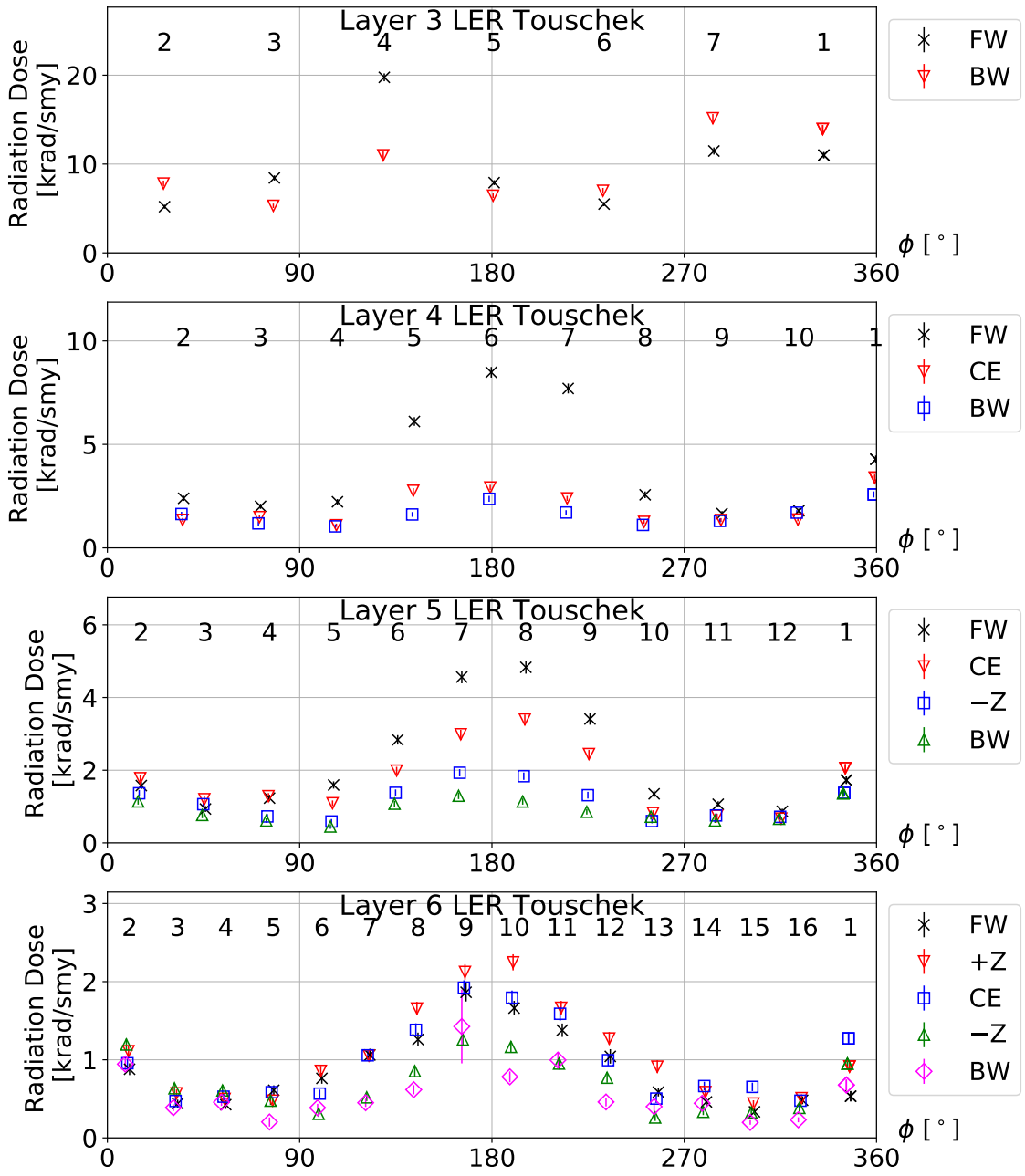

Figure B.26: The azimuthal angle dependence of the radiation dose in the Phase 3 simulation. The radiation dose from LER Touschek background is plotted for each SVD sensor. The plots are separated by the layers. For each layer, the x-axis shows the azimuthal angle of the center of the sensor. The ladder numbers are shown above the data points. Markers denote the sensor position on the ladder.

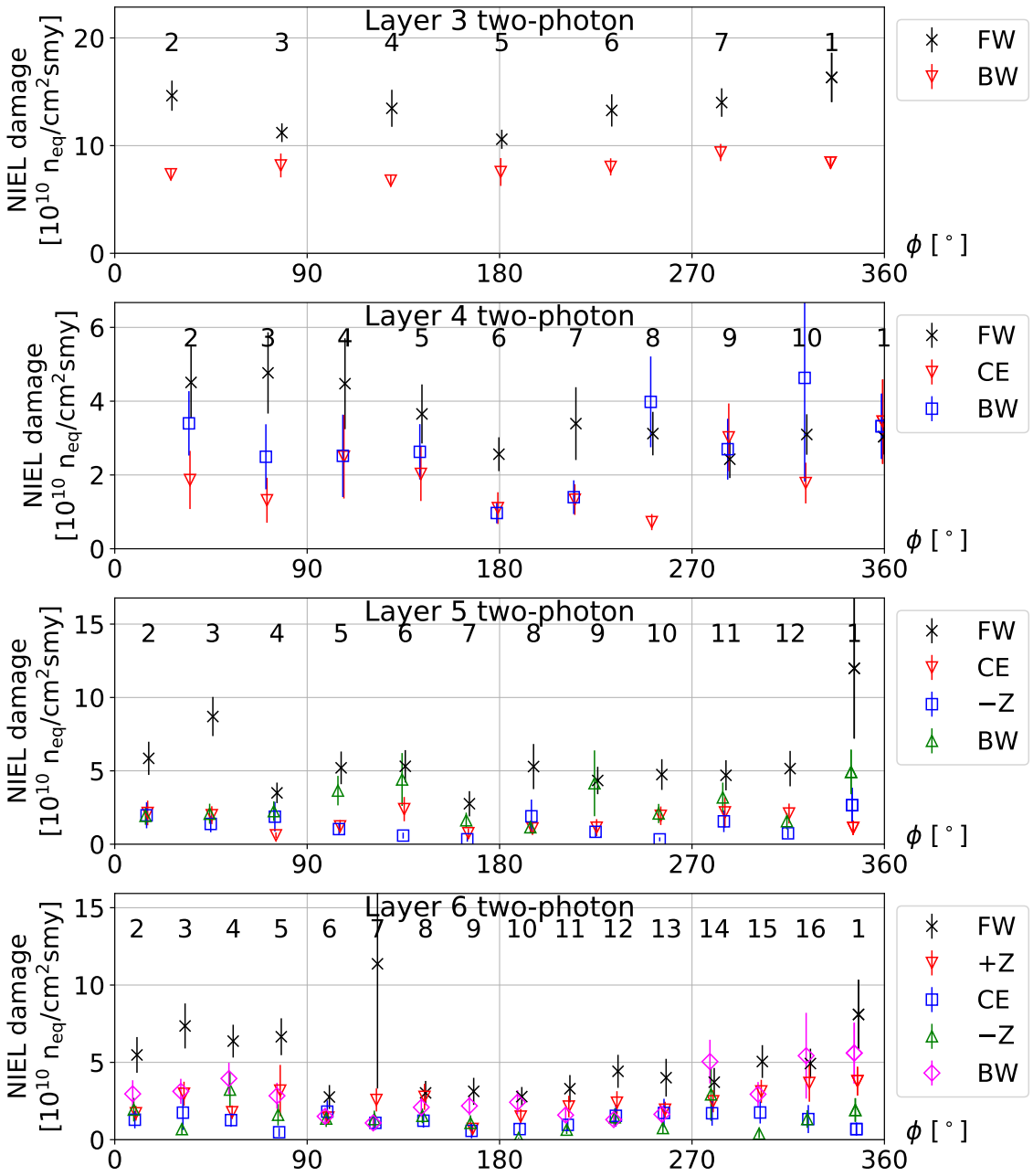

Figure B.27: The azimuthal angle dependence of the NIEL damage in the Phase 3 simulation. The NIEL damage from two-photon background is plotted for each SVD sensor. The plots are separated by the layers. For each layer, the x-axis shows the azimuthal angle of the center of the sensor. The ladder numbers are shown above the data points. Markers denote the sensor position on the ladder.

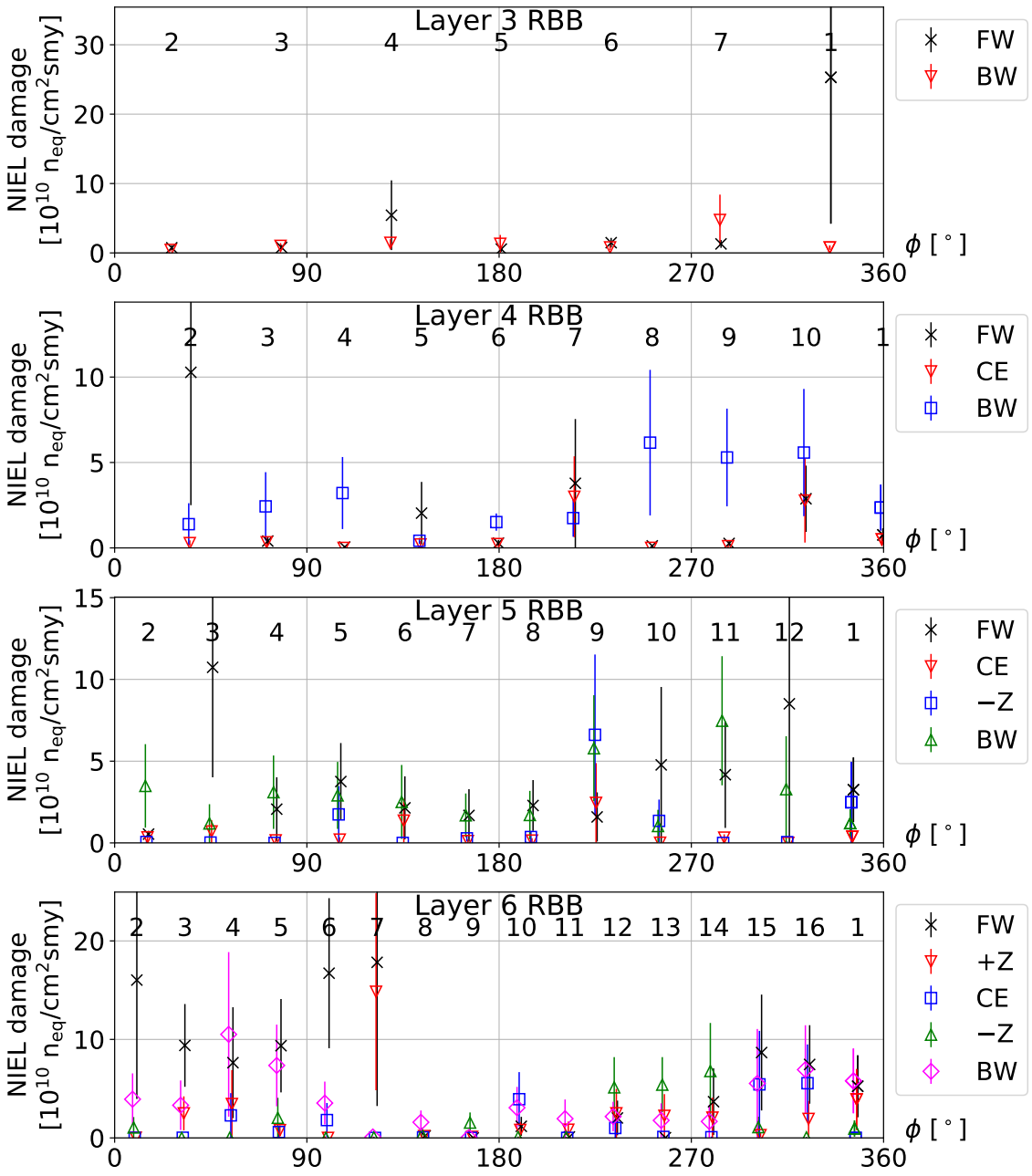

Figure B.28: The azimuthal angle dependence of the NIEL damage in the Phase 3 simulation. The NIEL damage from RBB background is plotted for each SVD sensor. The plots are separated by the layers. For each layer, the x-axis shows the azimuthal angle of the center of the sensor. The ladder numbers are shown above the data points. Markers denote the sensor position on the ladder.

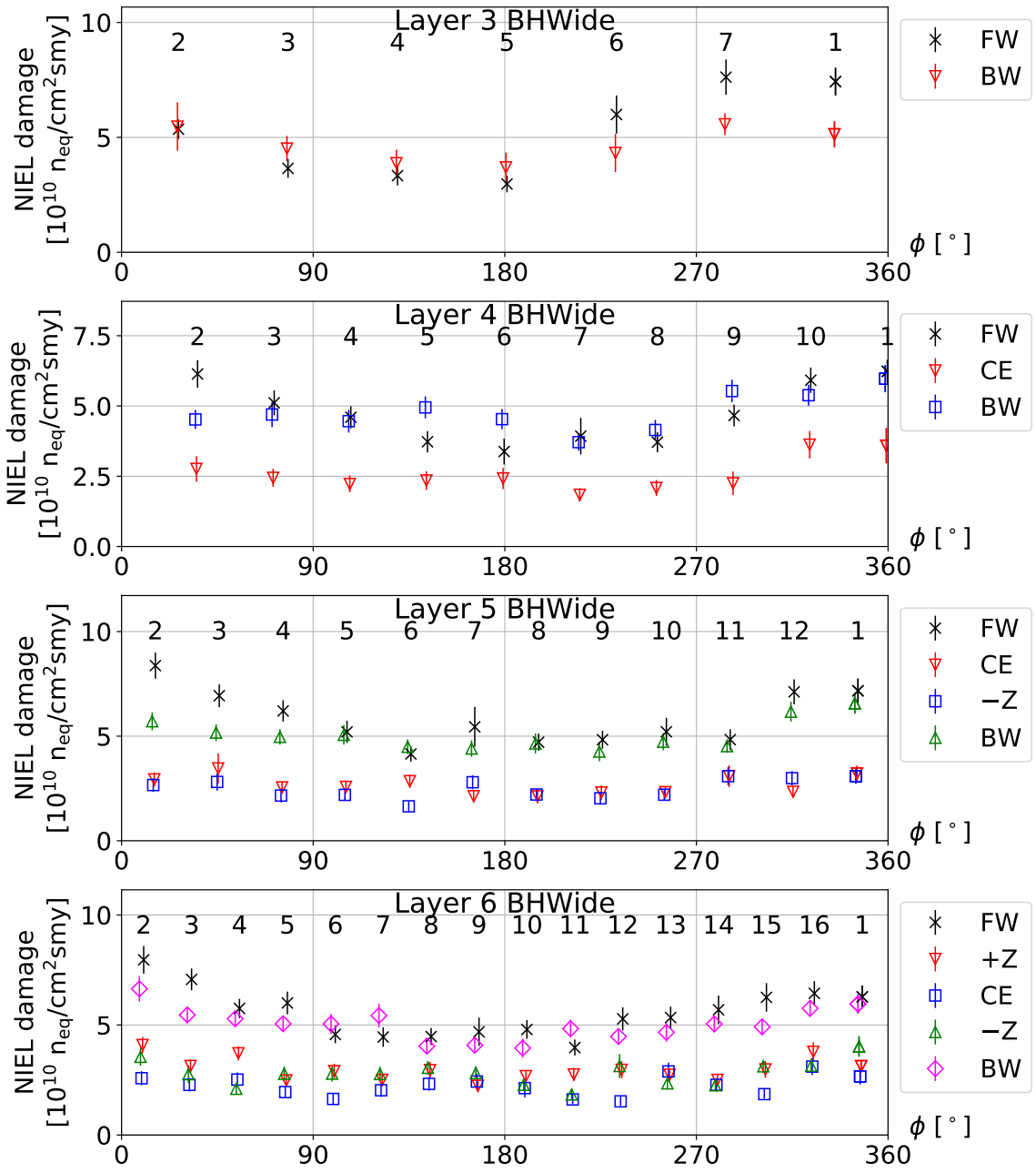

Figure B.29: The azimuthal angle dependence of the NIEL damage in the Phase 3 simulation. The NIEL damage from BHWide background is plotted for each SVD sensor. The plots are separated by the layers. For each layer, the x-axis shows the azimuthal angle of the center of the sensor. The ladder numbers are shown above the data points. Markers denote the sensor position on the ladder.

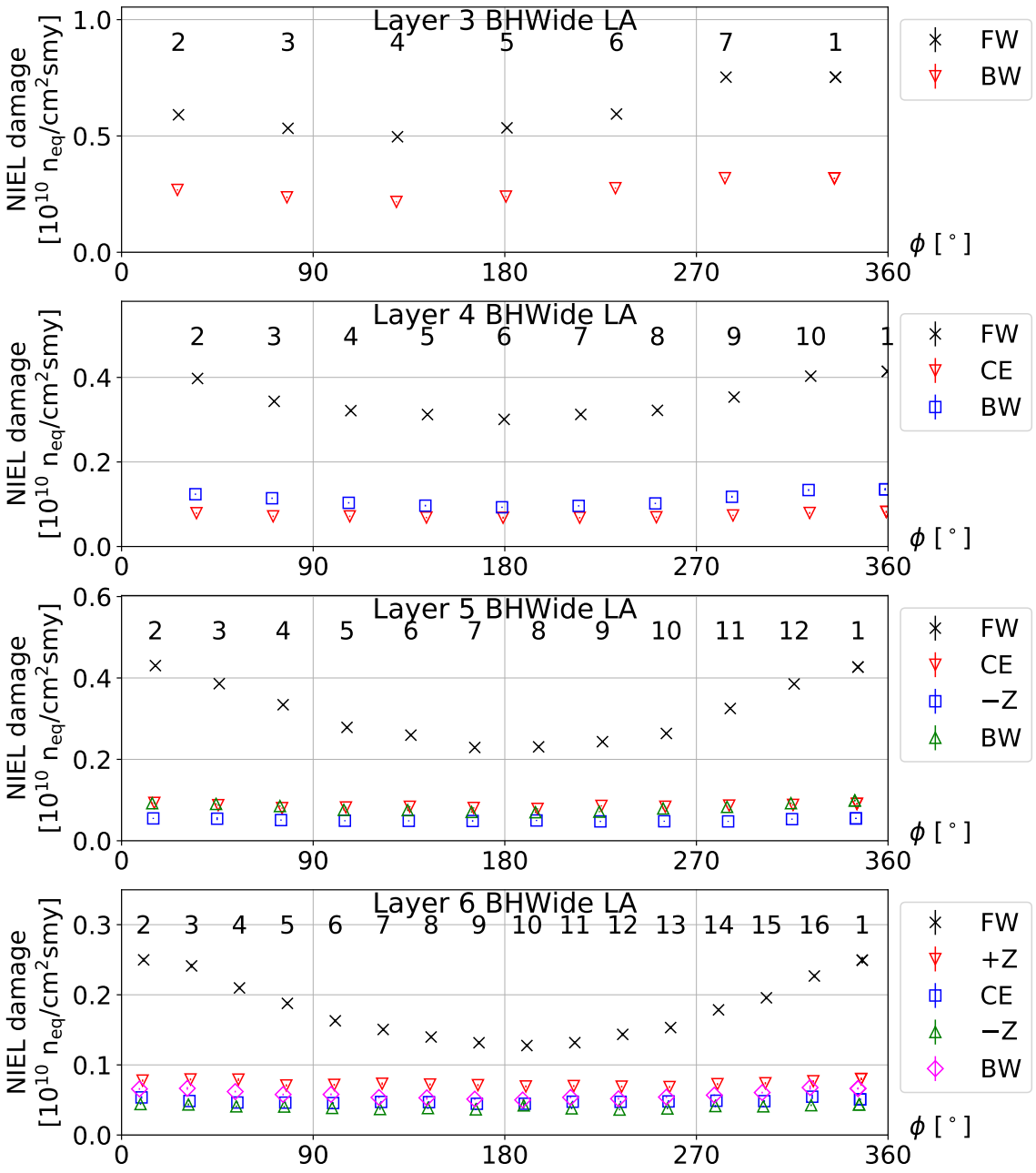

Figure B.30: The azimuthal angle dependence of the NIEL damage in the Phase 3 simulation. The NIEL damage from BHWide LA background is plotted for each SVD sensor. The plots are separated by the layers. For each layer, the x-axis shows the azimuthal angle of the center of the sensor. The ladder numbers are shown above the data points. Markers denote the sensor position on the ladder.

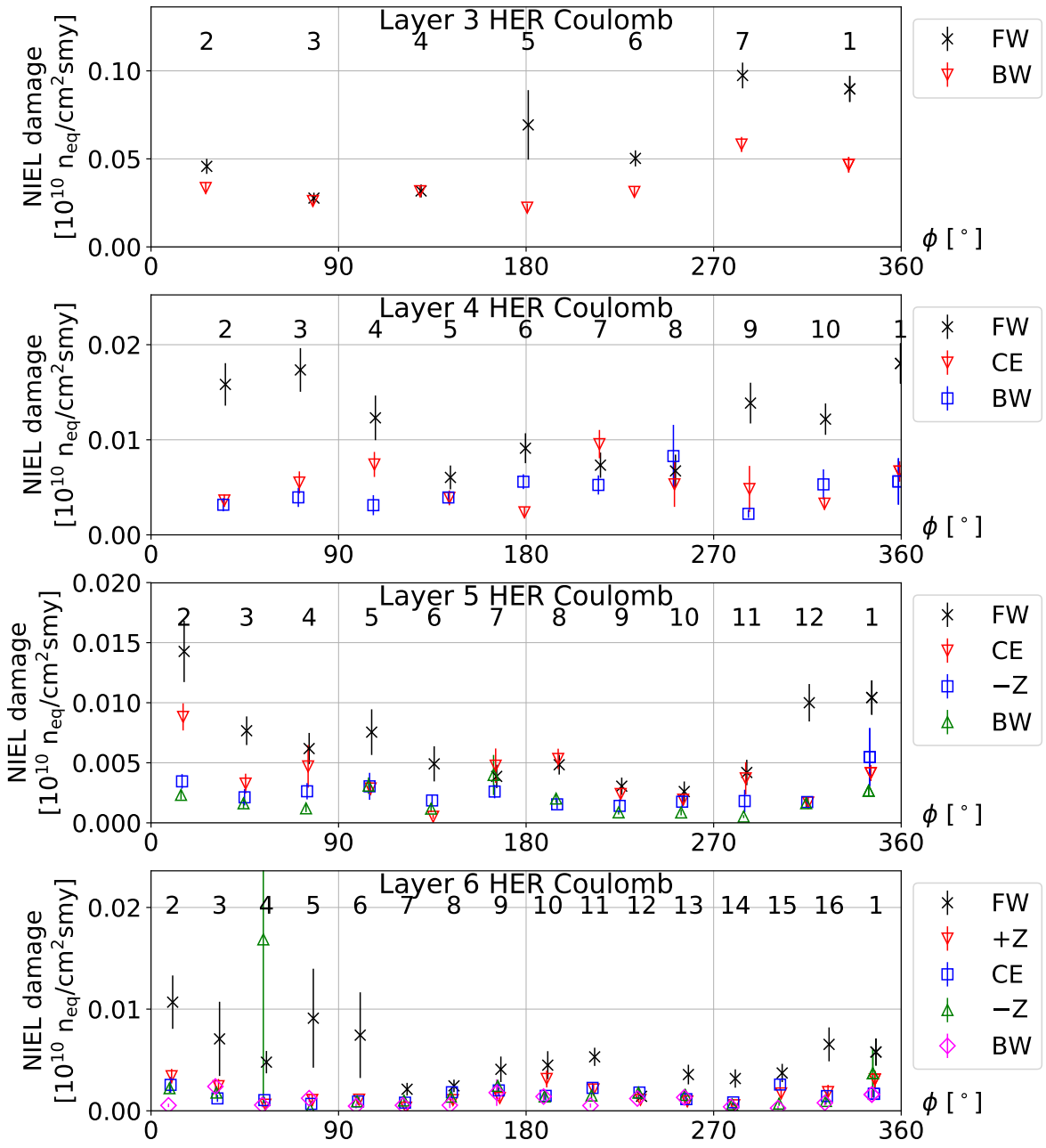

Figure B.31: The azimuthal angle dependence of the NIEL damage in the Phase 3 simulation. The NIEL damage from HER Coulomb background is plotted for each SVD sensor. The plots are separated by the layers. For each layer, the x-axis shows the azimuthal angle of the center of the sensor. The ladder numbers are shown above the data points. Markers denote the sensor position on the ladder.

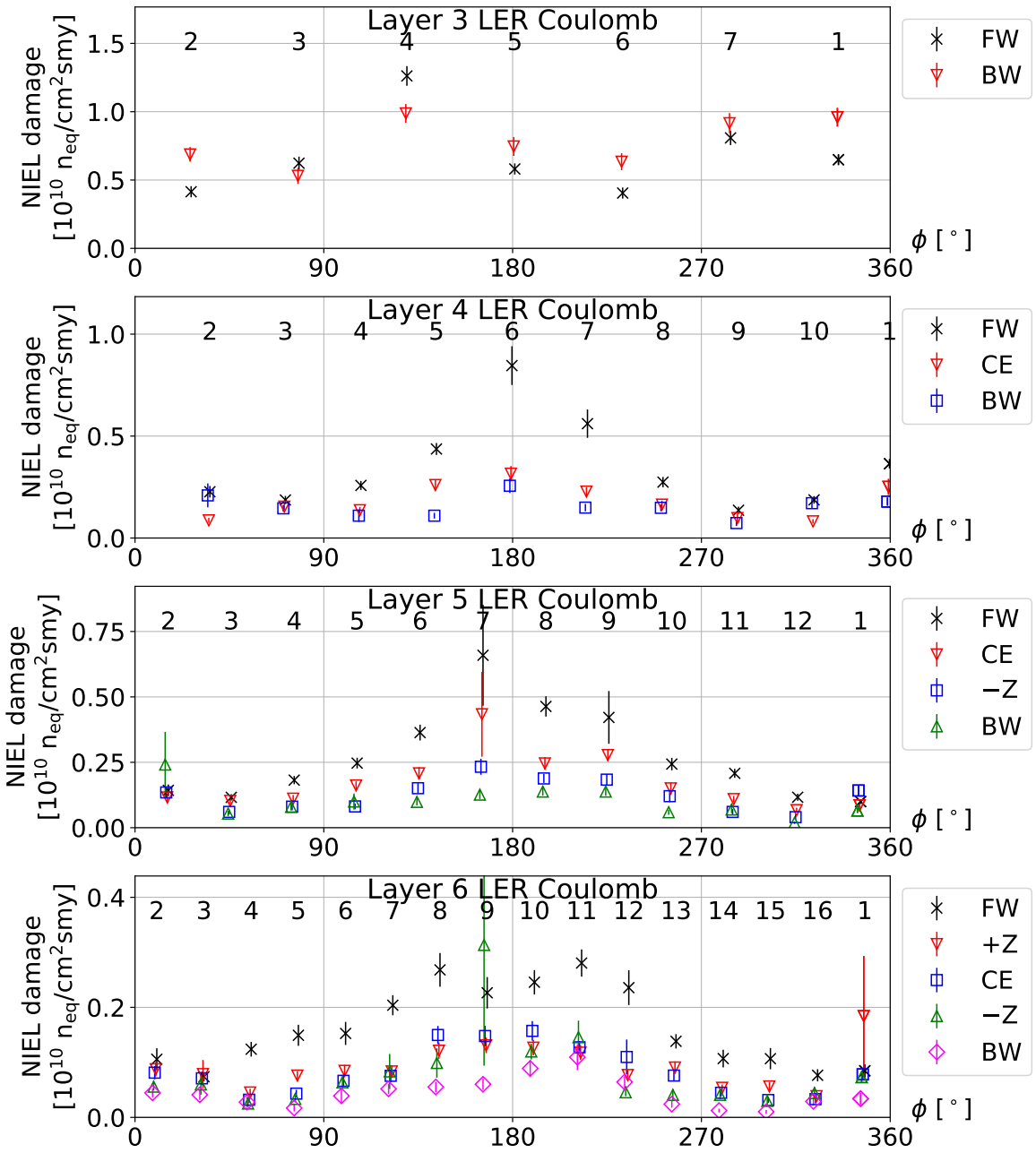

Figure B.32: The azimuthal angle dependence of the NIEL damage in the Phase 3 simulation. The NIEL damage from LER Coulomb background is plotted for each SVD sensor. The plots are separated by the layers. For each layer, the x-axis shows the azimuthal angle of the center of the sensor. The ladder numbers are shown above the data points. Markers denote the sensor position on the ladder.

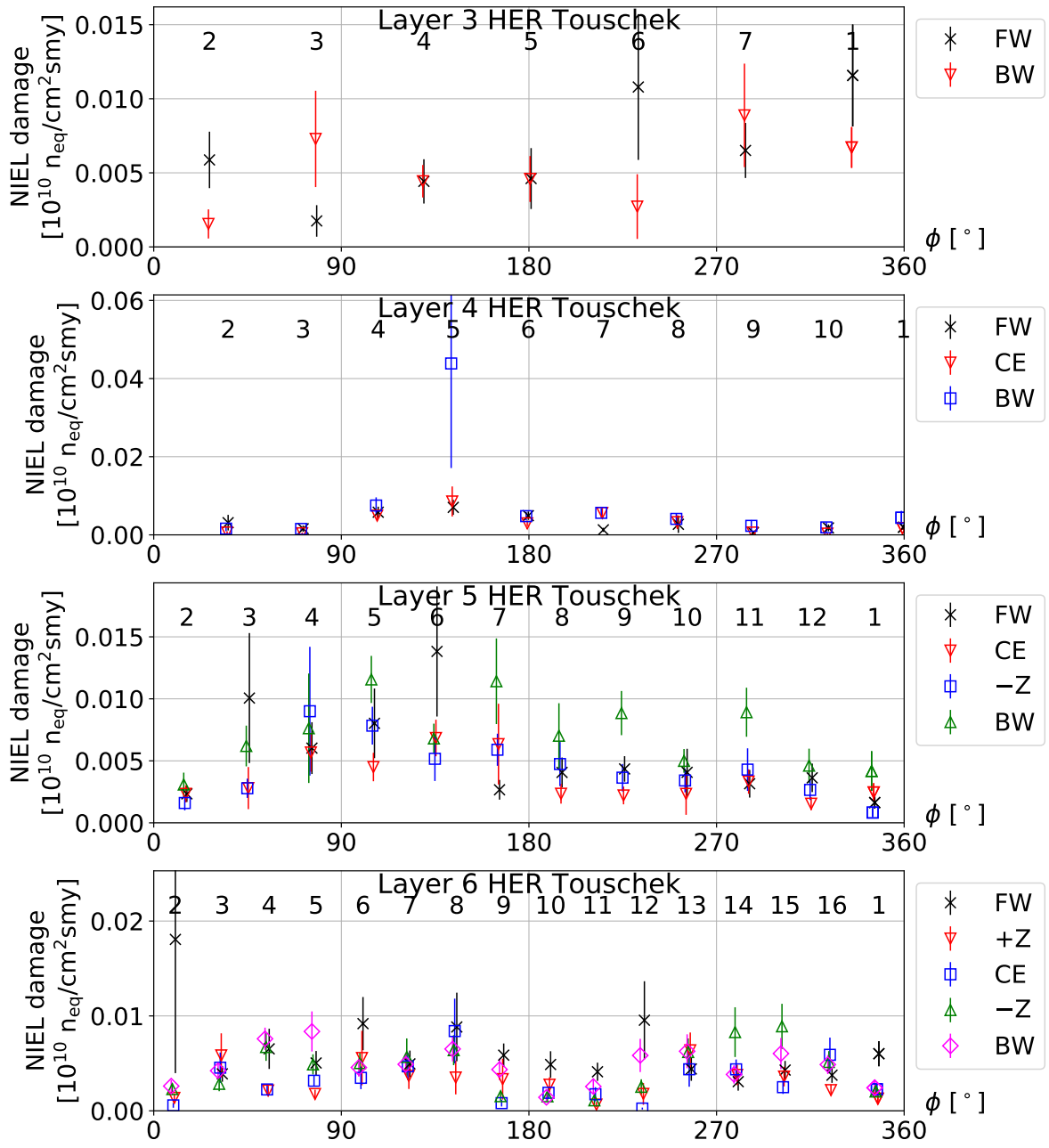

Figure B.33: The azimuthal angle dependence of the NIEL damage in the Phase 3 simulation. The NIEL damage from HER Touschek background is plotted for each SVD sensor. The plots are separated by the layers. For each layer, the x-axis shows the azimuthal angle of the center of the sensor. The ladder numbers are shown above the data points. Markers denote the sensor position on the ladder.

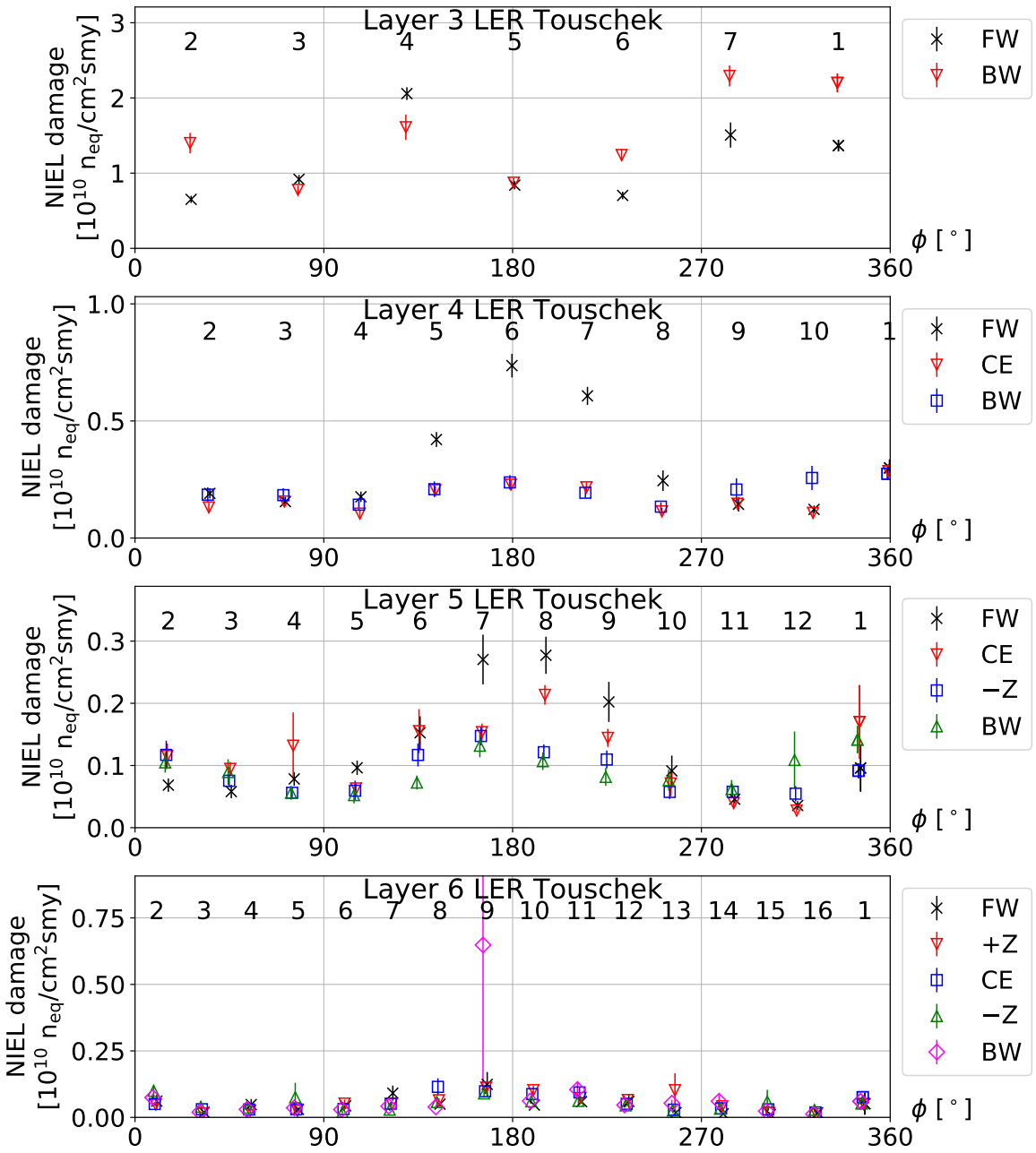

Figure B.34: The azimuthal angle dependence of the NIEL damage in the Phase 3 simulation. The NIEL damage from LER Touschek background is plotted for each SVD sensor. The plots are separated by the layers. For each layer, the x-axis shows the azimuthal angle of the center of the sensor. The ladder numbers are shown above the data points. Markers denote the sensor position on the ladder.

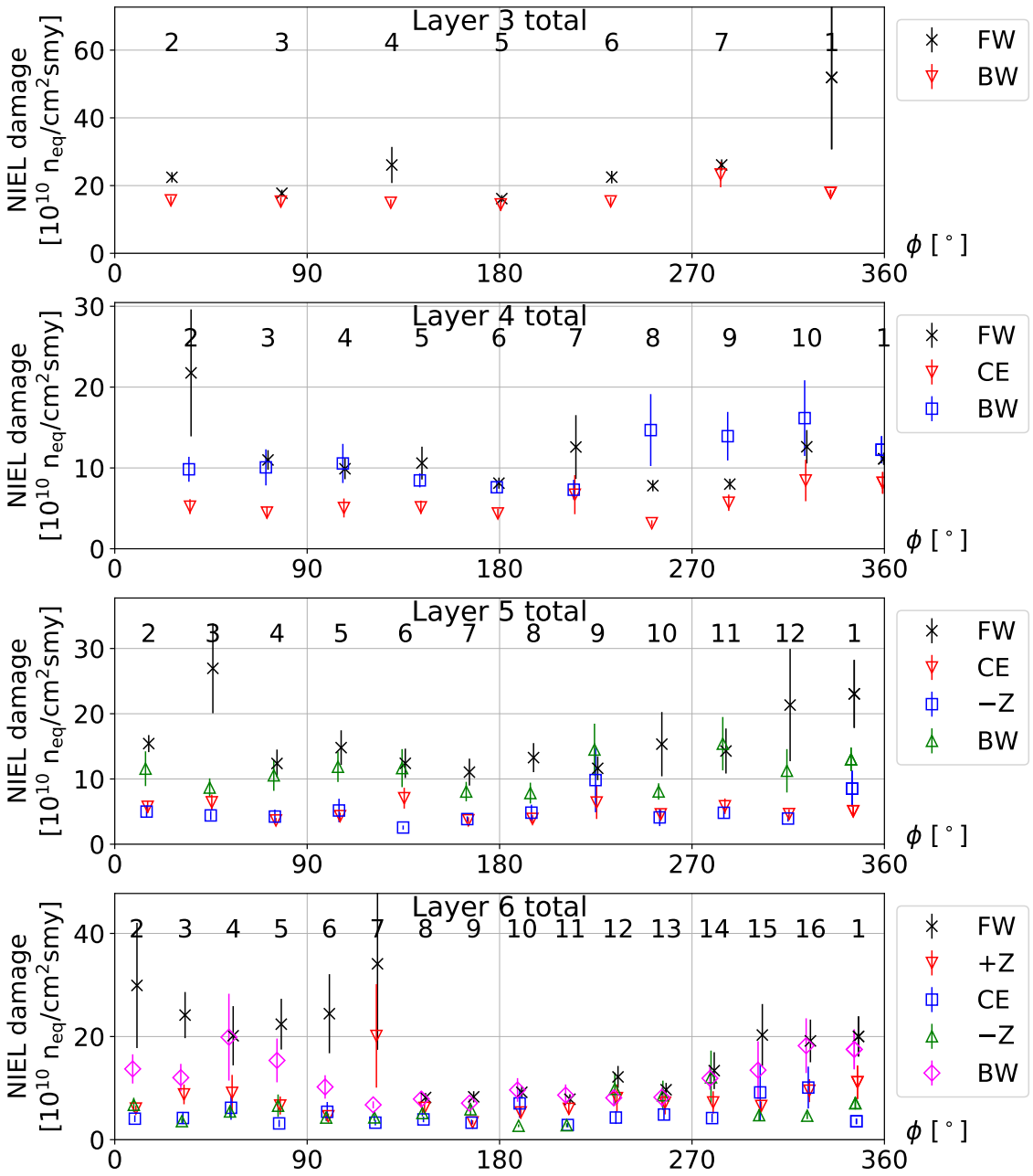

Figure B.35: The azimuthal angle dependence of the NIEL damage in the Phase 3 simulation. The total NIEL damage is plotted for each SVD sensor. The plots are separated by the layers. For each layer, the x-axis shows the azimuthal angle of the center of the sensor. The ladder numbers are shown above the data points. Markers denote the sensor position on the ladder.

Appendix C

The result of the Phase 3 beam background estimation

We show the result of the Phase 3 background estimation described in Section 7.7 about the L4–6 sensors. In the following figures, the background rates (U and V side occupancy, radiation dose, and NIEL damage) are plotted for each sensor, which name is denoted by the x-axis. The contributions from different background sources are plotted in different colors denoted by the legend. The shown errors do not include the errors of the scale factors and originate from only the statistical errors of the Phase 3 simulation. The red dotted lines denote the acceptable background rates.

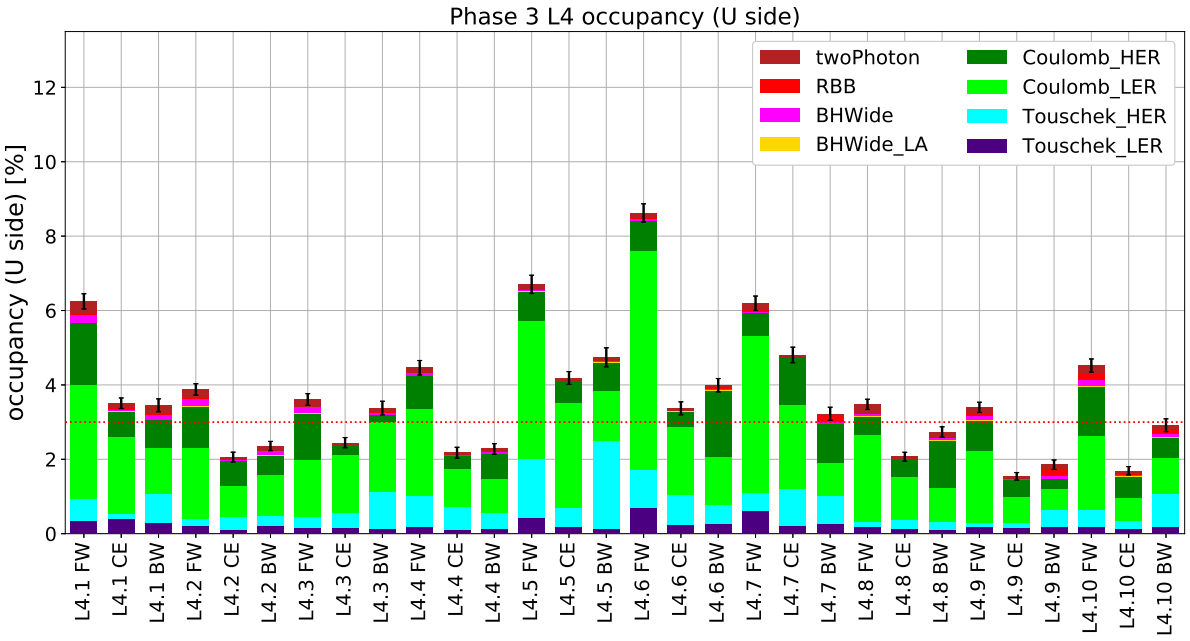

Figure C.1: The Phase 3 U side occupancy in the L4 sensors. The Phase 3 simulation is corrected by the Phase 2 observation.

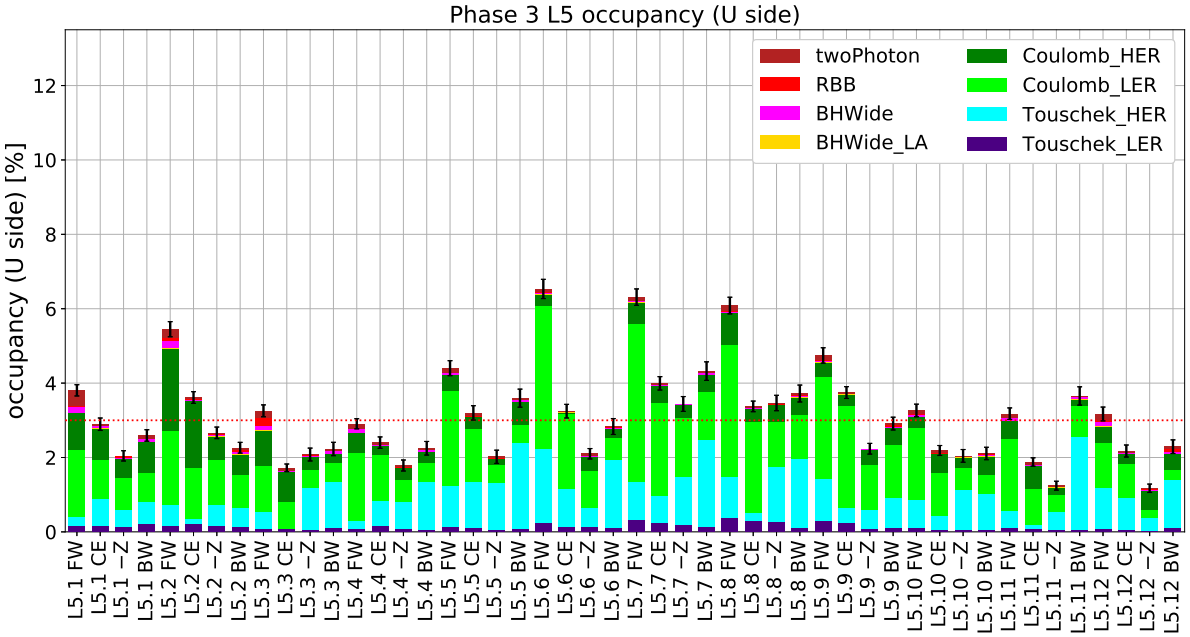

Figure C.2: The Phase 3 U side occupancy in the L5 sensors. The Phase 3 simulation is corrected by the Phase 2 observation.

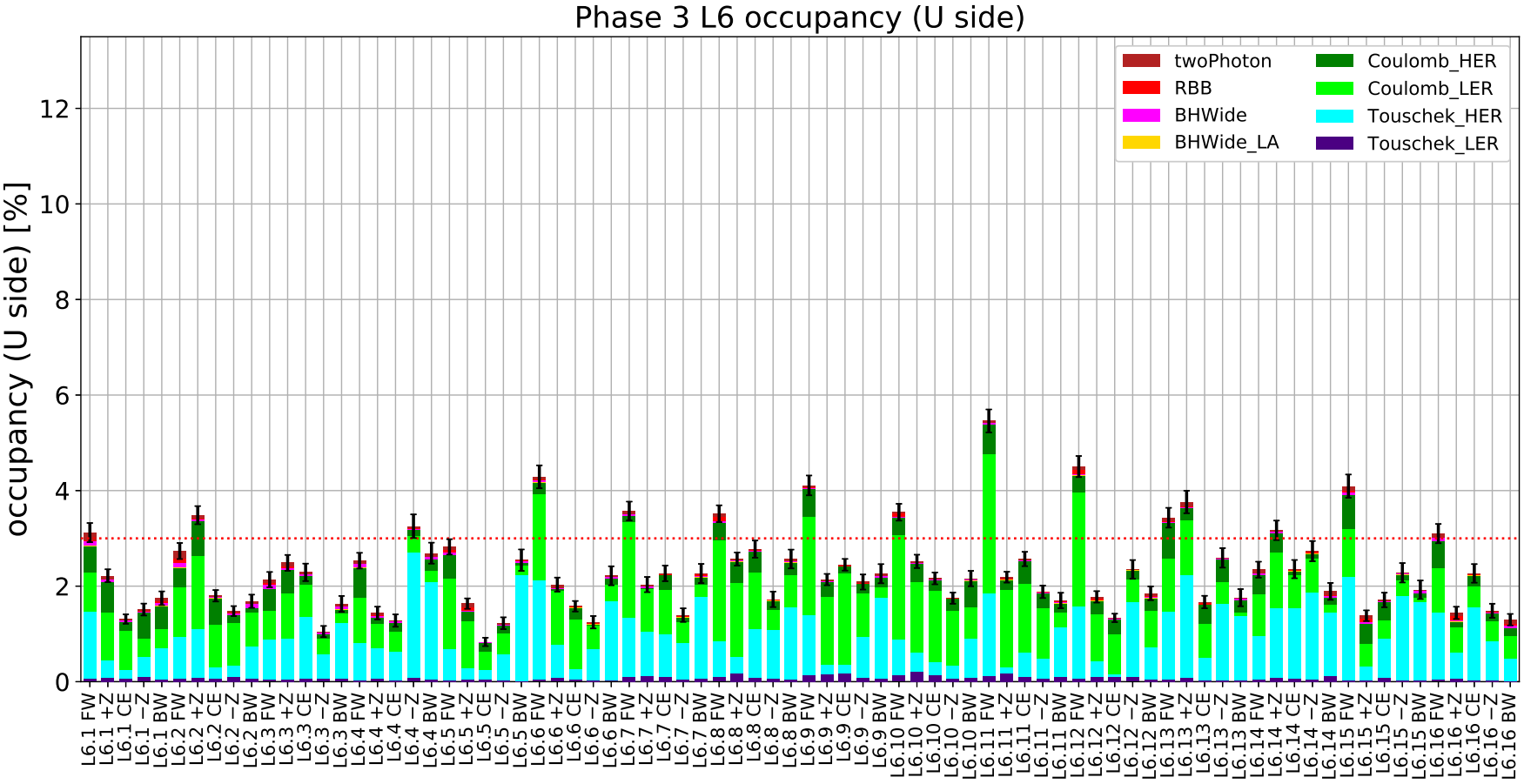

Figure C.3: The Phase 3 U side occupancy in the L6 sensors. The Phase 3 simulation is corrected by the Phase 2 observation.

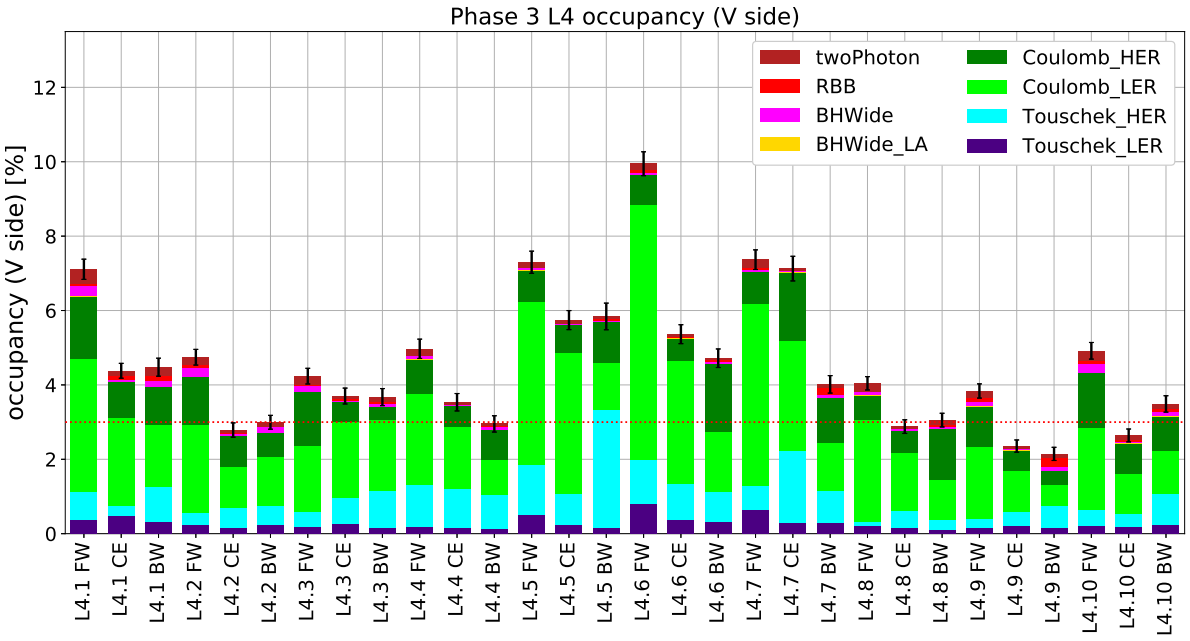

Figure C.4: The Phase 3 V side occupancy in the L4 sensors. The Phase 3 simulation is corrected by the Phase 2 observation.

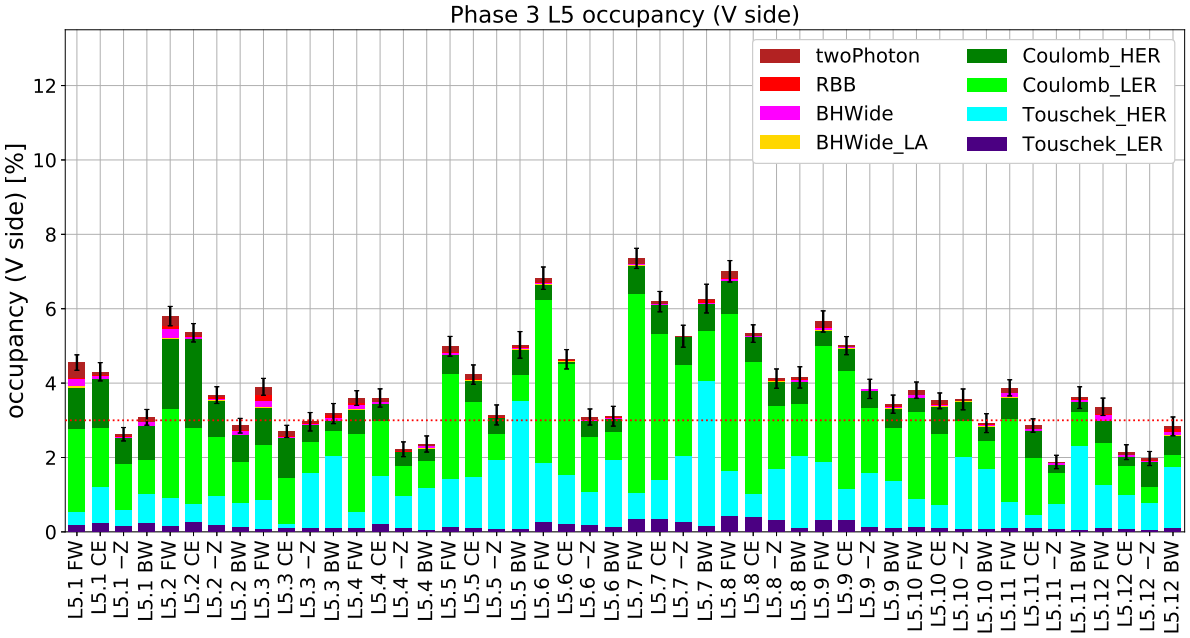

Figure C.5: The Phase 3 V side occupancy in the L5 sensors. The Phase 3 simulation is corrected by the Phase 2 observation.

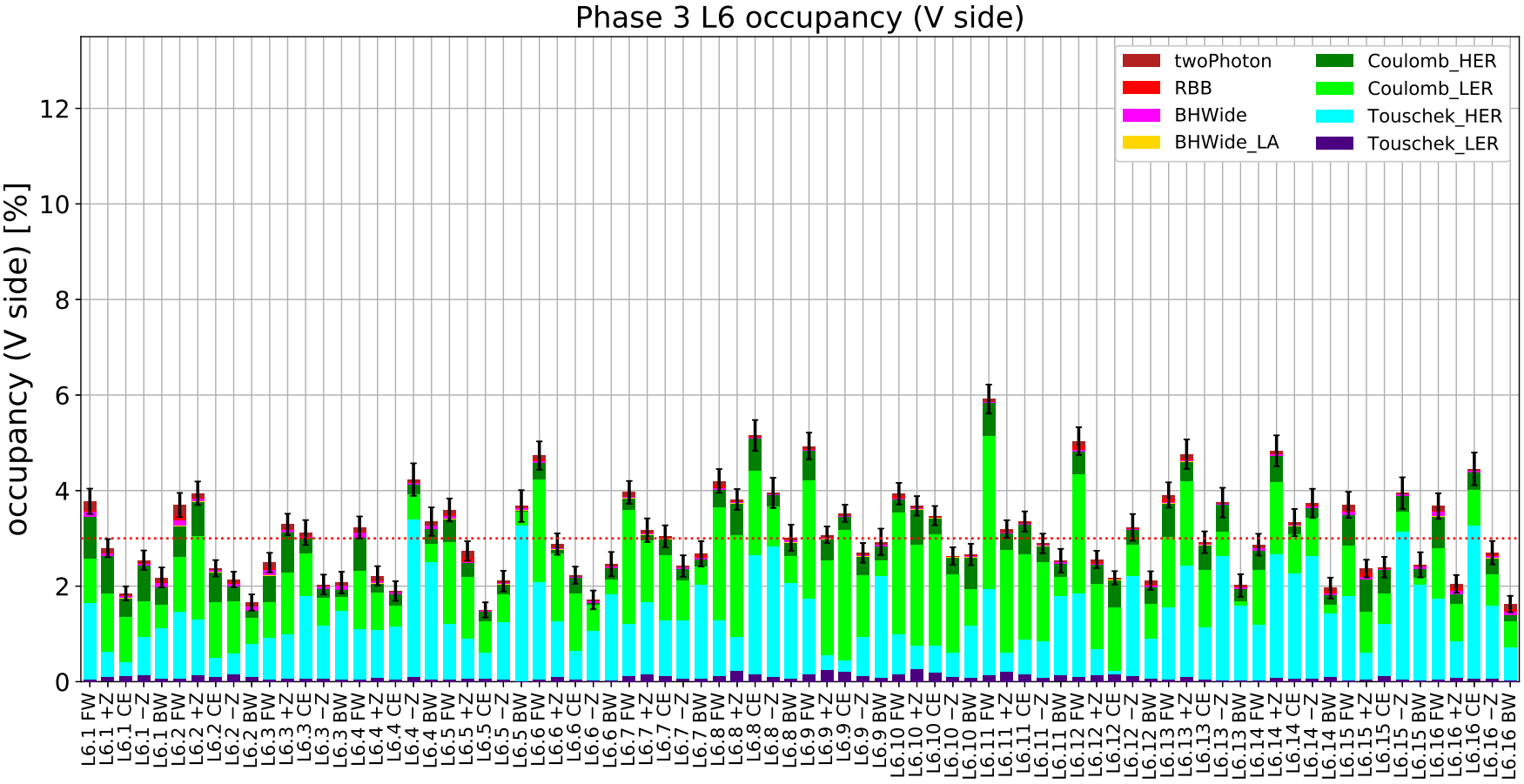

Figure C.6: The Phase 3 V side occupancy in the L6 sensors. The Phase 3 simulation is corrected by the Phase 2 observation.

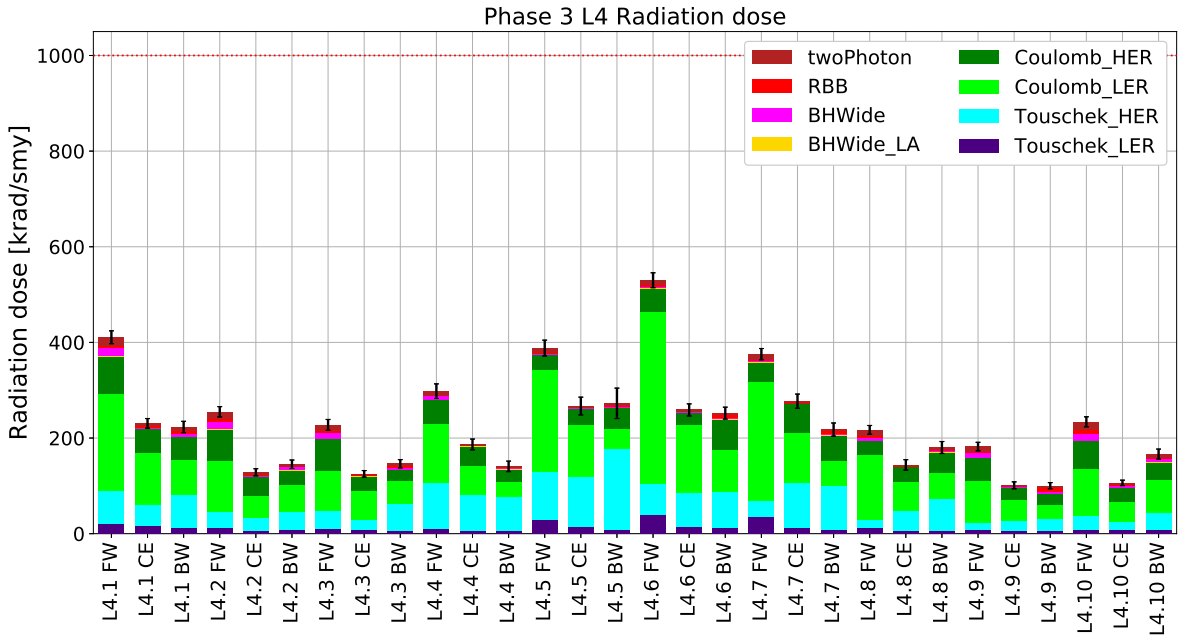

Figure C.7: The Phase 3 radiation dose in the L4 sensors. The Phase 3 simulation is corrected by the Phase 2 observation.

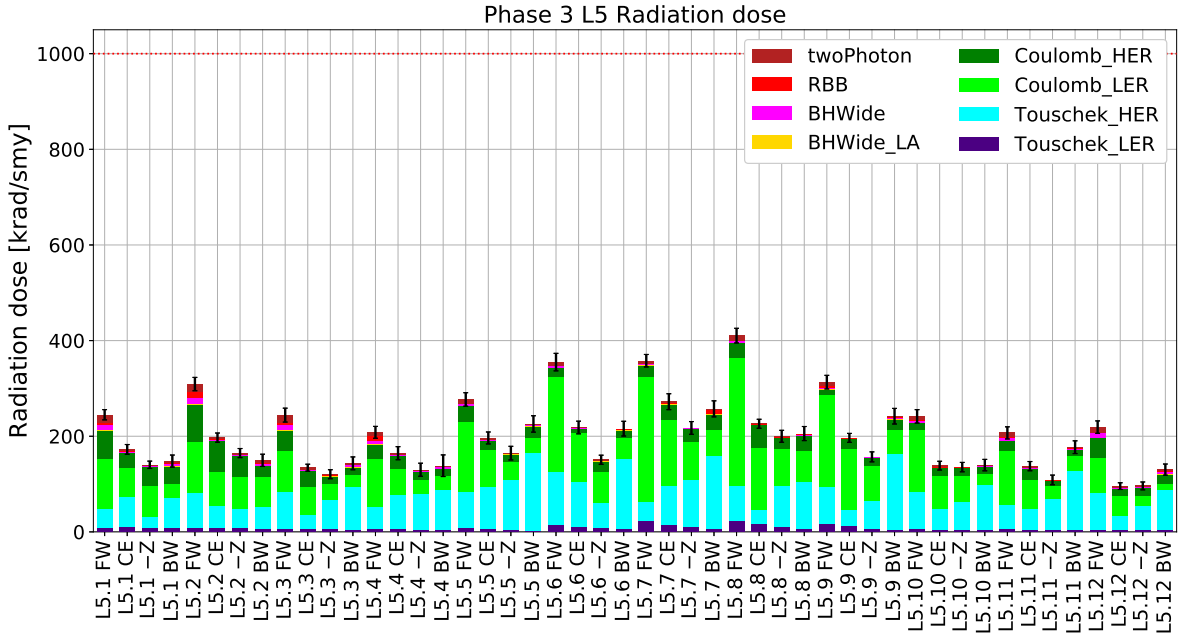

Figure C.8: The Phase 3 radiation dose in the L5 sensors. The Phase 3 simulation is corrected by the Phase 2 observation.

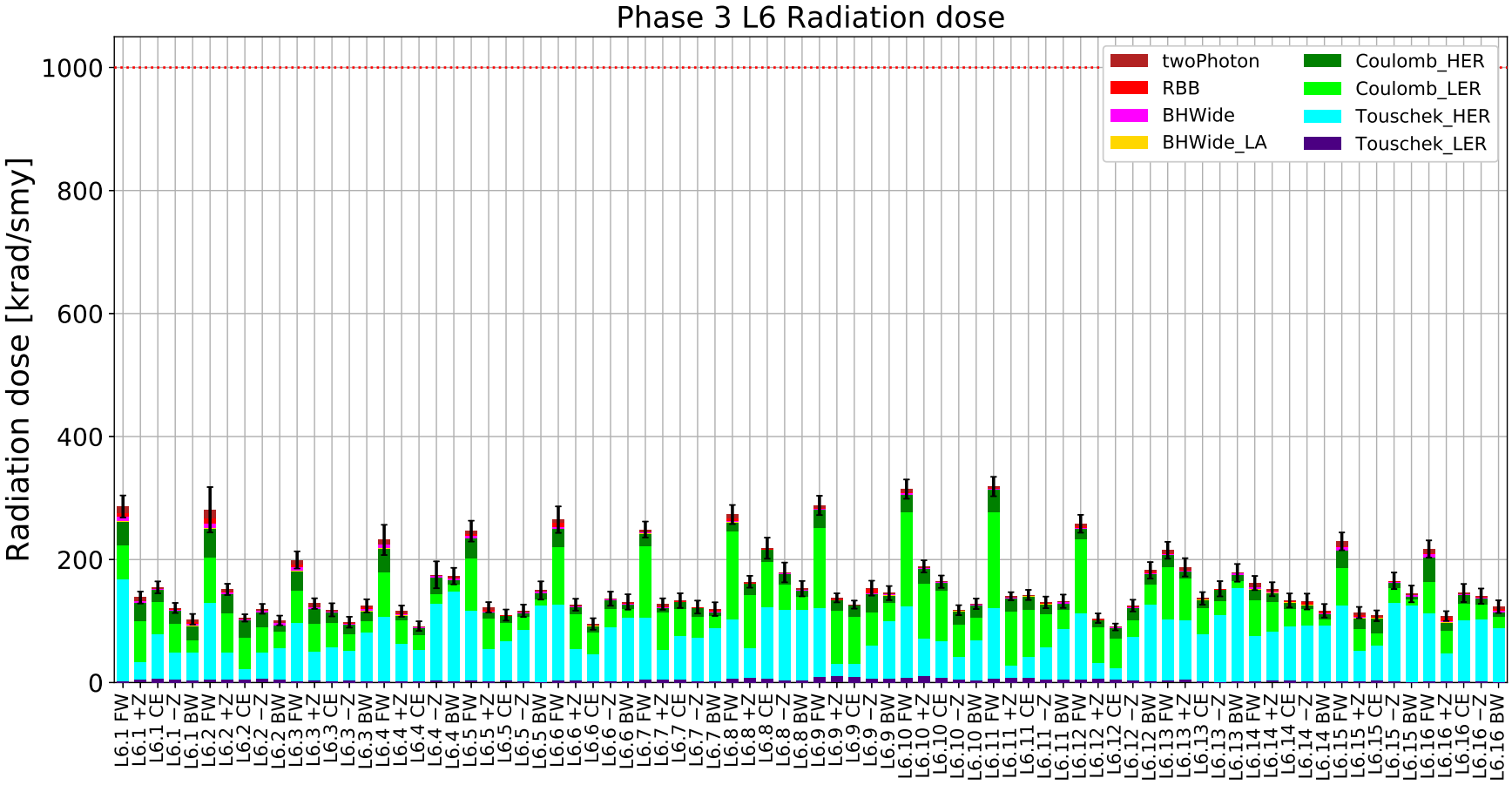

Figure C.9: The Phase 3 radiation dose in the L6 sensors. The Phase 3 simulation is corrected by the Phase 2 observation.

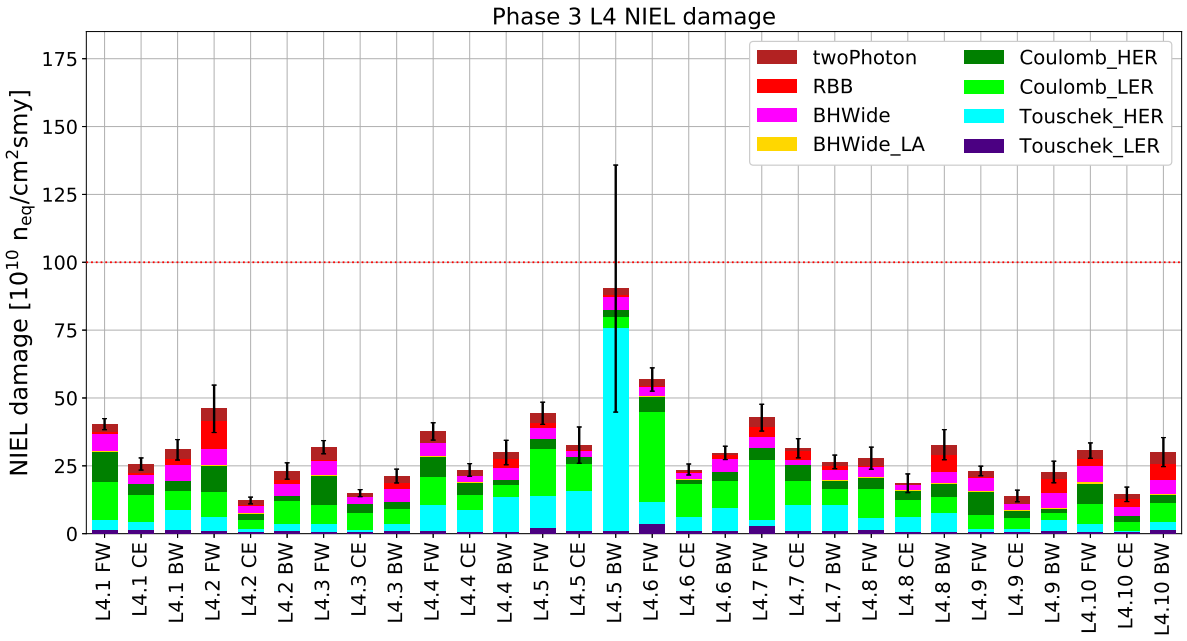

Figure C.10: The Phase 3 NIEL damage in the L4 sensors. The Phase 3 simulation is corrected by the Phase 2 observation.

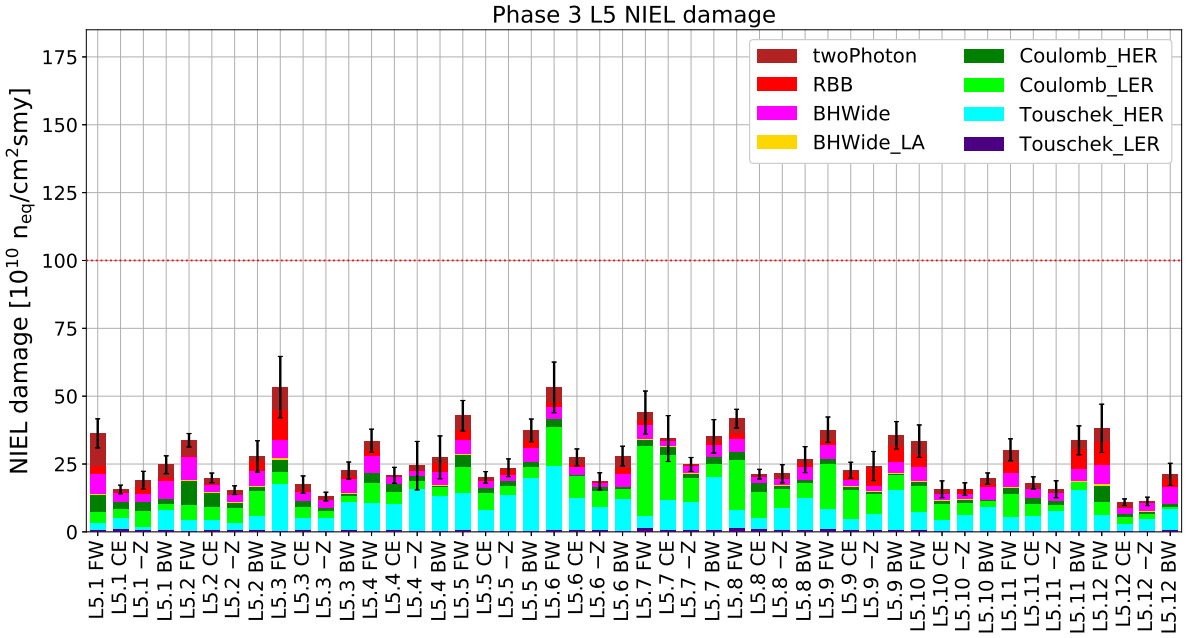

Figure C.11: The Phase 3 NIEL damage in the L5 sensors. The Phase 3 simulation is corrected by the Phase 2 observation.

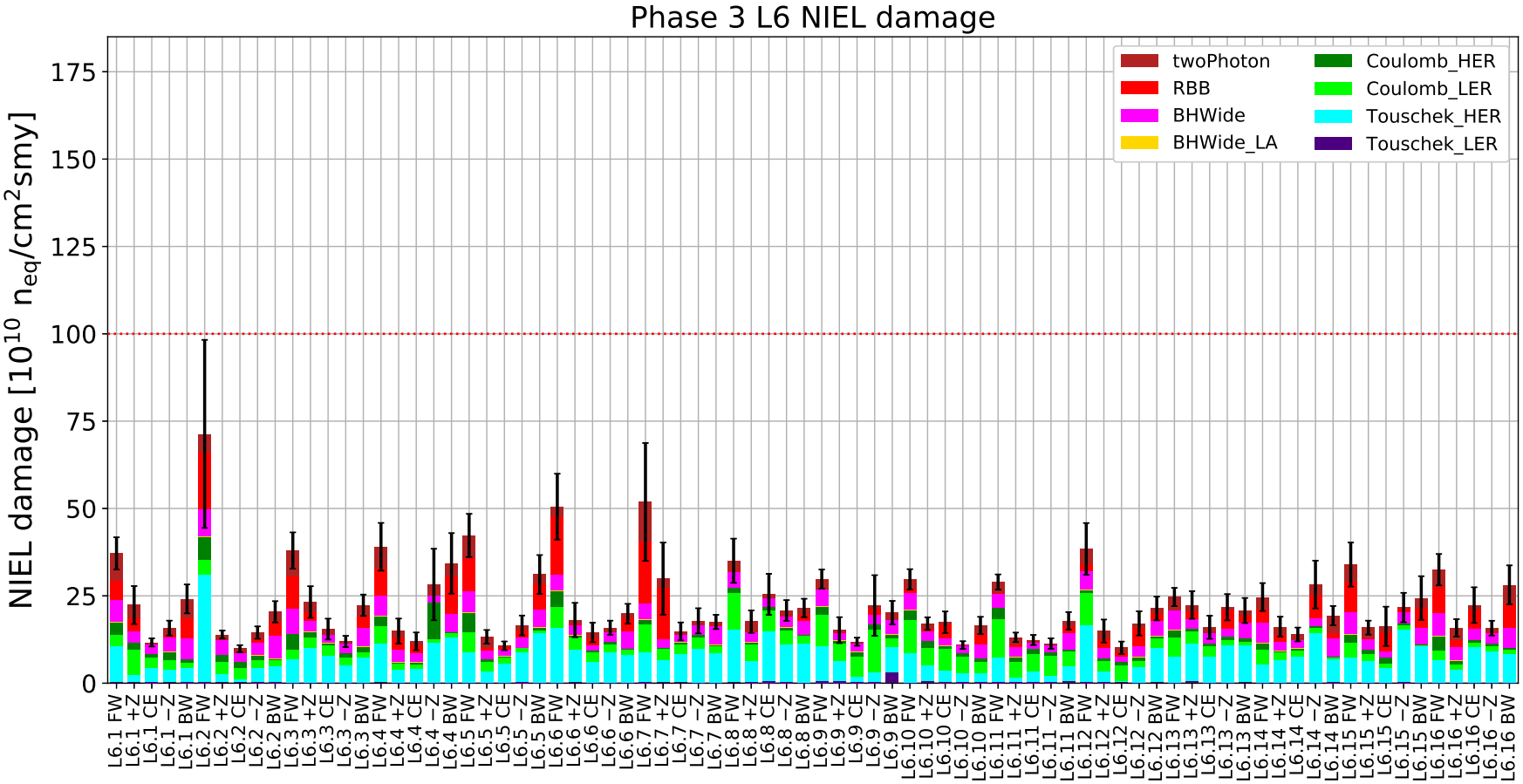

Figure C.12: The Phase 3 NIEL damage in the L6 sensors. The Phase 3 simulation is corrected by the Phase 2 observation.

Acknowledgment

I would first like to thank my supervisor, Prof. Yutaka Ushiroda, for offering me the opportunity to participate in the Belle II experiment and encouragement for my work.

I would also like to thank Dr. Katsuro Nakamura, Dr. Toru Tsuboyama, Dr. Koji Hara, Dr. Takeo Higuchi, Dr. Yoshiyuki Onuki and all the collegues in the SVD group, for spending their precious time to help me with their knowledge and experience.

I am deeply grateful to Dr. Hiroyuki Nakayama and the BEAST group for fruitful discussions about the beam background studies. I am also grateful to Prof. Mikihiko Nakao and the DAQ group for their cooperation which was essential for the development of the trigger veto module.

I would like to acknowledge Dr. Taku Gunji and Dr. Yasuyuki Okumura as the vice committees of this thesis and I am gratefully indebted to them for their valuable comments on the thesis. Also I would like to thank Dr. Zachary Liptak for kindly proofreading my poor English.

I would like to thank K. Nakamura, T. Tsuboyama, K. Hara, Yuma Uematsu, Ryohei Sugiura, and Nobuhiko Sato, who all have made my life in Tsukuba comfortable.

Finally, I would like to thank my family for their endless support.

Bibliography

[1] E. Kou et al., "The Belle II Physics book", arXiv:1808.10567.

[2] M. Tanabashi et al. (Particle Data Group), "The Review of Particle Physics (2018)", Phys. Rev. D 98, 030001 (2018).

[3] A. G. Akeroyd et al. [SuperKEKB Physics Working Group], "Physics at Super B Factory", hep-ex/0406071.

[4] P. M. Lewis et al., "First Measurements of Beam Backgrounds at SuperKEKB", Nuclear Instruments and Methods in Physics Research Section A: Accelerators, Spectrometers, Detectors and Associated Equipment, ISSN: 0168-9002 (2018)

[5] http://www.prisma.uni-mainz.de/Illustrationen/08_kernphysik_superkekb.jpg

[6] Kazunori Akai, Kazuro Furukawa, Haruyo Koiso, "SuperKEKB collider", Nuclear Instruments and Methods in Physics Research Section A: Accelerators, Spectrometers, Detectors and Associated Equipment, Volume 907, 2018, Pages 188-199, ISSN 0168-9002, https://doi.org/10.1016/j.nima.2018.08.017.

[7] Y. Iwasaki, et al., "Level 1 trigger system for the Belle II experiment", IEEE Transactions on Nuclear Science, vol. 58, no. 4 PART 1, 5740389, pp. 1807-1815.

[8] Abe, T. et al., "Belle II Technical Design Report',' Tech. Rep. KEK REPORT2010-1, KEK, edited by: Z.Doležal and S.Uno (Nov 2010)

[9] J. Kandra.

[10] M. French, et al., "Design and results from the APV25, a deep sub-micron CMOS front-end chip for the CMS tracker", Nucl. Instr. and Meth. A, 466 (2001)

[11] M.Raymond, "APV25-S0 Analogue Test Results, December 1999"

[12] T. Kuhr, et al., "The Belle II Core Software", arxiv:1809.04299 [physics.comp-ph]

[13] G. Bassi, "Radiation monitor with diamond sensors for the Belle II experiment at SuperKEKB,"

[14] K. Nakamura, et al., "Development of a Data Acquisition System for the Belle II Silicon Vertex Detector", PoS(TIPP2014)198

[15] M. Matsumoto and T. Nishimura, "Mersenne twister: a 623-dimensionally equidistributed uniform pseudo-random number generator", ACM Trans. Model. Comput. Simul. 8, 1 (January 1998), 3-30. DOI: https://doi.org/10.1145/272991.272995

[16] Document about Data Quality Monitor for data taking shift in the Belle experiment.

[17] T. Lück, Private communication.

[18] G. Lutz, "Semiconductor Radiation Detector", Springer, 2nd edition (1999).

[19] Valentan, M. (2013), "The Silicon Vertex Detector for b-tagging at Belle II", Bibliographic information available from INIS: http://inis.iaea.org/search/search.aspx?orig_q=RN:46127226; Available from Vienna University of Technology Library, Resselgasse 4, 1040 Vienna (AT) and available from http://www.ub.tuwien.ac.at/diss/AC11413158.pdf

[20] Araldite 2011 data sheet, http://www.dawex.cz/userFiles/technicke-listy/huntsman/araldite-2011.pdf.

[21] F. Guarino, C. Hauviller and M. Tavlet, "Compilation of radiation damage test data. 4. Adhesives," CERN-2001-006.

[22] T. Kondo, "Radiation damage status of the ATLAS silicon strip detectors", 11th International "Hiroshima" Symposium on the Development and Application of Semiconductor Tracking Detectors.

[23] http://acc-physics.kek.jp/SAD/

[24] F.A. Berends, et al., "Complete lowest-order calculations for four-lepton final states in electron-positron collisions", Nuclear Physics B, Volume 253, 1985, Pages 441-463

[25] R. Kleiss, et al, "BBBREM — Monte Carlo simulation of radiative Bhabha scattering in the very forward direction", Computer Physics Communications, Volume 81, Issue 3, 1994, Pages 372-380,

[26] S. Jadach, et al., "BHWIDE 1.00: O(α) YFS exponentiated Monte Carlo for Bhabha scattering at wide angles for LEP1/SLC and LEP2", Physics Letters B,Volume 390, Issues 1–4, 1997,Pages 298-308

[27] Y. Soloviev, Private communication.

[28] " EPICS " [Online]. Available: https://epics.anl.v

[29] L. Santelj, Private communication.

[30] M. Tobiyama, Private communication.